Numerical and Experimental Investigation of Minichannel Heat Sinks with Supercritical Working Fluids

A Thesis
Presented in
Partial Fulfillment
of the Requirements for the Doctoral Degree

Nitesh Kumar

Department of Mechanical Engineering
Indian Institute of Technology Guwahati

[Nov 2022]

Dedicated to my beloved parents

Acknowledgement

I would like to convey my deepest gratitude to those who offered help and encouragement to me in different ways during the long journey of Ph.D. in IIT Guwahati.

I am very much thankful to my thesis supervisor, Dr. Dipankar Narayan Basu, for his immeasurable guidance, invaluable technical advice, and approaches to critical thinking. His thought processes and ideas aided in the methods and output of my research work. I was greatly benefited by the independent yet competitive working environment created while doing research work. By working with him, I gained experience in academic research and, most importantly, of life.

I would like to thank my doctoral committee chairman, Prof. Ujjawal kumar Saha, doctoral committee members Prof. Amaresh Dalal, and Dr. Amit Kumar for their constructive criticism and valuable suggestions during my research work.

I would like to thank my departmental colleagues and friends Dr. Milan Krishna Sinha Sarkar, Dr. Kiran Saikia, Dr. Bhaskar Jyoti Sarma, Dr. Aritra Mukherjee, Dr. Sudip Shyam, Dr. Hirakh Jyoti Das, Mr. Krishan Chand, Mr. Mukesh Sharma, Mr. Tanuj Srivastava, Mr. Ashok Kumar Gond, Mr. Biswajyoti Baishya, Mr. Pranab Sutradhar, Mr. Santanu Kumar Das, Mr. Brijesh Kumar Singh, Mr. Niraj Prasad, Mr. Abhijit Pal, Mr. Deepak Kumar Rathour, Dr. Anusuya Talukdar and Mr. Mukesh Kumar for their valuable suggestions and support during my research. I want to thank my hostel mates Mr. Deepak Kumar, and Mr. Bedobrata Ghosh whose support pushed me though the Ph.D. life.

I am grateful to my friends Mr. Utkarsh Kumar, Mr. Om Prakash, Mr. Manish Kumar Thakur, Mr. Sagar gupta, Mr. Amrendra Bharti, Mr. Maniranjan Singh for their support and encouragement.

I would like to express my sincere gratitude and affection to my parents Mr. Dilip Kumar Singh and Mrs. Munni Devi, for their incomparable love, sacrifices, and encouragement throughout the Ph.D. journey. It would not be possible without their blessings. I am thankful to my siblings, my elder brother Dr. Alok Kumar, Dr. Ashutosh Kumar, Mr. Abhishek Kumar and younger sister Vandana Singh for their constant encouragement and support for the completion of the Ph.D.

At last I would like to thank the whole Department of Mechanical Engineering and the institute for their constant supervision, guidance and support.

Nitesh Kumar

CERTIFICATE

This is to certify that the work presented in this thesis entitled "**Numerical and Experimental Investigation of Minichannel Heat Sinks with Supercritical Working Fluids**" is carried out by **Nitesh Kumar** for the award of Doctor of Philosophy in the Department of Mechanical Engineering, Indian Institute of Technology Guwahati. The thesis embodies the results of original work and studies carried out by the student himself under my supervision and has not been submitted elsewhere for a degree.

Dr. Dipankar Narayan Basu
Associate Professor,
Department of Mechanical Engineering,
IIT Guwahati, 781039, Assam.

Date: November, 2022
Place: Guwahati

Signature of Thesis Examiner

Dr. Santosh K. Sahu

Professor,
Department of Mechanical Engineering,
IIT Indore, 453552, Madhya Pradesh, India.

Declaration

I certify that

1. the work contained in this thesis is original and has been done by myself under the general supervision of my supervisors.

2. the work has not been submitted to any other Institute for degree or diploma.

3. I have followed the Institute norms and guidelines and abide by the regulation as given in the Ethical Code of Conduct of the Institute.

4. whenever I have used materials (data, theory and text) from other sources, I have given due credit to them by citing them in the text of the thesis and giving their details in the reference section.

5. the thesis document has been thoroughly checked to exclude plagiarism.

Signature of the Student

Roll No. _____

Abstract

The rapid advancement of high performance tiny electronic devices has been sparked by the growing dependence of modern human life on digitization and artificial intelligence. To ensure dependable performance during the full designated operating regime as well as a satisfactory life term, designers now face the additional problem of thermal management due to the sharp increase in the power density requirements for such equipment. Heat generation is an irreversible process, and it must be removed for components to function continuously. Since the temperature rise in the circuits is the primary cause of component failures, the thermal energy generated during operation needs to be effectively reduced for the components to operate continuously. As a result, a significant amount of study has been focused on the evaluation of alternative working fluids as well as the creation and augmentation of effective cooling strategies over the past ten years. The high area-to-volume ratio of a miniaturised or mini-channel heat sink (MCHS) and the favourable thermophysical properties of the medium have been identified as two factors that make this option particularly enticing.

Both numerical and experimental appraisal of sCO_2 is presented in the present thesis. Thorough numerical investigation have been performed to explore the steady-state, as well as transient characteristics of sCO_2. The applicability of macrochannel scaling laws explored to study the thermalhydraulic characteristics of five different supercritical fluids flowing through minichannel. Comparing supercritical fluids to single-phase and even boiling channels, supercritical fluids consistently have a higher heat transfer coefficient. As a result of the forced scaling, a significant degree of similarity has been seen in the visual character of the dimensionless momentum and heat fields as well as local recirculation patterns across the fluids. The scaling model, however, falls short when it comes to defining dimensionless groups since there are noticeable differences between local Reynolds number and local and area-averaged Nusselt number. For enhancing the used scaling methods, it is advised to take into account the Prandtl number profiles and dimensionless thermal conductivity with dimensionless enthalpy.

With a focus on the impact of local buoyancy, the numerical characterisation of thermal hydraulics of supercritical carbon dioxide flowing through a horizontal minichannel is investigated. It is discovered that buoyancy-induced local recirculation, which results from density stratification, has a significant impact on both azimuthal and axial profiles. Due to thermal asymmetry, the average heat transfer coefficient over the bottom half of the surface

is substantially higher than the same over the top half, allowing for delayed heat transfer degradation there. This discrepancy increases at larger heat fluxes but decreases with pressure. The maxima in average heat transfer coefficient corresponds to the pseudocritical temperature. Increased heat transport is aided by larger mass flux, with the peak occurring downstream. Finally, a buoyancy parameter that accurately describes the loop performance is established in accordance with the macrochannel literature.

Flow of sCO_2 is prone to heat transfer deterioration, therefore, modulation of the thermal-hydraulic characteristics of the miniaturized heat sink by geometric alteration is mandatory. In order to determine an ideal orientation and design, the current thesis evaluates the response of a square minichannel by including rectangular obstructions. The primary variable is a performance assessment criterion, which is defined as a combined change in both heat transfer coefficient and pressure drop as a result of geometric adjustment. The installation of the obstructions significantly increases the turbulent mixing between the fluid layers, resulting in a smaller temperature difference between the wall and the fluid and an improved heat transfer coefficient. A relatively lower level of temperature is maintained within the baffled section, thereby delaying the appearance of heat transfer deterioration. However, obstructions significantly increase pressure losses, making careful selection of the dimensions necessary. The most practical choice has been determined to be the employment of three pairs of baffles. Along with a thorough thermalhydraulic analysis of the role of the operating variables with the ideal design, desirable values of the height, thickness, and inclination angle for individual plates in this orientation have also been determined.

It is apparent that flow obstructions improves heat transfer performance of minichannel heat sinks but at the cost of higher pressure drop. Therefore, it is necessary to compare the thermalhydraulic performance of various flow obstacle shapes. The installation of airfoil-shaped flow obstacles in a CO_2-driven heated minichannel with a square cross-section is being investigated computationally. The use of obstacles is found to be efficient over the whole range of supply flow rate with three or more pairs, but advantageous only over a small range of Reynolds number for single and two pairs of airfoils. Performance is enhanced overall by increasing the separation between adjacent airfoils and the breadth of each obstacle, as well as by vertical orientation. The performance of an airfoil-shaped flow obstruction is superior to a rectangular one for a variety of geometric configurations, according to a study of their thermalhydraulic performance. A multi layer feed forward NN (MLFF-NN) is trained by the back propagation (BP) technique for the successful prediction of the supercritical mini channel heat sink (MCHS) performance corresponding to various geometric configurations of the heat sink and the model is able to predict the performance for several test cases with satisfactory level of accuracy.

To enlarge the corresponding experimental database for sCO_2 flow through minichannels experiments have been performed under heating conditions. The governing parameters are mainly the heat flux ($\dot{q}''$), mass flux (G), operating pressure (p), and inlet temperature (T_{in}) of the supercritical carbon dioxide. The wall temperature measurement of the test section was performed using an infrared thermal imaging camera to capture continuous wall temperature variation in the axial direction. The comparison of experimental data with

simulated results showed similar qualitative trend with largest deviation of 7.69% which is very near the uncertainty value of ±7%.In order to reach pseudocritical point with the same inlet temperature, the system needs to be heated for a longer period of time, which causes a delay in peak HTC, albeit with substantially increased magnitude. Because pseudocritical temperature is reached earlier and there is less asymmetry in the flow domain as a result, the impact of a change in system pressure is significantly less noticeable at larger heat fluxes. It is also reasonable to infer that pressure has less of an effect on HTC than does heat flux.

The stability behaviour and flow acceleration caused by variations in the non-linear thermophysical parameters have a significant impact on the supercritical fluids' capability to transfer heat. With an emphasis on the impact of flow oscillation, numerical analysis has been done to examine the transient properties of sCO_2 at supercritical pressures. A wide range of system parameters, including time period of oscillations, operating pressure, amplitude of the wall heat flux, and mass flow, have been used in the transient simulations. It is discovered that axial profiles are significantly affected by flow acceleration-induced local oscillation, which results from the fluctuation in thermophysical characteristics. Lower response times and longer transient behaviour are caused by higher mass flux. Higher operating pressure subsided fluctuation in both mass flow rate and wall shear stress, indicating that higher operating pressure can aid to reduce system instability, which is caused by the combined effect of reduced viscosity and velocity variation at higher pressure.

Contents

List of Figures

List of Tables

Acronyms

HTC	Heat transfer coefficient
$MCHS$	Minichannel heat sink
NCL	Natural Circulation Loop
$NIST$	National institute of Standard and Technology
PEC	Performance evaluation criterion
SCF	Supercritical fluid
$SCNCL$	Supercritical Natural Circulation Loop
sCO_2	Supercritical Carbon Dioxide

Greek symbols

β	Volume expansion coefficient (1/K)
Δp	Pressure difference (N/m^2)
κ	Turbulence kinetic energy (m^2/s^2)
λ	Thermal conductivity (W/mK)
μ	Dynamic viscosity ($kg - s/m^1$)
ω	Specific turbulence dissipation (1/s)
ρ	Density (kg/m^3)
θ	Angular position (-)

θ	Inclination angle (–)

Roman symbols

A	Cross-sectional area (m^2)
b	Baffle height (mm)
Bu	Buoyancy parameter (−)
d	Center-to-center distance (mm)
D	Diameter (m)
h	Enthalpy (kJ/kg)
H	Channel height (mm)
Fr	Froude number (–)
Gr	Grashof number (−)
$\dot{q}''$	Heat flux (W/m^2)
g	Gravitational acceleration (m/s^2)
G	Mass flux (kg/m^2s)
$\bar{h}, \alpha$	Heat transfer coefficient (W/m^2K)
L	Length (m)
$\dot{m}$	Mass flow rate (kg/s)
M	Molar mass (kg/kmol)
Nu	Nusselt number (–)

Pr	Prandtl number (–)
p	Pressure (N/m^2)
$\dot{Q}$	Power (kW)
Re	Reynolds number (−)
$\dot{S}_{gen}$	Entropy generation rate(kW/K)
x, y, z	Space coordinates (m)
c_p	Specific heat (J/kgK)
$\overline{\overline{\tau}}$	Stress tensor(N/m^2)
s	Specific entropy(kJ/kgK)
t	Baffle thickness (mm)
T	Temperature (K)
T^*	Normalized temperature(−)
u, v, w	Velocity components(m/s)
W	Channel width (mm)

Subscripts

ac	Accelerational
b	Bulk
$*$	Dimensionless value
eff	Effective

fr	Frictional
in	Inlet
max	Maximum
M	Model
out	Outlet
P	Prototype
pc	Pseudocritical
c_p	Specific heat (J/kgK)
w	Wall

Chapter 1

Introduction

1.1 Power Density and Miniaturization

The growing dependence of modern human life on digitization and artificial intelligence has stimulated rapid augmentation in the development of high performance miniaturized electronic devices. The steep increase in the power density requirement of such appliances has introduced the added challenge of thermal management to the designers; to ensure reliable operation over the entire designated operating regime, coupled with a satisfying life span. Heat generation is an irreversible process and heat removal is essential for the continuous operation of components. The thermal energy produced during the operation needs to be essentially removed for the continuous operation of components because the temperature rise in the circuits is the major factor for the failures of the components. Consequently, substantial research effort has been channelized in the recent decade to the development and enrichment of efficient cooling techniques and the appraisal of alternate working fluids.

The growing trend of higher packaging densities gained significant momentum with the development of the integrated circuit by Kilby at Texas Instruments and Noyce at Fairchild semiconductors in 1959. Moreover, development of small scale integration (SSI) and large scale integration (LSI) resulted in a single device per chip to multiple devices per chip. This trend continued through the development of large scale integration, where hundreds to thousands of devices per chip can be used. Then in the 1980s, the development of very large scale integration (VLSI) made integration of tens of thousands of devised per chip possible.

This trend continued further with the development of microprocessors whereas nowadays INTEL and other companies producing chips with a billion or more transistors.

The growing circuit density is accompanied by higher power dissipation per circuit which reduces circuit delay (i.e., increased speed),and the further necessity to gain packaging density and increase speed resulted in the invention of multi-chip modules from the previous decades to the present day. As shown in Fig. 1.1a, the heat load of electronic components has been documented by the thermal management consortium of 17 companies and published in collaboration with the Uptime Institute. With the heat loads depicted in the figure, the thermal management of such equipment is necessary for its optimal operation. Figure 1.1b depicts the evolution of chip heat flux and module heat flux. As it is evident from the figures that chip heat flux increased at a cumulative growth rate (CGR) of 7% per year, and heat flux associated with bipolar circuit technologies steadily increases in the beginning and then rapidly started to increase from the 1980s. After that, the ever-increasing demand for higher packaging density and performance of components has caused to increase in heat flux at a challenging rate. The cooling of components and thermal management have played a significant role in adapting to the increase in power density and at the same time preserving the temperature of components at a reasonable level to meet the performance requirement and reliable objectives. Thermal management has played a key role for all the electronic components and it will continue to do so and the increasing heat flux generated during several levels of packaging from chip to system to facility present a leading cooling challenge. Consequently, substantial research effort has been channelized in the recent decade to the development and enrichment of efficient cooling techniques and the appraisal of the alternate working fluids.

In general, the miniature systems have several advantages over macrochannels and the associated advantages includes the following:

- Compact heat exchanger design
- Smaller working fluids requirement (cast, safety and environmental benefits)
- Less weight (Important in mobile and airborne applications)
- High heat transfer capability and plant efficiency
- Low waste production (environmental impact benefits)
- Higher ratio of surface area to volume

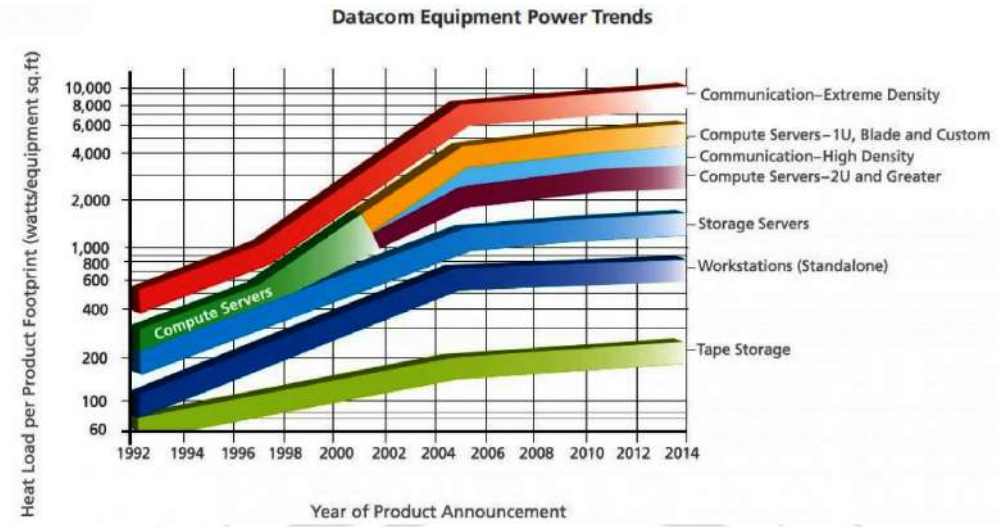

(a)

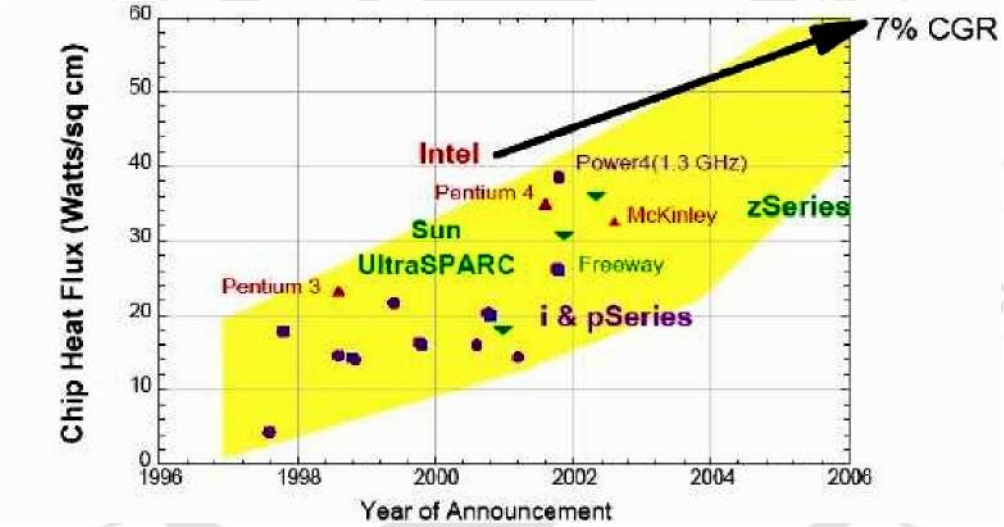

(b)

Fig. 1.1: (a) Heat load per product foot print (b) The chronological evolution of chip heat flux [1]

- Higher heat transfer coefficient for both laminar and turbulent single-phase flows
- A little rise in bulk temperature owing to lesser channel length which increases plant efficiency

The growing dependence of modern human life on digitization and artificial intelligence has stimulated rapid augmentation in the development of high-performance miniaturized electronic devices. The steep increase in the power density requirement of such appliances

has introduced the added challenge of thermal management to the designers; to ensure reliable operation over the entire designated operating regime, coupled with a satisfying life span. Consequently, substantial research effort has been channelized in the recent decade to the development and enrichment of efficient cooling techniques and appraisal of the alternate working fluids. A miniaturized or mini-channel heat sink (MCHS), fortified with supercritical fluid (SCF), has been identified as a particularly alluring choice, owing to the high area-to-volume ratio of MCHS and favorable thermophysical properties of the medium.

1.2 Mini/micro-scale Physics Involving Supercritical Fluid

A supercritical fluid is a state of fluid when it is heated above its critical pressure and temperature. The physical and transport attributes of supercritical CO_2 are rather different from those of traditional refrigerants. Generally, all thermophysical properties undergo significant changes near the critical and pseudocritical points. Figure 1.2 shows variations in various transport properties with temperature and pressure. Fluid property varies non-linearly near the critical point and with an increase in pressure, these variations become less significant. For a given pressure, specific heat increases with temperature, reaches to a peak value, and then it decreases rapidly. The point at which the value of specific heat reaches a maximum is known as the pseudocritical point (P_{pc}). As the pressure tends to critical value peak of the specific heat becomes narrower and sharper. Properties such as density and dynamic viscosity undergo a sudden drop within a very narrow temperature range, whereas specific enthalpy and kinematic viscosity undergo a sudden increase. Volumetric expansivity, specific heat, thermal conductivity, and Prandtl number have a peak near the critical and pseudo-critical points. Thermal diffusivity tends to zero as fluid reaches near to critical point and becomes highly compressible. This particular property causes the coupling process of thermal relaxation and mechanical instability. In a closed system, it causes unusual compression of thermal boundary, seen in the form of pressure waves that rapidly compresses the bulk fluid, named as piston effect (PE), which has been discovered by numerous researchers [2, 3]. The waves travel very quickly and increase the temperature of the bulk fluid homogeneously or rapidly than ordinary thermal relaxation processes by diffusion. This mechanism is also acknowledged as the fourth mode of heat transfer apart from conduction, convection, and radiation. This mechanism plays an important role in the heat transfer of a supercritical fluid. Temperature perturbation depends strongly on the piston effect; density variations are strongly dependent on the convection or diffusion effect and acoustic waves greatly affect

pressure variations. The time scales for each of these mechanisms are of great significance. The Piston effect has smaller time-scales as compared to diffusion and convection relaxations. Therefore, for supercritical fluids temperature and density equilibrium processes are usually decoupled [4]. Piston effect was proposed as the major heat transfer mechanism by Zappoli [3] based on one-dimensional Navier-Stokes equation and the van der Walls equation of state [3]. It has attracted many researchers, especially in very low gravity and thermal convection anomalies in terrestrial conditions. Onuki [2] first developed the distinctive timescale for the piston effect as:

$$t_{PE} = \frac{t_D}{(\gamma - 1)^2} \tag{1.1}$$

where $t_D = L^2/\alpha$ is heat diffusion characteristics time, and γ is specific heat ratio.

In a typical sCO_2 supercritical cycle, as cooling is realized near the pseudocritical temperature, density increases along with a local-maxima in specific heat, allowing the compressor to transport fluid with higher density, leading to reduced power consumption and improved overall thermal performance of the cycle. For optimal design and safe operation of microchannel heat exchange devices, prediction of heat transfer coefficient and pressure drop is a basic requirement. Higher pressure drop in the microchannel results in higher pumping power. Flow instability and dry-out greatly deteriorate microchannel performance. Heat transfer and fluid flow in macrochannels have been extensively investigated since the beginning of the 20th century, and theoretical and analytical models and widely-accepted empirical correlations for predicting pressure drop and heat transfer have been developed.
Although, numerous studies have been carried out on fluid flow and heat transfer in microchannels, inconsistencies in results are still encountered. Despite the higher degree of discrepancies exist among different authors it seems that while single-phase flow and heat transfer is in agreement with classical theory, two-phase heat transfer, and pressure drop cannot be properly predicted by the existing macro-scale correlations. Previous studies have reported higher heat transfer capability in microchannels than in ordinary sized large tubes. This difference is commonly explained by the fact that the physical mechanisms that are potentially dominant in microchannels are less important in macrochannels, and vice versa. However, the governing phenomena are not yet well understood and before predictions of flow and heat transfer rates in microchannels can be made with confidence, high quality, reliable experimental data is needed to resolve the discrepancies in the literature.

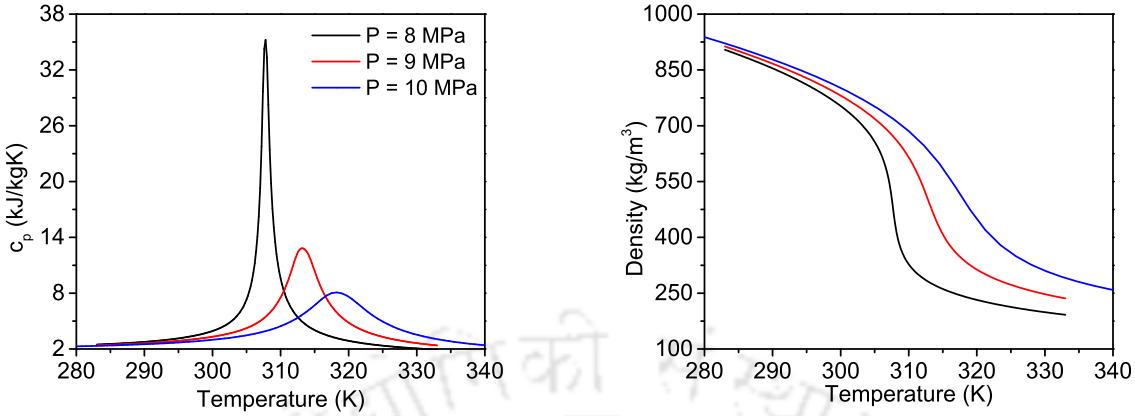

(a) Specific heat **(b)** Density

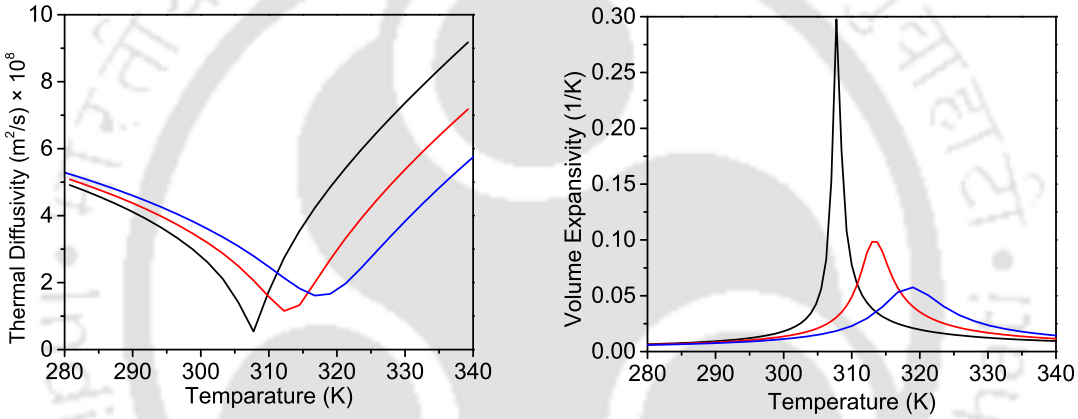

(c) Thermal diffusivity **(d)** Volume expansivity

Fig. 1.2: Variations in some important thermophysical properties of CO_2 with pressure and temperature

1.3 Application of Supercritical Heat Transfer

The growing need for higher power density and enhanced energy efficiency, owing to the depleting reserve of the conventional sources and miniaturization of devices, have necessitated researchers exploring alternate working fluids, as well as performance augmentation for the existing cycles. Supercritical fluids are of prime interest in this precise context due to their superior heat transport characteristics, particularly around the pseudocritical point. While supercritical water is being deliberated for designing Gen-IV nuclear reactors, supercritical carbon dioxide (sCO_2) has attracted special consideration in smaller utilization, primarily because of its easily-realizable critical point parameters (7.38 MPa and 304.13 K) compared

to those for water (22.06 MPa and 647.1 K). Accordingly, in recent years, newer engineering concepts involving sCO_2 have been proposed in various fields, promising improved efficiency and safety. For example, the sCO_2-based Brayton cycle is being peddled as the power generating option in gas/liquid-metal cooled thermal reactors [5], fast reactors [6], fusion reactors [7], and renewable energy systems [8]. Application of sCO_2 can also be found to develop compact gas coolers and internal heat exchangers for high-pressure transcritical compression cycles in air-conditioners and heat pumps [9, 10], and as substitute refrigerant for automotive air-conditioning systems [11].

With the extensive application of the Micro-Electro-Mechanical system(MEMS) processing technology and the rapid development of electronic packaging technologies, the high power density generated in the electronic components and devices in various high-tech fields, such as in the military, space, and automotive applications, is seriously threatening the safe and reliable operation of the equipment. Microscopical channel flow can be of big importance while treating MEMS systems and in solving the issue of high intensity microscopical heat and mass transport. In recent years, supercritical fluids have been purported in mini/micro-scale energy transfer systems. The stability and heat transfer characteristic of supercritical fluids present advantages over conventional systems and new physics have also been found in mini/micro-scale systems. Near-critical fluids are generally chosen due to their favourable specific heat and transport properties. CO_2 is more chosen as its critical operation pressure (7.38 MPa) is much lower than that of water (22.06 MPa).

1.4 Thermalhydraulics of Supercritical Fluid in Macrochannel

1.4.1 Supercritical fluid in power cycles

The first sCO_2 Brayton cycle was proposed by Sulzer [12] in 1950. In order to improve the efficiency of the cycle a single regenerative sCO_2 was developed by Feher [13]. During the 1960s, several researchers started working on the applications of the sCO_2 power cycle [13] which were mainly focused on space power generation and the ship industry. Thereafter, the sCO_2 power cycle was implemented in pressurized water reactors [14, 15], fourth generation nuclear reactors [16], small and medium sized reactors and, nuclear fusion reactors [17, 18]. The effect of different operating and design parameters on the performance and irreversibility of sCO_2 recompression cycle was investigated by Sarkar [19] using energetic and exegetic analyses. The heat transfer performance of the sCO_2 power cycle was studied by Cardemil and da silva [20]. The effect of different parameters such as type of cycles, configuration,

and different operational heat source temperatures was investigated. The thermodynamic analysis of the recompression sCO_2 power cycle generation system for high temperature gas-cooled reactors was performed by Middleton *et al.* [21]. The performance of the power cycle under dry cooling conditions was also investigated by the same group. The sCO_2 cycle was proposed as a potential application in Mochovce nuclear power station by Santini *et al.* [22]. The results showed that the sCO_2 cycle can be employed for the medium to high-temperature range only. Yu *et al.* [23] reported the development of a micro modular reactor, namely KAIST MMR, where the sCO_2 is directly used to cool the core and the need for an intermediate heat exchanger is removed. The study by [24] suggested that the performance of the sCO_2 power cycle may surpass the steam power cycle providing the heat-source temperature is above 460°C. The thermodynamic analysis and optimization of the recompressed sCO_2 cycle were performed by Hu *et al.* [25]. The efficiency of the sCO_2 Brayton cycle at a core outlet temperature of 650°C is reported as 44.9%.

Apart from nuclear power, the sCO_2 power cycle has various applications as depicted in Fig. 1.3. Other applications of the sCO_2 power cycle include solar power and geothermal power. A detailed discussion on solar power and geothermal power can be found in the review article [26–28]

Fig. 1.3: The applications of sCO_2 cycle in different industries [26] [1]

1.4.2 Supercritical fluid in transcritical heat pump

Since the development of the vapor compression refrigeration system (VCRS), the development of normally used refrigerants has been in four stages. Ethyl-ether, carbon dioxide, and ethanol which represents the first generation of refrigerants only meet the demand of providing refrigeration function [29]. Therefore, it was replaced by a freon group of refrigerants such as R11, R12, and R22. The utilization of chlorofluorocarbon (CFCs) was stopped due to the discovery of the detrimental effect of free chlorine ions present in the CFCs which causes the depletion of the ozone layer. Thereafter, under the direction of the Vienna Convention for the protection of the Ozone layer (1985) and Montreal Protocol (1987), the third generation of refrigerants that do not contain Chlorine was proposed. The proposed refrigerants are known as HFCs such as R134a, R32, R404A, R410A, and R407C. But Kyoto Protocol has enlisted the HFCs as potent greenhouse gases [30] having high global warming potential (such as 1430 for R134a) and stated that the use of HFCs should be reduced gradually by 2019 in the developed countries and between 2024 to 2028 in the developing countries(The United Nations Industrial Development Organization (UNIDO), 2017; [31]. The limitation posed by the previous generation of refrigerants impelled researchers to search for alternate refrigerants. In this respect, sCO_2 was proposed as interesting choice due to not only its zero ODP and minor GWP [32] but also decent fluidity under lower temperatures [33]. White *et al.* [34] introduced sCO_2 into high temperature heating applications and the performance of sCO_2 was enhanced in both heating and cooling with the advent of the transcritical cycle by Lorentzen and Pettersen [35]. Excellent performance of the sCO_2 cycle was reported under heating conditions by [36] with heating COP about $1.70-1.80$. In a subsequent study by [37], a CO_2 AC/HP system with a two-stage and intermediate cooling compressor was experimentally studied. At low ambient temperature and cooling temperature between 35-45°C, the heating capacity and COP enhanced by $50-132\%$ and $18.9-61.9\%$, respectively. The heating COP of sCO_2 heat pump was further investigated by Jefferies *et al.* [38] with the result showing 70% less power consumption in CO_2 heat pump than that of the resistance heating as the ambient temperature reduced from 15°Cto15°C. In further studies, the cooling performance of transcritical CO_2 systems was studied by [39, 40]. In order to further

[1]"Reprinted from Applied Thermal Engineering, 126, Ming-Jia Li,Han-Hui Zhu,Jia-Qi Guo,Kun Wang,Wen-Quan Tao, The development technology and applications of supercritical CO_2 power cycle in nuclear energy, solar energy and other energy industries, 255-275, 2017, with permission from Elsevier [OR APPLICABLE SOCIETY COPYRIGHT OWNER]." Also Lancet special credit - "Reprinted from The Lancet, 126, Ming-Jia Li,Han-Hui Zhu,Jia-Qi Guo,Kun Wang,Wen-Quan Tao, The development technology and applications of supercritical CO_2 power cycle in nuclear energy, 255-275, Copyright (2017), with permission from Elsevier."

enhance the CO_2 system performance, the performance of a two-stage compression cycle was compared with the baseline cycle with the result showing heating COP getting doubled and heating capacity getting tripled at $-40°C$ in ambient [41].

Hot water supply and building space heating has become the leading way of energy consumption among industries, commercials, and residential areas. The sCO_2 heat pump can be effectively used to heat water directly to very high temperatures [42] due to the heat dissipation process with high temperature glide in the supercritical region. The development of the transcritical CO_2 cycle by [43, 44] made CO_2 heat pump a perfect source of water heaters. In recent years, CO_2 heat pump water heater has been considered as having great potential [45] to improve energy efficiency and human life quality. Cao *et al.* [46] studied transcritical CO_2 heat pump experimentally and showed that the consumption of power in the compressor can be minimized and performance can be improved by internal-heat-exchanger (IHX). Another study by the same group showed that by using IHX, exergy destruction of the compressor, gas-cooler and evaporator can be increased while system exergy efficiency can be decreased [46]. Sarkar [47] was the first one to modify a transcritical CO_2 pump to work it as a space heater with a 25.6% enhancement in COP and a 15.4% reduction in discharge pressure. Thereafter, several improvements have been proposed to further improve its performance [48–50]

1.4.3 Supercritical fluid in natural circulation loop (NCL)

Natural circulation loops are characterized by the transportation of thermal energy from a high-temperature source to a low-temperature sink, without bringing them in direct contact. The elimination of the pump and other accessories made its fabrication and maintenance costs come down significantly. The possibility of low driving head and thermalhydraulic instabilities are a major concern for researchers and a lot of research has been focussed on studying the system stability. Chatoorgoon [51] was the first one to propose an analytical model of single-channel SCNCL to study the effect of both distributed and point heat sources and sinks. The result showed steady state mass flow rate to increase with power supply until it attains a maxima and then decreases afterward. In subsequent studies by Chatoorgoon *et al.* [52], the effect of different parameters such as heater and cooler lengths, loop height, inlet, and outlet restriction coefficients on the stability behavior of SCNCL with water, carbon dioxide and hydrogen as working fluids were studied. A general 3-D theoretical model was proposed by Yadav *et al.* [53] to study the steady-state behavior of a rectangular NCL with specified source and sink temperatures. Both water and CO_2 were chosen as the

working fluid to study thermalhydraulic aspect of NCL. sCO_2 was observed to exhibit higher velocity magnitude for all the power levels. Based on the simulation data a correlation was proposed to estimate friction factor (f) and Reynolds number (Re) in terms of Grashof number (Gr). For high temperature difference between the heater and cooler, a reduced mass flow rate was reported by [53, 54]. A similar effect with increasing heater power was also reported by *et al.* [55]. With CO_2 as a working fluid, the enhanced heat transfer coefficient was reported by Chen *et al.* [56] compared to single-phase and comparable with boiling loops. A similar observation with heat transfer coefficient as high as 1.6 kW/m^2K was reported by Tokanai *et al.* [57]. Periodic variation of Nu and pressure difference along with symmetric geometry, turbulence, and larger heater temperature can cause flow reversal. The significant variation in density across the heater cross-section induces strong buoyancy force and reduction in thermal conductivity with temperature does not permit adequate cooling in the cooler section, which causes the phenomena of reverse flow [54, 58]. The effect of orientations on thermalhydraulic performance of SCNCL was studied by Chen et al. [59] and for all vertical configurations, Nu remained the same for the entire range of power levels. However, horizontal configuration resulted in phase lag in Nu and significant deviation from lower heat flux values. In a similar study by Swapnalee *et al.* [60], horizontal-heater-horizontal-cooler configuration resulted in higher values of Re and Gr than other orientations.

The stability analysis of SCNCL was performed by Chatoorgoon [61] by developing an in-house code SPORTS which determines flow instability by introducing a perturbation in the inlet flow rate. Chatoorgoon [51] modified the SPORTS code to analyse the stability response of a rectangular loop with both distributed and point heat source and sink which is shown in Fig. 1.4. The point heat source was found to predict flow instability earlier than the distributed source. In a further study by Chatoorgoon *et al.* [52, 62], the effect of various geometric and operating parameters along with different working fluids was investigated. Another non-linear analysis code was developed by Jain and Rizwan-uddin [63]. In a subsequent study by Sharma *et al.* [64], NOLSTA code was used to investigate the instability behavior of an open CO_2 loop. A stability threshold value of 7.5 kW was predicted as 8 MPa and 297 K. At higher loop diameters, flow instability increases as the stabilizing frictional forces decrease. Step down of power resulted in reduced flow instability, whereas power step up resulted in a significant decrease in unstable oscillations. A similar observation was reported in the experimental study by Sharma *et al.* [64, 65]. It was also observed that instability occurs for all the considered cases where the heater inlet temperature was

near the critical point. A similar facility was developed by Swapnalee *et al.* [60], where no flow instability was reported for sCO_2 as a working fluid. In another study, at high pressure and very low inlet temperature, flow instability was reported by Yu et al.[66]. Chen *et al.* [56] also developed a SCNCL loop ad was found that flow pattern changes from unstable sub-critical two-phase flow to stable liquid flow, and then to stable supercritical circulation with the increase of system initial pressure.

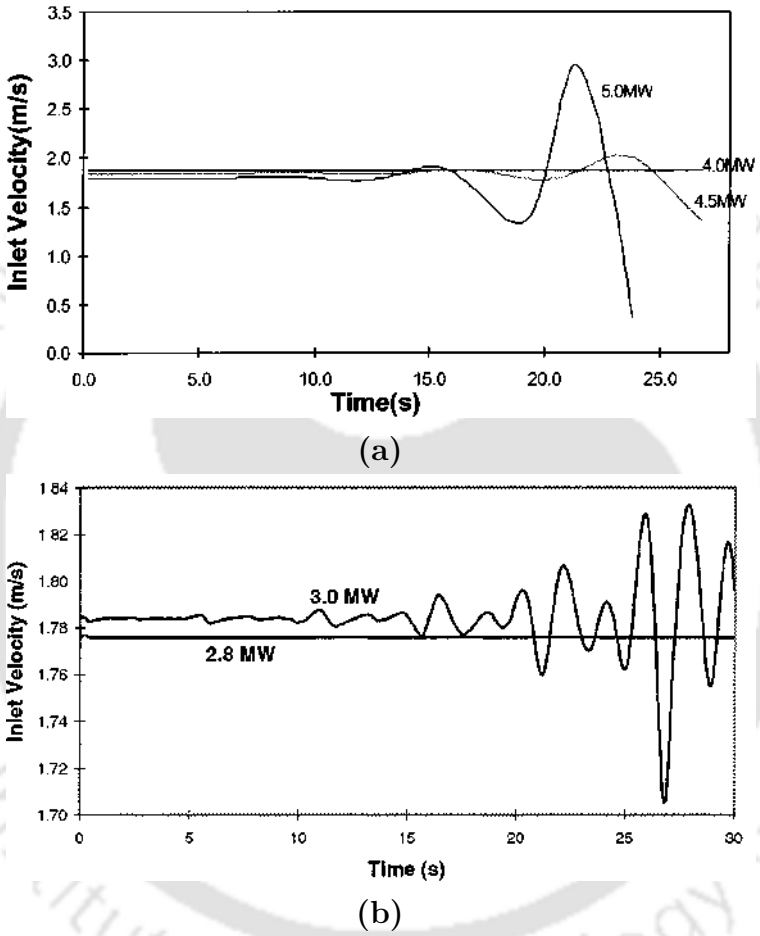

Fig. 1.4: Transient response of rectangular loop with (a) distributed (b) point heat source and sink [51] [2]

[2]"Reprinted from International Journal of Heat and Mass Transfer, 44, Vijay Chatoorgoon, Stability of supercritical fluid flow in a single-channel natural-convection loop, 1963-1972, 2001, with permission from Elsevier [OR APPLICABLE SOCIETY COPYRIGHT OWNER]." Also Lancet special credit - "Reprinted from The Lancet, 44 , Vijay Chatoorgoon, Stability of supercritical fluid flow in a single-channel natural-convection loop, 1963-1972 , Copyright (2001), with permission from Elsevier."

1.4.4 Supercritical fluid in heat exchangers

Extensive research on heat transfer in macrochannel under both forced and mixed convection using supercritical fluids has been done in past decades by numerous researchers encompassing Petukhov [67], Hall [68], Jackson *et al.* [69], Krasnoschekov [70], Yamagata *et al.* [71], Protopopov [72], Popov and Valueva [73], Kurganov and Kaptilnyi [74], and He *et al.* [75], just to name a few. Both heat transfer deterioration and enhancement have been reported depending on the operating conditions. The effect of buoyancy and flow acceleration on thermalhydraulic behavior of sCO_2 in macrochannel has also been explored, resulting in several correlations to predict the heat transfer coefficient. Song *et al.* [76] experimentally studied the flow and thermal behavior of sCO_2 in vertical channel and observed that a larger diameter channel is more susceptible to heat transfer deterioration because of the buoyancy effect. Kim and Kim [77] experimented with the upward and downward flow of sCO_2 in a channel with a hydraulic diameter of 4.5 mm. Different nature of wall temperature variation for upward and downward flows was observed, and to understand the effect of buoyancy and flow acceleration on heat transfer, two new dimensionless groups were defined. Experimental and numerical study of Jiang *et al.* [78] at low Reynolds number (less than 2500) revealed that at low heat flux, buoyancy effect and decrease of dynamic viscosity with temperature along the axial direction are not significant. At moderate heat fluxes, however, a higher heat transfer coefficient was observed, accompanied by deterioration in heat transfer performance with continual increment in supplied energy. A porous vertical channel of 4 mm inner diameter was employed by Jiang *et al.* [79]. It was observed that for inlet temperatures higher than the pseudocritical temperature (T_{pc}), heat transfer coefficient decreases along the tube. Liu *et al.* [80] experimentally studied heat transfer and pressure drop behavior of sCO_2 in circular tubes of 4, 6 and, 10.7 mm inner diameter. A correlation was proposed in terms of the average Nusselt number [81]. A similar study by Oh and Son [82] with a horizontal channel of inner diameter 4.55 and 7.75 mm reported the effects of operating pressure, inlet temperature, tube diameters, and mass flux. Decreasing the channel diameter from 7.75 mm to 4.55 mm, heat transfer improved by 8-35.6 % which was also predicted by [77]. Son and Park [83] and Yoon *et al.* [84] studied flow and thermal behavior and reported that the heat transfer coefficient exhibit peak value at the pseudocritical point and pressure drop reduces as the operating pressure was increased much higher than critical pressure. This is due to less variation in thermophysical properties in the region away from the critical point. Yoon *et al.* [84] further proposed a correlation by separating flow regimes below and above the pseudocritical point.

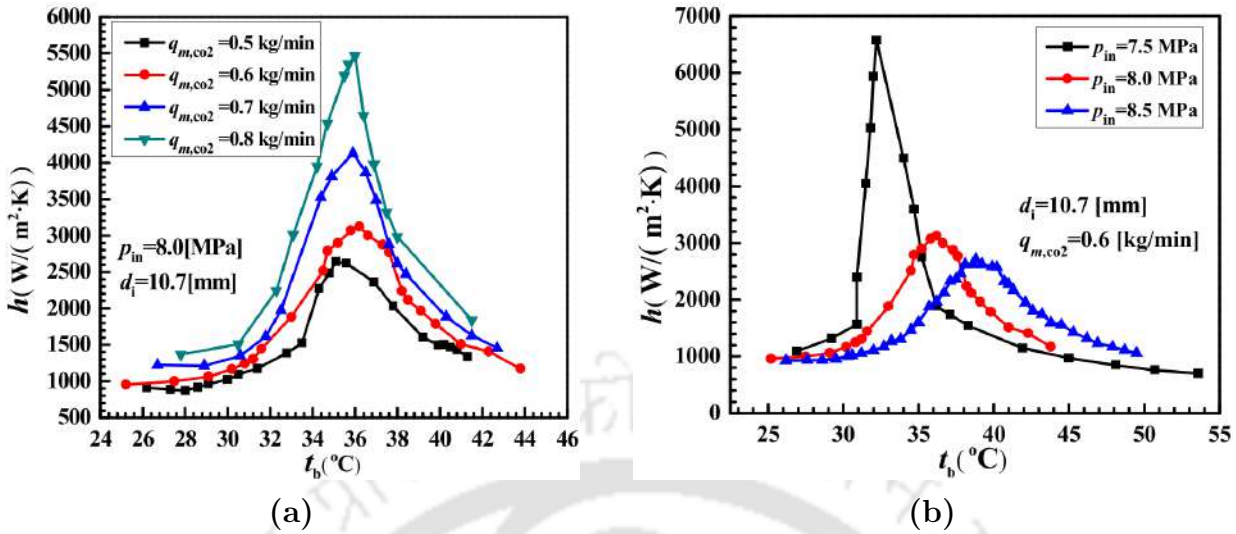

Fig. 1.5: Variations in heat transfer coefficient at different (a) mass flow rate (b) operating pressure [80] [3]

Heat transfer correlations were proposed by Bae and Kim [85] and Gupta *et al.* [86] by experimentally studying the heat transfer behavior of vertical channels under heating conditions. The correlations were proposed by taking into account the effect of buoyancy by considering the mean bulk, wall and, film temperature effect, where correlation based on mean wall temperature predicted a better heat transfer coefficient. Jiang *et al.* [79], in a vertical channel, studied the effect of flow orientation, buoyancy force, inlet pressure, and temperature on heat transfer coefficient and friction factor. In a subsequent study by Bae *et al.* [87], thermalhydraulics of sCO_2 in a heated vertical channel of 6.32 mm diameter were investigated. The effect of Reynolds number, heat flux and, buoyancy force on heat transfer behavior was studied which showed M shape velocity profile caused by thermal acceleration and buoyancy force. As an effect, a large shear stress gradient and heat transfer deterioration was observed for upward flow condition. Kim *et al.* [88] performed experiments to explore the effect of the mass flux, the heat flux, and other operating conditions on the wall temperature profile and heat transfer effectiveness in a tube of 4.4 and 9 mm of inner diameter. A correlation for normal and deteriorated heat transfer was proposed by consid-

[3] "Reprinted from Applied Thermal Engineering, 70, Zhan-Bin Liu,Ya-Ling He,Yi-Fan Yang,Ji-You Fei, Experimental study on heat transfer and pressure drop of supercritical CO_2 cooled in a large tube, 307-315, 2014, with permission from Elsevier [OR APPLICABLE SOCIETY COPYRIGHT OWNER]." Also Lancet special credit - "Reprinted from The Lancet, 70, Zhan-Bin Liu,Ya-Ling He,Yi-Fan Yang,Ji-You Fei, Experimental study on heat transfer and pressure drop of supercritical CO_2 cooled in a large tube, 307-315, Copyright (2014), with permission from Elsevier."

ering the effect of buoyancy. In another study by the same group [89], heat transfer and wall temperature profiles were studied. The experiments were performed with three different cross-section geometry namely, circular, triangular, and square under turbulent flow conditions. For non-circular cross-section, an earlier peak in wall temperature caused heat transfer deterioration with the same boundary conditions. Shiralkar and Griffith [90] reported heat transfer deterioration when wall temperature was above pseudocritical temperature and fluid bulk temperature was below pseudocritical temperature. Due to the strong buoyancy force, velocity in the boundary layer becomes higher than in the core region which caused negative shear stress at the wall. Therefore, the wall temperature exhibited a peak value due to the degraded heat transfer significantly influenced by the buoyancy force under certain heat flux and mass velocity. Depending on the operating pressure and the mass velocity, a limit of heat flux existed over which heat transfer rate significantly degraded [91]. Ankudinov and Kurganov [92], Bourke and Pulling [93], Bae *et al.* [87] and Kurganov and Kaptilnyi [94] also performed experimentation to study the heat transfer deterioration by the influence of buoyancy and other flow parameters. A similar observation was also reported by Du *et al.* [95] where heat transfer deterioration in a square annular channel with a hydraulic diameter of 13.6 mm was investigated. Heat transfer deterioration (HTD) in the form of blurred shadow was visualized near the heated wall region at lower mass flux and significant heat transfer recovery was reported at higher mass fluxes.

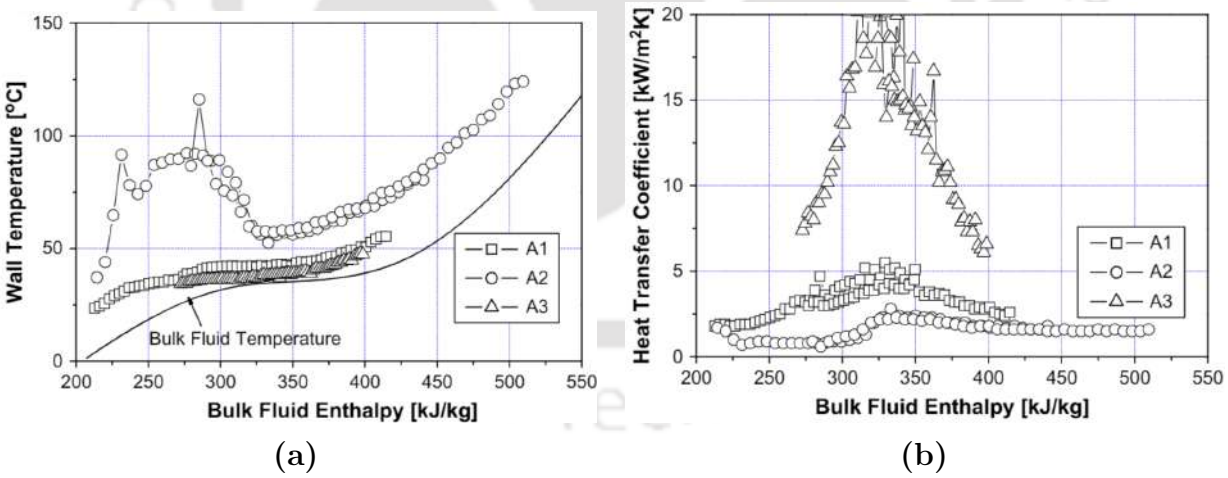

(a) (b)

Fig. 1.6: Variations of (a) wall temperature (b) heat transfer coefficient for different channel configuration [88] [4]

[4]"Reprinted from Progress in Nuclear Energy, 50, Hyungrae Kim, Hwan Yeol Kim,Jin Ho Song,Yoon Yeong Bae, Heat transfer to supercritical pressure carbon dioxide flowing upward through tubes and a narrow

Pitla *et al.* [96, 81] compared numerical results with experimental data for sCO_2 flowing in a circular channel of 4.72 mm diameter. Two different methodologies: density-weighted averaging and time averaging were adopted to solve the turbulence model. Comparing their numerically predicted values with experimental findings, a heat transfer correlation in terms of Nusselt number was proposed. Petrov and Popov [97] proposed heat transfer and friction factor correlation having relevance for sCO_2 cooled in a horizontal channel. Petrov and Popov [98] further modified the correlation using the reference temperature method. The proposed correlation has the limit of applicability: $3.1 \times 10^4 < Re_b < 8 \times 10^5$, $1.4 \times 10^4 < Re_w < 7.9 \times 10^5$ and $350 < q/G < -29$ J/kg. In another study, Lee and Howell [99] compared numerical results with experimental data with good agreement between them. A similar observation was reported in the numerical study by Zhang and Yamaguchi [100] for Reynolds number varying between 210 to 1800 in a circular channel of 6 mm diameter. The augmentation of heat transfer coefficient was observed with increasing mass flux and wall heat flux. Liu *et al.* [101] numerically investigated the effect of buoyancy on heat transfer of sCO_2 in a heated channel. The result showed the occurrence of heat transfer deterioration when Bu is greater than 1.3×10^{-4} and recovery of heat transfer starts to begin as Bu crosses 1.8×10^{-4}. With further increase in Bu, enhanced heat transfer was observed when Bu crosses 5×10^{-4}. Two different velocity profile characteristics were observed: (a) the appearance of a zero velocity-gradient region and (b) a steep slope of the velocity gradient profile near the wall. The steep slope enhances the sensitivity of the velocity gradient to the flow development. The thermalhydraulics of sCO_2 during upward and downward flow under cooling conditions were investigated numerically by Guo *et al.* [102]. The result showed minimum local entropy generation near the pseudocritical point corresponding to the enhanced heat transfer. The entropy generation due to pressure drop was lesser than entropy generation due to heat transfer. The buoyancy has the opposite effect on flow direction with enhanced heat transfer during upward flow and heat transfer deterioration during downward flow. Moreover, an upward flow was associated with more uniform entropy generation, which confirms that an upward flow is associated with less irreversibility.

annulus passage, 518-525, 2008, with permission from Elsevier [OR APPLICABLE SOCIETY COPYRIGHT OWNER]." Also Lancet special credit - "Reprinted from The Lancet, 50, Hyungrae Kim,Hwan Yeol Kim,Jin Ho Song,Yoon Yeong Bae, Heat transfer to supercritical pressure carbon dioxide flowing upward through tubes and a narrow annulus passage, 518-525, Copyright (2008), with permission from Elsevier."

[5]"Reprinted from Energy, 256, Jiangfeng Guo,Jian Song,Zengxiao Han,Konstantin S. Pervunin,Christos N. Markides, Investigation of the thermohydraulic characteristics of vertical supercritical CO_2 flows at cooling conditions, 124628, 2022, with permission from Elsevier [OR APPLICABLE SOCIETY COPYRIGHT OWNER]." Also Lancet special credit - "Reprinted from The Lancet, 256, Jiangfeng Guo,Jian Song,Zengxiao Han,Konstantin S. Pervunin,Christos N. Markides, Investigation of the thermohydraulic characteristics of

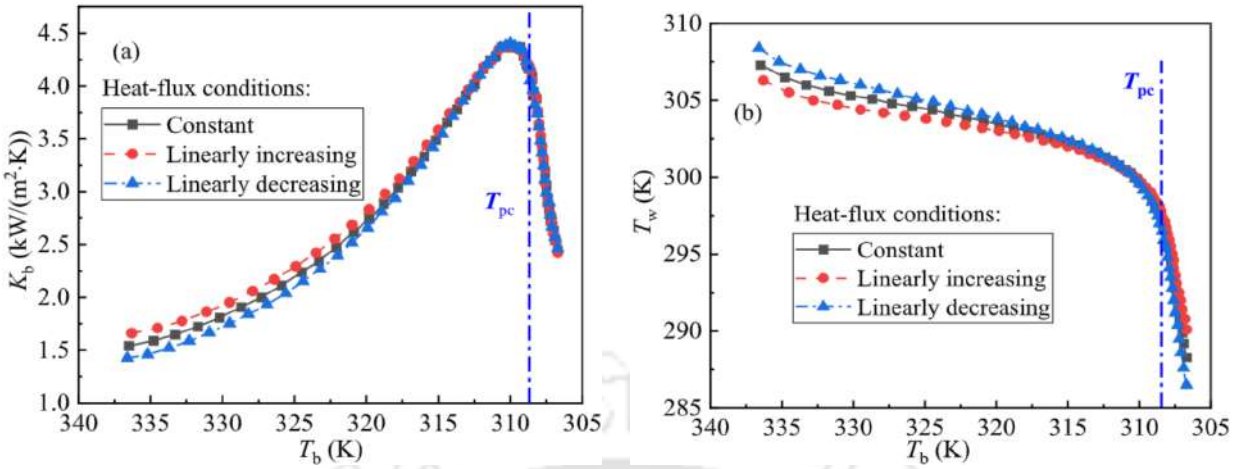

Fig. 1.7: Variations in (a) heat transfer coefficient and (b) wall temperature for three different heat flux boundary conditions [102] [5]

While most of the above studies are for macrochannel, researchers recently have shown an increased inclination towards exploring the flow and thermal characteristics of sCO_2 in minichannel owing to the requirement of high-intensity heat and mass transportation. Here the classification proposed by Kandlikar and Grande [103] is followed to categorize a channel according to its dimension, which identifies a duct with hydraulic diameters within 3 mm and 200 μm as minichannel. The most important factor which differentiates minichannels from microchannels is that formers are less susceptible to heat transfer deterioration, and due to high surface area/volume ratio, an enhanced rate of heat transfer can be obtained.

1.5 Thermalhydraulics of Conventional Fluid in Mini/micro Channel

The physical state of the cooling fluid has found particular attention, with each of the single-phase, two-phase, two-component, non-Newtonian, and nano-fluids being explored. Various numerical and experimental studies have been conducted on understanding the two-phase-flow heat transfer through miniature systems. Pfahler *et al.* [104] studied the fluid flow and friction factor of N-propanol flowing through a rectangular microchannel. The result showed, pressure drop decreases with the Reynolds number in the smallest diameter

[5] vertical supercritical CO_2 flows at cooling conditions, 124628, Copyright (2022), with permission from Elsevier."

channel and the polar nature of fluids significantly affects the friction factor. Yu *et al.* [105] investigated the flow of nitrogen and water in different mini/microchannels and showed that the value of the friction factor depends on the relative surface roughness. In a similar study by Hwang and Kim [106], the pressure drop of R134a as working fluid was reported. Thermalhydraulic comparison of HCFC123 and FC-72 was reported by Yen *et al.* [107] and comparison with analytical laminar value showed good agreement for the Reynolds number range of 20-265. Celata *et al.* [108] investigated water flow in a microchannel both experimentally and analytically, in the Reynolds number range from 20 to 4000. Shilder *et al.* [109] conducted an experimental investigation for single-phase flow in a microchannel that had a hydraulic diameter of 0.6 mm. Admas *et al.* [110] performed experimental work in the turbulent region with water flow in circular microchannels of diameters 0.76 and 0.109 mm. Based on their data, a correlation to predict the Nusselt number and friction factor were predicted.

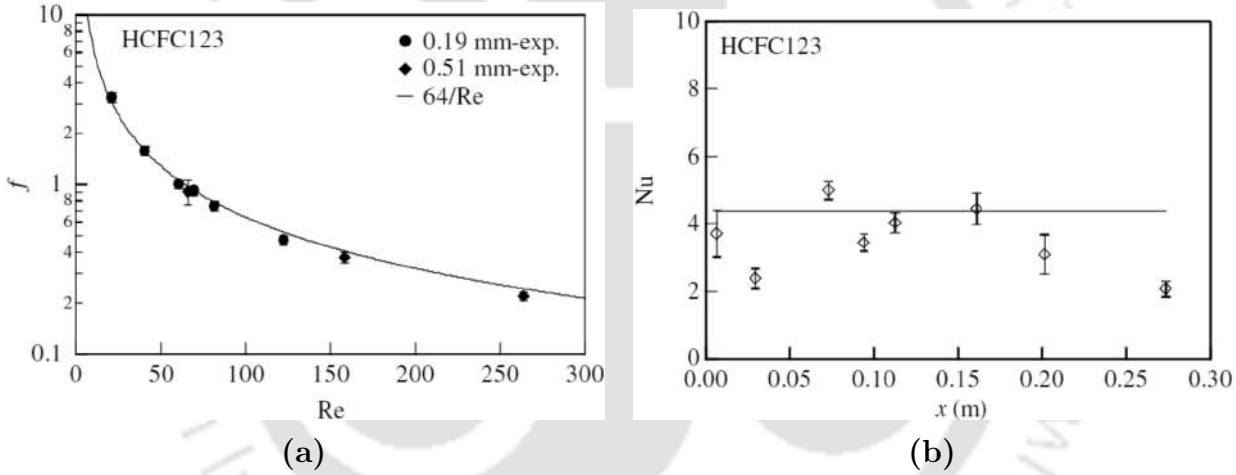

Fig. 1.8: Variations in (a) friction factor and (b) Nusselt number for single-phase flow [107] [6]

The flow boiling heat transfer performance investigated by Park and Hrnjak [111] with CO_2 at a mass flux of 200 kg/m^{2}s indicated a large influence of nucleate boiling, whereas those at a mass flux of 400 kg/m^{2}s indicated that the convective boiling contribution to heat flux was significant, especially at low heat flux conditions. Dang *et al.*[112] investigated the

[6]"Reprinted from International Journal of Multiphase Flow, 29, Tzu-Hsiang Yen,Nobuhide Kasagi,Yuji Suzuki, Forced convective boiling heat transfer in microtubes at low mass and heat fluxes, 1771-1792, 2003, with permission from Elsevier [OR APPLICABLE SOCIETY COPYRIGHT OWNER]." Also Lancet special credit - "Reprinted from The Lancet,29, Tzu-Hsiang Yen,Nobuhide Kasagi,Yuji Suzuki, Forced convective boiling heat transfer in microtubes at low mass and heat fluxes, 1771-1792, Copyright (2003), with permission from Elsevier."

thermalhydraulic behavior of carbon dioxide boiling in a single smooth tube and a microfin tube with 2 mm internal diameter and an area enlargement ratio equal to 2. The result showed that heat flux had a significant effect on the heat transfer coefficient in both the microfin and smooth tubes. A similar observation was also reported by Ducoulombier *et al.* [113] and Gao *et al.* [114] in their experimental study. In a study by Miyata *et al.* [115] a correlation to predict heat transfer coefficients with vaporization of HFCs, CO_2, and water in minichannels. This takes into account nucleate boiling, forced convection evaporation and evaporation heat transfer through thin liquid film around vapor plugs in slug flow. Maqbool *et al.* [116] showed that the dryout heat flux for propane increases with increasing mass velocity, with the decrease in vapor quality and with the increase in internal diameter. In another study by the same group(Maqbool *et al.* [117]), the boiling of Ammonia was investigated. For a channel with 1.7 mm, the heat transfer coefficient is strongly dependent on heat flux, whereas for the 1.224 mm channel, it is a function of heat flux only at lower quality and vapor quality affects HTC significantly at higher qualities.

Jovanovic *et al.* [118] experimentally and numerically studied thermalhydraulics of water-toluene and ethylene glycol/water-toluene as liquid-liquid flow in channels with 248 and 498 μm internal diameter. It was observed that film velocity does not affect pressure drop. Two-phase flow of oil-water in a T junction horizontal microchannel was experimentally investigated. Pressure drop, two-phase flow patterns, and wettability of oil-water were studied. Heat transfer enhancement with mineral oil with water droplets as working fluid was numerically studied by Ubrant *et al.* [119] Heat transfer performance was reported to be significantly enhanced by making oil drops in water and increasing the oil droplet size. This was due to enhanced flow circulation in the droplets and flow disruption due to droplets. Che *et al.* [120] studied the heat transfer coefficient of a liquid plug flowing through a microchannel. It was observed that shorter plugs lead to higher transverse velocity which eventually leads to a higher heat transfer coefficient. In another study by the same group Che *et al.* [121], the heat transfer behavior of two immiscible water-mineral oil fluid flow. The influence of droplet length, the aspect ratio of channel cross section and the Peclet number (Pe) on heat transfer of droplet based microchannel with constant wall temperature was investigated. It was observed that the heat transfer coefficient is enhanced due to flow recirculation both in droplet and continuous phase which was also reported by Ubrant *et al.* [119]. A 100 μm internal diameter microchannel with water as coolant with light mineral oil or silicon oil was investigated by Bandara *et al.* [122] to characterize the heat transfer at Reynolds numbers ranging from 4.9 to 21.9. The results showed that the Nusselt number enhanced by up to

200% with liquid-liquid flow compared to single-phase flow.

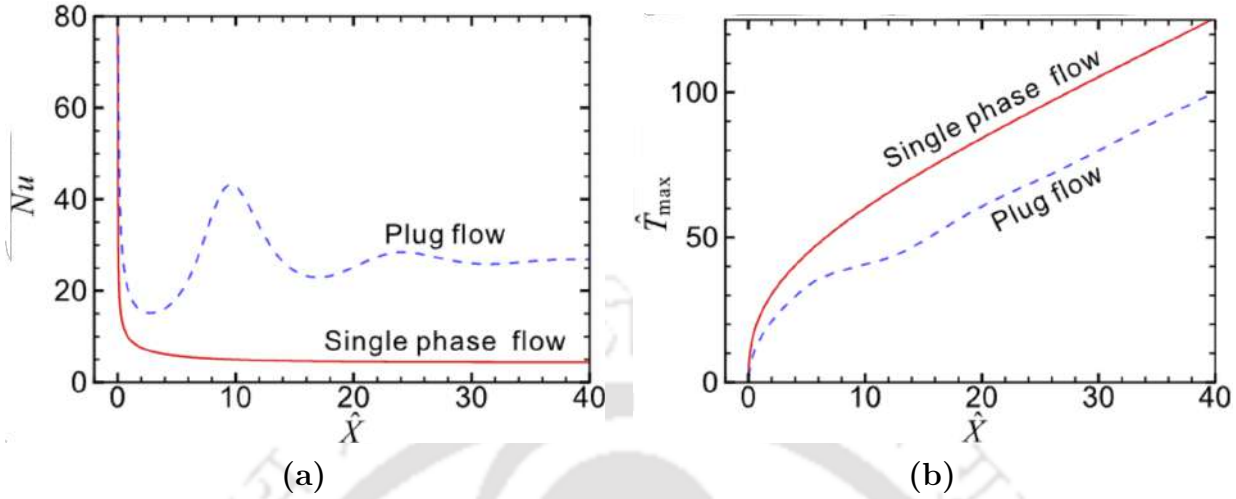

Fig. 1.9: Evolution and comparison of (a) Nu and (b) maximum fluid temperature for plug flow and single phase flow [121]

Asthana *et al.* [123] studied experimentally the heat transfer of Water-light mineral oil in a six turn Serpentine microchannel with a square cross-section of dimensions 100 × 100 μm. The presence of oil slug caused flow circulation and disruption of boundary layers which leads to enhanced mixing and heat transfer. Moreover, a Nusselt number value of up to four times was observed for water-oil slug flow compared to pure water flow. In another liquid-liquid flow heat transfer was experimentally investigated by Eain *et al.* [124] considering Pd5, Dodecane, and AR20 silicon oils with water as working fluids and infrared thermography were utilized to measure wall temperature. It was observed that the heat transfer coefficient was enhanced up to 600% with immiscible liquids as working fluids and the heat transfer rate increased by decreasing the carrier slug length and increasing the dispersed slug length. Moreover, maximum heat transfer augmentation of flow happens with carrier slug length of channel diameter. In a similar study by Dai *et al.* [125] heat transfer behavior of Water-hexadecane in a vertical circular channel with uniform heat flux boundary conditions on the walls. The experiments and numerical results were in good agreement and a correlation to predict heat transfer was proposed.

1.6 Thermalhydraulics of Supercritical Fluids in Mini/micro Channel

Huai *et al.* [126] studied heat transfer and pressure drop characteristics in a horizontal multiport channel under cooling conditions. The test section consists of 10 multiport aluminium circular channels having an inner diameter of 1.31 mm, length 500 mm, width 20 mm, and thickness 2 mm. Experiments were performed for the pressure varying from $7.4 - 8.5$ MPa, inlet temperatures ranging from 22-53 °C, heat flux from $0.8 - 9$ kW/m^2, and mass flux from $113.7 - 418.6$ kg/m^{2}s. It was reported that pressure drop and heat transfer coefficient changes drastically near the pseudocritical point. The pressure drop increases with increasing mass flux and it decreases with increasing operating pressure. With the decrease in operating pressure and increasing mass flux, heat transfer coefficient was reported to be enhanced with peak value appearing near the pseudocritical point. Based on experimental data a new correlation was proposed which reasonably predicts the heat transfer in a horizontal multiport channel with a maximum relative error of 30%. Liao & Zhao [127] experimentally studied supercritical CO_2 heat transfer in a horizontal and vertical channel having diameters of 0.7 mm, 1.4 mm, and 2.16 mm under heating conditions. Experiments were performed for pressure varying from $7.4 - 12$ MPa, temperature varying from $20 - 110$ °C, and mass flow rate varying from $0.02 - 0.2$ kg/min. The heat transfer coefficient for downward flow was reported to be lowest in three different flow configurations namely, upward flow, downward flow, and horizontal flow. Also, the heat transfer coefficient decreased as the channel diameter was reduced. Three different correlations were proposed for horizontal flow, upward flow and downward flow. The correlation for horizontal flow showed maximum relative error of 21.8% and mean relative error of 13.5% with experimental results. The correlation for upward flow showed a maximum relative error of 18.6% and a mean relative error of 12.3% with experimental results, whereas the correlation for downward flow showed a maximum relative error of 22.4% and a mean relative error of 15.6% with experimental results. In a subsequent study by Dang and Hihara [128] with pressure ranging from $8 - 10$ MPa, heat flux ranging from $6 - 33$ kW/m^2, mass flux ranging from $200 - 1200$ kg/m^{2}s and channel diameter ranging from $1 - 6$ mm. With increasing heat flux, a reduction in the peak value of the heat transfer coefficient because of decreasing cross-sectional mean specific heat was reported. Also, this reduction is relatively less under the cooling condition as compared to the reduction under heating conditions. For $T_b > T_{pc}$, heat transfer coefficient increases with increasing heat flux because of increasing thermal conductivity and specific heat with heat flux, whereas for

$T_b < T_{pc}$, heat transfer coefficient is less affected by varying heat flux due to the reason that thermal conductivity increases but specific heat decreases. With the increase in inlet pressure peak value of the heat transfer coefficient decreases and the greater the pressure more significant drop in the peak value of heat transfer coefficient is observed. A higher heat transfer coefficient is reported at higher heat flux because of increasing turbulent intensity as mass flux increases.

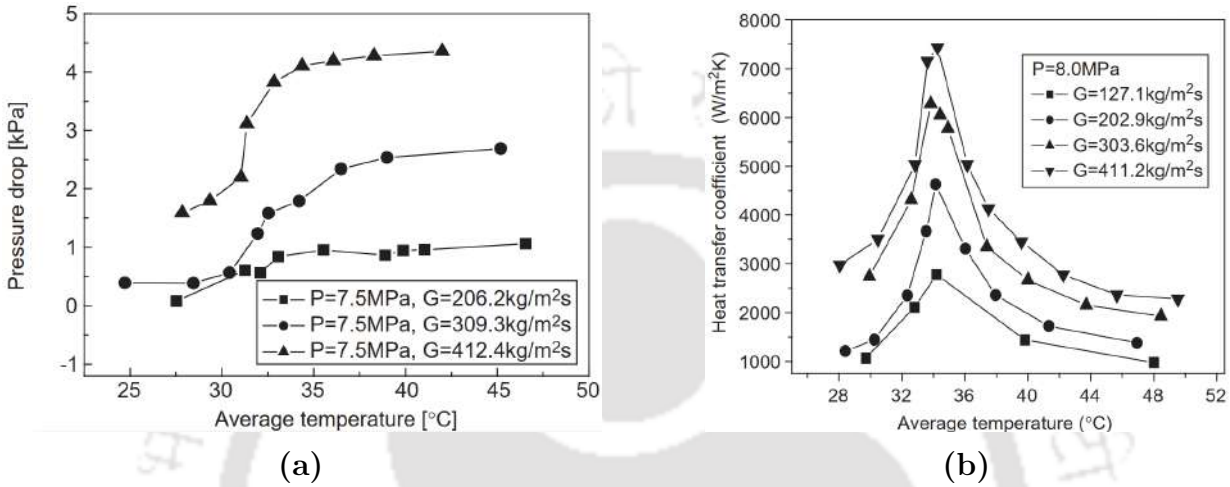

(a) **(b)**

Fig. 1.10: Variations in (a) pressure drop and (b) heat transfer coefficient with mean fluid temperature [126] [7]

Convective heat transfer of sCO_2 is investigated by Jiang *et al.* [78] in a vertical tube at a low Reynolds number (less than 2500). In upward flow and moderate heat flux ($8.90 - 35$ kW/m^2)condition, local wall temperature does not increase continuously but even decreases along the flow direction. This is due to the transition of flow from laminar to turbulent which improves heat transfer and reduction of viscosity along the channel. For large heat flux ($61 - 94$ kW/m^2) condition, local wall temperature increases, then decrease and again increases along the channel. Downward and high heat flux ($20 - 95$ kW/m^2) conditions resulted in a continuous increase in local wall temperature. Buoyancy induced transition of flow from laminar to turbulent in downward flow resulted in improved heat transfer coefficient compared to upward flow condition. For both upward and downward flow, an initial increase

[7] "Reprinted from Chemical Engineering Science, 60 , X.L. Huai,S. Koyama,T.S. Zhao, An experimental study of flow and heat transfer of supercritical carbon dioxide in multi-port mini channels under cooling conditions, 3337-3345, 2005, with permission from Elsevier [OR APPLICABLE SOCIETY COPYRIGHT OWNER]." Also Lancet special credit - "Reprinted from The Lancet, 60, X.L. Huai,S. Koyama,T.S. Zhao, An experimental study of flow and heat transfer of supercritical carbon dioxide in multi-port mini channels under cooling conditions, 3337-3345, 2005, with permission from Elsevier."

in heat flux resulted in a higher heat transfer coefficient with further increase causing heat transfer reduction. Moreover, heat transfer enhancement due to buoyancy occurs along the entire channel length in downward flow conditions whereas heat transfer improves in the latter part of the channel only in upward flow conditions. In a similar study of heat transfer in vertical mini-tube by Xu *et al.* [129] based on continuous wall temperature distribution with pressure ranging from $7.6 - 9.5$ MPa, heat flux ranging from $12 - 63$ kW/m^2, mass flux ranging from $255 - 685$ kg/m^{2}s, and channel diameter 0.953 mm. An infrared thermometer has been utilized to find continuous wall temperature distribution and gather more information on abnormal heat transfer phenomena. The experimental results showed that for y^+ at $T_f(r) = T_{pc}$, less than 5, the buoyancy effect causes heat transfer deterioration in downward flow conditions and heat transfer enhancement in upward flow conditions. Also, the onset of heat transfer deterioration in a vertical channel under upward flow condition occurs at $y^+ = 5$. The study of Guo *et al.* [130] in a minichannel ($d = 2$ mm) for pressure ranging from $7.6 - 8.4$ MPa, heat flux ranging from $100 - 200$ kW/m^2, and mass flux ranging from $400 - 700$ kg/m^{2}s. Reduction in heat transfer coefficient is reported with an increase in heat flux and a decrease in mass flux. The effect of change in pressure on the heat transfer coefficient is insignificant. Under high heat flux, heat transfer deterioration occurs due to pseudo film boiling. The effect of buoyancy remains significant which is reflected by temperature asymmetry at a particular cross-section. A new correlation was proposed for sCO_2 under high $q^{"}/G$ condition with a maximum deviation from experimental data with a maximum error of less than 15%. The proposed correlation is recommended for $q^{"}/G$ ranging from $250 - 500$ J/kg.

Numerical simulation of sCO_2 and water turbulent heat transfer in the vertical channel was performed by Bovard *et al.* [131] using RSM turbulent models to investigate the effect of mass flow rate and pressure on heat transfer performance, flow acceleration, and buoyancy. Increasing mass flow rate resulted in lower wall temperature, buoyancy and flow acceleration in the vertical channel. A larger effect of non-dimensional heat flux on flow acceleration compared to the Reynolds number was reported. A correlation data was proposed with maximum variance with the experimental data within $\pm$ 30%. Direct numerical simulation of heat transfer in a vertical tube coupled with buoyancy and flow acceleration was reported by Cao *et al.* [132]. In upward flow conditions, higher heat flux leads to a sharp increase in wall temperature. However, in downward flow conditions, no significant effect of heat flux was observed. The heat transfer behavior displays four developing periods in which buoyancy and flow acceleration show alternate dominant behavior. For upward flow, the

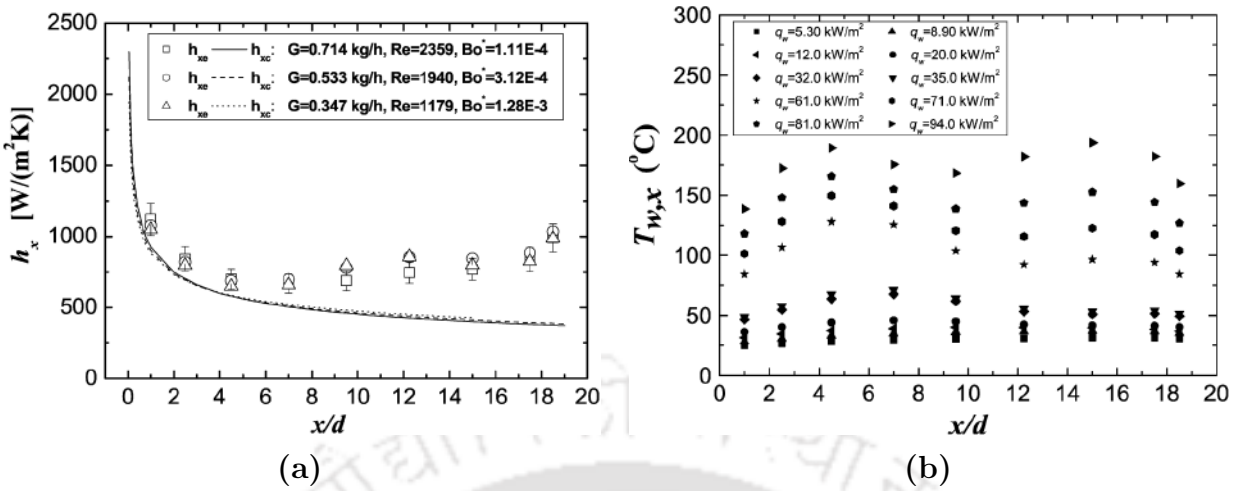

Fig. 1.11: Variations in (a) local heat transfer coefficient and (b) local wall temperature for upward flow [78]

buoyancy effect shows dominant behavior in the first two periods and thermal acceleration becomes dominant in the later periods. This is because the density gradient requires larger time scale to develop, and thermal acceleration takes effect later. The generative mechanism of the turbulent structure showed the streak becomes regular and wide in acceleration region and in the deteriorated heat transfer region, the streamwise vortices are reduced. The flow acceleration was anisotropically distributed and stretches the vortices until it destroys. Direct numerical simulation of sCO_2 heat transfer in vertical channels of hydraulic diameter 1 to 2.5 mm was performed by Pandey *et al.* [133]. A parametric study was performed to study the effect of mass flux, channel diameter and inlet temperature on the flow and thermal behavior of sCO_2. Increasing mass flux yields higher Nu which is due to increases turbulent intensity at higher mass flux. Also at lower mass flux, the peak of Nu shifted towards the inlet because bulk fluid temperature reaches pseudocritical temperature earlier at lower mass flux. With increasing inlet temperature, Nu decreases because of lower specific heat and thermal conductivity at higher temperature. Moreover, shifting of the peak of Nu towards the inlet was also reported at higher inlet temperature and it disappeared after 306 K. For the same inlet conditions, smaller diameter channels gives a higher heat transfer coefficient.

Chu and Laurien [134] explored a horizontal minichannel employing DNS for low inlet Reynolds number($Re = 5400$), and reported flow stratification and circumferential variation, while providing an extensive appraisal of turbulence statistics. The result showed circumferential variation in wall temperature as well as inhomogeneous distribution of skin friction

coefficient. The wall temperature on the top half surface was significantly higher compared to that on the bottom half surface. Buoyancy induced secondary flow occurs due to density difference which carries heated fluid to the top surface and resulted in higher wall temperature at the top half surface. Due to the motion of low velocity flow near the wall, an anchor shape high velocity profile is observed. Moreover, shear induced by reduced velocity gradient and Reynolds shear stress suppresses turbulent production near the top surface. This further suppresses turbulent kinetic energy and leads to significant flow stratification and reduced convective heat transfer. In a further study by Chu and Laurien [135], direct numerical simulation was performed to study sCO_2 in a heated vertical channel. The inlet Reynolds number was kept at $Re = 5400$ to ensure the dimensionless resolution requirement. In forced convection flow, turbulent kinetic energy reduces due to flow acceleration caused by thermal expansion. In upward flow with mixed convection, relaminarization of flow occurs which follows turbulence recovery in the downstream direction due to the buoyancy effect. This process reduces Reynolds shear stress to zero and changes its sign to negative eventually leading to heat transfer deterioration. Under downward flow conditions, buoyancy has the opposite effect, leading to increased flow turbulence and heat transfer enhancement. Numerical investigations for horizontal channels under cooling conditions were reported by Xiang *et al.* [136] to yield similar conclusions to Pandey *et al.* [133]. The effect of buoyancy leads to higher wall temperature at the top surface compared to the bottom surface. The heat transfer coefficient was found to be higher at the bottom half surface, while temperature stratification and secondary flow was observed because of the buoyancy effect. Asymmetric radial velocity and turbulent kinetic energy profiles were also observed owing to the buoyancy effect, an observation similar to Cao *et al.* [132]. The heat transfer coefficient peak occurs earlier on the bottom surface than on the top surface. Heat flux was found to have no effect on the peak of the heat transfer coefficient. Moreover, buoyancy force has a significant effect on heat transfer behavior before the pseudocritical point whereas the effect subsided after the pseudocritical point.

In another study by Cao *et al.* [137], a direct numerical study was performed to ascertain the effect of buoyancy and thermal acceleration on the flow of sCO_2 in a heated vertical channel. The coupling of buoyancy and thermal accelerations leads to the growth of a streamwise velocity profile, which affects the turbulent intensity by hindering the energy transition from the average flow kinetic energy to the turbulent kinetic energy. Four different phases of heat transfer were observed. For the first two phases, the buoyancy force is a dominating factor to affect heat transfer. This is because the bulk density gradient taking

time to develop, therefore effect on thermal acceleration comes later than the buoyancy effect. As the fluid transitions to supercritical fluids, the bulk density gradient becomes insignificant and the effect of buoyancy becomes a significant factor to decide heat transfer behavior in the last phase. Two different parameters namely, $A_{c,bulk}$ and $A_{c,near-wall}$ were proposed to identify significant factors in deciding heat transfer in different phases. The numerical study performed by Xu *et al.* [129] showed that when pseudocritical points exist inside the laminar sublayer, heat transfer enhancement occurs for upward flow and it deteriorates for downward flow. This is due to increased velocity gradient under upward flow conditions and decreased velocity gradient under downward flow condition due to buoyancy. Thermalhydraulics of sCO_2 flow in a semi-circular channel were numerically ascertained by Kruizenga *et al.* [138] to propose a new correlation for the Nusselt number by modifying the Jackson correlation.

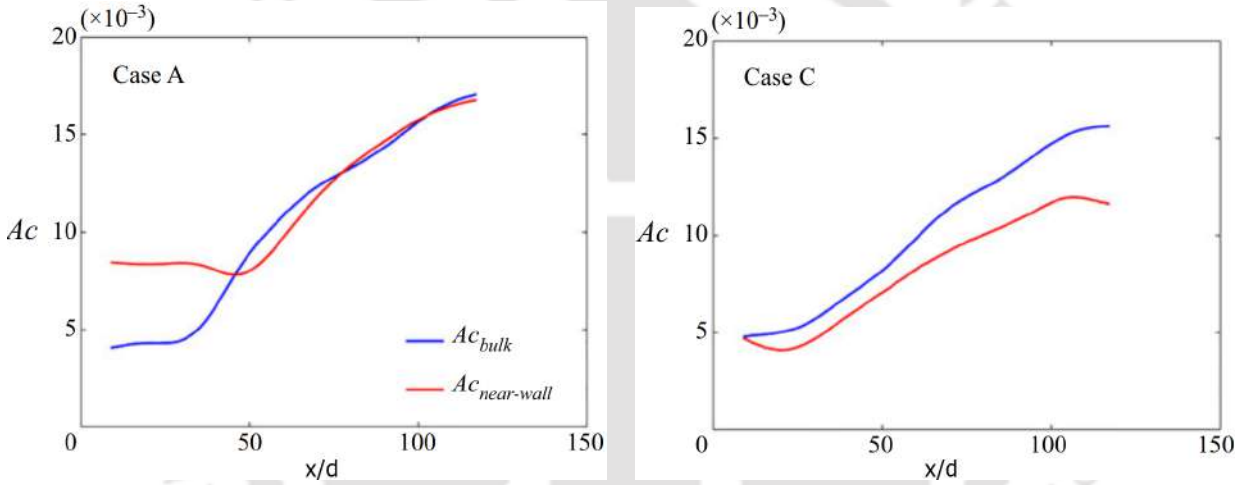

Fig. 1.12: Variations in Ac_{bulk} and $Ac_{near-wall}$ [137]

The thermalhydraulic characteristics of supercritical fluid flowing through non-adiabatic mini-/microchannel can be significantly different from the conventional macrochannels. As noted by [139] during their experiments involving six tubes having diameters in the range of 0.50 to 2.16 mm, the effect of buoyancy diminishes with the reduction in the tube diameter and existing heat transfer relations over-predict considerably. The use of different relations for horizontal, upward, and downward flows was suggested in another work of theirs, conceding mean relative errors of 13.5%, 12.3%, and 15.6% respectively [127]. Jiang *et al.*[78] observed no deterioration during both upflow and downflow in a 0.27 mm-diameter vertical tube, primarily because of the inconsequential role of buoyancy in such a slender channel. Another work from the same group [140], involving a pipe diameter of 0.0992 mm, also

reported the same trend, substantiating flow acceleration as the factor governing the rate of heat transfer in such dimensions. A novel thermal management approach with sCO_2 as working was investigated by Fronk and Rattner [141] and thermalhydraulics of single-phase liquid water and FC-72, two-phase boiling R-134a, and sCO_2 were discussed. The result showed that sCO_2 yields lowest heat-sink wall temperature than other considered working fluids. For heat flux up to 650 kW/m^2, the required pumping power is the lowest of other single and two-phase fluids, which suggests that an equivalent volumetric flow rate and potentially greater cooling capacity can be achieved at lower pumping power requirements for sCO_2. The effect of non-uniform heat flux on sCO_2 based MCHS was investigated by Nabil and Rattner [142] using large eddy simulations (LES). The results showed non-uniform heat transfer coefficients due to mixed convection induced flow stratifications similar to other studies. All available correlations were to be under-predict heat transfer coefficient at higher heat fluxes ($q^{"} = 58$ - 62 kW/m^2). A new criterion to quantify the peak of HTC was found to correspond to the bulk temperature attaining T_{pc} during the experiments of [143], while the authors provided a scrupulous analysis of the influence of both buoyancy and acceleration effects at miniscale. As the bulk fluid temperature increases above pseudocritical temperature, the heat transfer coefficient decreases monotonically. Increasing the heat flux causes a peak in the heat transfer coefficient to attenuate and for the same applied heat flux, an increase in the mass flux will cause an increase in the average heat transfer coefficient. These general trends are in agreement with prior work. The heat transfer correlations proposed for cooling conditions in the present study failed to predict the heat transfer data with reasonable accuracy. A more comprehensive design recommendation in a subsequent study was proposed by Jajja *et al.* [144]. It was proposed that at high heat fluxes ($\geq$ 50 kW/m^2) and low mass fluxes ($\leq$ 500 kg/m^2s), microchannel equipment with a higher aspect ratio is preferred over square channels. This is because a high aspect ratio suppresses the flow acceleration for equivalent heat and mass fluxes. Moreover, the results showed that MCHS performance is independent of its orientation for microchannel with aspect ratio 1.

1.7 Summary of Literature Review

Application of supercritical and near-critical fluids has offered improvement in the associated fluid flow process and energy conversion efficiency. Surely, the analysis and designing

[8]"Used with permission of [American Society of Mechanical Engineers ASME], from [High-Flux Thermal Management With Supercritical Fluids, Brian M. Fronk and Alexander S. Rattner, 138, 12 and 2016]; permission conveyed through Copyright Clearance Center, Inc."

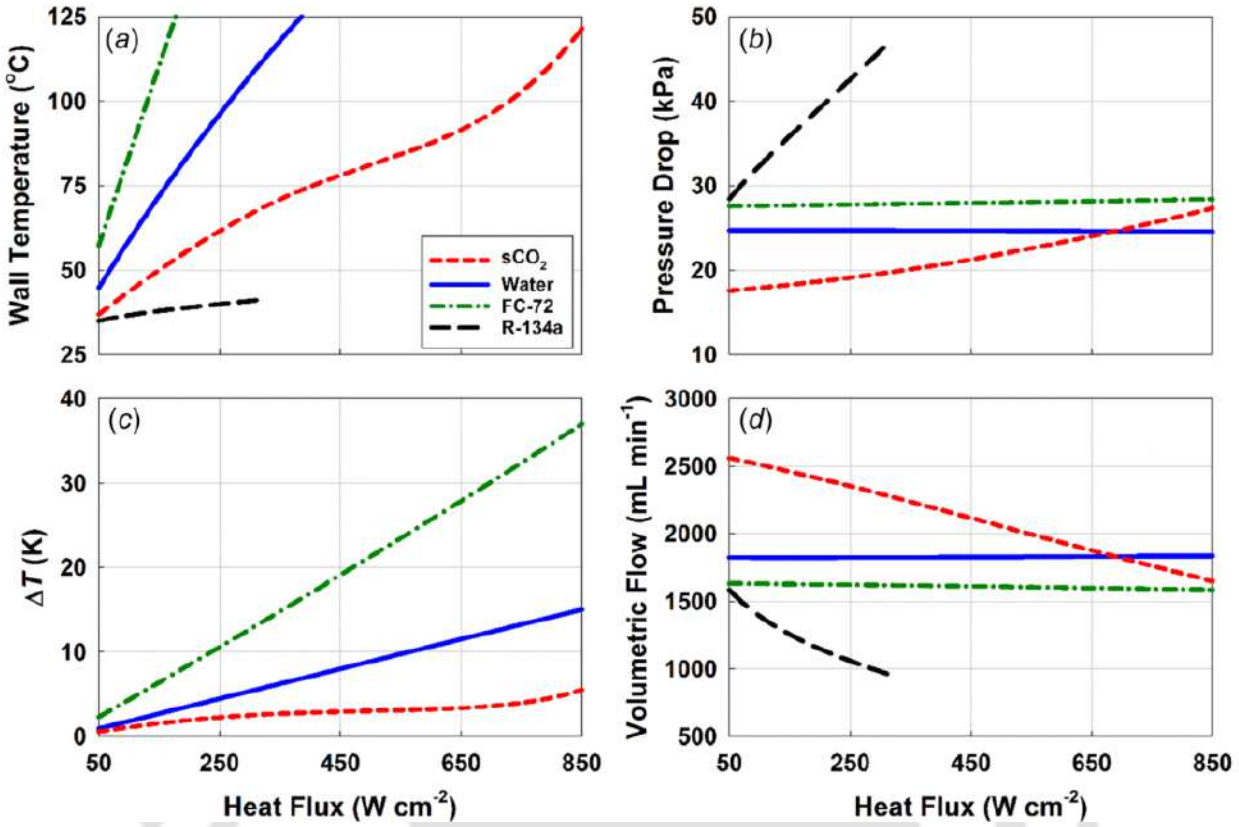

Fig. 1.13: Comparison of (a) average wall temperature, (b) pressure drop, (c) temperature change, and (d) inlet volumetric flow rate for water, FC-72, sCO_2, and two-phase R134a at pumping power of 0.75 W [141] [8]

of supercritical fluid based systems are mainly dependent on how the flow dynamics of supercritical flow could be understood and controlled. The flow dynamics and transport mechanism associated with macro scale systems are not suitable for mini/micro scale systems. Hence, the investigation of the behaviors of supercritical fluids in mini/micro has become necessary and an important need. It is therefore very much evident that, despite immense practical relevance, a substantial void exists in the research database on sCO_2 flow through minichannel. Besides, a scrupulous literature survey suggests that most of the reported efforts concern cooling conditions, to suit HVAC applications, and primarily vertical orientation, which negates the local buoyancy effects. However, the heat transfer characteristics of the horizontal channel under heating conditions can considerably deviate from that depending on the imposed conditions and unexpected wall temperature variations are pertinent under heating conditions [145]. With the advent of mini- and micro-sinks, and progressively higher power density requirements in electronic cooling applications, horizontal heated mi-

crochannels also become a very germane configuration, necessitating a comprehensive study to envisage the concerning dynamics of the supercritical flow. Consequently, the flow variables are expected to experience complete three-dimensional variations, making it difficult to predict the same through simple scaling laws, which are often based on one-dimensional conservation equations. Localized effects like circulation and azimuthal variation are also more prominent with the reduction in channel dimension, making the macroscale scaling principles vulnerable to minichannels. Buoyancy-induced flow stratification in horizontal boiling channels is a well-established fact, that demands a regime-specific-approach during modelling. Current consideration of SCF-filled minichannel, despite being a very new topic, is quite similar, and hence, careful deliberation is imperative while imposing scaling rules developed for macrochannels to the ones with smaller characteristic dimensions.

A careful review of the available literature review suggests that no research where the thermalhydraulics of supercritical fluids in mini/micro channels in the presence of flow obstruction was explored. The intrinsic thermalhydraulics of minichannel in the presence of flow obstruction are likely to exhibit interesting features due to complex local flow dynamics owing to non-uniform velocity and temperature distribution inside the channel. The relative distribution of velocity and temperature field plays a significant role in heat transfer behavior. Moreover, the influence of different geometric parameters associated with the baffles plays a vital role in accomplishing an optimum design with the most worthwhile performance. Insights into the primary design variables under consideration such as the height, thickness, and inclination angle of the individual obstructions could shed light on intricate details, which might be beneficial to understand the flow dynamics in the presence of flow obstruction. The role of operating variables, such as heat flux, mass flux, pressure, and inlet temperature, also needs to be explored in the preferable configuration. The present study can be viewed as an important step leading to the incorporation of microscale geometries in MCHS, specifically involving supercritical heat transfer.

The literature review suggests that MCHS with flow obstruction results in an extreme pressure drop. Heat performance and fluid flow are often a trade-off between heat transfer maximization and pressure drop minimization. In most cases, enhancing heat transfer means enhancing pressure drop too, thereby providing conflicting objective functions. Minimizing the pressure drop is an important requirement in the thermal management of high-heat-flux electronic systems. Increasing pressure drop is undesirable in electronic systems because an appreciable pressure drop significantly increases the required pumping power, and the corresponding increase in power consumption compromises the energy efficiency of the entire

system. Moreover, drastic pressure changes can severely degrade the reliability of electronic devices. Thus, except for applications in which pressure drop and pumping power are not an issue, a trade-off between these two performance indicators needs to be achieved. For this purpose, multi-objective optimization can have a primary role. Therefore, attempts need to be made on optimizing cooling fluids and the geometric shape and arrangements of micro-fins for optimizing the overall thermal performance.

A scrupulous literature survey suggests that there has been some emphasis on exploring the flow oscillations during the transient behavior of supercritical fluids flowing through mini/micro channels. The transient flow behavior of supercritical fluids could offer a better understanding of thermoacoustic and thermal-induced flow oscillations. Important to acknowledge that the application of non-uniform wall heat flux has not been explored extensively which could give better insight thermal relaxation process associated with supercritical fluids flow.

1.8 Research Objectives

From the above discussions, it may be inferred that several aspects of supercritical fluid dynamics are yet to be investigated in the purview of thermalhydraulics characterization. Accordingly, the scope of the present dissertation is outlined as follows.

1. Thermalhydraulic assessment and performance comparison of several supercritical fluids in a minichannel using macroscopic scaling laws.

2. Thermalhydraulic assessment and design optimization of incorporating flow obstructors in a supercritical minichannel heat sink

3. Investigation into the thermalhydraulic of supercritical carbon dioxide flowing through miniature channel by Infrared Thermography.

4. Flow dynamics in transient heat transfer of carbon dioxide at supercritical pressure in microchannel.

1.9 Outline of the Thesis

1. Chapter 1: This chapter deals with the introduction and historical background of the requirement of miniaturization, its practical application, and its advantages. There-

after, extensive literature survey on the use of conventional and supercritical fluids is discussed with the importance and relevance of supercritical fluids in mini-/microchannel in heat transfer enhancement.

2. Chapter 2: This chapter deals with the computational investigation of CO_2, R134a, N_2O, NH_3, and C_2H_4 as working fluids in a minichannel under heating conditions. The equivalent boundary conditions were obtained using scaling analysis and the thermal-hydraulic behavior of all fluids is compared.

3. Chapter 3: This chapter represents the computational investigation of CO_2 as working fluids in a minichannel under heating conditions with special emphasis on the effect of buoyancy. Three-dimensional turbulent simulations are performed over a reasonably wide range of system pressure, heat flux, and mass flux.

4. Chapter 4: This chapter deals with the numerical investigation of a sCO_2-filled heated square minichannel, designed with flow obstructions in the shape of rectangular baffles. The influence of different geometric parameters associated with the baffles has been investigated systematically to accomplish an optimum design. The primary design variables include the height, thickness, and inclination angle of the individual obstructions.

5. Chapter 5: This chapter represents a comparison of rectangular shaped obstructions and airfoil shaped obstructions in MCHS. Thereafter, the optimization of different geometric parameters associated with the baffles has been obtained using genetic algorithm (GA) based artificial neural network (ANN) methodology.

6. Chapter 6: This chapter deals with the experimental investigation of sCO_2 flowing through minichannel under heating conditions. Effect of different parameters such as heat flux, mass flux, inlet temperature, and operating pressure on steady state behavior of sCO_2 is discussed.

7. Chapter 7: This chapter deals with the two-dimensional simulation of sCO_2 inside a microchannel under transient heat flux boundary conditions.

8. Chapter 8: This chapter deals with the conclusion and future recommendations.

Chapter 2

Thermalhydraulic comparison of supercritical fluids in MCHSs

2.1 Preamble

The utilization of SCF, however, is primarily restricted to macrochannels till now, to suit the conventional applications, with only sporadic appearances in miniature geometries. Following [146], a minichannel can be characterized by a length scale of 0.2-3 mm, which perfectly is in accord with the requirement of MCHS. Examples of SCF-driven MCHS is quite rare in open literature, with the uncertainty about the choice of working fluid being a possible reason. Heat transport characteristics of any SCF on either side of the pseudocritical temperature (T_{pc}) can be radically diverse, while T_{pc} itself is a nonlinear function of pressure. Critical temperature (T_c) for common fluids also differ extensively, ranging from 5.3 K for helium to 647.1 K for water, making it difficult to facilitate a fluid-to-fluid comparison. A probable solution can be envisaged by defining a complete set of scaling rules, with consistent dimensionless groups, capable of representing the relative strength of relevant thermalhydraulic forces. A few such efforts are available in open literature to propose suitable dimensionless groups for SCFs forced through heated channels [147–149], a brief review of which is available in [150]. Similar approach has been used in nuclear water reactor where the feasibility of performing experiments using water under supercritical conditions is limited by technical and financial difficulties. These difficulties can be overcome by using model fluids that are characterized by feasible supercritical conditions, that is, lower critical pressure and critical temperature. Several research work has been performed to recognize suitable fluid-to-fluid scaling methodology to investigate the thermalhydraulics of water cooled nuclear reactor. A

extensive scaling analysis can be found in the study by [151–153]. Jackson and Hall[154] used three dimensionless numbers to scale pressure, bulk fluid temperature and mass flux, and suggested two others for scaling heat flux and heat transfer coefficient. A novel approach was proposed by Ambrosini and Sharabi [155], analogous to the classical phase-change and subcooling numbers employed for boiling channels, evaluating the reference properties at the pseudocritical point. That was subsequently extended by Ambrosini [156] to compare heat transfer characteristics of multiple fluids, including NH_3, H_2O and CO_2, with NH_3 exhibiting more similarity to water compared to CO_2 and R23. Cheng *et al.* [157], however, predicted greater feasibility of R134a as a model fluid to SC water, following their novel proposal, where a product of pseudo-boiling number, Reynolds number and Prandtl number was used for heat flux scaling and a distortion approach for mass flux. Reasonable accuracy was reported for their validation studies. Another interesting numerical attempt toward fluid-to-fluid scaling of heat transfer characteristics of SCFs using RANS models was reported by Pucciarelli and Ambrosini [158]. The dimensionless results showed amicable similarity or repeatability over the entire range of heat flux and mass flux considered by them. In their follow-up study [159], the same formulation was employed for scaling with a variety of fluids at supercritical pressure, subsequently emphasizing on maintaining similar expansion characteristics of the fluids within the heated section. The Zahlan-Groeneveld-Tavoularis (ZGT) fluid-to-fluid scaling principles [160] were adopted by Mouslim and Tavoularis [161] to characterize vertical upflow of H_2O, CO_2 and R134a in a 8 mm diameter tube. The scaling errors in the region of deterioration was reported to be noticeably larger than normal heat transfer regions, and the same was attributed to the difference in contours of thermophysical properties around T_{pc}. The importance of boundary conditions on predictions was emphasized by Kassem *et al.* [162]. A novel dimensionless group was proposed by Yu *et al.* [163], which signified relative enthalpy rise per unit length of the test section, thereby encompassing the experimental conditions and fluid types. Their predictions showed 3% and 2% respective average deviation from R134a to H_2O and CO_2 with the experimental data. All such scaling suggestions provided necessary impetus toward the planning of experiments involving SCFs, and also facilitated fluid-to-fluid comparison to envisage the thermalhydraulic characteristics of heat sinks involving variety of fluids.

All the studies mentioned above, however, concern conduits with macro-level dimensions. While there have been quite a few recent research efforts to explore the thermalhydraulic characteristics of SCF-filled minichannels, lack of consensus is palpable, primarily owing to the scant database. A scrupulous literature review suggests that some of the available ones

concern cooling condition in vertical ducts for HVAC applications [164–166], which negates the local buoyancy effects. On the contrary, flow of SCF through heated horizontal channel can experience considerable deviation depending on the imposed boundary conditions [167, 134, 168, 130]. Presence of non-axisymmetric profile in horizontal flows, originating because of the local buoyancy effects, is one of the consistent observations. Consequently, the flow variables are expected to experience complete three-dimensional variations, making it difficult to predict the same through simple scaling laws, which are often based on one-dimensional conservation equations. Localized effects like circulation and azimuthal variation are also more prominent with reduction in channel dimension, making the macro-scale scaling principles vulnerable for minichannels. Buoyancy-induced flow stratification in horizontal boiling channels is a well-established fact, which demands regime-specific-approach during modelling. Current consideration of SCF-filled minichannel, despite being a very new topic, is quite similar, and hence, careful deliberation is imperative while imposing scaling rules developed for macrochannels to the ones with smaller characteristic dimensions.

That prepares the backdrop for the present study, where the thermalhydraulic characteristics of several SCFs are compared for a specified minichannels, while adopting an existing set of scaling laws, developed originally for macrochannel. Here the focus is on identifying the most suitable heat transport fluid for MCHS, while also analysing the suitability of macroscopic scaling rules for such configurations. Five different SCFs have been selected, and their performances as coolant have been compared in terms of the dimensionless groups proposed by Ambrosini and Sharabi [155]. More details about the modelling and simulation procedure are available in the next section.

2.2 Development of Computational Model

2.2.1 Physical geometry

A heated horizontal minichannel is considered as the domain of interest, schematic representation of which is available in Fig. 2.1. It is a cylindrical tube of 2 mm diameter and 840 mm length, where an upstream adiabatic section of length of 240 mm is provided to ensure the flow to be fully-developed at the entrance to the heated section, which, in turn, is subjected to uniform wall heat flux. Mass flux at the inlet and uniform pressure at the exit plane are specified as the boundary conditions.

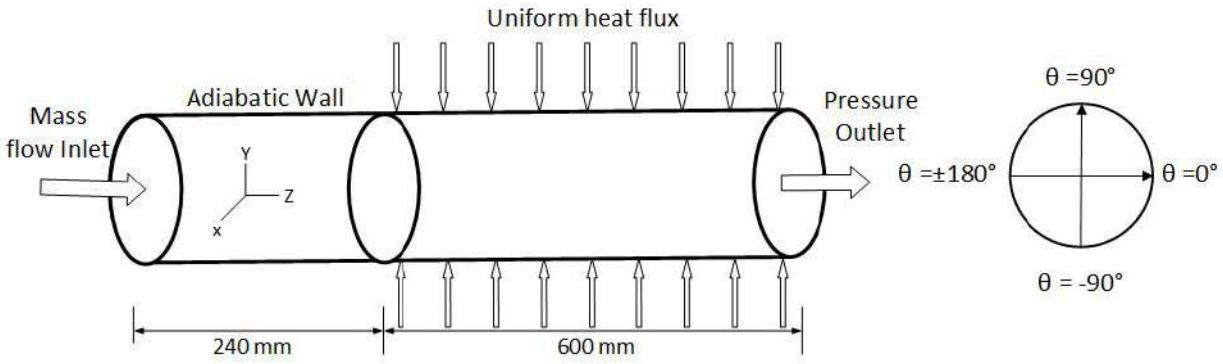

Fig. 2.1: Schematic representation of the computational domain

2.2.2 Governing equations

Steady-state mass, momentum and energy conservation equations are summarized below, three-dimensional versions of which in Cartesian coordinate are solved as a part of the present study.

$$\nabla \cdot (\rho \mathbf{w}) = 0 \tag{2.1}$$

$$\nabla \cdot (\rho \mathbf{w}\mathbf{w}) = -\nabla p + \nabla \cdot \bar{\bar{\tau}} + \rho \mathbf{g} \tag{2.2}$$

$$\frac{\partial}{\partial t}(\rho h) + \nabla \cdot (\rho \mathbf{w} h) = \nabla \cdot (k \nabla T) \tag{2.3}$$

Here $\mathbf{w}$, ∇p and $\bar{\bar{\tau}}$ are the local velocity vector of the fluid, the pressure gradient and the stress tensor respectively, while $\mathbf{g}$ is the gravitational acceleration. h, ρ and k are respective indicators of the enthalpy, density and thermal conductivity of the fluid being explored.

As mentioned above, the scaling laws defined by [155] have been adopted in the present study, using the mass flux (G), channel length (L) and the pseudocritical point properties to formulate the reference quantities. They envisaged analogy of supercritical flow channels with the boiling ducts and treated the pseudocritical temperature (T_{pc}) similar to the saturation temperature along an isobar. As the differentiation between the liquid and vapor phases is non-existent for any SCF, the ratio of the change in volume across the vapor dome to the same in enthalpy reduces to the concerned derivative ($\frac{v_{fg}}{h_{fg}} \rightarrow \frac{\partial v}{\partial h}$). Accordingly, replacing the saturated liquid properties with the pseudocritical ones, the following dimensionless

definitions can be identified.

$$\rho^* = \frac{\rho}{\rho_{pc}} \qquad \Delta p^* = \frac{\rho_{pc}\Delta p}{G^2} \qquad h^* = \frac{\beta_{pc}}{c_{p,pc}}(h - h_{pc}) \qquad T^* = \beta_{pc}(T - T_{pc})$$
$$Re_L = \frac{GL}{\mu} \qquad Pr = \frac{\mu c_p}{k} \qquad Fr_L = \frac{G^2}{\rho_{pc}^2 g L} \tag{2.4}$$

with β, μ and c_p respectively being the volumetric expansion coefficient, dynamic viscosity and isobaric specific heat, and T being the absolute local temperature. The characterizing dimensionless groups, namely, Re_L, Fr_L and Pr, involve nodal thermophysical properties, and hence are local in nature. For all the combinations of control variables considered here, Re_L is of the order of 10^4, necessitating the adoption of a turbulence model, and the SST $\kappa - \omega$ scheme is incorporated here. It theoretically has the dual advantage of using $\kappa - \omega$ in the bulk flow and $\kappa - \epsilon$ in the near-wall region, and is quite common for simulation of SCF [169–171].

2.2.3 Scaling methodology

In order to perform fluid-to-fluid comparison through scaling, it is necessary to designate a fluid as the reference. CO_2 has found reasonable level of acceptance as the working fluid in macrochannels, particularly with applications such as transcritical heat pumps and reactor core cooling [172, 173, 59, 174], mostly because of its favourable critical temperature. Therefore, CO_2 is considered as the reference fluid in the present work, and the operating conditions for the other fluids, namely, R134a, NH_3, C_2H_6 and N_2O, are identified using the scaling parameters. Critical point properties for all the five fluids involved here are detailed in table 2.1. Among the selected ones, R134a is having lowest critical pressure, while its critical temperature is also not very high, and can be suitable for the moderate temperature-level heat sinks. Ammonia, on the contrary, has the highest levels of both T_c and p_c, and can be adept for high-temperature applications. Ethane seems to have a very favourable combination of T_c and p_c, while the critical-point parameters, as well as the molar mass, for N_2O are remarkably similar to that of CO_2, and may well be an able substitute.

It is imperative to impose precisely-scaled boundary conditions for each of the fluids, to ensure equivalence of the operating parameters. To analyze the minichannel shown in Fig. 2.1, the required conditions are exit pressure, inlet temperature, mass flux and heat flux, and the scaling procedure for each are delineated below.

Table 2.1: Critical point properties of the fluid under consideration [175]

Fluid	**M** (kg/kmol)	$\mathbf{T_c}$ (K)	$\mathbf{p_c}$ (MPa)	ρ_c (kg/m^3)
Carbon dioxide CO_2	44.01	304.13	7.377	467.6
Tetrafluoroethane $C_2H_2F_4$ (R134a)	102.03	374.21	4.060	511.9
Ammonia NH_3	17.03	405.40	11.333	225.0
Ethane C_2H_6	30.07	305.32	4.872	206.2
Nitrous oxide N_2O	44.01	309.52	7.245	452.0

2.2.3.1 Scaling of pressure (p)

The first step in achieving proper fluid-to-fluid scaling is the identification of equivalent system pressures among the working fluids under consideration, and that can be attained following the variations in the thermophysical properties with temperature along several isobars. At a specified pressure, both enthalpy and density of a supercritical fluid are functions of temperature alone, and experience shows that the dimensionless versions of these two properties (h^* and ρ^* respectively), defined earlier, follow a unique relationship at their respective equivalent pressures, regardless of the fluid itself. To facilitate a proper comparison, CO_2 at 8 MPa pressure is selected as the reference condition and the corresponding $\rho^* - h^*$ profile is presented in Fig. 2.2(a) using Refprop [176]. Subsequently, the $\rho^* - h^*$ profiles of each of the other fluids are plotted on the same plane at different pressures, to identify the one exhibiting the closest allegiance. A demonstration with N_2O is presented in Fig. 2.2(a). Definitely the most amicable consonance is evident at a pressure level of 7.5 MPa and therefore, the same can be earmarked as the equivalent pressure for NH_3 to CO_2 at 8 MPa. The same procedure is repeated for the remaining three fluids, till a gratifying level of correspondence is achieved for each, and the perceived magnitudes are marked in Fig. 2.2(b). It is possible to identify equivalent pressures with any other choice of reference condition and reference fluid, adhering to the same procedure. It can be seen that, there is some deviation among the profiles in the liquid-like (higher density) region, mostly because of the difference in their respective molecular structures [177]. Fluids, however, adhere perfectly to the principles of corresponding states in the gas-like region, and profiles virtually overlap

with each other.

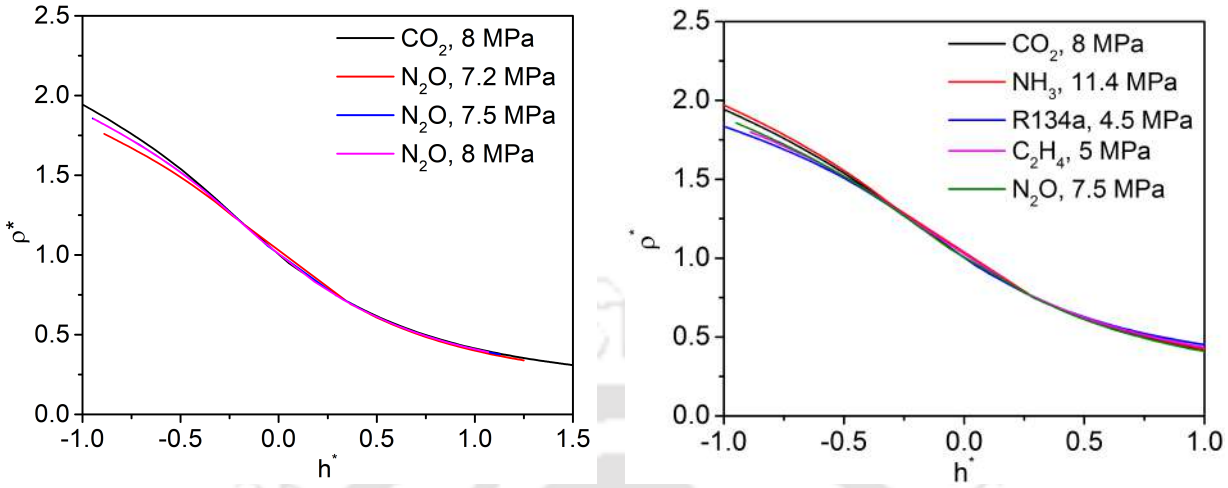

(a) Identification of equivalent pressure for N_2O **(b)** Equivalent pressures for all the five fluids

Fig. 2.2: Variation in dimensionless density (ρ^*) with dimensionless enthalpy (h^*) for the fluids under consideration at their respective equivalent pressure levels, with CO_2 at 8 MPa pressure as the reference condition

2.2.3.2 Scaling of inlet temperature (T_{in})

In order to warrant equivalence of the inlet temperature, the dimensionless enthalpy at the inlet plane is maintained identical for all the fluids, *i.e.*, $h^*_{CO_2}|_{in} = h^*_{other}|_{in}$. The true value of the inlet temperature is subsequently estimated from the knowledge of this h^* and p identified in the previous step [175]. It is pertinent to mention here that the pressure variation along the channel length is ignored while calculating the inlet temperature. As can be found later, the magnitude of the inlet-to-exit pressure differential ($\sim 1-2$ kPa) is inconsequential in comparison to the exit pressure, and hence, this assumption is not expected to invoke any significant impact on calculations. The thermophysical properties at different computational volumes, however, are estimated using the local pressure and temperature only.

2.2.3.3 Scaling of mass flux (G)

The procedure described by [157] is employed for scaling of the mass flux through the channel by forming a Pi-group involving all the three dimensionless numbers available ($\Pi = Re_L^{n_1} Pr^{n_2} Fr_L^{n_3}$). As per their postulate, the mass flux scaling must ensure the similar-

ity of the heat transfer characteristics in the zone of normal heat transfer, which is commonly affiliated with low heat flux or temperatures sufficiently away from T_{pc}. The Dittus-Boelter relation can be assumed to be valid in such regions, demanding the equality of the group $Re^m Pr^n$ between the model and prototype. Accordingly, setting $n_3 = 0$, and choosing values of n_1 and n_2 for a conventional heating channel, the scaling relation can be defined at the inlet plane as:

$$\left(Re^{0.8} Pr^{1/3}\right)_P = \left(Re^{0.8} Pr^{1/3}\right)_M \tag{2.5}$$

2.2.3.4 Scaling of heat flux ($\dot{q}''$)

The heat flux scaling is accomplished by adhering to the criterion proposed by [155] in terms of the dimensionless power-to-flow ratio. They drew analogy to a conventional boiling channel and defined a true trans-pseudocritical number (N_{TPC}) using the channel inlet velocity as the reference one. This particular dimensionless groups must be equal between the prototype and model ($N_{TPC,P} = N_{TPC,M}$), yielding

$$\left[\left(\frac{\dot{Q}}{GA}\right)\frac{\beta_{pc}}{c_{p,pc}}\right]_P = \left[\left(\frac{\dot{Q}}{GA}\right)\frac{\beta_{pc}}{c_{p,pc}}\right]_M \tag{2.6}$$

where $\dot{Q}$ is the imposed external power and A is the cross-sectional area of the circular flow passage. The scaled values of mass and heat fluxes for certain test cases are enumerated in table 2.2.

It must be acknowledged here that each of the scaling principles described above were originally developed for channels having larger characteristic dimensions compared to the present study. However, the absence of any criteria developed specifically for mini- or microchannels has compelled for their adoption here. The results presented in section 5.3 are going to provide an assessment about their applicability at smaller dimensions.

Table 2.2: Scaled values of mass and heat fluxes for some test cases

Fluid	**Mass flux** (G) ($\mathrm{kg/m^2s}$)		**Heat flux** ($\dot{q}''$) ($\mathrm{kW/m^2}$)		
CO_2	300	450	30	40	50
R134a	383.014	574.53	22.4523	29.9364	37.4205
NH_3	131.02	182.75	38.676	53.0306	66.2882
C_2H_6	132.56	198.85	17.6066	23.4755	29.3444
N_2O	229.48	344.22	21.9290	29.2387	36.5484

2.2.4 Numerical scheme

The conservation equations (Eq. 2.1-2.3) are solved using the finite volume based platform of ANSYS-Fluent. Both the convective and diffusive terms of the governing equations are discretized following the second-order upwind scheme, which makes use of the upstream magnitude and gradients for computing the values at the faces of the control volumes. Pressure-velocity coupling is resolved through the PISO algorithm. To encounter the non-linearity in temperature and pressure-dependence of the relevant transport properties, NIST Standard Reference Database 23 version 9 (Refprop) [176] is used, as already quoted earlier, thus rendering relatively precise qualitative predictions [178, 179]. The solutions are assumed to be converged when following criteria are satisfied for the flow variables:

$$\left|\frac{\phi^{n+1}-\phi^{n}}{\phi^{n}}\right| \leq 10^{-6} \text{ where } \phi \equiv w_j,\ \kappa \text{ and } \omega$$

$$\left|\frac{\phi^{n+1}-\phi^{n}}{\phi^{n}}\right| \leq 10^{-12} \text{ where } \phi \equiv T$$

2.2.5 Grid-independency test and validation

Non-uniform mesh structure is employed for all the simulations, with finer meshes near the wall and also in certain inner portions, to ensure grid-independent nature of the solutions and also to maintain accurate resolution of flow variables in zones experiencing steeper gradients. SST $\kappa - \omega$ model demands the y^+ value to be around one [180], and that is secured using the inflation technique with a first layer thickness of 0.002 mm and a total of 9 such layers. A cross-sectional view of the adopted mesh structure is shown in Fig. 2.3. Refinement is done in the axial direction as well, with different mesh densities in the adiabatic and heated sections. Four different mesh structures are initially set up to test the grid-independent nature of the solutions with CO_2 as the working fluid, and the resultant magnitudes are summarized in table 2.3. It is evident that increasing the number of elements from mesh 3 to mesh 4 yields about 0.59% change in the temperature differential and 0.5% difference in pressure drop, both of which can be considered to be negligible. Accordingly, mesh 3 is continued with for all the subsequent simulations and also for all the fluids.

The experimental results of [130] are used to ascertain the validity of the proposed numerical framework for the simulation of SC heat transfer. They experimented with a test section of 500 mm length, with inner and outer diameters of 2 mm and 3 mm respectively. Quite similar to the present configuration (Fig. 2.1), an unheated upstream length of 100 mm was provided to ensure the flow to be fully-developed at the entrance of the heated section. Predicted variation in the heat transfer coefficient with the bulk temperature is compared with

Table 2.3: Details of various mesh systems employed

Mesh structure	**Number of elements**	**Bulk temperature near outlet** (K)	**Rise in bulk temperature** (K)	**Pressure drop** (kPa)
Mesh 1	163578	317.45	12.45	1.205
Mesh 2	460840	317.20	12.20	1.190
Mesh 3	642800	316.89	11.89	1.191
Mesh 4	751400	316.96	11.96	1.185

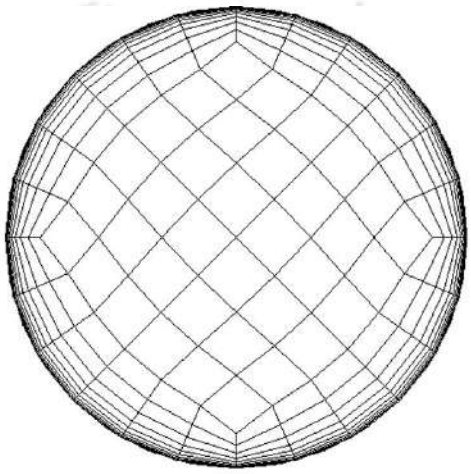

Fig. 2.3: Cross-sectional view of the adopted mesh structure at the heater center

the experimental profile in Fig. 2.4(a), which shows reasonable degree of conformity. The difference around the peak in heat transfer coefficient (HTC) can be attributed to the simplified approach followed while obtaining the experimental numbers, where the bulk enthalpy was estimated using mere energy balance and measured values of the outer wall temperature were employed in calculations. [130] reported ±6.62% uncertainty in their HTC values, whereas the largest difference between present simulation results and their experimental observation is about 4.90%, which is well within that range.

It is implausible to conceive the azimuthal variation during experiments, despite the acknowledged significance, limiting concerned measurements to global observations. Local thermalhydraulic characteristics can be acquired only from detailed multidimensional simulation, the volume of which itself is not very encouraging. To judge the performance of the present framework in depicting such variations, wall temperature profiles along the periphery at four different axial locations are compared with the DNS results of [134] in Fig. 2.4(b) for two different sets of operating conditions. While the qualitative trend match-

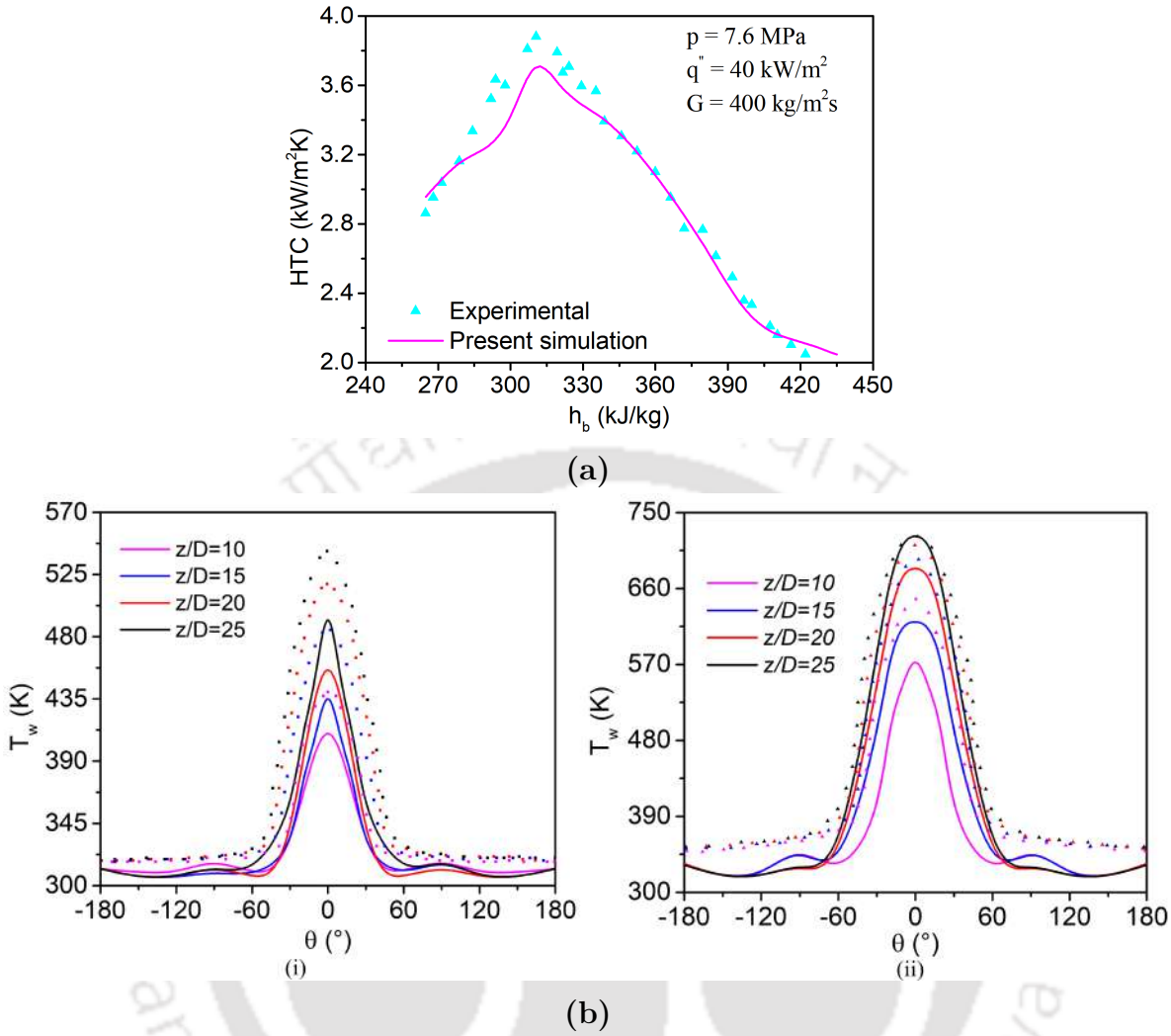

Fig. 2.4: (a) Comparison of the predicted results with the experimental observation of [130]; (b) Comparison of the predicted variation in the wall temperature along the periphery with the computational observation of [134]: (i) $\dot{q}'' = 30$ kW/m^2, (ii) $\dot{q}'' = 60$ kW/m^2 ($Re_{in} = 5400$, $T_{in} = 301.15$ K); here continuous lines refer to present results and symbols refer to results of [134]

ing is reasonable, the values are noticeably under-predicted within the range of $\theta = \pm 30°$, with the largest difference of 11.8% for $\dot{q}'' = 30$ kW/m^2. The predictions are much closer for $\dot{q}'' = 60$ kW/m^2, particularly in the downstream locations. The RANS-type turbulence model embraced in the present study is fundamentally weaker than DNS, which is capable of resolving all length scales till the smallest possible dissipative one, albeit at the expense of substantially greater computational resources. As the primary objective of the present study is the thermalhydraulic characterization of MCHS with several SCFs, along with the

assessment of macroscopic scaling laws for the minichannels, exhaustive local quantitative information is not necessary. The reported azimuthal variation with the present numerical setup, therefore, is sufficient and hence is continued with.

2.3 Results and Discussion

Simulations are performed for the circular minichannel shown in Fig. 2.1 for all the five fluids, with CO_2 at $p = 8$ MPa as the reference condition, having inlet temperature (T_{in}) of 305 K, mass flux (G) range of 300 to 450 kg/m^{2}s and heat flux ($\dot{q}''$) ranging from 30 to 50 kW/m^2. Corresponding parametric ranges for the other four fluids can be estimated using the scaling laws referred earlier. Six test cases have been defined using different combinations of heat and mass fluxes for each of the fluids, and associated details for CO_2 are elaborated in table 2.4. The particulars for the other fluids can be obtained using the analogy presented in table 2.2. For example, heat and mass fluxes involved with CO_2 in Case I are 30 kW/m^2 and 300 kg/m^{2}s respectively, while the corresponding values for R134a are 22.4523 kW/m^2 and 383.014 kg/m^{2}s (from table 2.2).

Table 2.4: Heat and mass flux values for the simulated cases with CO_2 as the working fluid

Fluid	**Mass flux** (G) (kg/m^{2}s)	**Heat flux** ($\dot{q}''$) (kW/m^2)
Case I	300	30
Case II	300	40
Case III	300	50
Case IV	450	30
Case V	450	40
Case VI	450	50

2.3.1 Important definitions

One of the most common observations with supercritical heat transfer in horizontal flows is the possibility of having azimuthal asymmetry. In order to appraise the same, it is important to separately analyze the top half and bottom half surfaces of the heated wall at any axial location. Referring to Fig. 2.1, $\theta = 0$ to 180° corresponds to the top half surface and $\theta = 0$

to -180° describes the bottom half. Associated area-averaged HTCs can be defined as:

$$\bar{H}_t = \frac{\dot{q}''}{(T_w^t - T_b)} \tag{2.7a}$$

$$\bar{H}_b = \frac{\dot{q}''}{(T_w^b - T_b)} \tag{2.7b}$$

where, T_w^t and T_w^b are the wall temperatures averaged over the top and bottom half surfaces respectively. The bulk mean enthalpy h_b is estimated as:

$$h_b = \frac{\int_A \rho u h dA}{\int_A \rho u dA} \tag{2.8}$$

which is subsequently used to evaluate the bulk temperature T_b.

Inlet-to-exit pressure differential is another important parameter to characterize the performance of a minichannel. Dimensionless pressure drop across the duct is estimated here using the inlet plane values as:

$$\Delta p^* = \frac{\rho_{in} \Delta p}{G_{in}^2} \tag{2.9}$$

where, Δp is the dimensional pressure drop, G_{in} is the mass flux at the inlet and ρ_{in} is the density at the inlet.

2.3.2 General performance of SCF-based MCHS

It is critical to carefully inspect the performance of SCF-based MCHS with respect to the conventional ones, before embarking into a fluid-to-fluid based appraisal, in order to ascertain the technical feasibility. Simulations are, therefore, performed using single-phase water at 8 MPa as the coolant, and correlated in Fig. 2.5 with the observations obtained using CO_2 at the same pressure. Clearly, sCO_2 is capable of yielding substantially larger HTC compared to single-phase water, and this observation is generally true for most of the common combinations of SCF and single-phase liquid. HTC possible with single-phase water remains virtually invariant with changes in pressure, unless the selected level is very close to the critical limit, as the relevant thermophysical properties are only weakly-sensitive to pressure. Consequently, the coolant temperature along the MCHS rises with a steep gradient for water, while sCO_2 administers a near-isothermal boundary condition, which is often desirable in heat sinks. The temperature level of the coolant also remains much lower with SCF, despite all the simulations being carried with identical inlet temperatures. Similar trend can be

observed with other SCFs as well, after imposing equivalent operating conditions. NH_3 is the only exception among the considered SCFs, which shows steep temperature variation with higher level of wall temperature, as can be observed from Fig. 2.5(b). It is a direct manifestation of the worst heat transport characteristics of NH_3 within the five fluids explored here, the rationale behind which can be found later on in §2.3.4. So, regardless of the nonlinear axial variation of HTC, SCFs substantiate themselves as more potent option as coolant in MCHSs.

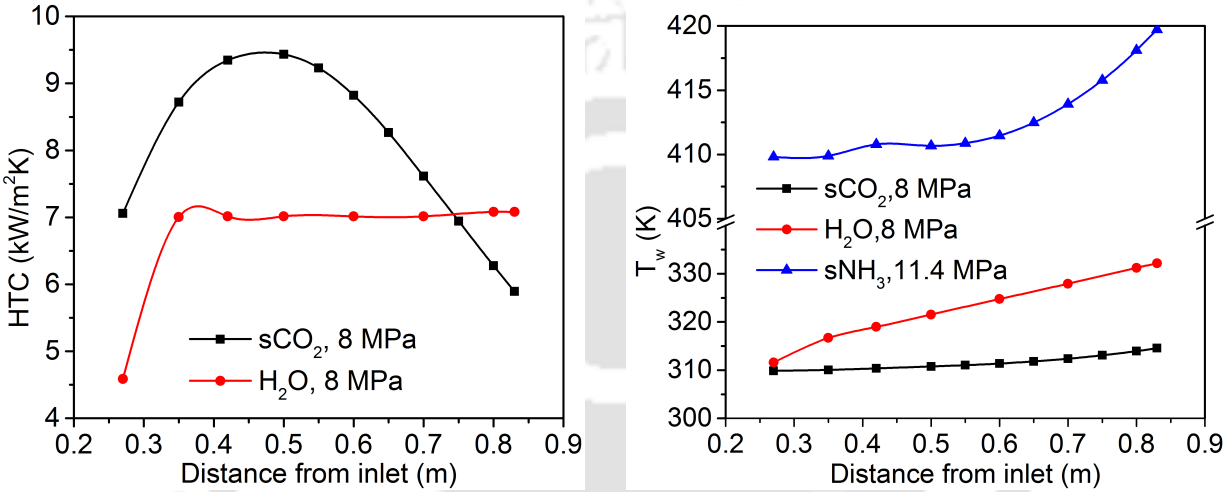

(a) Average heat transfer coefficients **(b)** Average wall temperatures

Fig. 2.5: Comparison of heat transfer coefficient and wall temperature, both averaged over the bottom half surface, of sCO_2 with single phase water at $G = 450$ kg/m^{2}s, $\dot{q}'' = 30$ kW/m^2 and $T_{in} = 305$ K; Variation in wall temperature for sNH_3 is also shown in (b) under equivalent operating condition

Two-phase heat sinks, where energy is absorbed as the latent heat of vaporization, are capable of actuating greater levels of HTCs than single-phase, while maintaining isothermal boundary condition, precisely the advantages claimed with SCF. Simulated magnitudes of HTCs in the present work are, therefore, compared with such observations available in open literature. Supercritical R134a has shown superior heat transfer as compared to the ones reported in the experimental study by [181]. During subcooled flow boiling of R134a, they found Nu of the order of 100, whereas the numerical value obtained with supercritical R134a in the present study is of the order of 500. HTCs comparable with the study by [182] has also been observed, with magnitudes around 3.5 kW/m^{2}K. The continuous nature of the fluid domain with SCF also avoids any apprehension of interfacial instability and dryout, which are major concerns in any boiling channel.

2.3.3 Hydrodynamic characteristics

As an adiabatic section has been provided upstream to the heated segment, the flow necessarily attains parabolic velocity profile before coming in contact with the heated surface. The addition of thermal energy raises the fluid enthalpy, inducing nonlinear variation in the local temperature and other thermophysical properties, resulting in distorted thermal and velocity contours. The consequences are particularly severe in the vicinity of the pseudo-critical point. Rapid decline in density around T_{pc} can result in stiff density gradient in the radial direction, congenial to the temperature gradient, which stimulates buoyancy-induced transverse motion. Fluid particles in contact with the heated wall experiences an increase in their temperature and reduction in density, allowing them to move upwards, while staying in contact with the wall. Accordingly, a high-temperature layer is developed on the heated surface, with lighter fluid particles continually moving upward. The bulk fluid around the center of a cross-section, however, has no option of directly acquiring energy from the external source. Heat can be transferred to such central mass only via conduction from the near-wall fluids, which commonly is quite small owing to the poor thermal conductivity of the supercritical fluid, particularly beyond T_{pc}. Consequently, it continues to be cooler and heavier, and descends to the lower half. Radial velocity vectors at the axial location of $z = 0.42$ m are compared in Fig. 2.6 for all the five fluids corresponding to case I (table 2.4). Local upward motion is clearly evident for all, with two vertically-symmetric recirculation zones. Noticeable increase in the magnitude of the velocity vectors can also be perceived beyond the boundary layers. There is, however, definite difference in the magnitude of the largest radial velocity for all the fluids, which is expected considering the variation in the nature of temperature-dependence of thermophysical properties, other than density.

Despite the variation in the magnitudes across different working fluids, owing to their distinct critical points, visual nature of the momentum field can be remarkably similar, as has already been observed in Fig. 2.6 at a particular axial location of $z = 0.42$ m. The same can further be reinforced by following the development in the velocity contours along the flow direction. Figure 2.7 inspects the velocity fields at three axial locations for three fluids, subjected to the boundary conditions specified as case I (table 2.4). While there are some disparities in the dimensional values, which is always expected, there is hardly any discernible digression in the visual demeanor. At the first selected plane ($z = 0.42$ m), the profiles are still under development. However, a relatively thinner boundary layer around the bottom surface is already visible, hinting toward a steeper radial gradient there compared to the top surface. The profiles evolve gradually in the axial direction, and well-developed

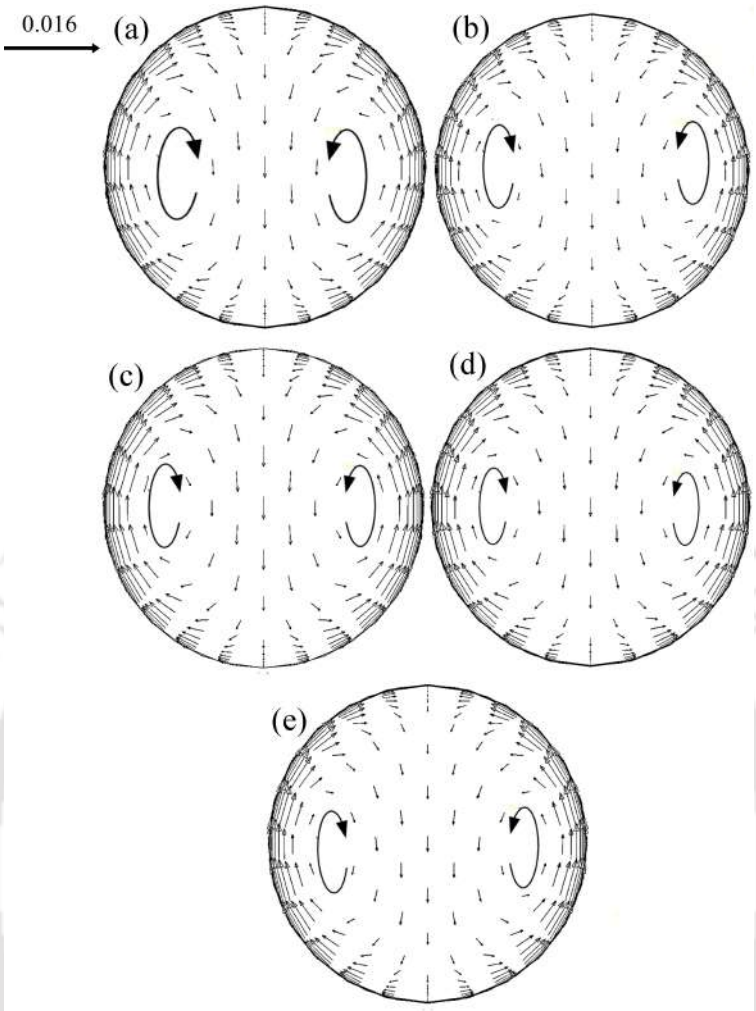

Fig. 2.6: Radial velocity vectors at the axial location of $z = 0.42$ m for all the five fluids corresponding to case I: (a) CO_2, (b) NH_3, (c) R134a, (d) C_2H_6 and (e) N_2O

contours are visible at $z = 0.83$ m. The thickness of the boundary layers at both top and bottom surfaces are definitely comparable for all the five fluids, again authenticating the similarity of the scaled conditions.

Despite the visual resemblance, their is difference not only in magnitude of the dimensional parameters, but also for the dimensionless groups. The values of bulk-averaged local Reynolds number (Re_b) at all the three selected locations and for all the five fluids are summarized in table 2.5. Here the fluid viscosity corresponding to the bulk temperature has been used during calculations. Re_b increases in the flow direction owing to the reduction in fluid viscosity with rise in temperature. While R134a registers the largest magnitude, the smallest numbers are reported for NH_3. Here it is pertinent to refer to the adopted mass flux scaling

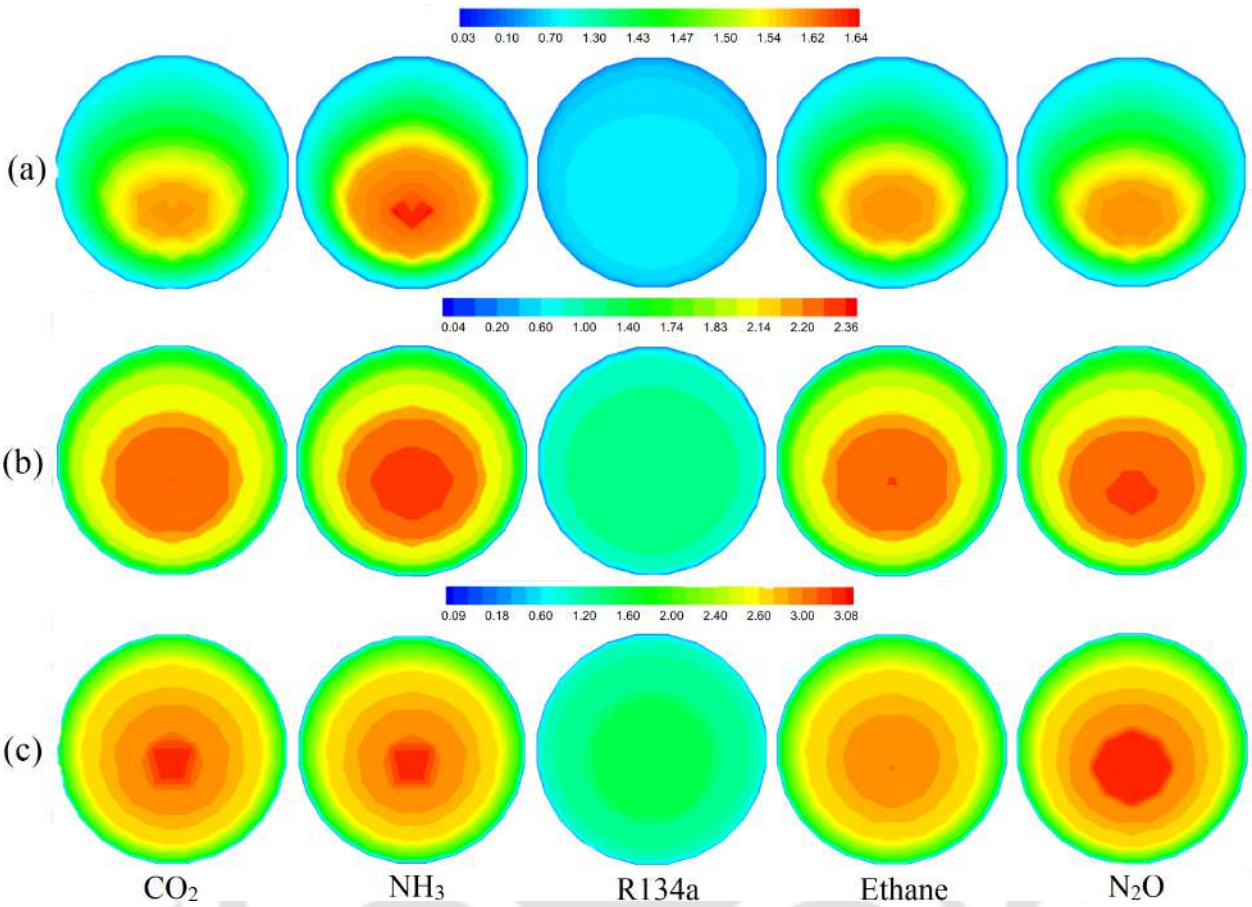

Fig. 2.7: Velocity contours at the axial locations of (a) $z = 0.42$ m, (b) $z = 0.65$ m and (c) $z = 0.83$ m for all the five fluids corresponding to case I

defined in Eq. 2.5. The combination of Re_b and Pr_b raised to certain powers is scheduled to be maintained constant across different fluids. Therefore, the difference in the magnitude of Re_b can be explained following respective variations in Pr_b along the minichannel. Any supercritical fluid exhibits a peak of Pr at the pseudocritical point, in accordance to the variation in c_p. However, the magnitude and mode of decline beyond that can be different, and the same can be confirmed from Fig. 2.8(a). NH_3 is characterized by the highest peak, followed by a steep descent, whereas R134a exhibits the lowest level of Pr and a very moderate variation over the entire range of h^* considered here. That comprehensively elucidate the trend observed in table 2.5. This is a crucial inference, as the adopted scaling methodology employs solely the density, in terms of $\rho^* - h^*$ profile, for identifying the system pressure, while disregarding the possible disparity in the characteristics of other relevant properties. The same is resulting in a deviation in Re_b values here, which is expected to influence all

Table 2.5: Bulk-averaged Reynolds number (Re_b) at selected axial planes corresponding to Case I

Axial location (z) (m)	**CO_2**	**R134a**	**NH_3**	**C_2H_6**	**N_2O**
0.42	18603.0	20729.2	11679.8	13719.7	15862.3
0.65	24432.9	29790.3	12536.4	16188.6	19894.2
0.83	28051.8	34610.2	14008.7	18365.2	21838.6

types of thermalhydraulic interactions. Quite intriguingly, the profiles of non-dimensional dynamic viscosity ($\mu^* = \mu/\mu_{pc}$) versus h^* is near-identical for all the fluids studied here (Fig. 2.8(b)), which indicates an immediate impact of the disparity in Re_b on the mass flux and velocity level. Beyond T_{pc} ($h^* > 0$), magnitude of μ^* for R134a is the lowest, while the same for NH_3 is the the highest, which also contribute to the trend reported for Re_b. The disparity in the level of Pr and μ^* between CO_2 and N_2O also needs to be noted, which contributes toward the difference in their flow characteristics, despite near-identical critical points.

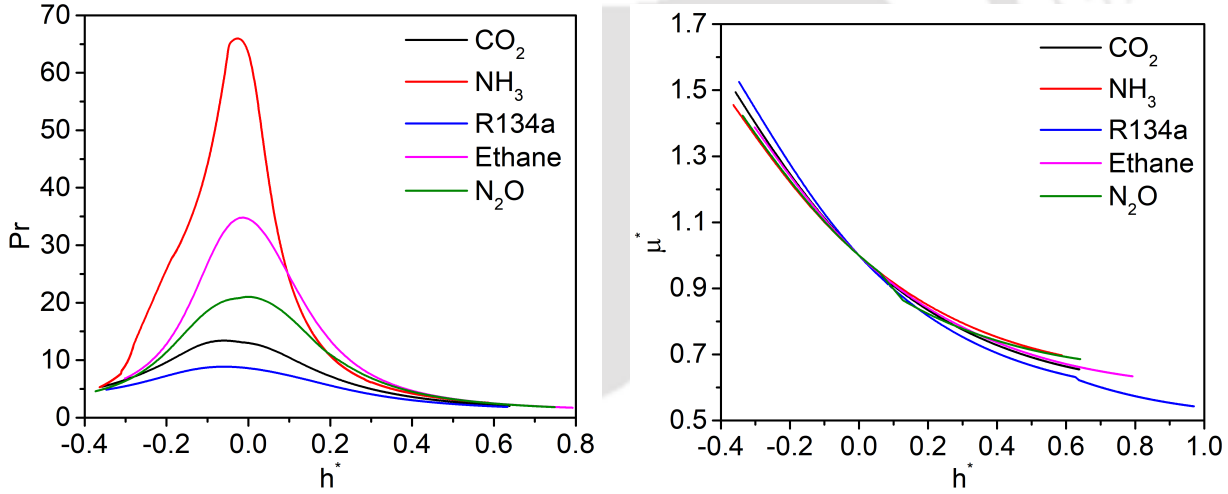

(a) Prandtl number (Pr) **(b)** Non-dimensional viscosity (μ^*)

Fig. 2.8: Variation in Prandtl number (Pr) and non-dimensional dynamic viscosity ($\mu^* = \mu/\mu_{pc}$) with non-dimensional enthalpy (h^*) for all the five fluids under consideration

An important characterizing criterion for evaluating the performance of MCHSs is the incurred pressure drop, as that directly influences the driving power requirement. Dimensionless pressure drop has already been defined by Eq. 2.9, the primary contributions toward which in horizontal channel are from the frictional and accelerational components. Owing to

the smaller dimensions, friction is always expected to be higher in such channels, inflicting additional emphasis on the accelerational counterpart, which, in turn, is directly dependent on the inlet-to-exit density differential as,

$$\Delta p^*_{ac} = \frac{\rho_{pc}}{G^2} \int_{in}^{out} d\left(\frac{G^2}{\rho}\right) = \frac{1}{{\rho^*_{out}}^2} - \frac{1}{{\rho^*_{in}}^2} \tag{2.10}$$

As the similarity of $\rho^* - h^*$ profile has been employed at the very first step of scaling, the accelerational pressure drop is anticipated to be similar for all the fluids, and that is indeed the case, as can be confirmed from table 4.3. N_2O is the one to exhibit the largest deviation in the magnitude of Δp^*_{ac} with CO_2, and that amounts only about 8.5%. With increase in energy supply, inlet-to-exit density differential is enhanced, causing monotonic rise in Δp^*_{ac} with the dimensionless heat flux ($q^* = \beta_{pc}\dot{q}''/Gc_{p,pc}$), and the same is presented in Fig. 2.9 for two different mass flux levels. All the five fluids exhibit near-linear profiles, while staying reasonably close to each other.

Table 2.6: Dimensionless total and accelerational pressure drops corresponding to Case I

	CO_2	**R134a**	**NH_3**	**C_2H_6**	**N_2O**
Δp^*	6.019	5.757	6.840	6.591	6.435
Δp^*_{ac}	1.127	1.055	1.061	1.090	1.223

Disparity in total pressure drop (Δp^*) can, however, be more substantial, and its variations with q^* are presented in Fig. 2.10. The linear nature is again palpable. The magnitudes are, however, noticeably distinct, with NH_3 and R134a respectively reporting the highest and lowest levels, despite having almost identical Δp^*_{ac}. The dimensionless version of the total pressure drop (Δp^*) is directly dependent on the friction factor, which, in turn, is inversely proportional to the prevailing level of Re_b. The dependence, in conjunction with the values presented in table 2.5, modulates the frictional pressure drop (Δp^*_{fr}) and comprehensively explains the trend observed in Fig. 2.10. Increase in the level of mass flux enhances the Re_b, causing further reduction in Δp^*, and the same is clearly visible here as well. It can, therefore, be concluded that, despite the concordance in ρ^* and μ^* profiles along the length of the minichannel, the substantial difference in Pr across the five fluids engender considerable discrepancy in the Re_b-level and consequently in the pressure drop characteristics, notwithstanding the visual similarity in dimensionless velocity fields.

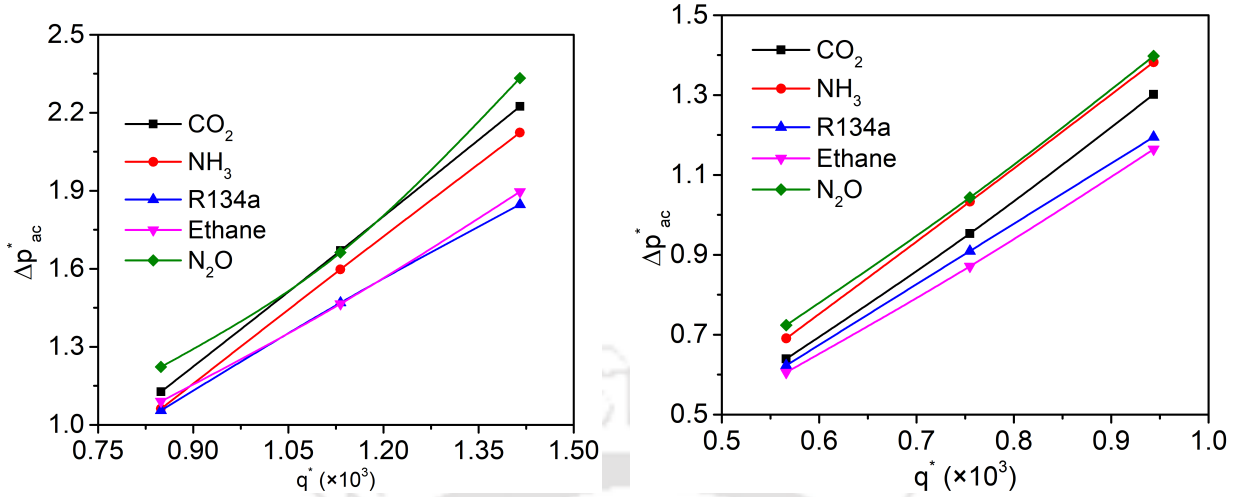

(a) $G = 300$ kg/m^{2}s **(b)** $G = 450$ kg/m^{2}s

Fig. 2.9: Variation in dimensionless accelerational pressure drop (Δp^*_{ac}) with dimensionless heat flux (q^*) for all the fluids; here mentioned mass flux values refer to CO_2 and corresponding mass fluxes for other fluids are available in table 2.2

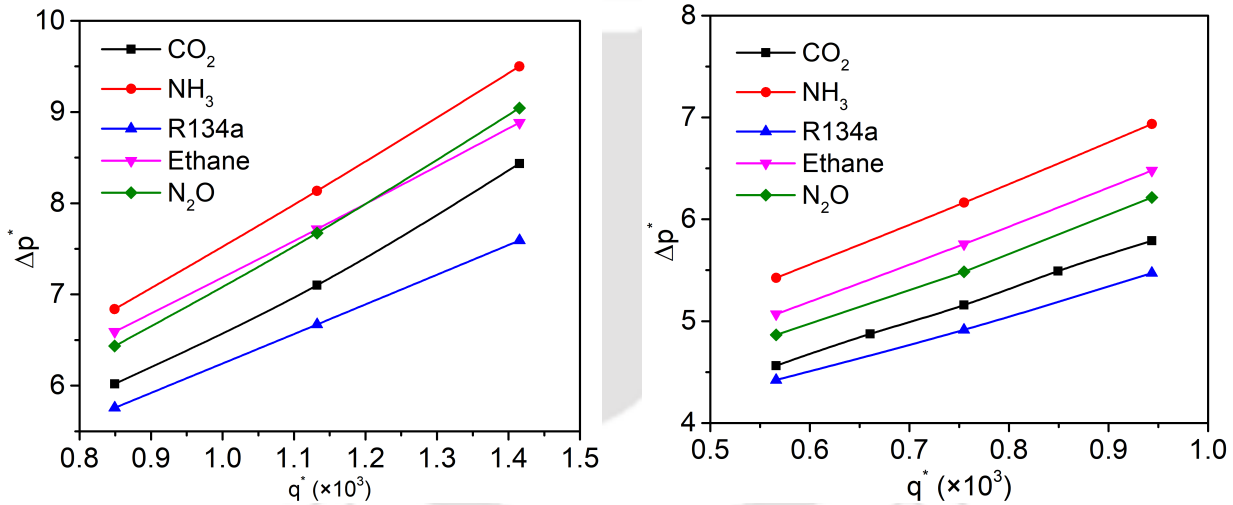

(a) $G = 300$ kg/m^{2}s **(b)** $G = 450$ kg/m^{2}s

Fig. 2.10: Variation in dimensionless total pressure drop (Δp^*) with dimensionless heat flux (q^*) for all the fluids; here mentioned mass flux values refer to CO_2 and corresponding mass fluxes for other fluids are available in table 2.2

2.3.4 Thermal characteristics

The azimuthal asymmetry in the velocity profile directly influences the strength of the wall-to-fluid thermal communication, which is also regulated by the thermophysical properties of

the fluid layer in immediate vicinity of the heated surface. As has been noted earlier, warm fluid climbs along the heated wall and acquires more energy in the process, while the fluid adjoining to the centreline and in the lower half of a cross-section remains cooler. The same is illustrated in Fig. 2.11 for three different axial locations. The growth in the thickness of the higher-enthalpy fluid layer in both axial and radially-upward direction is very much evident, along with the substantially thinner thermal boundary layer in contact with the lower wall. Therefore, steep temperature gradient is expected in the lower half of the channel, indicating notable variation in the thermal characteristics along the periphery. It must also be remembered that the supercritical fluid experiences a drastic reduction in thermal conductivity (k) as it crosses T_{pc}, which can severely affect the rate of heat transmission from the solid wall to the adjacent fluid layer. As can be observed from Fig. 2.12, the nature of variation in non-dimensional thermal conductivity ($k^* = k/k_{pc}$) with h^* for the considered fluids are not similar, quite contrary to the correspondence noted earlier for μ^* (Fig. 2.8(b)). R134a consistently registers the highest level of k^*, several times greater than the same for NH_3, while the other three fluids report comparable values. That is expected to inflict substantial dissimilitude on the corresponding heat transfer characteristics along the peripheral direction, as discussed below.

The variations in Nusselt number (Nu) averaged over the bottom half surface ($\theta = 0^\circ \rightarrow -180^\circ$) and top half surface ($\theta = 0^\circ \rightarrow +180^\circ$) along the length of the channel are presented respectively in Fig. 2.13(a) and (b) for case I, and similarly for case VI in Fig. 2.14(a) and (b). Differences in both visual countenance and magnitude within the surfaces are very much palpable, which is a direct consequence of the above deliberation. A detailed discussion in this regard was presented in the earlier work by the authors [183] for a similar minichannel involving sCO_2. It can be observed here the concerned deliberation is true for any supercritical fluid. The difference between the bulk fluid temperature (T_b) and the bottom wall temperature keeps on reducing in the flow direction within the heated segment, and approaches the lowest level with the bulk attaining the pseudocritical point ($h^* = 1$). Heat flux being a constant, minima in temperature differential results in the maxima in corresponding heat transfer coefficient and consequently in Nu. Downstream of this location, the gas-like fluid ($h^* > 1$) has weakened thermal conductivity, engendering a noticeable deterioration in Nu for each of the fluids. There is, however, considerable difference in the magnitude of Nu among the fluids, and the nature of such divergence is mostly consistent with the corresponding profiles of k^*. As expected, the highest value conforms to R134a and the peak magnitude of Nu for R134a is about 40% greater than the same for CO_2, which is

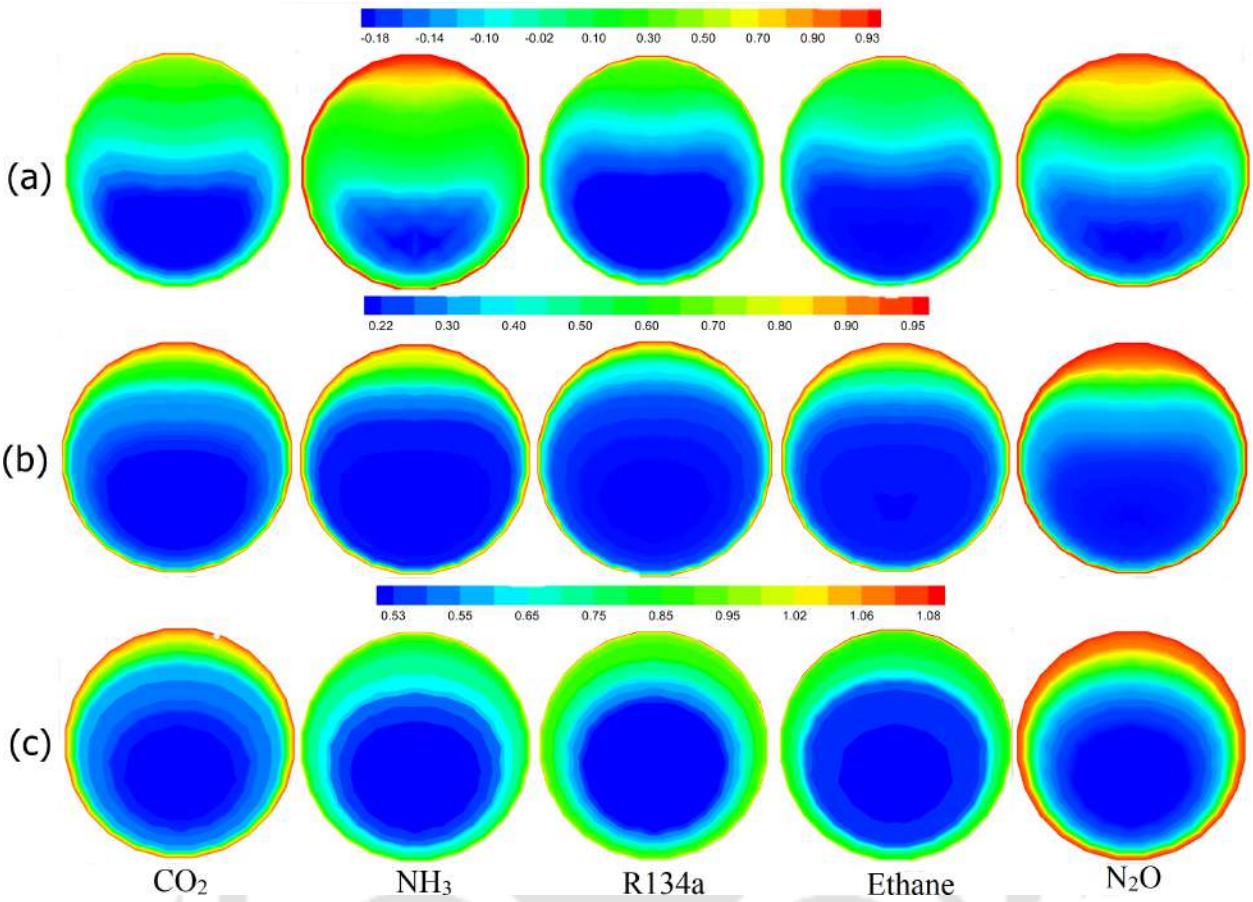

Fig. 2.11: Non-dimensional enthalpy (h^*) contours at the axial locations of (a) $z = 0.42$ m, (b) $z = 0.65$ m and (c) $z = 0.83$ m for all the five fluids corresponding to case I

the closest neighbor, for both the cases. It is interesting to note that the highest value of thermal conductivity (k_{pc}) of CO_2 is about 40.16% greater than that for R134a under the conditions of case I, and the deviation in Nu_{max} is also of similar order. The lowest level expectedly is reported for NH_3 owing to its smallest k^*. The trend is quite similar along the top half surface as well. As discussed earlier, the temperature level of the fluid in the top half of any cross-section is consistently higher than the same in the bottom half. It has already been illustrated in Fig. 2.11 that the non-dimensional enthalpy (h^*) of the fluid layer in contact with the upper surface is very high, invariably being greater than 0.3 and even having $h^* > 0.8$ in the downstream segments, corresponding to a temperature well above T_{pc}. The thermal conductivity of supercritical fluid with such high temperature is considerably low (Fig. 2.12), resulting in degraded heat transfer performance. That can be substantiated from the comparatively lower magnitudes of Nu displayed in both Figs. 2.13(b) and 2.14(b).

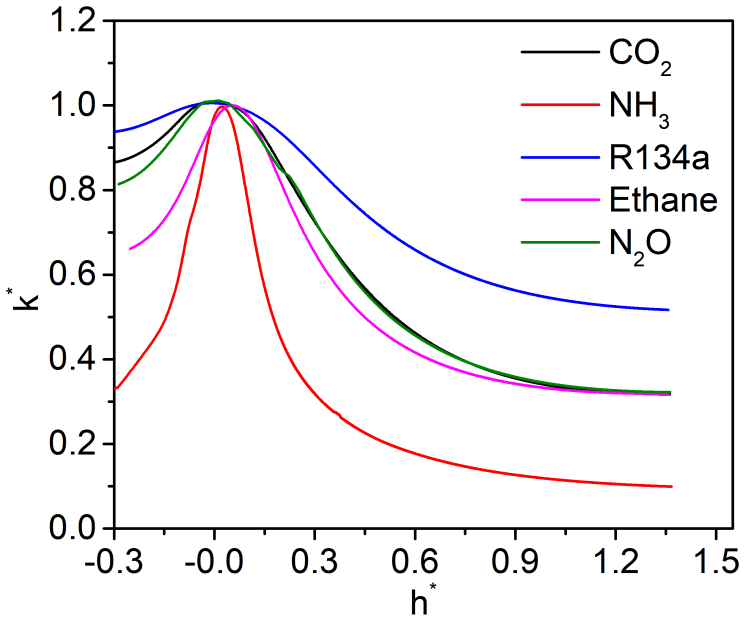

Fig. 2.12: Variation in non-dimensional thermal conductivity ($k^* = k/k_{pc}$) with non-dimensional enthalpy (h^*)

Overall variation in Nu is also much lesser along the top half surface in comparison with the same along the bottom half surface (only about 19.27 along the top surface in contrast to 128.65 along the bottom for R134a in case I), which is another consequence of the lower thermal conductivity. k^* of NH_3 drops with the steepest slope among all the considered fluids, resulting in little peaks in the corresponding Nu-profiles downstream of the $h^* = 0$ location in both Figs. 2.13(b) and 2.14(b). There is also substantial rise in Nu-level at both the surfaces in case VI compared to case I, which possibly is a consequence of the higher level of heat and mass fluxes.

In order to have a better illustration of the azimuthal asymmetry in thermal interaction, the variations in the local Nusselt number over the periphery at a particular axial location of $z = 0.65$ m is compared in Fig. 2.15. Staying harmonious to the area-averaged profiles, R134a consistently registers the largest level of Nu and NH_3 the lowest. All the fluids attain the peak at $\theta = 0°$ and $\theta = \pm 180°$, which refer to the two ends of the horizontal centreline.

Immediate impact of such azimuthal asymmetry and substantial difference in HTC levels across different fluids is on the wall temperature. Higher level of HTC will lower T_w for identical wall heat flux, and hence the profiles of T_w^* are expected to complement the same for Nu, which is evident from the axial variations presented in Fig. 2.16 for both the bottom and top half surfaces for case I, and similarly for case VI in Fig. 2.17. While the

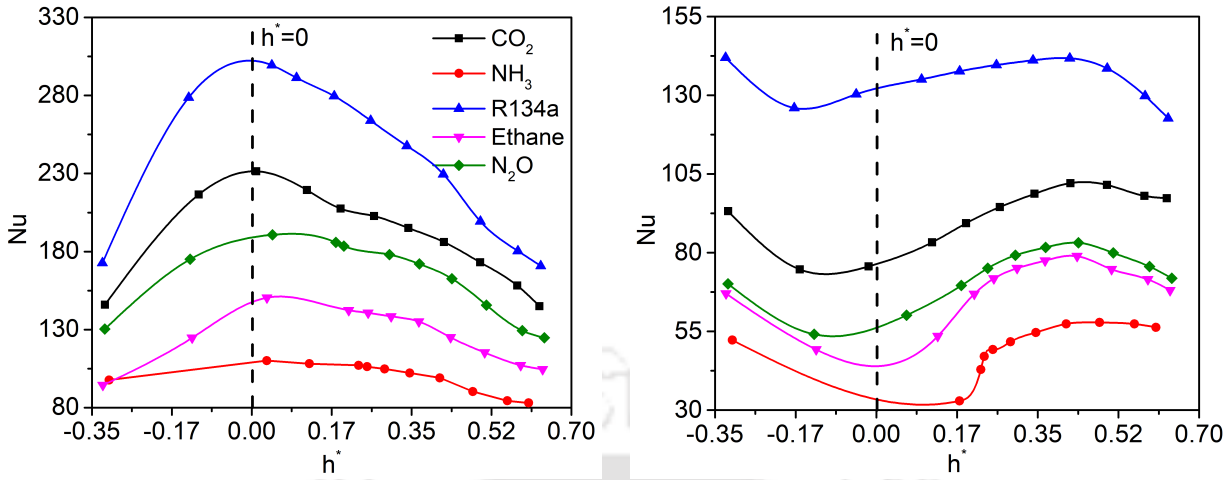

(a) Bottom half surface **(b)** Top half surface

Fig. 2.13: Variation in Nusselt number (Nu) in the axial direction averaged over the bottom and top half surfaces corresponding to case I

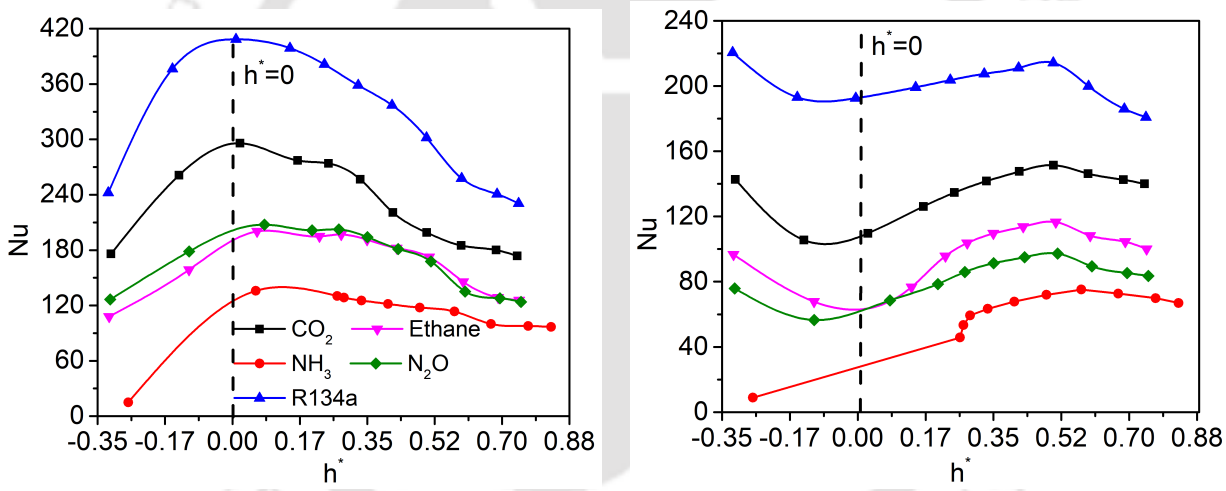

(a) Bottom half surface **(b)** Top half surface

Fig. 2.14: Variation in Nusselt number (Nu) in the axial direction averaged over the bottom and top half surfaces corresponding to case VI

wall temperature remains mostly uniform in the flow direction for R134a and CO_2-based MCHSs, it is considerably higher for NH_3-filled ones, which is a testimony of its inferior heat transport characteristics. There is also noticeable difference in the average T_w^* values at the two surfaces, in coherence to the corresponding Nu-profiles. Greater rise in T_w^* can be observed in case VI (Fig. 2.17), again as a direct reflection of the higher level of energy addition. It is, therefore, logical to resolve that the heat transport characteristics of the

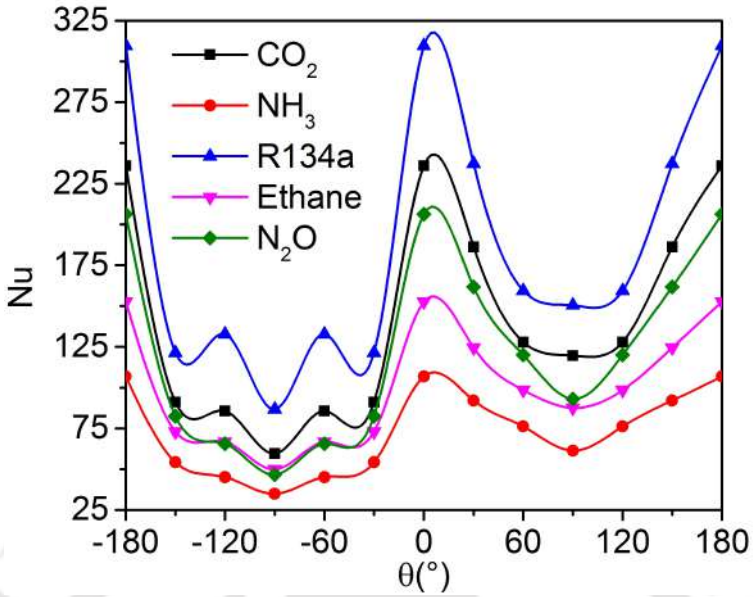

Fig. 2.15: Azimuthal variation in local Nusselt number at $z = 0.65$ m for all the five fluids corresponding to case I

selected five supercritical fluids are sufficiently different from each other for the selected MCHS, essentially as a consequence of the disparity in their k^*-h^* profiles, which has not been considered while proposing the scaling laws.

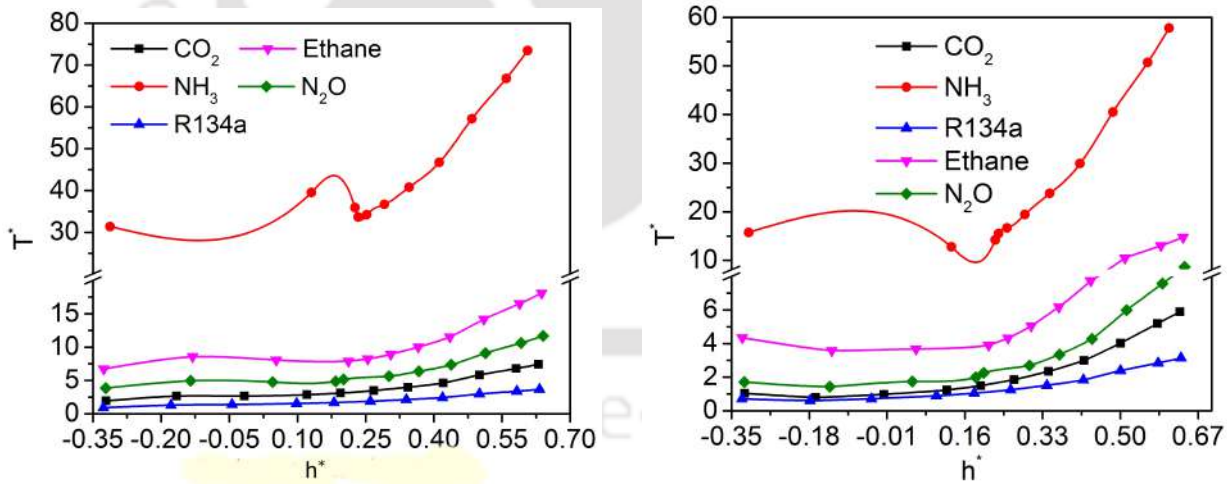

(a) Bottom half surface **(b)** Top half surface

Fig. 2.16: Variation in dimensionless wall temperature (T_w^*) in the axial direction averaged over the bottom and top half surfaces corresponding to case I

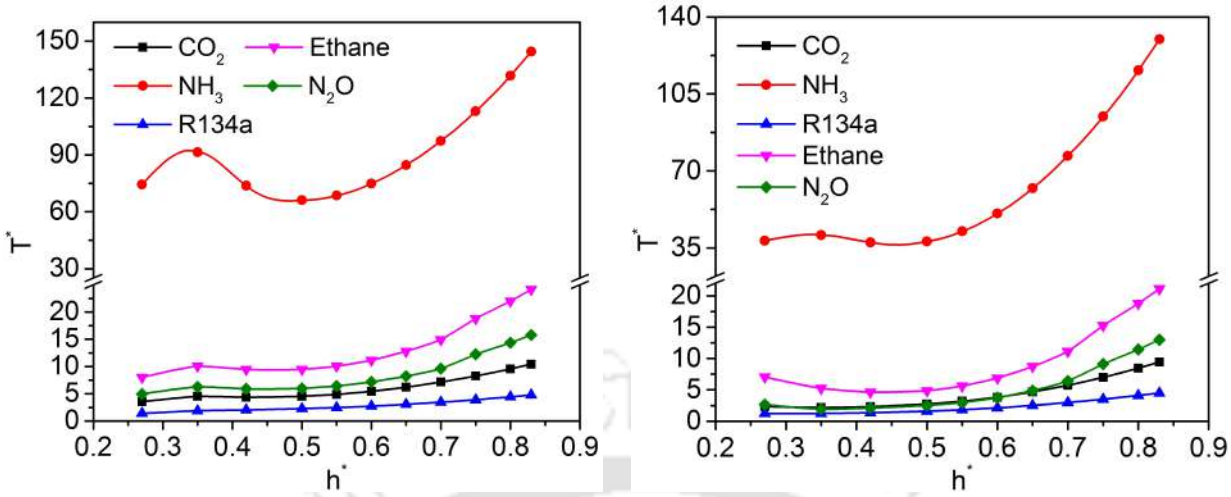

(a) Bottom half surface **(b)** Top half surface

Fig. 2.17: Variation in dimensionless wall temperature (T_w^*) in the axial direction averaged over the bottom and top half surfaces corresponding to case VI

2.3.5 A second-law perspective

In order to complement the thermalhydraulic analyses, a brief second-law appraisal, with emphasis on entropy generation, is presented here. While the pioneering studies on entropy-based thermodynamic evaluation can be credited to [184], hardly any reliable one is available on supercritical MCHS. Recently, [185] reported an exergetic investigation on MCHS utilizing sCO_2 and compared that to normal water, to find lower thermal resistance with sCO_2-based one for certain ranges of inlet temperature. Entropy generation in an open system can have contribution from both heat transfer and mass transfer, with the former being defined as,

$$\dot{S}_{gen,Q} = \dot{Q}\,(\pi D)\int_0^L \frac{dl}{T_w} \tag{2.11}$$

The entropy generation associated with the mass flux can be estimated as,

$$\dot{S}_{gen,G} = \dot{m}(s_{out} - s_{in}) \tag{2.12}$$

Consequently, total entropy generation inside the MCHS in dimensionless form can be given as,

$$\dot{S}^*_{gen} = \frac{\dot{S}_{gen,Q} + \dot{S}_{gen,G}}{G\rho_{pc}c_{p,pc}D} \tag{2.13}$$

Both $\dot{S}_{gen,Q}$ and $\dot{S}_{gen,G}$ are found to increase with rise in supplied power, with the former contributing about 53-56% in the total generation. $\dot{S}_{gen,Q}$ is a direct function of $\dot{Q}$, while the other component increases owing to the rise in exit enthalpy consequent to the temperature. A comparative view about the total entropy generation is available in table 2.7 for all the five fluids under consideration. Interestingly, largest $\dot{S}_{gen}$ can be associated with R134a, which has also demonstrated the best heat transport characteristics, closely followed by CO_2. On the contrary, entropy generation with NH_3 as the working fluid is an order lower than the above two, despite experiencing the highest level of heat flux. $c_{p,pc}$ for NH_3 is about 135 times higher than the same for R134a and about 50 times than CO_2, which explains this trend.

Table 2.7: Scaled values of total dimensionless entropy generation ($\dot{S}^*_{gen} \times 10^5$) for all the five fluids

	CO_2	**R134a**	**NH_3**	**C_2H_6**	**N_2O**
Case I	8.202	9.197	0.748	4.898	4.279
Case II	10.297	12.038	0.846	6.386	5.561
Case III	12.290	14.727	1.005	7.692	6.612

2.4 Summary

The thermalhydraulic assessment of five different SCFs have been performed here for a specified minichannel, with the objective of earmarking the superior one. At the absence of scaling rules developed specifically for smaller dimensions, macroscopic scaling principles have been employed, which also provides an opportunity of justifying the validity of such laws for MCHSs. Followings are the major observations regarding the flow and heat transport characteristics.

- HTC-level with a SCF-filled MCHS is substantially greater than conventional single-phase fluids and comparable with boiling channels, without any constraint of critical heat flux.

- Strong recirculation in radial velocity vectors can be observed, with visible similarity in the nature of momentum field among all the selected fluids.

- Owing to the difference in the level of the bulk Reynolds number (Re_b), considerable deviation in the total pressure drop (dimensionless) across the channel can be observed, with R134a experiencing the smallest one.

- R134a has also been found to register the best heat transfer behavior, in terms of both local and area-averaged Nu, despite considerable azimuthal asymmetry in the same for all the fluids.

- The difference in pressure drop characteristics can be attributed to the Pr, thermal profile of which has not been considered during scaling. Similarly, the variation in the dimensionless thermal conductivity can be identified as the primary contributor toward the deviation in thermal profiles.

It can, therefore, be concluded that R134a is definitely the best working fluid for the selected MCHS, taking into account both the pressure drop and heat transport behavior. The adopted scaling methodology, however, needs a serious revisit. While the $\rho^* - h^*$ contour is the only one considered for finalizing the operating pressure for any of the fluids, similar profiles of Pr and k^* also must be taken into consideration, which can possibly lead to proper platform for thermalhydraulic comparison of supercritical fluids at miniscale. Present analysis also has the potential of facilitating the designing of nuclear reactors using newer SCFs, characterized by easily-achievable critical point properties, in lieu of supercritical water, which can result in substantial savings in capital investment and enhanced operational safety. This is particularly relevant to modular or portable reactor concept, promising a new domain of research on future reactors.

Chapter 3

Role of buoyancy on the thermalhydraulics of supercritical CO_2 in MCHS

3.1 Preamble

With the growing demand of higher power density, at the expense of lesser environmental encroachment, use of supercritical carbon dioxide in miniature systems is becoming increasingly lucrative. However, a scrupulous literature survey suggests that most of the reported efforts concern cooling condition, to suit HVAC applications, and primarily vertical orientation, which negates the local buoyancy effects. However, the heat transfer characteristics of horizontal channel under heating condition can considerably deviate from that depending on the imposed conditions and unexpected wall temperature variations are pertinent under heating condition [145]. With the advent of mini- and micro-sinks, and progressively higher power density requirement in electronic cooling applications, horizontal heated microchannels also become a very germane configuration, necessitating a comprehensive study to envisage the concerned dynamics of supercritical flow. Present paper focuses on abridging this particular void through quantification of the heat transfer characteristics of sCO_2 in a horizontal minichannel subjected to heating condition, with particular emphasis on the role played by local buoyancy force. Attempt is made to understand the possible heat transfer enhancement/deterioration in the horizontal configuration and possible azimuthal variation, which remain unexplored till date. Relevant parametric effects on the heat transfer characteristics and the effect of buoyancy on local and overall profiles are also discussed in detail.

3.2 Computational Model Development

3.2.1 Physical geometry

As mentioned above, present study explores the thermalhydraulics of sCO_2 flow through a heated horizontal minichannel. Corresponding schematic representation is shown in Fig. 5.1. A computational domain of 840 mm length and 2 mm diameter is selected, where an adiabatic section of length 240 mm is provided for flow to be fully developed before entering the heated section. Specified mass flux inlet and constant outlet pressure boundary conditions have been imposed, along with no-slip wall and uniform wall heat flux in the heated section.

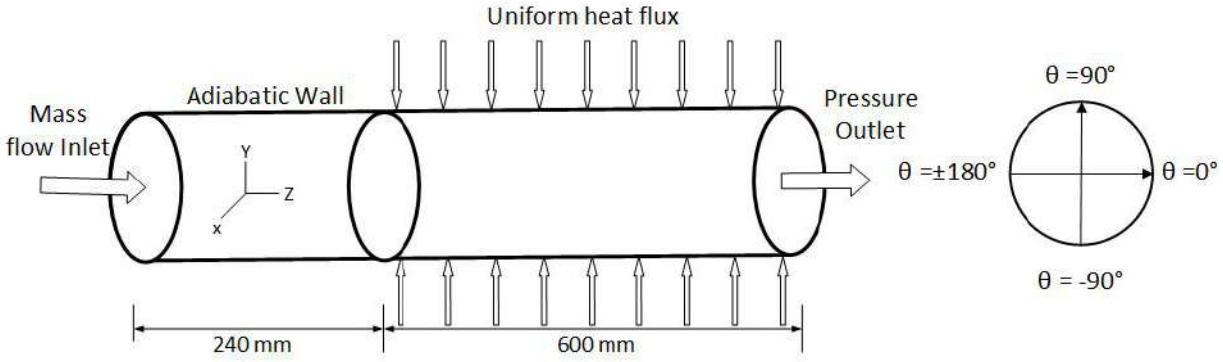

Fig. 3.1: Schematic of the computational domain under consideration

Steady-state versions of the mass, momentum and energy conservation equations in Cartesian coordinate are adopted in the present study, which has been discussed in Chapter 2.

The conservation equations have been solved following the finite-volume approach of ANSYS-Fluent and has been discussed in Chapter 2.

3.2.2 Mesh-independency study and validation

Non-uniform mesh is used in the current simulation, with finer meshes near the wall and certain internal areas to achieve mesh-independent results, and also to ensure accurate resolution of the flow characteristics in the regions experiencing steep gradient. For SST $\kappa - \omega$ turbulence model, y^+ value should be in the range of one [186]. To ensure that, inflation technique is used with the first layer thickness of 0.002 mm and a total of 9 such layers. Figure 2.3 shows the cross-sectional view of the adopted mesh structure. Numbers of elements in the adiabatic and heated sections are different, and the mesh is also refined in the

axial direction within the heated section. To eliminate the mesh-dependency of the solution, four different structures are tested, and corresponding values of bulk temperature near the outlet, rise in bulk temperature of the fluid during its passage through the heated section and pressure drop across the channel are presented in Table 5.2. It is evident that increasing the number of elements from mesh 3 to mesh 4 yields about 0.59% change in the temperature differential and 0.5% difference in pressure drop, both of which can be considered to be negligible. Steep temperature and velocity gradients are expected near the wall, and the mesh system must be robust enough to replicate that efficiently. The azimuthal variations in the wall shear stress, which is representative of the velocity gradient normal to the wall, and the local heat transfer coefficient, which is proportional to the wall temperature gradient, are shown in Fig. 3.2 for two different axial locations. The profiles produced by mesh 3 and 4 are almost indistinguishable, despite the number of elements in the later being about 17% more. Therefore, mesh 3 is continued with for all the simulations reported below.

Validation of the present numerical framework is achieved by comparing the simulated results with the experimental data of Guo *et al.* [187] and has been discussed in Chapter 2.

3.3 Results and Discussion

3.3.1 General thermalhydraulic characteristics

Simulations are performed in a circular channel having diameter of 2 mm for supercritical CO_2 at p = 80 - 90 bar, inlet temperature T_{in} = 305 K, and heat flux ($\dot{q}''$) ranging from 30 - 50 kW/m^2. The area-averaged heat transfer coefficients (HTCs) on top half surface and bottom half surface (as shown in Fig. 3.1, where $\theta = 0^\circ$ to 180° represent top half surface and $\theta = 0^\circ$ to -180° represent bottom half surface) are respectively defined as:

$$\bar{h}_t = \frac{\dot{q}''}{(T_w^t - T_b)} \tag{3.1}$$

$$\bar{h}_b = \frac{\dot{q}''}{(T_w^b - T_b)} \tag{3.2}$$

where, T_w^t and T_w^b are the wall temperatures averaged over the top and bottom half surfaces respectively. The bulk mean enthalpy H_b is estimated as:

$$H_b = \frac{\int_A \rho u H dA}{\int_A \rho u dA} \tag{3.3}$$

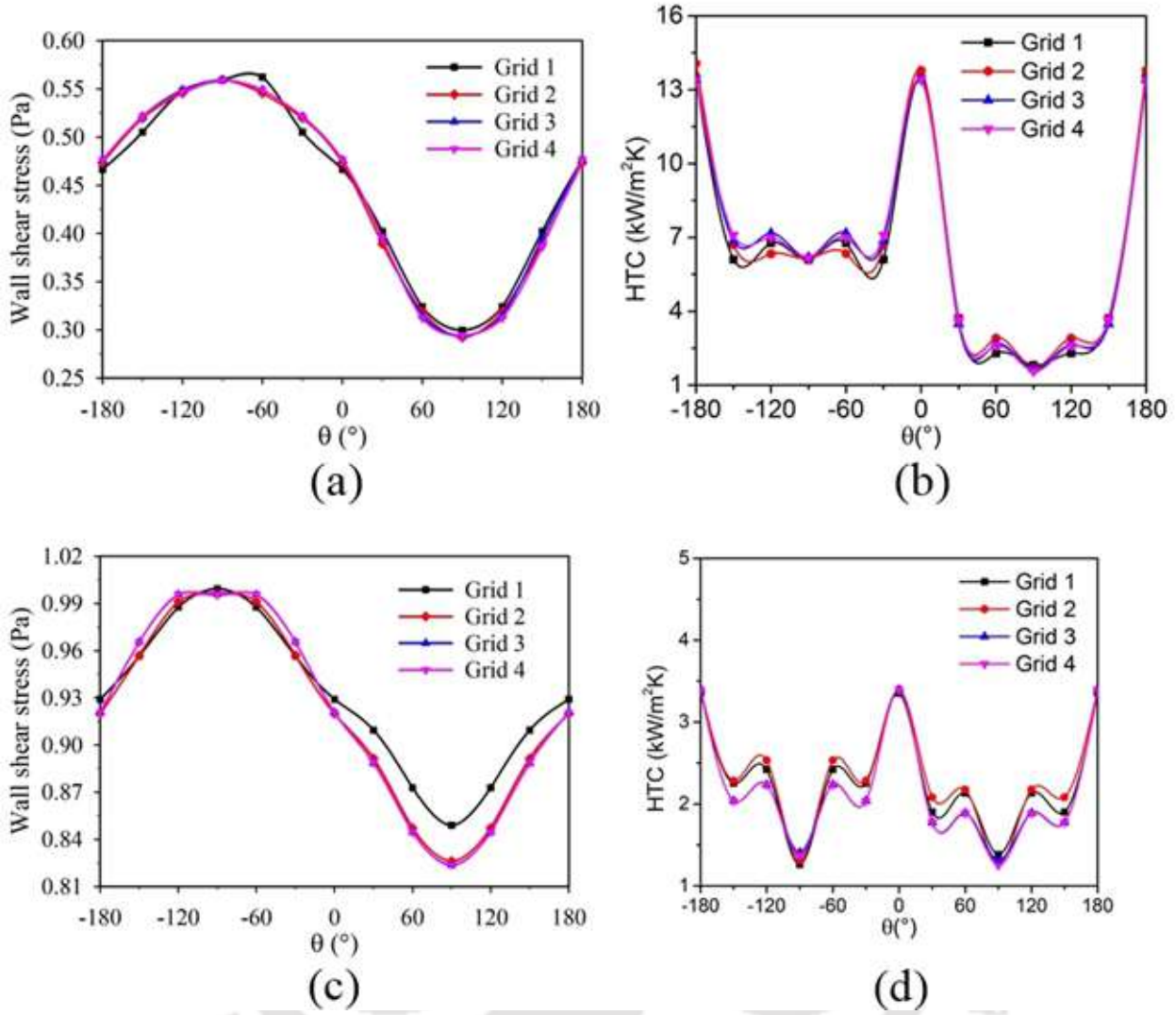

Fig. 3.2: Effect of the choice of mesh structure on the azimuthal distribution of the wall shear stress (a and c) and wall heat transfer coefficient (b and d) at the mid-vertical (a and b) and exit- (c and d) planes of the heated section

which is subsequently used to evaluate the bulk temperature T_b.

The general nature of axial variations in the area-averaged HTCs, average wall temperatures and bulk fluid temperature for a particular set of parameters are shown in Fig. 3.3. On the bottom half surface, area-averaged HTC increases in the downstream direction till it attains a maxima and decreases afterwards. The maximum value of area-averaged HTC corresponds to the lowest difference between average temperature of concerned wall section and bulk fluid temperature, as is indicated by the vertical dashed line in Fig. 3.3a. The difference between averaged wall temperature and bulk temperature increases in downstream

direction, which leads to the consequent reduction in the area-averaged HTC. It is interesting to note that the bulk fluid temperature attains the pseudocritical value (307.8 K corresponding to 8 MPa, shown by dotted horizontal line) at that precise location. Further increase in fluid temperature is expected to lower its thermal conductivity, explaining the associated reduction in HTC. The nature of variation in area-averaged HTC over the top half surface considerably differs from that on the bottom half surface. The average wall temperature shows a point of inversion around $z = 0.35$ m, distance being calculated from the inlet of the adiabatic section, which leads to a local minima for the area-averaged HTC. In Fig. 3.3b, dotted vertical line (1), represents location of that minima, whereas the vertical dotted line (2), corresponds to the initiation of heat transfer deterioration (HTD). Sharp decline in the HTC and noticeably sharper rise in wall temperature can be observed beyond this location, despite moderate rate of change in bulk fluid temperature. Magnitude of HTC at the top surface is distinctly lower compared to the same at the bottom one, along with slightly higher wall temperatures, hinting towards weaker wall-to-fluid thermal interaction there. The highest value of c_p must have appeared earlier on the bottom half surface, to provide a plausible explanation. The maxima in HTC and consequently the initiation of HTD also appears upstream at the bottom surface, signifying the presence of substantial thermal asymmetry in the azimuthal direction within the fluid domain.

The same can be demonstrated following the contours presented in Fig. 3.4. The profiles are non-axisymmetric, with low-temperature zone inclined more towards the bottom part of the channel, leading to steeper temperature gradient near the bottom wall compared to the top. Because of the drastic reduction in fluid density around the pseudocritical point, small temperature change can cause large alteration in fluid density. The low-density fluid tends to rise towards the upper part of a cross-section, with the heavier section of the fluid descending below (Fig. 3.4b), which leads to this asymmetry in temperature (Fig. 3.4a). Such disparity in temperature gradients on either walls explains the appearance of higher HTC at the bottom wall of any cross-section for all axial positions. This cross-sectional variation also yields strong local buoyancy effect. Corresponding natural convection induced local recirculation can clearly be seen following the velocity vectors in Fig. 3.4c. While the momentum boundary layer thicknesses on both the walls seem quite similar, average viscosity level is expected to be higher for the fluid layer in contact with the bottom wall owing to the relatively thinner thermal boundary layer thickness. That results in enhanced level of average wall shear stress, allowing the fluid to move relatively slower along the bottom wall. Thermal conductivity of the fluid in contact with this bottom surface is also higher, allowing

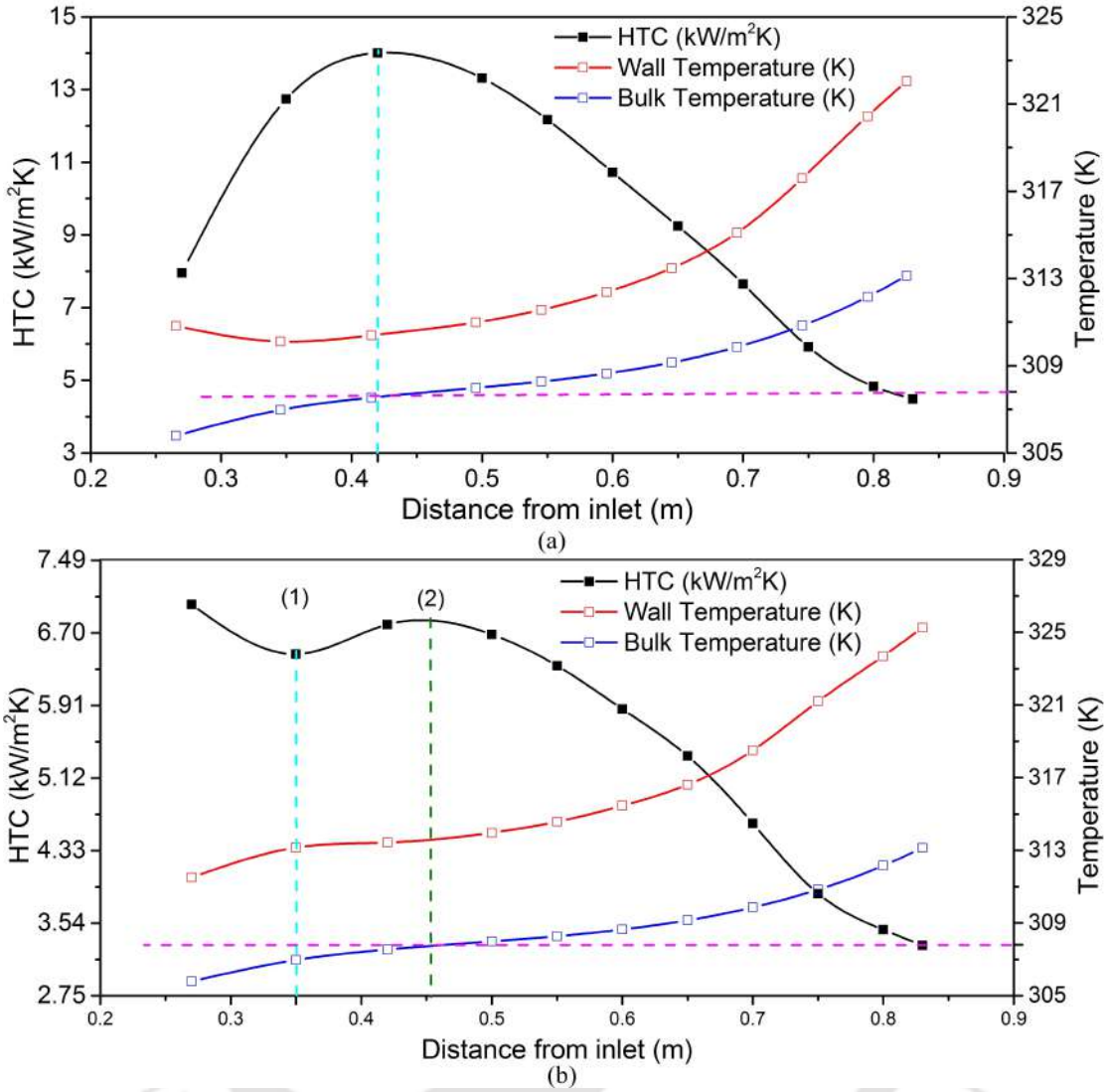

Fig. 3.3: Variations in area-averaged HTC, average wall temperature and bulk fluid temperature at $p = 80$ bar, $G = 450$ kg/m^{2}s and $\dot{q}'' = 40$ kW/m^2: (a) Bottom half surface and (b) Top half surface

better thermal communication, as mentioned before. Consequently the bottom layer attains the pseudocritical condition comparatively earlier, which explains the early appearance of HTC at the bottom wall.

Appearance of HTD in supercritical channels is a well-known phenomenon, particularly for large-dimension vertical channels. In order to put the present set of observations into context, comparisons were drawn with observations from literature. Following the Kim criterion (from [187]), the critical heat flux for initiation of HTD with $G = 450$ kg/m^{2}s is

about 40.5 kW/m^2, which is very close to the one employed here. Zhu *et al.* [188] defined a supercritical boiling number (SBO) to distinguish between normal and deteriorated heat transfer regimes, and a critical value of 5.126×10^{-4} was identified for channels of diameter 2-10 mm. The value of SBO for the present combination of simulation parameters equals 2.69×10^{-4}, which is not very far from the transition criterion. With increase in the $\frac{\dot{q}''}{G}$ term, SBO values comprehensively satisfying the criterion can be obtained.

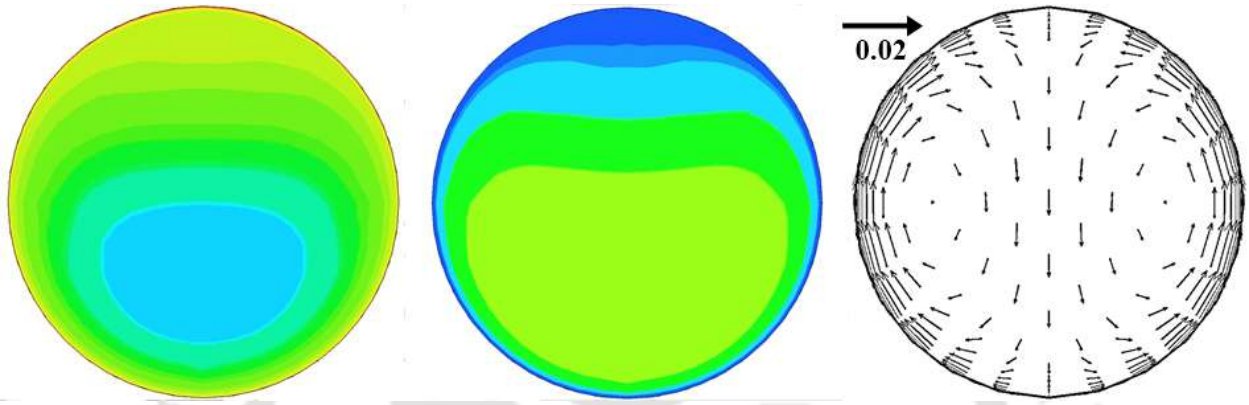

Fig. 3.4: Asymmetric variations in temperature and density contours, and velocity vectors demonstrating local recirculation at the axial location of $z = 0.42$ m: (a) Temperature contour, (b) Density contour and (c) Velocity vectors

In order to demonstrate the effect of gravity even further, a solitary simulation is performed for the hypothetical condition of zero-gravity ($g = 0$), and corresponding observations are compared in Fig. 3.5. Temperature contours are very much symmetric (Fig. 3.5a), as expected. No upward buoyancy force is developed here owing to the absence of gravity, suppressing any kind of local recirculation. That also results in zero azimuthal variation in local HTC and uniform wall temperature at every axial position. It is interesting to note that the magnitude of HTC for the zero-gravity situation lies within the two limits observed earlier (Fig. 3.5b), indicating identical magnitude of the bulk fluid temperature, which is again consistent with overall energy balance. It can, therefore, be concluded that the impact of gravity on the bulk behavior of supercritical flow channels seems similar to the subcritical ones. However, substantial local variation can be expected, with non-axisymmetric thermal profiles, recirculating flows and significant disparity in the nature of thermal communication along the top and bottom half surfaces.

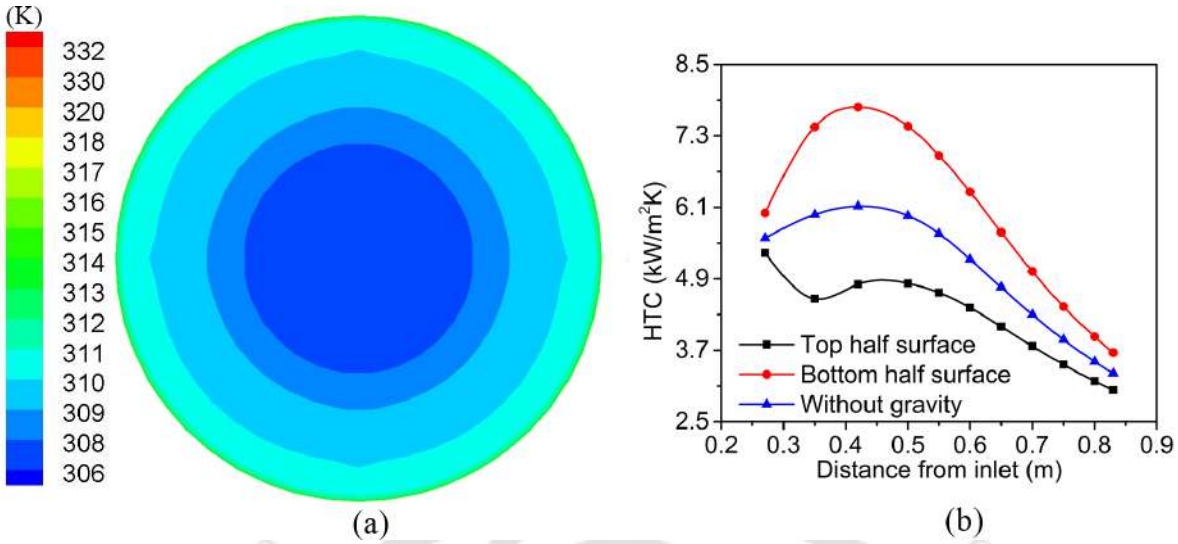

Fig. 3.5: Temperature contours at $z = 0.42$ m and axial variations in area-averaged HTC at the absence of gravity for $p = 80$ bar, $G = 450$ kg/m^{2}s and $\dot{q}'' = 40$ kW/m^2: (a) Temperature contour and (b) Average heat transfer coefficients

3.3.2 Effect of wall heat flux

With increase in wall heat flux for the same T_{in}, axial temperature gradient becomes steeper, entailing an early arrival to the pseudocritical point, which lessens the impact of enhancement in c_p around that, resulting in flow being separated into gas-like regime near the channel wall and liquid-like regime in the core. The thickness of the low-density layer around the wall, however, varies considerably at every axial location, yielding considerable deviation in concerned temperature profiles. Axial variation in area-averaged wall temperature on both bottom and top half surfaces are shown in Fig. 3.6 for $G = 450$ kg/m^{2}s and three different heat fluxes. While the profiles are quite consistent at the bottom surface, characterized by monotonic rise with augmented slopes at higher power level, couple of inversion points can be observed at the top surface, similar to the observation from 7.2b. Such inversions are more pronounced at higher heat fluxes, emphasizing the role of axial temperature gradient, which plays a major role in determining the nature of thermal asymmetry.

The fluid temperature contours at four axial locations are shown in Fig. 3.7 for two different heat fluxes. As the fluid proceeds through the heated channel, while the temperature level continually increases, the stratification is also very much evident because of the rapid changes in the thermophysical properties. The density stratification is more pronounced at higher heat flux, with the warmer fluid progressively being pushed towards the top surface, leading to the gradual shrinking of the thermal boundary layer at the bottom wall. The top

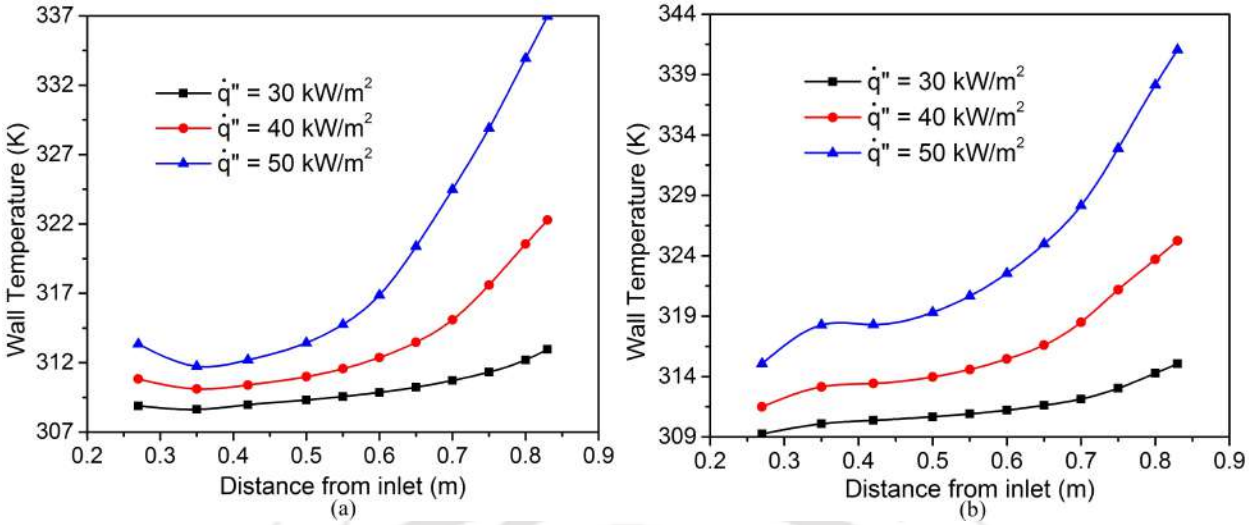

Fig. 3.6: Axial variation in average wall temperature with heat flux at $p = 80$ bar and $G = 450$ kg/m^{2}s: (a) Bottom half surface and (b) Top half surface

half of any cross-section primarily gets occupied by the low-density fluid, where the density variation over a single cross-section can be as high as 450 kg/m^3. Such large difference in local density contributes to the development of substantial buoyancy forces and hence recirculatory motion. The velocity vectors at the same axial locations are presented in Fig. 3.8 for $G = 450$ kg/m^{2}s and $\dot{q}'' = 40$ kW/m^2. Buoyancy-induced local circulation is very much evident, with larger velocity magnitude near the core and reducing rather uniformly towards the wall. Lessening in the magnitude of radial velocity is also noticeable, as the fluid approaches exit. Local recirculation effect is the largest around $z = 0.42$ m. The expanse of fluid temperature at that particular location is quite significant, encompassing the pseudocritical value as well. That allows large density variation at that cross-section and hence substantial local buoyancy. Fluid temperature close to inlet is mostly below pseudocritical, whereas that near exit is well above T_{pc}, thereby yielding comparatively weaker buoyancy force, and hence decrement in recirculating flow. While the cross-sectional velocity vectors are shown solely for $\dot{q}'' = 40$ kW/m^2 in Fig. 3.8, such weakening of local buoyancy induced recirculation towards the exit is expected to be more pronounced for higher heat fluxes. As can be noted from Fig. 3.7b, for axial positions downstream of $z = 0.42$ m, the entire cross-section is covered by fluid warmer than T_{pc}. Therefore, despite substantial thermal asymmetry and stratification, local recirculation is less effective there. For lower heat fluxes, however, fluid can remain below pseudocritical state for much longer flow path. For $\dot{q}'' = 30$ kW/m^2, reasonable portion of the pipe cross-section is occupied by sCO$_2$ cooler than T_{pc} even at $z = 0.65$ m (Fig. 3.7a),

contributing towards meaningful local recirculation virtually over the entire channel, which is manifested in the overall heat transport characteristics.

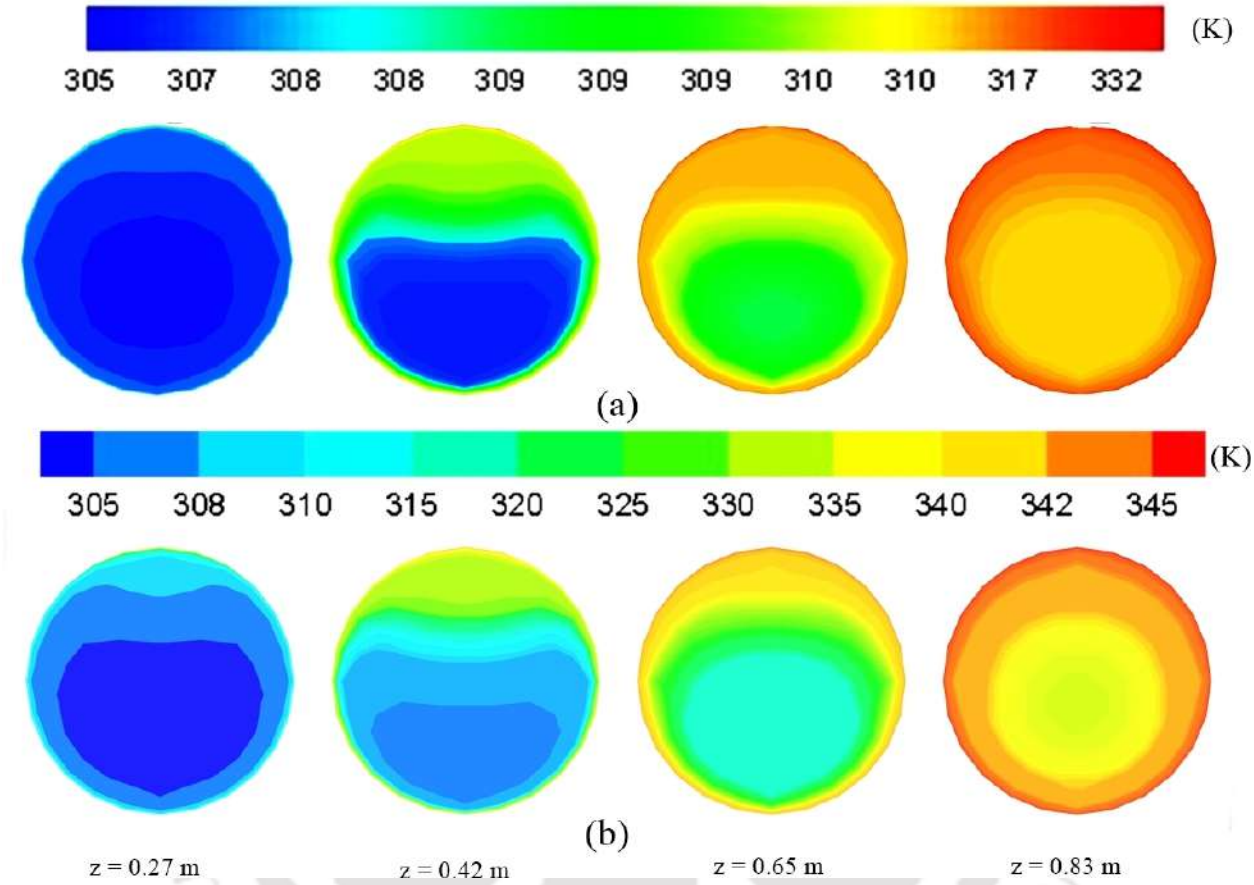

Fig. 3.7: Development of asymmetry in fluid temperature contours at axial locations of z = 0.27 m, 0.42 m, 0.65 m and 0.83 m for two different heat fluxes at p = 80 bar and G = 450 kg/m^{2}s: (a) $\dot{q}''$ = 30 kW/m^2 and (b) $\dot{q}''$ = 50 kW/m^2

Figure 3.9 shows the effect of heat flux on axial variation of the area-averaged HTC. As has already been shown in Fig. 7.2, HTC at the bottom half surface increases till a maxima and then decreases further downstream. The location of the maxima corresponds well to the point of T_b attaining T_{pc}. As long as the fluid temperature crosses the pseudocritical value in a single cross-section, local recirculation remains strong, yielding higher wall-to-fluid thermal interaction and hence larger HTC. Larger heat flux forces the fluid to cross this critical limit further upstream, consequently shifting the point of maximum HTC closer to inlet. Level of HTC is also lower for larger heat fluxes, which is indicative of augmented wall-to-bulk temperature differential. Average HTC at the top half surface is consistently lower than the

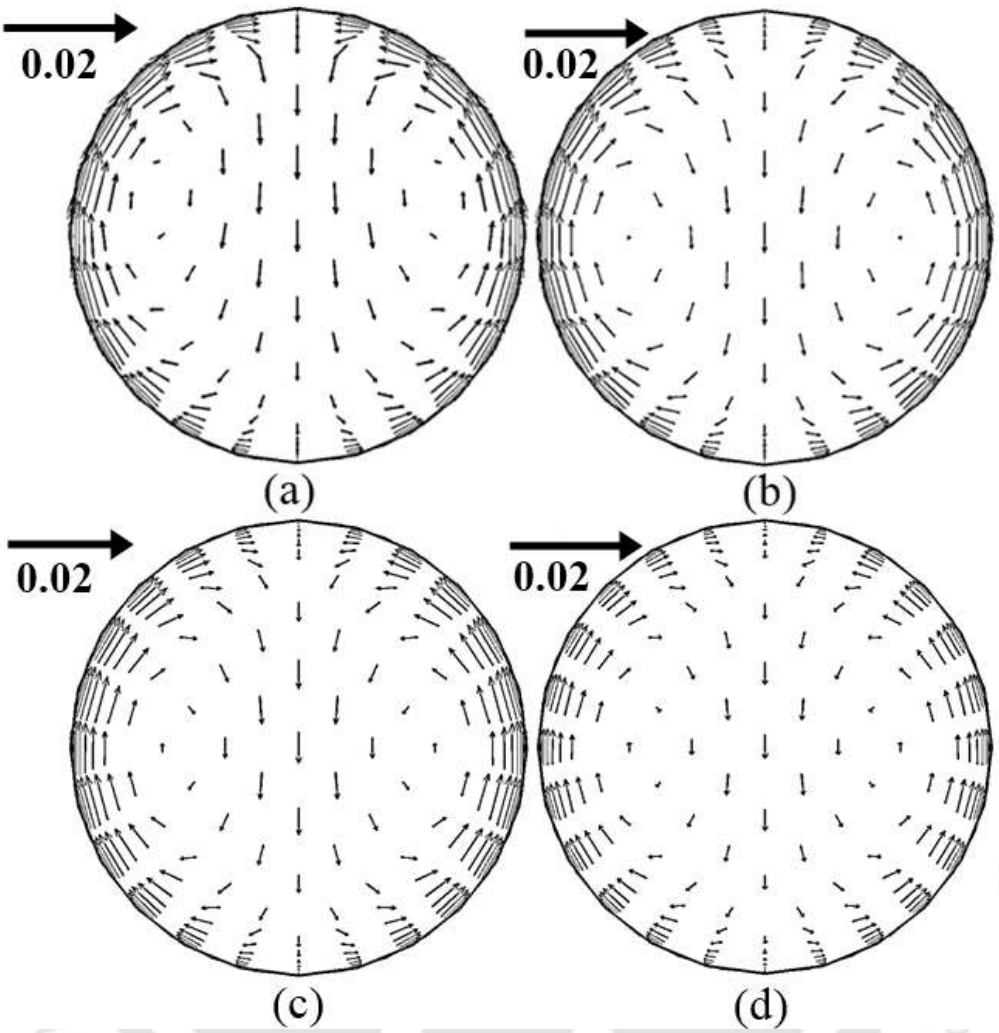

Fig. 3.8: Cross-sectional velocity vectors at different axial locations at $p = 80$ bar, $G = 450$ kg/m^{2}s and $\dot{q}'' = 40$ kW/m^2: (a) $z = 0.27$ m, (b) $z = 0.42$ m, (c) $z = 0.65$ m and (d) $z = 0.83$ m

same at the bottom half surface. For example, $\bar{h}_b = 9.43$ kW/m^{2}K and $\bar{h}_t = 6.83$ kW/m^{2}K at $\dot{q}'' = 30$ kW/m^2. This disparity between HTCs at both the surfaces gets further enhanced with rise in imposed power level.

To ascertain the impact of such asymmetry on the essence of the wall-to-fluid communication from a different perspective, azimuthal variation in certain parameters have subsequently been explored. Profiles of local wall temperature and local HTC at the axial location of $z = 0.42$ m are presented in Fig. 3.10a, whereas the change in local HTC profiles at different axial locations can be seen from Fig. 3.10b. Asymmetric nature is very much palpable. It is really interesting to observe that the largest value of local HTC appears at either ends of the

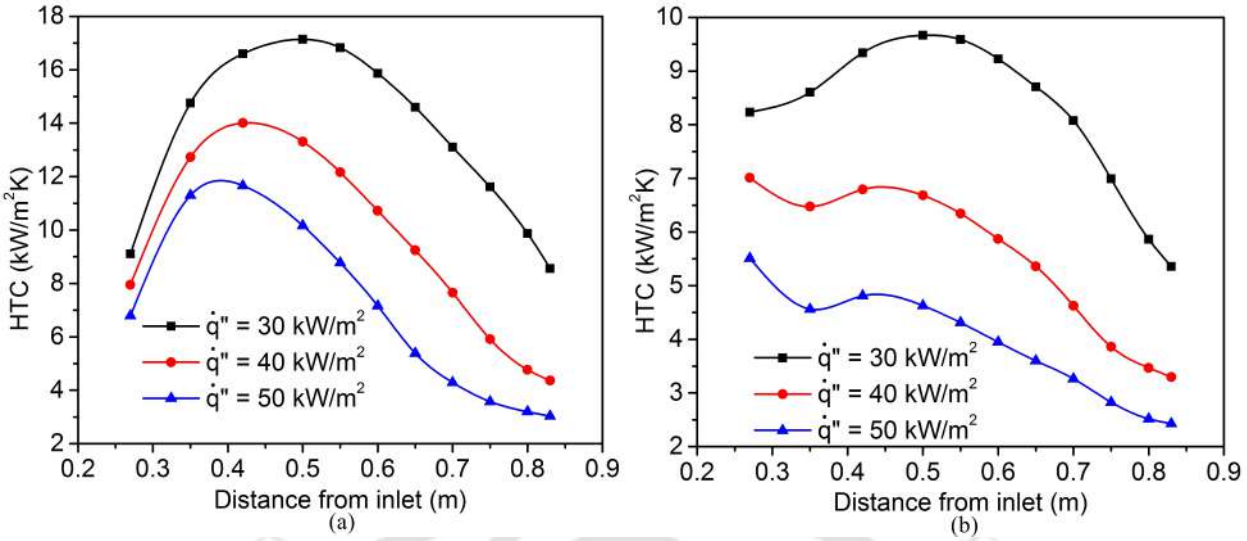

Fig. 3.9: Axial variation in area-averaged heat transfer coefficient with heat flux at $p = 80$ bar and $G = 450$ kg/m^{2}s: (a) Bottom half surface and (b) Top half surface

horizontal plane, accompanied by the lowest wall temperature. More than 400% variation in local HTC and about 6 K change in local wall temperature is discernible in a single axial location. Magnitude of local HTC, however, remains nearly unchanged off the horizontal plane, *i.e.*, over $\theta = 30°$ to $150°$ at the top half surface and $\theta = -30°$ to $-150°$ over the bottom half surface, with higher average level at the bottom section, as already discussed. Both the maximum HTC and average level continually decreases in the downstream locations, approaching a more symmetric distribution. Such non-uniformity in fluid temperature within the layer adjacent to the wall can infuse considerable property variation as well, which can be established following Fig. 3.11a. Reduction in fluid temperature enhances both thermal conductivity (λ) and viscosity (μ). Greater thermal conductivity intensifies local rate of heat transfer, thereby affirming the concerned raise in local HTC. The qualitative similarity in the profiles of local HTC (Fig. 3.10a) and thermal conductivity in the fluid layer contiguous to the wall (Fig. 3.11a) is unmistakable, which authenticates a greater role played by energy diffusion in determining the strength of thermal interaction in contrast to the temperature gradient. Appreciable reduction in λ can be noted downstream, with lesser lopsidedness, owing to regular rise in fluid temperature, resulting in lower HTC. Viscosity profile does not deviate much with axial position, but experiences large variation in the same section. Higher viscosity level at the bottom half surface leads to larger shear stress there, as can be confirmed from Fig. 3.11b. That substantiates earlier hypothesis of fluid drifting slowly along the bottom surface, despite similar velocity boundary layers.

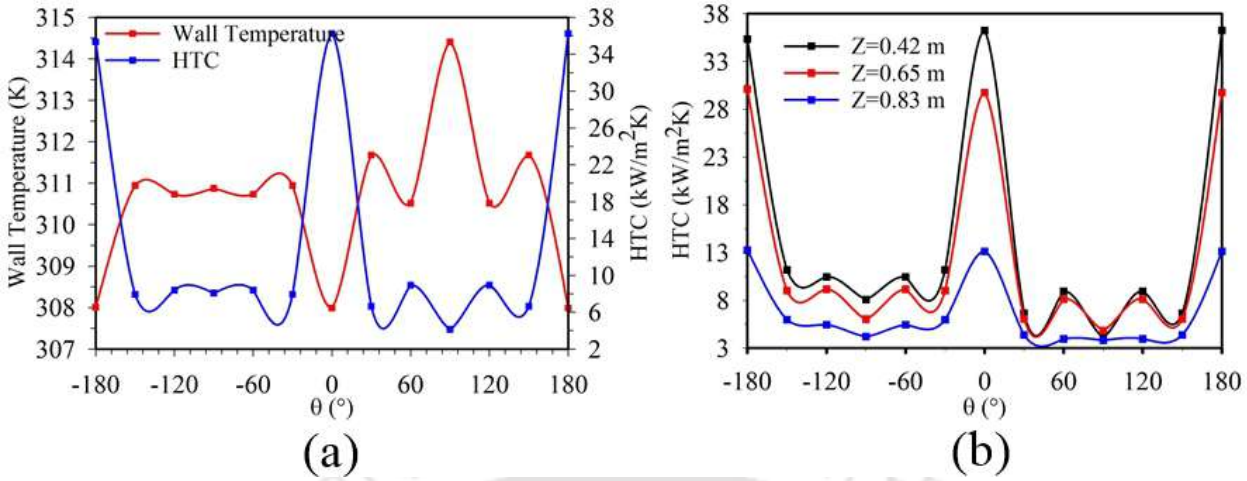

Fig. 3.10: Variation in wall parameters in the azimuthal direction at $p = 80$ bar, $G = 450$ kg/m^{2}s and $\dot{q}'' = 30$ kW/m^2: (a) local wall temperature and local HTC at $z = 0.42$ and (b) local HTC at different axial locations

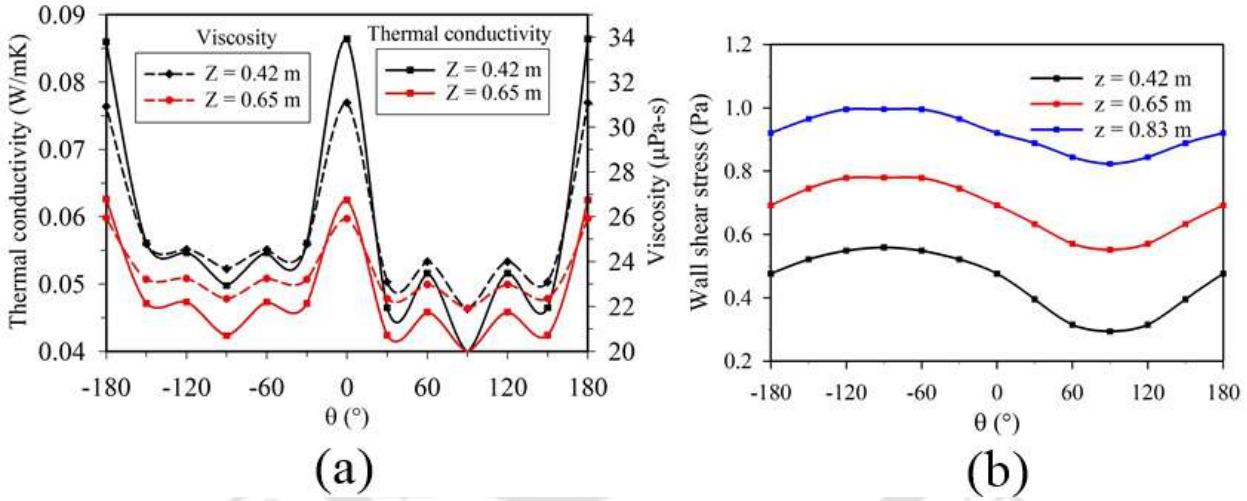

Fig. 3.11: Variation in fluid properties at wall and wall shear stress in the azimuthal direction at different axial locations at $p = 80$ bar, $G = 450$ kg/m^{2}s and $\dot{q}'' = 30$ kW/m^2: (a) Thermal conductivity and viscosity and (b) Wall shear stress

In an attempt to gain a more comprehensive exposure, the area-averaged HTC is plotted against the bulk temperature normalized using the pseudocritical value ($T^* = T_b/T_{pc}$) in Fig. 3.12. The maximum HTC always corresponds to $T^* \approx 1$, which, in turn, dovetails with the peak in c_p. The reduction in peak HTC with increase in imposed power is also evident, which is in consensus with Fig. 3.9. For $T^* < 1$, increase in temperature enhances both specific heat and thermal conductivity, resulting in augmentation in HTC. The reverse

is true for $T^* > 1$. The role of operating pressure can be apprised at this precise context by following Fig. 3.13. As the pressure of supercritical fluid diverges away from the critical point, the drastic nature of property variation also alleviates significantly, as shown in 1.2. That is manifested by the considerable reduction in HTC with rise in system pressure, while the trend remains the same. Similar observation was also reported by Liao and Zhao [9]. Impact of change in system pressure is much less apparent at higher heat fluxes, owing to the early attainment of $T^* = 1$ and consequent lesser degree of asymmetry within the flow domain. It is also safe to conclude that the heat flux has a more assertive impact on HTC compared to pressure.

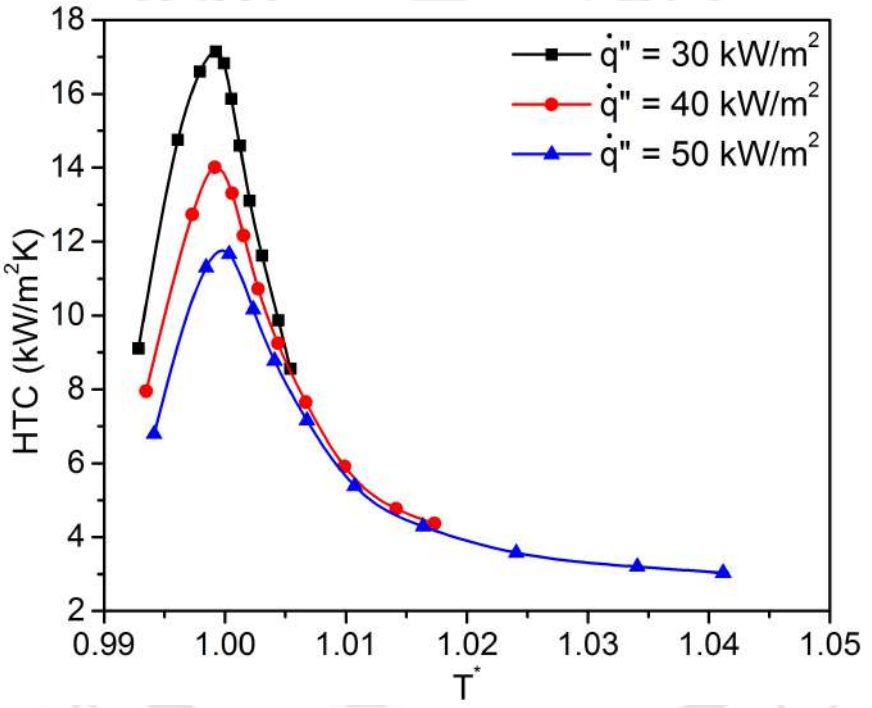

Fig. 3.12: Variation in heat transfer coefficient with normalized bulk temperature for different heat fluxes at $p = 80$ bar and $G = 450$ kg/m^{2}s

3.3.3 Effect of mass flux

The effect of mass flux on heat transport characteristics can be envisaged from Fig. 3.14 for three different heat fluxes. Higher mass flux leads to elevated HTC regardless of the power level. Larger flow rate yields greater Reynolds number, consequence of which is a rise in turbulent intensity, as is evident from Fig. 3.15. This leads to augmented turbulent mixing, which is characterized by velocity fluctuations and more randomized cross-motion,

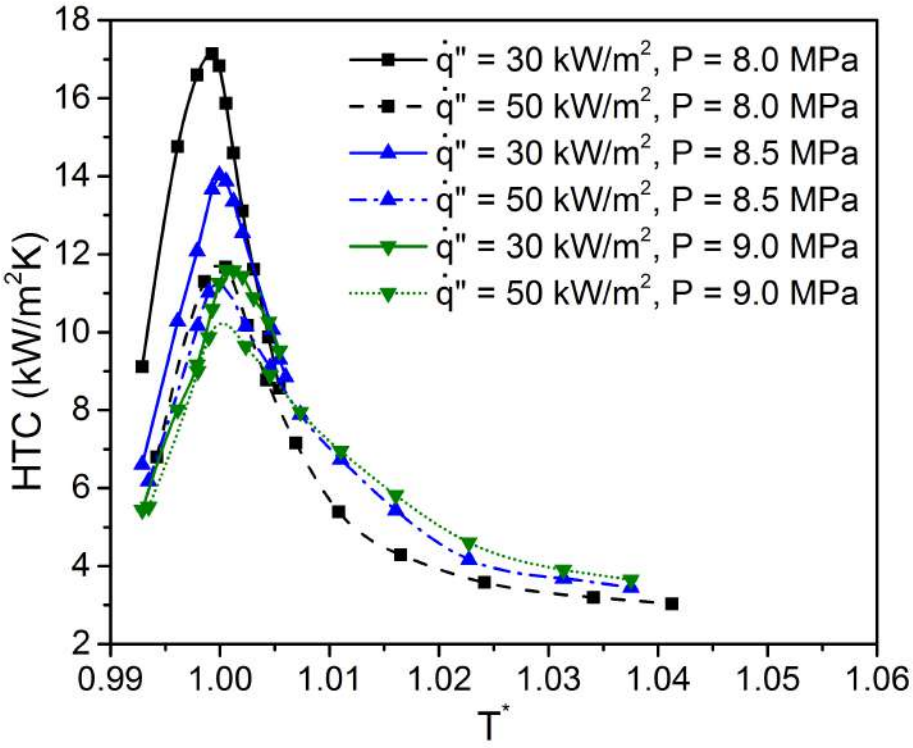

Fig. 3.13: Variation in average heat transfer coefficient with normalized bulk temperature for different combinations of pressure and heat flux at $G = 450$ kg/m^{2}s

eventually leading to greater interaction and hence amplified HTC. It is intriguing to note that the peak of HTC shifts downstream for higher mass fluxes. With T_{in} remaining the same, system requires longer heating length to attain $T^* = 1$, resulting in the delay in peak HTC, albeit with substantially increased magnitude.

3.3.4 A dimensionless perspective

The role of local buoyancy and consequent thermal asymmetry has repeatedly been stressed upon in the above paragraphs. Therefore an effort is made to quantify the same by defining a non-dimensional buoyancy parameter of the following form.

$$Bu = \frac{Gr}{Re_b^2} \tag{3.4}$$

where the Grashof number (Gr) is defined as:

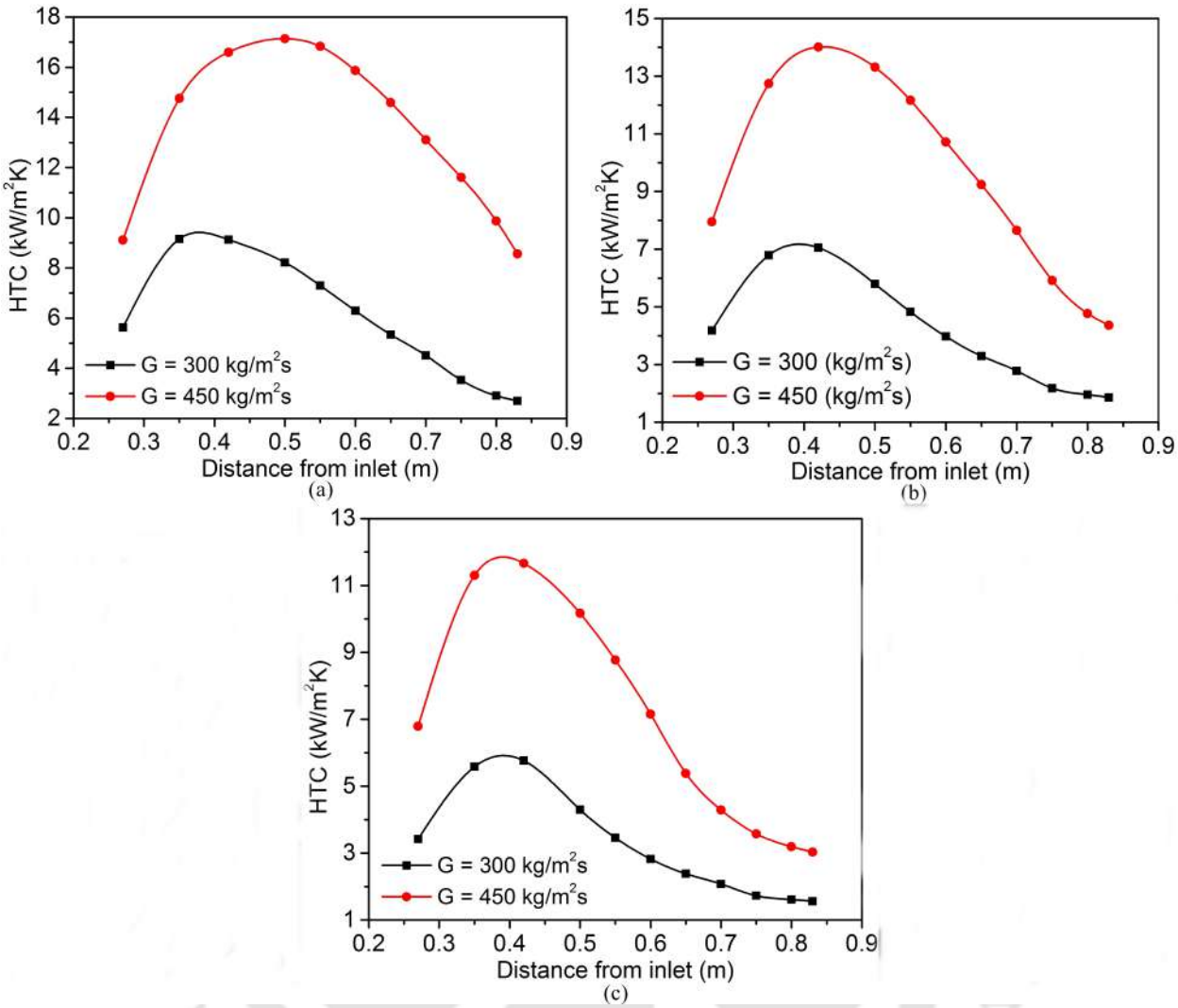

Fig. 3.14: Axial variation in average heat transfer coefficient for different mass fluxes: (a) $\dot{q}'' = 30$ kW/m^2, (b) $\dot{q}'' = 40$ kW/m^2 and (c) $\dot{q}'' = 50$ kW/m^2

$$Gr = \frac{(\rho_b - \rho_w)\, gd^3}{\rho_b \nu_b^2} = \frac{(\rho_b - \rho_w)\, \rho_b g d^3}{\mu_b^2} \tag{3.5}$$

Here ρ_b and ρ_w denote density of sCO_2 respectively at bulk temperature (T_b) and average temperature of either top or bottom half surface, based on the context. Similarly, μ_b and ν_b represents the dynamic and kinematic viscosity of the bulk fluid respectively. Reynolds number (Re) corresponds to the bulk fluid as:

$$Re = \frac{Gd}{\mu_b} \tag{3.6}$$

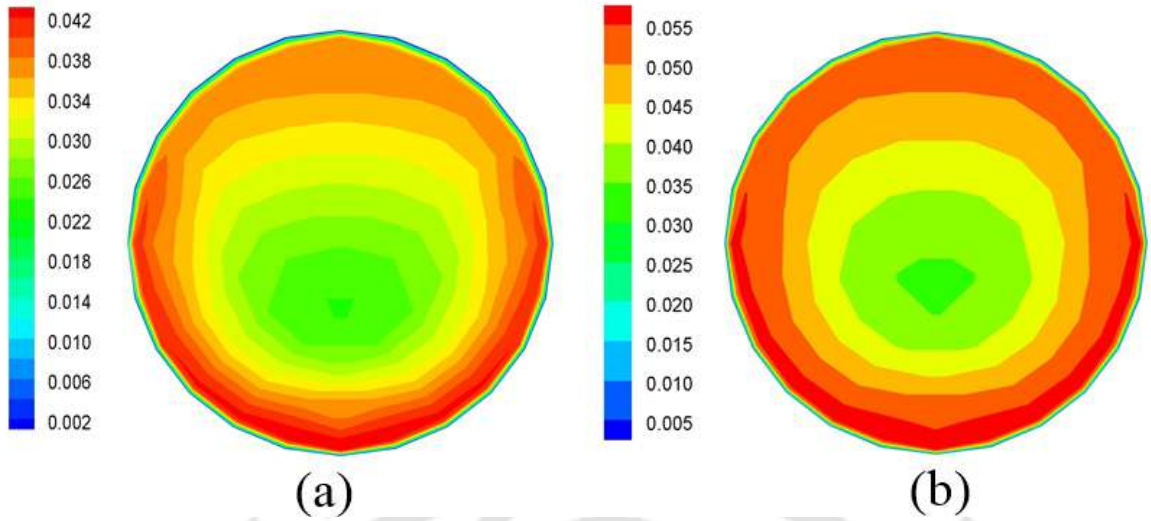

Fig. 3.15: Contours of turbulent intensity for two different mass fluxes: (a) $G = 300$ kg/m^{2}s and (b) $G = 450$ kg/m^{2}s

It is suggested that the effect of buoyancy can be neglected for $Bu < 10^{-3}$ [69], whereas the effects of both natural and forced convection need to be confronted for Bu in the range of 0.1 to 10. To envisage the scenario for the present minichannel, axial variation of Bu along both bottom and top half surfaces are presented in Fig. 3.16. Bu remains consistently greater than 10^{-3} for all the explored cases, thereby quantifying the presence of local buoyancy effect throughout the minichannel, which is consistent with density stratification reported earlier. Variation in heat flux seems to have inconsequential effect at the inlet and also near the exit. However, heat flux is more influential inside the channel, with larger buoyant force being generated at lower power, another observation already discussed above. In an effort to correlate Bu with T^*, concerned profiles are presented in Fig. 3.17 for three different heat fluxes. Here the vertical line in each represent the pseudocritical temperature ($T^* = 1$). It can be seen that with decrease in mass flux, effect of buoyancy increases significantly, as the forced convection effect reduces. At higher mass flux temperature variation is less and thus corresponding variation in density is also smaller, which is the driving force for buoyancy. For $T^* > 1$, Bu decreases significantly, while still remaining quite relevant till the channel exit. It can therefore be concluded that, despite originally being defined for supercritical macrochannels, the employed form of Bu can confidently be applied for minichannels.

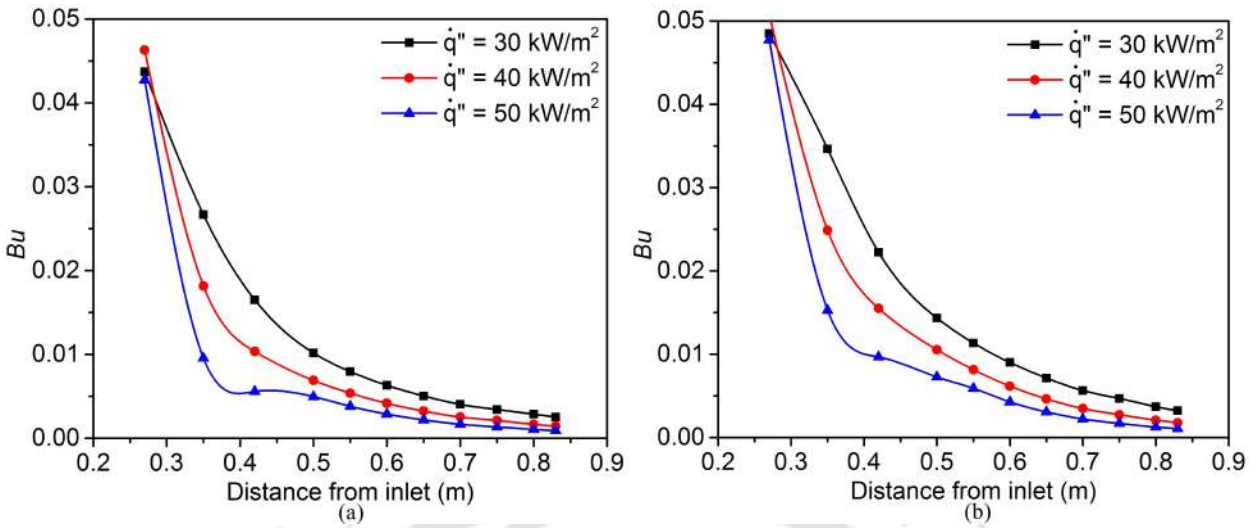

Fig. 3.16: Axial variation in buoyancy parameter (Bu) for $G = 300$ kg/m^{2}s: (a) Bottom half surface and (b) Top half surface

3.4 Summary

Steady-state simulations of supercritical CO_2 through a heated minichannel is performed to explore the influence of associated control parameters, such as heat flux, mass flux and system pressure, on the heat transport characteristics, with particular emphasis on the effect of buoyancy. Sharp property variation of supercritical fluid around the pseudocritical point can result in substantial property variation in certain axial locations of the channel, inducing noticeable thermal asymmetry and large azimuthal variation, which can lead to consequent heat transfer deterioration. The same is explored here for a horizontal minichannel under uniform heat flux condition and major observations are summarized below.

- HTC at the bottom half surface is consistently higher than the same at the top half surface, which, in turn, is characterized by slightly higher wall temperature and greater wall-to-bulk temperature differential. The disparity is more apparent at higher heat fluxes, but subside with rise in pressure.

- Substantial density stratification can be observed all through the channel, which emanates natural convection induced local circulation and variable thermal boundary layer thickness around the wall. Steeper temperature gradient is observed at the bottom half surface, explaining the higher HTC level there. Rise in heat flux lowers the HTC magnitude owing to lesser property variation. Local recirculation also weakens considerably, as the fluid approaches exit.

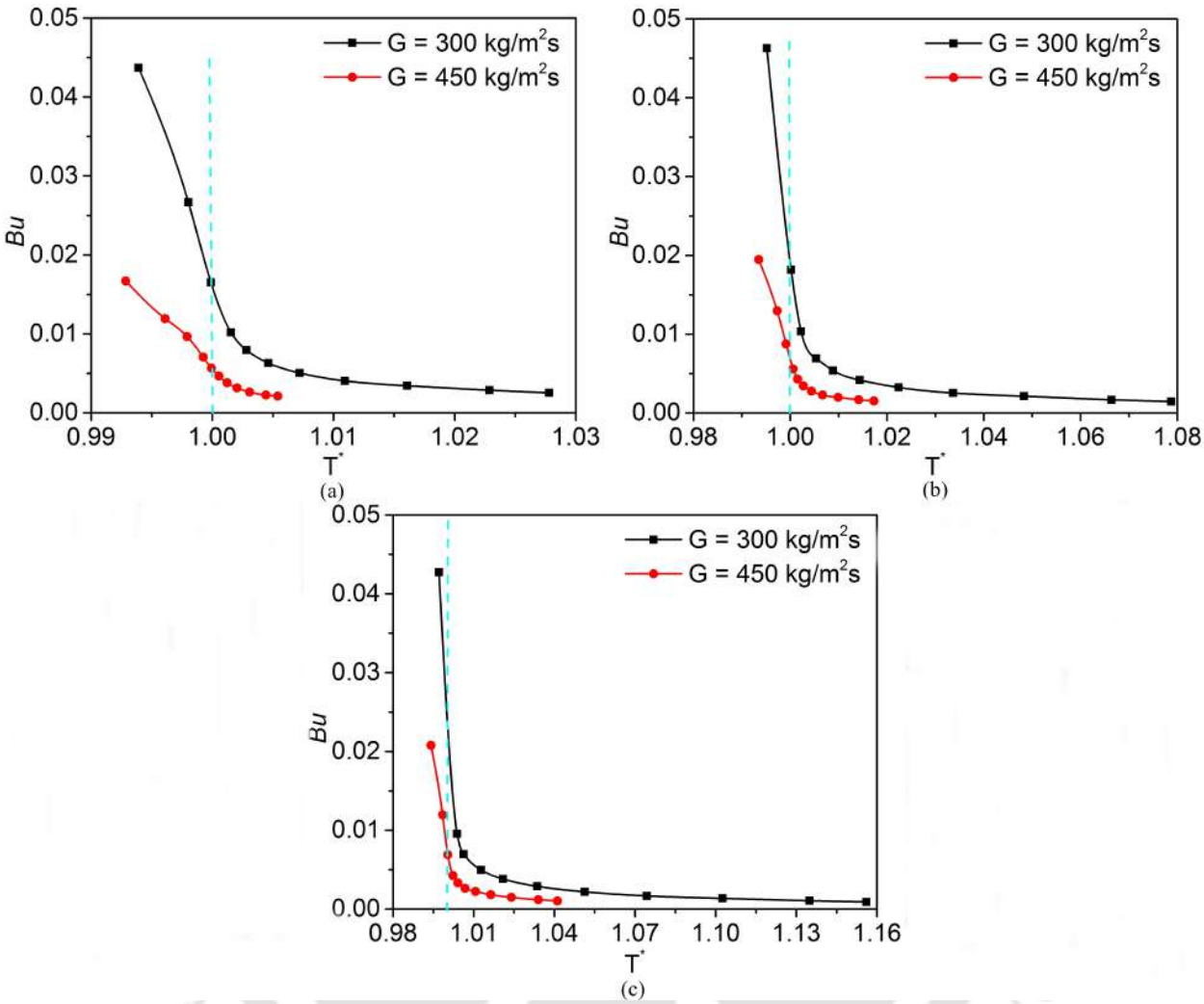

Fig. 3.17: Variation in buoyancy parameter (Bu) with normalized bulk temperature along top half surface for different heat and mass fluxes at $p = 80$ bar: (a) $\dot{q}'' = 30$ kW/m^2, (b) $\dot{q}'' = 40$ kW/m^2 and (c) $\dot{q}'' = 50$ kW/m^2

- Local recirculation is the strongest as bulk fluid attains pseudocritical value, accompanied by highest area-averaged HTC.
- Large azimuthal variation can yield more than 400% change in HTC and about 6 K variation in wall temperature in a single cross-section, with peak HTC appearing on the horizontal plane. Lower fluid temperature in contact with the bottom half surface provided enhanced local shear stress, allowing to fluid slid slower along the same.
- Larger mass flux augments heat transfer, as a consequence of increase in turbulent intensity, on both top and bottom half surfaces, with the peak moving downstream.

- Buoyancy parameter proposed by Jackson *et al.* [69] is able to represent the flow behavior reasonably well over the entire length of the minichannel and hence can subsequently be explored for corresponding scaling and development of heat transfer correlations.

Chapter 4

Thermalhydraulic assessment and design optimization of incorporating flow obstructions in supercritical MCHS

4.1 Preamble

One of the major concerns with the application of SCF in forced convective channels is the premonition of heat transfer deterioration (HTD). The sharp decline in the associated transport properties beyond the pseudocritical temperature (T_{pc}) considerably weakens the thermal communication between the heated wall and neighboring fluid layer, resulting in large deterioration in the HTC and a steep jump in the wall temperature. Several seminal works have provided a detailed characterization of HTD in macrochannels through arduous experiments, emphasizing the role of the pseudocritical region [189–191]. Such reduction in heat transfer was attributed by Bellinghausen and Renz [192] to the gravity-driven buoyancy effects originating from the steep density reduction near the heated surface, which was also hinted during the experiments of Adebiyi and Hall [193]. Two different mechanisms behind the initiation of HTD were numerically identified by Koshizuka *et al.* [194]. While the roles of thickening in viscous sub-layer and lessening in Prandtl number (Pr) were highlighted at higher flow rates, flattening of the velocity profile owing to the buoyancy-induced acceleration was emphasized as lower flows. While they predicted violent oscillations in wall temperature post-deterioration, a sudden halt in the flow was envisaged by Morshedy *et al.* [195] because

of the drastic variation in properties in the radial direction. Wen *et al.* [196] predicted the possible appearance of a second HTD, if complete turbulent recovery is possible after the first one at the presence of strong buoyancy. In a more detailed appraisal, Cheng *et al.* [197] also conferred on the identification of two peaks in the profiles of wall temperature, which were direct manifestations of dual HTD. The first one was attributed to the buoyancy effect and the other to the shear stress, with both flattening the velocity distribution and reducing the turbulent kinetic energy. Zhang *et al.* [198] talked about the variation in the nature of heat transfer depending on channel configuration and flow orientation, with both modulating the interaction between buoyancy and flow velocity. They also accentuated the roles of boundary layer thickness, effective thermal conductivity, secondary flows, and turbulence production, among others, in both enhancing and deteriorating the rate of heat transfer. It is, therefore, clearly evident that the heat transfer mechanism with supercritical fluid is markedly different from the same with the subcritical fluid, primarily because of the dependence on both external and thermophysical factors. An account of the relevant experimental studies, mostly focusing on the development of heat transfer correlations, is available in Pizzarelli and Marco [199].

It is apparent now that the phenomenon of HTD is definitely pertinent to SCF-driven MCHS as well, unless the characteristics dimensions are too small, with both buoyancy and flow acceleration having their individual implications. The decline in HTC with SCF is often compared with the initiation of film boiling, mainly because of the comparable order of reduction in the thermal conductivity of the fluid and hence in the rate of energy interaction between the solid wall and the adjacent fluid layer. However, while there are ample attempts to delay the departure from nucleate boiling in such channels using both active and passive means [200], analogous endeavor with SCF is rather sporadic. A few of the early-day researchers explored turbulence promoting inserts like twisted tapes or ribbed tubes with some success in enhancing the resistance coefficient [201, 202]. Kohler at al. [203] found the resistance coefficient to be almost double in the internally-ribbed tubes compared to the smooth ones. The numerical model of Zhao *et al.* [204] also predicted enhancement in heat transfer with internally-ribbed tubes for high mass flux and low heat flux, as they explored the impact of geometric parameters on the resistance coefficient. The intensification in the turbulent diffusion owing to the rotational flow imparted by the helical rib-roughened tubes was identified as the primary contributor to such heat transfer enhancement by Li *et al.* [205]. Quite a few studies focused on optimizing the geometric parameters associated with the ribbed structure [206–208], while coiling of the heated passage has also been explored

[209, 210], with the objective invariably being the modulation of the turbulent characteristics and impact of buoyancy. The novel proposals of the cylindrically-concaved tube [211] or spirally fluted tube [212] were able to increase HTC in comparison with the conventional ones but failed to eradicate the deterioration. The use of flow obstacles by Eter *et al.* [213] also resulted in both enhancement and deterioration in heat transfer depending on the imposed conditions.

All such efforts, however, were concentrated on channels with larger diameters, as inscriptions of ribs or grooves are not feasible on the walls of mini-/microchannels. As per the convention proposed by Kandlikar and Grande [146], a minichannel is expected to have hydraulic diameter in the range of 0.2 to 3 mm, whereas the summary presented in [206] shows that the typical rib height used in different experimental studies is around a millimeter, thereby discarding that as an option in SCF-driven MCHS. Hardly any relevant work can be identified in the open literature, exploring any procedure for enhancing the overall level of HTC in such a system, with the major focus being on eliminating or delaying the appearance of HTD. The attempt of Zhang *et al.* [214] with zigzag channel having hydraulic diameter of 1.1 mm is a reasonable one but rendered effective only for a small range of the bend angle. That creates the precise backdrop for the present work, where the thermalhydraulic characteristics of a sCO_2-filled heated square minichannel, designed with flow obstructions in the shape of rectangular obstructions, have been explored. The influence of different geometric parameters associated with the obstructions has been elucidated systematically to accomplish an optimum design with the most worthwhile performance. The primary design variables under consideration are the height, thickness, and inclination angle of the individual obstructions. The role of operating variables, such as heat flux, mass flux, pressure, and inlet temperature, have also been explored on the preferable configuration. The present study can be viewed as an important step leading to the incorporation of microscale geometries in MCHS, specifically involving supercritical heat transfer.

4.2 Development of Computational Model

4.2.1 Physical geometry and boundary conditions

As mentioned above, the present study concerns the thermalhydraulic characterization of the flow of sCO_2 through a square minichannel under heating conditions. A duct having cross-section of 500 μm $\times$ 500 μm and length of 10 mm is selected for that purpose, a schematic representation of which is available in Fig. 4.1. Rectangular plates have been placed on the

lower and upper walls of the duct in an alternate orientation (Fig. 4.1a), in order to alter the primary direction of motion of the fluid in a predesignated fashion. The width of each of the obstructions is the same as the channel width ($W = 500$ μm), and the other dimensions are modulated as a part of the present study. The corresponding dimensional details about the adopted geometry are available in table 4.1. While the mass flux and temperature have been specified at the inlet, constant pressure is imposed at the outlet plane. Both the side walls ($y - z$ planes) are subjected to an uniform heat flux, while the top and bottom walls ($x - z$ planes), as well as the exteriors of the obstructions mounted on those, are treated as adiabatic surfaces.

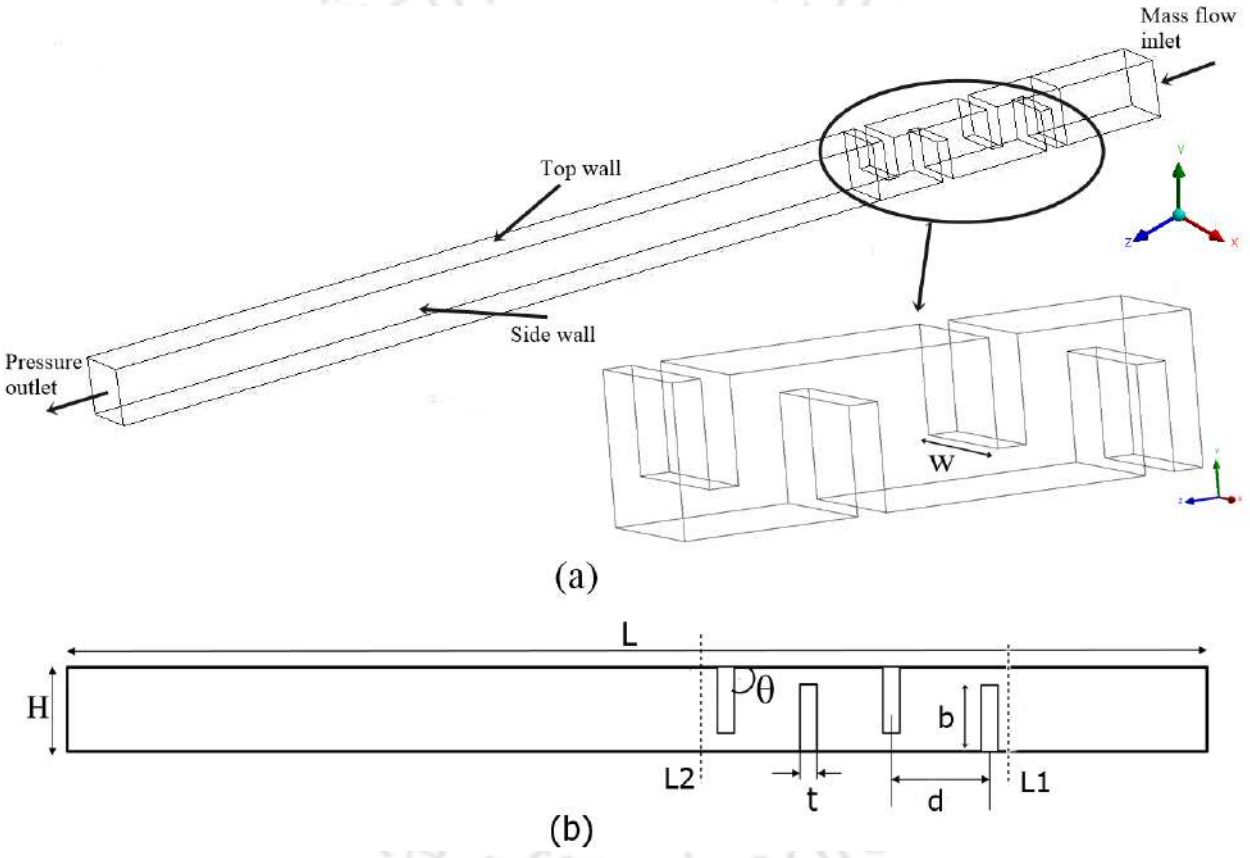

Fig. 4.1: Schematic representation of the computational domain: (a) Three-dimensional view, with the zoomed section showing two pairs of rectangular obstructions; (b) Two-dimensional side view, marking important dimensions of the considered minichannel

Steady-state versions of the mass, momentum, and energy conservation equations are solved as a part of the present work in three-dimensional Cartesian coordinate, which has been discussed in Chapter 2.

Table 4.1: Geometric details of the adopted minichannel

Parameter	Values
Channel height (H)	500 μm
Channel width (W)	500 μm
Channel length (L)	10 mm
obstruction height (b)	300 – 400 μm
obstruction thickness (t)	200 – 400 μm
Pitch (d)	0.5 and 1.0 mm
Inclination angle (θ)	30 – 90 $^\circ$

The conservation equations have been solved following the finite-volume approach of ANSYS-Fluent and has been discussed in Chapter 2.

4.2.2 Grid-independence study and numerical validation

The development of a legitimate mesh structure is extremely crucial for accurate numerical replication of any physical phenomenon on the discrete space. The non-continuous nature of the fluid domain in the present configuration makes the grid generation an even more arduous task, necessitating non-uniform meshes over the entire geometry, with finer meshes near the walls and in the regions expected to experience steep gradients in any flow variable. Meshing is done by dividing the geometry into three domains, namely, the domain with the obstructions and two domains on either side of it without having any, and hexahedral mesh is found to be appropriate for both. The SST $\kappa - \omega$ turbulence model requires the value of y^+ to be in the range of one [186], which is ensured by using the inflation model, with a first layer thickness of 0.2 μm and a total of 9 such layers. Multiple mesh structures have been considered for each of the configurations explored here to ensure the mesh-independent nature of each reported result. Predicted values of the bulk temperature at the outlet plane and total pressure drop across the channel have been employed as the selection criteria. Examples are available in table 4.2 for a plane minichannel and the one housing two pairs of obstructions (referred as FM-2P in section 4.3). It is clearly evident that the transition from mesh 3 to mesh 4 for the plane channel corresponds to about 78% increase in the total number of elements and hence, in the associated resource requirement. It, however, induces less than 0.3% change in the bulk temperature and just about 1% change in the pressure

drop, which itself is only a small fraction of the imposed system pressure. Therefore, mesh 3 is continued for all the simulations reported here involving plane MCHS. The mesh 3 corresponding to the other configuration has also been found to be the desirable one, as detailed in table 4.2, and a view of the same is presented in Fig. 4.2. While the pressure drop is significantly greater here owing to the presence of the obstructions, only about 1% change in the same is incurred with a move to mesh 4, despite a nearly 35% increase in the number of discrete elements, establishing the feasibility of the present choice. The same procedure has been repeated for all the orientations, as the mesh must be re-adjusted and re-examined for any change in the obstruction structure. The number of elements varies from 451 041 to 726 534, with the highest aspect ratio of 81 near the obstructions.

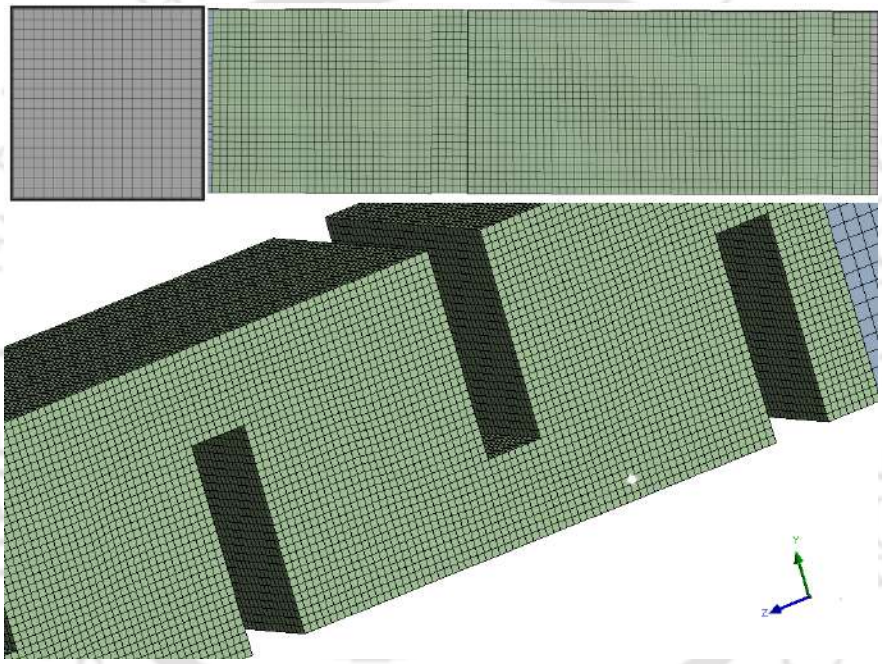

Fig. 4.2: View of the adopted mesh structure: Side view for the entire domain at the top and a zoomed presentation of the obstruction portion below

Because of the absence of data from a similar configuration in the open literature, direct validation is not possible. In order to gain confidence about the capability of the developed numerical framework in emulating supercritical heat transfer in minichannel, simulations have been performed for a duct having cross-section of 500 μm $\times$ 500 μm and length of 10 mm for $p = 8$ MPa, $G = 400$ kg/m^{2}s and $\dot{q}'' = 40$ kW/m^2. As can be seen from Fig. 4.3(a), predicted values of HTC are in excellent agreement with the semi-empirical correlation proposed by [215] along the entire length of the flow passage. Reasonable conformity can also

Table 4.2: Details of various mesh systems employed

Channel configuration	**Mesh structure**	**Number of elements**	**Bulk temperature** (K)	**Pressure drop** (kPa)
Plane minichannel (No obstructions)	Mesh 1	148326	317.48	0.42
	Mesh 2	300128	312.08	0.58
	Mesh 3	451041	308.16	0.60
	Mesh 4	805274	307.32	0.60
Minichannel with 2 pairs of obstructions	Mesh 1	312328	305.86	8.75
	Mesh 2	500904	305.57	8.48
	Mesh 3	612532	305.35	8.33
	Mesh 4	825178	305.22	8.21

be observed over the best part of the channel with the relations suggested by [126] and [216] as well. It must be noted here that the correlation proposed by Mokry *et al.* [216] concerns supercritical water in a macrochannel, which may well be the reason behind the small deviation between both curves. The correlation of Huai *et al.* [126] was developed for the cooling condition under lower heat flux, which may be responsible for behind concerned deviation. Another set of comparison is drawn using the pressure drop values obtained with several *Re* and the correlation proposed by Steinke and Kandlikar [217] in Fig. 4.3(b). Definitely, the trends are very much in accordance with each other, substantiating the appropriateness of the present numerical structure.

4.3 Important Definitions

The validated numerical framework is employed to explore the thermalhydraulics of the square MCHS shown earlier (Fig. 4.1), housing rectangular obstructions of varying orientations. Five different configurations are considered to comprise each of the sets, namely, plane minichannel without any obstructions (referred as PM), and minichannels with one, two, three, and four pairs of obstructions (referred to as FM-1P, FM-2P, FM-3P, and FM-4P respectively). The height (b), thickness (t), and inclination angle (θ) of the individual obstructions have been modulated in each such set, while a constant pitch (d) of 500 μm has been maintained to mark the center-to-center distance of the adjacent obstructions, with the focus being to identify an optimum arrangement in terms of the HTC and pressure drop.

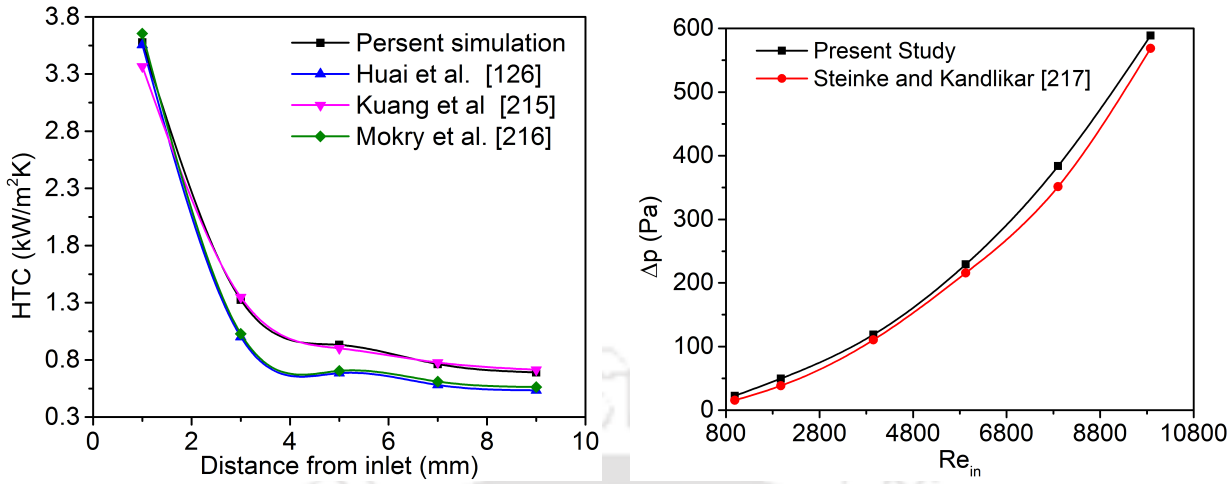

(a) **(b)**

Fig. 4.3: Validation of the present numerical framework: (a) Comparison of numerically-predicted HTC with the correlations of [215], [126] and [216]; (b) Comparison of pressure drop prediction with the correlation of [217]

Simulations have been performed over a reasonably wide range of parameters, with $\dot{q}''$ of 40 – 100 kW/m^2, G of 100 – 1000 kg/m^{2}s, p of 8 – 10 MPa and T_{in} of 305 – 320 K.

HTC at any particular cross-section can be estimated as,

$$\alpha_z = \frac{\dot{q}''}{T_{w,z} - T_{b,z}} \tag{4.1}$$

where $T_{w,z}$ is the wall temperature averaged over the solid surface at that particular axial (z) location. The bulk mean enthalpy at that cross-section can be calculated as,

$$h_{b,z} = \frac{\int_A \rho u h dA}{\int_A \rho u dA} \tag{4.2}$$

which is subsequently employed to evaluate the bulk temperature $T_{b,z}$ using the knowledge about the local pressure. The local Nusselt number (Nu_z) can consequently be computed utilizing the associated values of α_z and thermal conductivity corresponding to $T_{b,z}$.

The use of obstructions in the flow passage of any MCHS is expected to enhance the heat transfer performance but at the expense of augmented pressure drop (Δp). It is, therefore, improper to quantify the impact of the obstructions solely in terms of either of these two competing parameters. To envisage the consequences of incorporating obstructions on both of these quantities simultaneously, a Performance Evaluation Criterion (PEC) has been

defined following [218].

$$PEC = \frac{\overline{Nu}/\overline{Nu}_o}{(\Delta p/\Delta p_o)^{1/3}} \tag{4.3}$$

Here both $\overline{Nu}_o$ and Δp_o correspond to the unobstructed channel (PM), while the others are associated with any specific configuration under scrutiny. The average Nusselt number ($\overline{Nu}$) for any MCHS has been defined as the average of the local ones over a large number of axial locations. PEC can be viewed as the ratio of HTCs at an equal pumping power and a value in excess of one signifies an overall improvement in the thermalhydraulic performance of any configuration over the plane channel.

The total thermal resistance (R_{th}) for MCHS is given as

$$R_{th} = \frac{T_w - T_b}{q} \tag{4.4}$$

4.4 Optimization of the Geometric Configuration

4.4.1 Effect of introduction of baffles

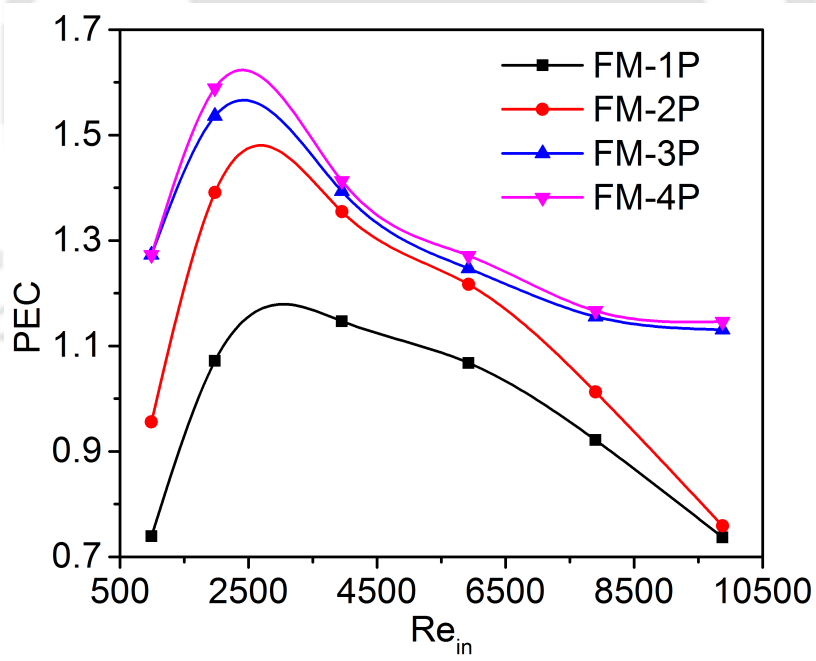

Fig. 4.4: Variation in PEC with the inlet Reynolds number (Re_{in}) for all the four channels with obstructions considered here at $\dot{q}'' = 40$ kW/m^2

The first logical step of appraisal is to decipher the impact of the introduction of obstruc-

tions in MCHS on overall thermalhydraulics. Accordingly, simulations have been performed with all the five configurations mentioned before, with each baffle being characterized by b = 0.3 mm, W = 0.5 mm, t = 0.1 mm and $\theta = 90^o$, and a center-to-center distance d = 0.5 mm. Here a pair refers to two adjacent rectangular plates mounted on the opposite walls, with the first one being placed on the bottom surface. PEC has already been earmarked as the parameter facilitating comparison, and hence the variations in PEC for all the four channels with obstructions are presented in Fig. 4.4 over a considerably wide range of Re_{in}. Here the inlet Reynolds number ($Re_{in} = GW/\mu_{in}$) is defined in terms of the fluid viscosity at the inlet plane. PEC increases quite steeply with an increase in the supplied mass flux for all the configurations at lower levels of Re_{in}, before attaining a respective maxima and falls thereafter with a lesser gradient. Such a trend clearly indicates a faster rate of enhancement of $\overline{Nu}$ at smaller Re_{in} in comparison to the induced pressure loss, implicitly suggesting an augmentation in the effective thermal conductivity of sCO_2 adjacent to the heated surface. At larger Re_{in}, however, magnification in Δp suppresses the gain in heat transfer, constraining a gradual decline in PEC for all the configurations. For both FM-1P and FM-2P channels, PEC is greater than one only for a limited range of Re_{in}, advocating caution about their use. For FM-1P, a favorable value is possible for $1900 \lessapprox Re_{in} \lessapprox 6000$, with a peak of mere 1.15, which may not be a significant gain considering the practical intricacies involved in fabricating such a channel. The maxima increases to about 1.39 for FM-2P, with the upper limit of operation tending to $Re_{in} \approx 7900$. For FM-3P and FM-4P, however, it is possible to consistently maintain PEC significantly above one, with a peak of about 1.55. There is no significant difference between the two profiles over the entire range of Re_{in} explored here and also in terms of their respective peak magnitudes, with FM-4P being capable of yielding just about 2.6% higher value for PEC_{max}. In fact, the gain in the highest achievable level of PEC gradually diminishes with the increase in the number of pairs of baffles, which is the main reason for not considering more than four pairs. The optimum value of Re_{in} corresponding to the highest level of PEC also reduces slightly with the presence of more obstructions, possibly as a consequence of the elevated level of overall flow resistance. It can, therefore, certainly be concluded that the MCHS with rectangular obstruction can result in performance enhancement over a plain minichannel. However, the extent of enrichment and associated technical feasibility rely on the specific nature of the configuration, which demands more in-depth analyses.

4.4.2 Number of pairs of obstructions

Significant disparity in performance has been observed above with change in the number of obstructions interior to the channel and hence the first important design decision pertains to the pairs of baffles to be installed. In order to gain more insight about the local-level thermalhydraulics, axial variations in the local HTC (α_z) are compared for all the configurations in Fig. 4.5(a). After the initial zone of development in the flow field, HTC remains virtually unchanged for an unhindered channel (PM) over a Re_{in}-range of 987 to 9877, albeit with quite low magnitude. This can be explained following the temperature contours presented in Fig. 4.6. The inlet temperature being reasonably close to T_{pc}, the fluid layer in contact with the heated surface crosses the same within a short downstream distance from the inlet, enforcing a steep decline in the corresponding thermal conductivity (Fig. 1.2). That leads to poor thermal communication between the surface and the adjacent fluid layer, as is manifested by the small HTC. Once the fluid temperature crosses 330 K for sCO_2 over the pressure range explored here, the change in thermal conductivity is quite moderate. That describes the absence of any significant change in HTC beyond $z \approx 3$ mm. The streamlines are also quite smooth here, because of the absence of any obstructions, allowing the stream to approach a fully-developed condition.

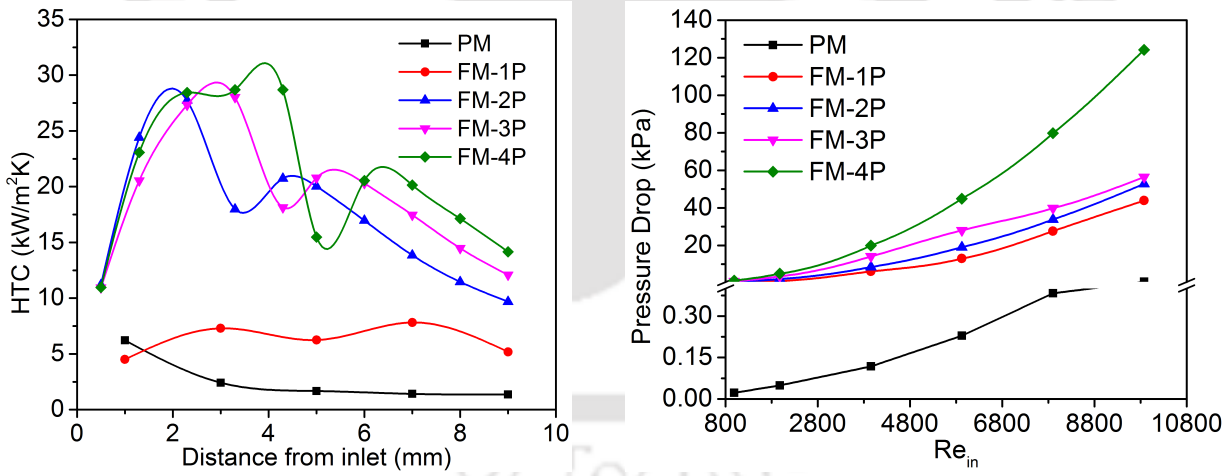

Fig. 4.5: Performance comparisons for all the 5 configurations under consideration at $\dot{q}''$ = 40 kW/m^2, p = 8 MPa and T_{in} = 305 K: (a) Variations in area-averaged HTC at G = 400 kg/m^{2}s and Re_{in} = 3950.8; (b) Variations in pressure drop (Δp) with inlet Reynolds number (Re_{in})

The introduction of a single pair of baffles can noticeably alter the level of HTC, allowing

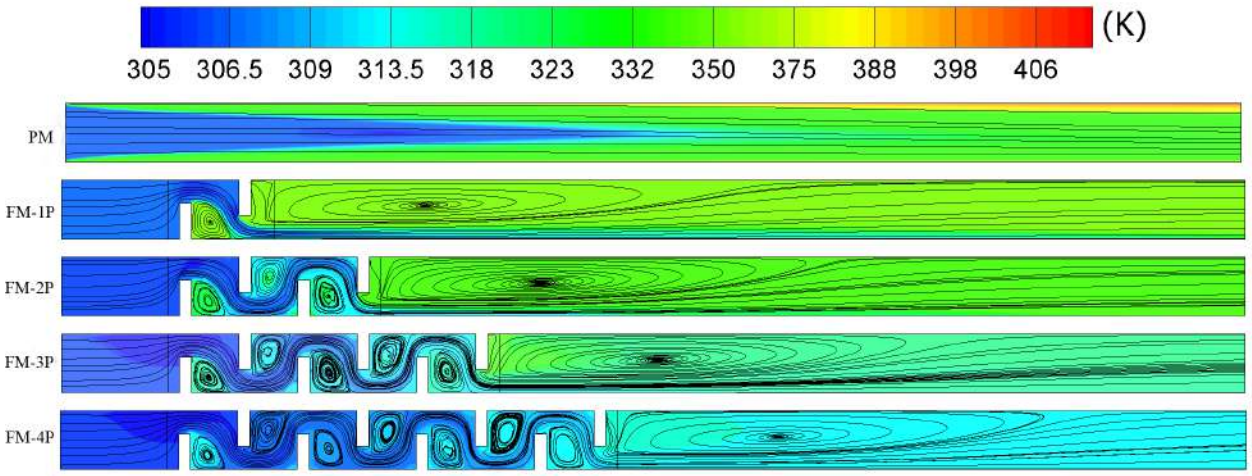

Fig. 4.6: Contours of the absolute temperature and streamlines along the mid-vertical ($y-z$, $x = 250$ μm) plane for all the 5 configurations under consideration at $\dot{q}'' = 40$ kW/m^2, $G = 400$ kg/m^{2}s, $p = 8$ MPa and $T_{in} = 305$ K

a reasonably higher value throughout the flow passage and about 137.7% rise in the average magnitude. The presence of the obstructions obliges the fluid to deviate from the natural flow direction and find a route around them, as can be substantiated following the streamlines presented in Fig. 4.6 for the mid-vertical plane. Flow separation and development of local recirculation zones are evident at the rear face of the first baffle, while the fluid is also able to maintain temperature lower than T_{pc} over a longer path, particularly in contact with the heated surface. The most notable impact of the presence of the baffles is the disruption in the development of the thermal boundary layer and also degradation in the momentum of the fluid around them. The baffles allow better mixing among the fluid layers, particularly upstream of the first vertical plate, as the fluid is forced to move upward. The streamlines are sufficiently compressed near the baffles and very much dilated after passing through the segment with obstructions. That accelerates the fluid adjacent to the vertical plates, which is manifested by the increase in the maximum velocity level within the domain from 0.46 m/s for the plane channel to 1.8 m/s in the present one. It is more clearly illustrated in Fig. 4.7. Absolute fluid velocity is significantly higher for FM-1P over PM and sCO_2 is able to sustain the flow around that velocity level over the entire baffled segment, and even in the lower part of the duct in the downstream of the last obstruction. The augmented level of mixing is the primary contributor toward the enhanced HTC for the FM-1P configuration, with further encouragement from the favorable fluid properties. Variations in the fluid temperature across the channel (in the x-direction) in the mid-plane ($y = 250$ μm) for the

axial location of $z = 0.9$ mm, which is marked as the location L1 in Fig. 5.1, are compared in Fig. 4.8(a). While the temperature of the fluid layers in contact with both the heated walls for the unhindered channel (configuration PM) is reasonably higher than T_{pc}, it is below T_{pc} for FM-1P. That inflicts a substantial difference in the effective magnitude of the thermal conductivity of sCO_2, which rises from 40.38 mW/mK for PM to 77.96 mW/mK for FM-1P, thereby explaining the enhanced HTC with the later configuration. There is, however, notable inflation in the pressure drop across the channel (Δp), partly because of the higher average kinetic head of the fluid and the presence of the vortices, and definitely owing to the greater dynamic viscosity of the low-temperature fluid.

The impact of increased fluid velocity in FM-1P channel is limited to a slender region, as the flow is allowed to expatiate in the immediate downstream of the second plate, eliciting an early appearance of the large recirculation bubble. Just about 24% increase in the velocity averaged over the entire domain is a direct proof of the same, despite the maximum velocity being nearly about four times, as reported above. Consequently, the augmentation in HTC in FM-1P over PM is also limited. Installation of more pairs of baffles can better the situation quite noticeably. The fluid is obliged to move through the constricted passage over a longer path, thereby maintaining the elevated velocity level. The incorporation of two pairs of baffles (FM-2P) inflicts about 37% rise in the average velocity, with a peak magnitude of 2.4 m/s. As a consequence of such elevated velocity over a greater distance and intensified mixing within the neighboring layers, the fluid is able to maintain the bulk temperature below T_{pc} inside the small cells formed by the baffles (Fig. 4.6). The temperature profiles in the x-direction along the mid-horizontal plane at the axial location of L2, which is anchored immediately after the last obstruction plate, are compared in Fig. 4.8(b) for all the four configurations. It needs to be kept in mind that the location L2 is pushed continually downstream with the addition of every pair of baffles, and the distance between L1 and L2 increases. Accordingly, the amount of energy received by the fluid between these two cross-sections, and hence the associated change in bulk enthalpy, also rise almost linearly. Still, the temperature of sCO_2 in contact with the heated surface is marginally lower for FM-2P channel than FM-1P, further substantiating the augmented level of mixing and hinting toward better heat transport characteristics. The axial profiles of area-averaged HTC for the FM-2P configuration are markedly different from FM-1P, as is presented in Fig. 4.5(a). A steep rise in HTC can be observed during the passage through the baffles till the attainment of maxima at a downstream distance of about 0.4 mm, measured from the rear face of the last baffle, followed by HTD and the subsequent appearance of a second peak. The magnitude

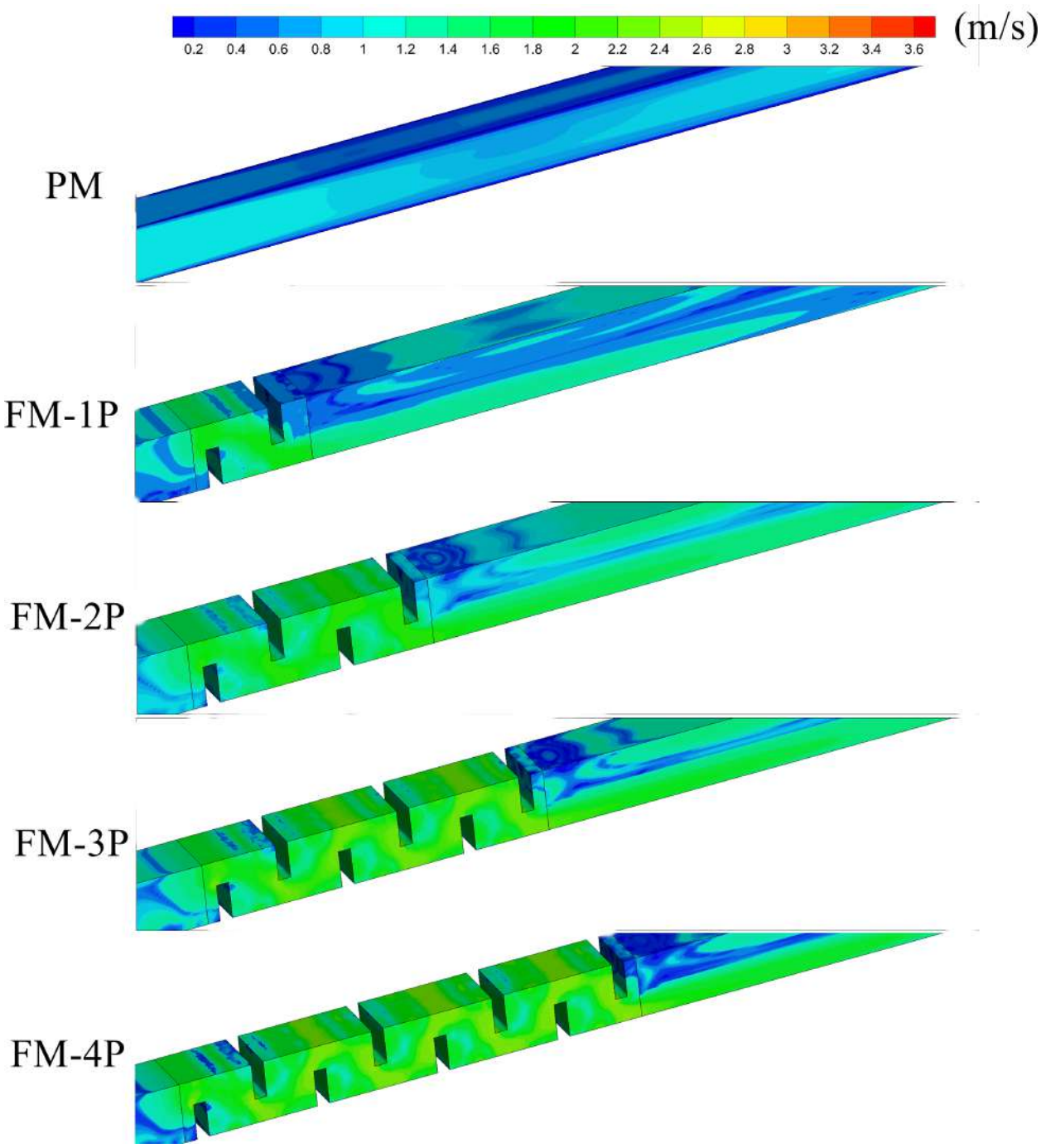

Fig. 4.7: Three-dimensional contours of the absolute velocity over the flow segments with obstructions for all the 5 configurations under consideration at $\dot{q}'' = 40$ kW/m^2, $G = 400$ kg/m^{2}s, $p = 8$ MPa and $T_{in} = 305$ K

of the maximum HTC for FM-2P is estimated to be 27.72 kW/m^{2}K, which is nearly four

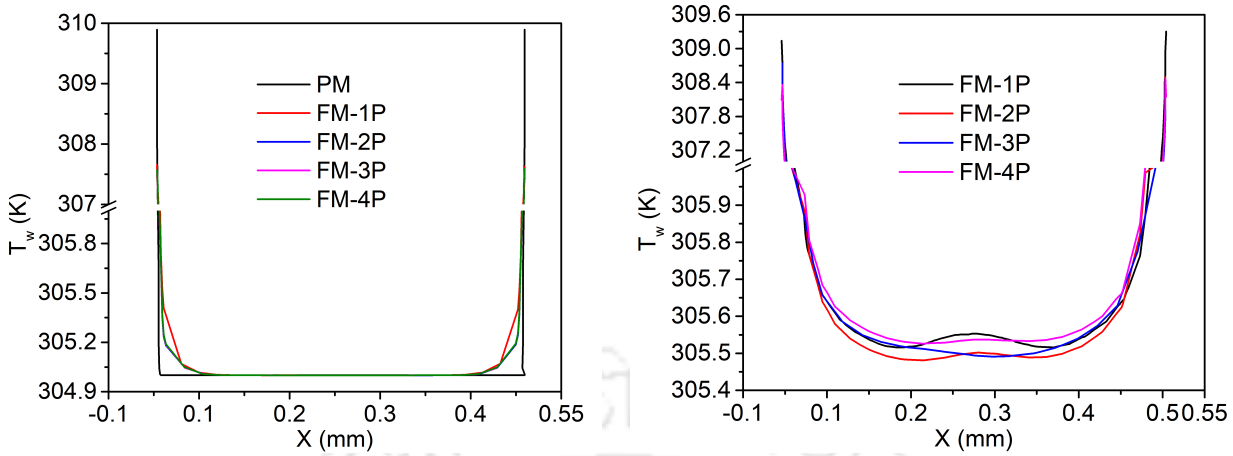

(a) Location L1 **(b)** Location L2

Fig. 4.8: Temperature profiles along the x-direction for $y = 250$ μm at the axial locations of L1 and L2 for all the 5 configurations under consideration

times of that for FM-1P. Both the average and peak velocities increase steadily with further addition of pairs of baffles, with the former parameter being about 50% and 64% greater in FM-3P and FM-4P channels respectively in comparison with PM, allowing expansion of the favorable temperature ($T < T_{pc}$) zone within the channel. The same can also be confirmed following Fig. 4.7, which lucidly demonstrates the expansion of the high-velocity regime over the entire baffled segment. While the bounding temperature values at the walls at location L1 reduce slightly, there is hardly any change in the profiles for location L2, as can be confirmed from the Fig. 4.8, and also following the temperature contours on the $y - z$ plane presented in Fig. 4.6. Consequently, the appearance of the peak of HTC is further delayed, invariably appearing at a downstream distance of about 0.3 to 0.4 mm, while the second peak of HTC is commonly observed at a distance of about 1.9 to 2.0 mm, both measured from the rear face of the last obstruction. The gain in peak HTC with an increase in the number of baffles, however, is not substantial, with FM-4P demonstrating only 9.36% greater magnitude over FM-2P.

Several studies in the literature have focused on enhancing turbulence in supercritical macrochannels, in an attempt to modulate the heat transfer behavior. To perceive the same in baffled minichannel, variations in the turbulent kinetic energy (κ) along the mid-vertical plane are presented in Fig. 4.9 for each of the geometries considered here. As a direct repercussion of enhanced mixing and heightened velocity, the average level of the turbulent kinetic energy is monotonically amplified with the rise in the number of baffles. While the

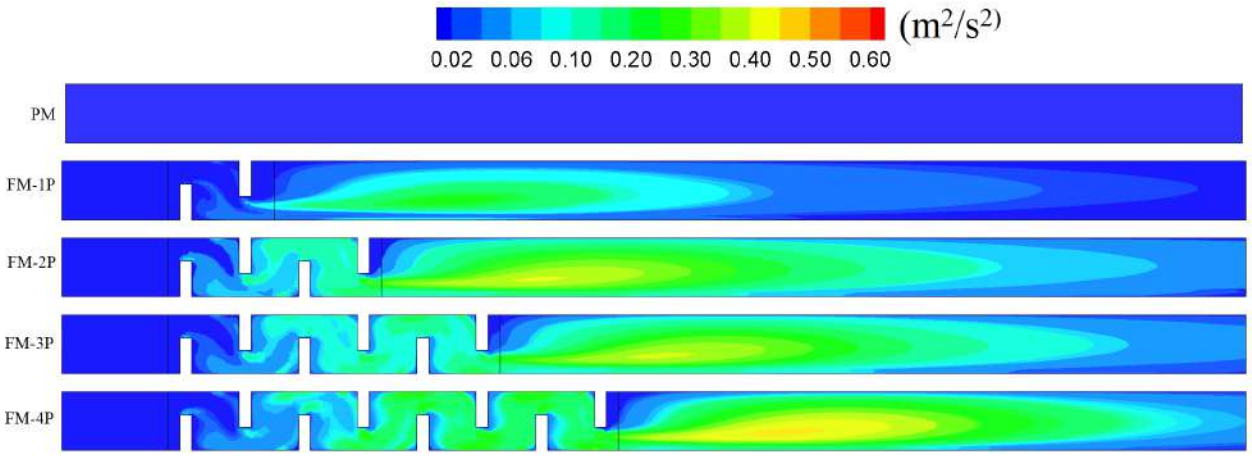

Fig. 4.9: Variations in the turbulent kinetic energy along the mid-vertical ($y-z$, $x = 250$ μm) plane for all the 5 configurations under consideration at $\dot{q}'' = 40$ kW/m^2, $G = 400$ kg/m^{2}s, $p = 8$ MPa and $T_{in} = 305$ K

energy level regularly increases in the flow direction, very high level can be observed after the fluid moves past the segment with obstructions, primarily owing to the expansion of the streamlines and development of the recirculation bubble. It has already been reported above that both the peaks of HTC appear in the region downstream of the last baffle. Therefore, the enhancement in κ can be correlated to the improvement in HTC in minichannel as well. Very smooth profiles of κ can be observed for the plain channel, characterized by the lowest level, with inconsequential variations over the entire flow passage. It can, therefore, be claimed that the insertion of adiabatic plates have promoted velocity fluctuations and turbulent mixing in the baffles MCHSs, and hence is a potent option of heat transfer enhancement.

The pressure drop, however, increases quite steeply with the incorporation of more pairs of baffles, as can be seen from Fig. 4.5(b). This is expected, with the development of local vortices inside each of the smaller cells and also the large recirculation bubble after the last plate. Enhanced mixing also reduces the overall temperature level of the fluid in contact with the solid surface, as has already been discussed above, enforcing an increase in the dynamic viscosity of the adjacent fluid layer and hence the shear stress. While the rise in Δp for any specific Re is quite linear till the installation of the third pair, steep upsurge can be noted with FM-4P, which can be explained using the information presented in table 4.3. Here segment 1 indicates the portion of the channel spanning from location L1 till the rear face of the last baffle in each configuration, whereas segment 2 starts from that very spot and extends till the re-attachment point downstream of the big recirculation vortex. Length of the segment 1, therefore, increases linearly with addition of each pair of baffles, while that for

the second segment remains quite similar. Consequently, pressure drop in the first segment is considerably higher than the same for the other segment, owing to the combined impact of longer flow path for the higher-viscosity sCO_2 with elevated flow velocity and the presence of multiple smaller vortices. Concerned magnitude also increases steeply with the rise in the flow velocity, as is manifested by the rapid climb in total pressure drop at higher Re. The immediate impact of the same is evident on the attainable level of PEC, as is shown in table 4.3 itself. Despite discernible improvement in both peak and average HTC for the FM-4P channel over FM-3P configuration with any set of boundary conditions, there is barely any emolument in terms of PEC. It can, therefore, be concluded that the thermalhydraulic gain with FM-4P is not substantial enough to justify associated pumping cost and manufacturing intricacies, particularly at higher Re. The FM-3P orientation, designed with three pairs of baffles, can accordingly be considered to be the optimum one and that is persuaded with for the remainder of the present study.

Table 4.3: Break-up of pressure drop in different channels for $G = 400$ kg/m^{2}s

Orientation	**Maximum velocity** (m/s)	**Re-attachment length** (mm)	Δp **in segment 1** (Pa)	Δp **in segment 2** (Pa)	**HTC**$_{max}$ (kW/m^{2}K)	PEC
FM-1P	1.8	4.43	5751.06	530.20	7.45	1.14
FM-2P	2.4	4.30	9032.22	639.00	27.72	1.35
FM-3P	3.2	4.20	14704.42	653.37	29.32	1.39
FM-4P	5.4	4.20	20844.39	680.70	31.42	1.41

4.4.3 Height of individual obstructions (b)

The next parameter of interest is the height of individual obstructions (b), as it directly governs the extent of obstruction at a particular axial location within the MCHS. To comprehend the associated impact, simulations have been performed with the FM-3P channel and three different obstruction heights, with the rest of the geometric dimensions remaining identical to the previous discussion. Consequent axial variations in area-averaged HTC and change in Δp with Re are presented in Fig. 4.10. Considerable increase in both peak and

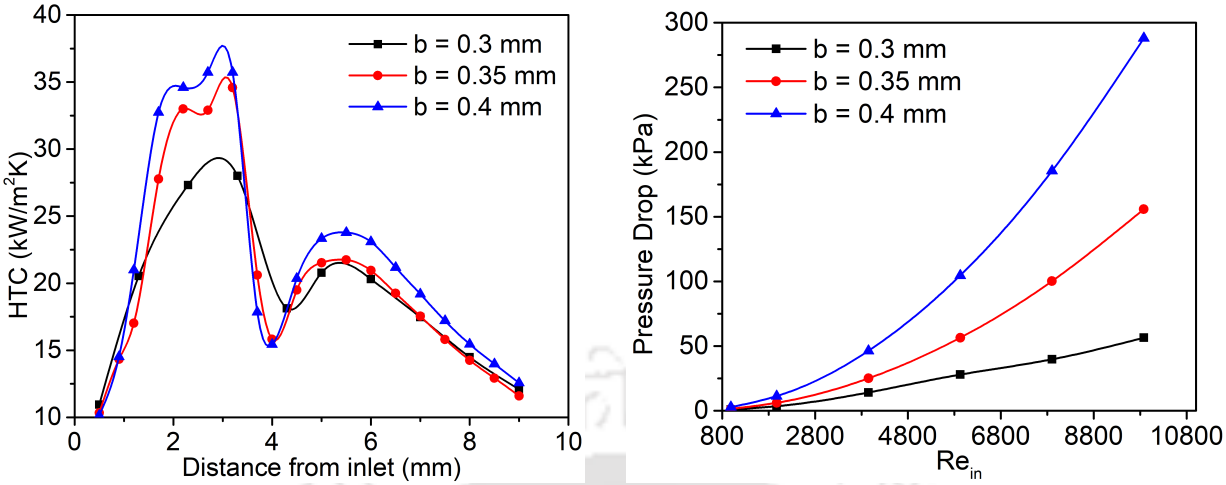

Fig. 4.10: Effect of obstruction height (b) on the (a) area-averaged HTC at $G = 400$ kg/m^{2}s and $Re_{in} = 3950.7$, and (b) pressure drop (Δp) for the FM-3P orientation; Here $\dot{q}'' = 40$ kW/m^2, $p = 8$ MPa and $T_{in} = 305$ K

average HTC can be noted for the channel with $b = 0.35$ mm over the one having $b = 0.3$ mm, while the gain with further revision to $b = 0.4$ mm is less significant. A taller obstruction creates greater constriction for the fluid to pass through, thereby simultaneously enhancing the local velocity and intensity of turbulence, both of which contribute to the augmentation in the mixing of fluid layers and help to maintain favorable temperature near the heated walls. The extent of enrichment can be gauged following the profiles of turbulent kinetic energy (κ) presented in Fig. 4.11 at the rear of the first and third obstructions. While the levels of velocity and κ remain near-identical on the upstream of the baffled segment, there are considerable differences after the first obstruction itself. A change in height from 0.3 mm to 0.4 mm upturns κ nearly by three times in the mid-section. The same can be observed after the third baffle as well, where the level of κ itself is significantly higher. The enhancement of velocity can also be substantiated following the streamlines shown in Fig. 4.12, which reveals that the size of the vortices on the rear face of the plates are magnified for the taller obstructions, allowing more fluid to participate in convection. The boundary layer under the influence of this magnified vortex tends to leave the surface early, facilitating well-mixed homogeneous bulk region and obstruction-facilitated thermal convection. Additionally, the elevated shear stress level induced by the enlarged transverse vortices also improves the turbulent kinetic energy and reinforces the transport of thermal energy in the transverse direction. That is evident from the temperature contours presented in Fig.

4.12, particularly from the high-temperature recirculation zones visible inside the small cells. There is no change in the axial positioning of both the peaks of HTC and also the minima in between. Taller obstruction, however, obligates larger loss in pressure, thereby affecting the overall thermalhydraulic acquisition. For the explored set of boundary conditions, about 20% improvement in PEC is possible by changing b from 0.3 mm to 0.35 mm. However, further increment to $b = 0.4$ mm results in about 26% drop in PEC, primarily owing to 80% greater Δp. Therefore, a obstruction height of $b = 0.35$ mm is considered for all the subsequent simulations.

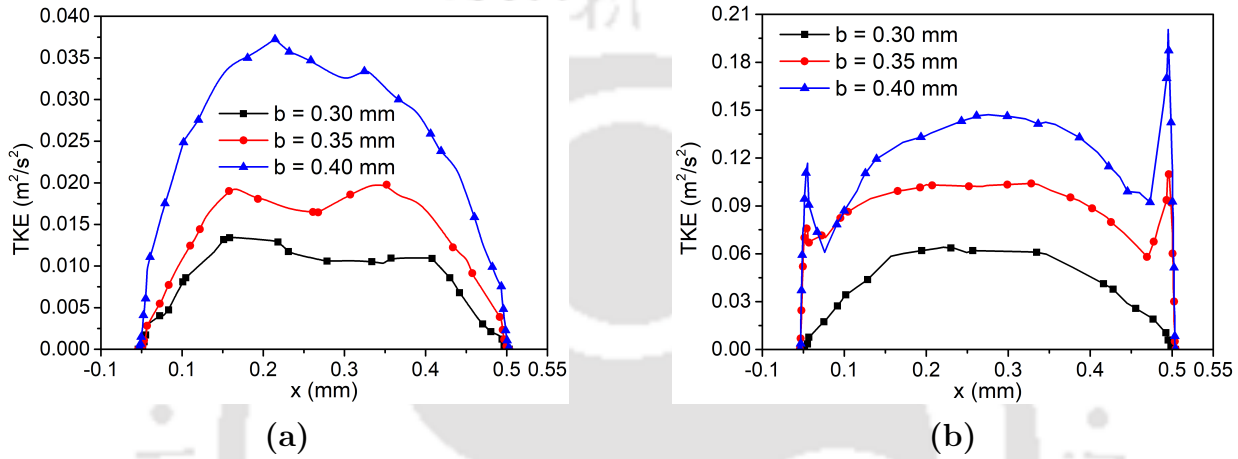

Fig. 4.11: Effect of baffle height (b) on the turbulent kinetic energy along the x-direction for $y = 250$ μm at the immediate downstream of (a) the first baffle and (b) the third baffle for the FM-3P orientation; Here $\dot{q}'' = 40$ kW/m^2, $G = 400$ kg/m^{2}s, $p = 8$ MPa and $T_{in} = 305$ K

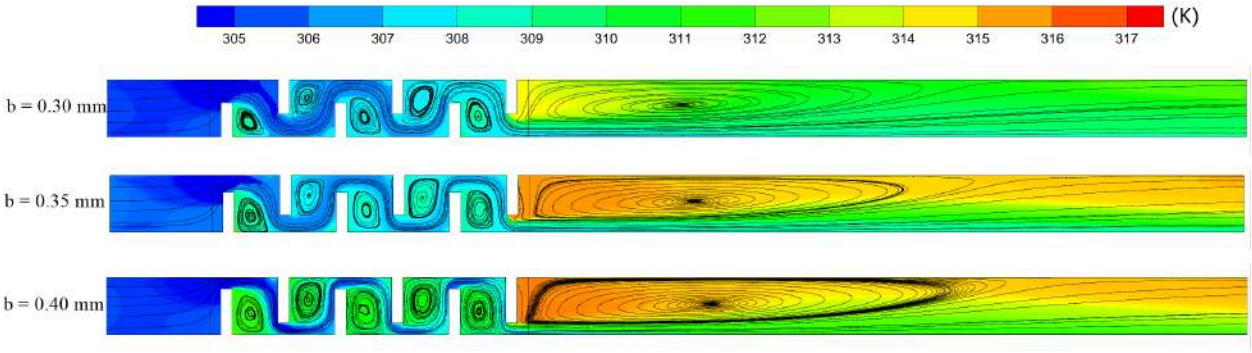

Fig. 4.12: Effect of obstruction height (b) on the contours of the absolute temperature and streamlines along the mid-vertical ($y - z$, $x = 250$ μm) plane for the FM-3P orientation at $\dot{q}'' = 40$ kW/m^2, $G = 400$ kg/m^{2}s, $p = 8$ MPa and $T_{in} = 305$ K

4.4.4 Thickness of individual obstructions (t)

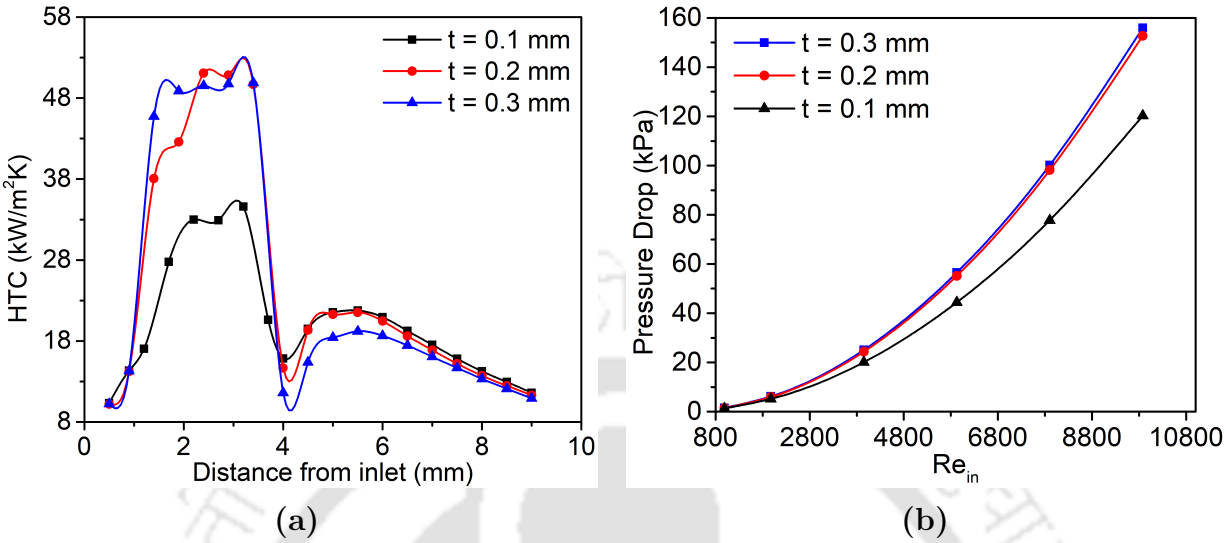

Fig. 4.13: Effect of obstruction thickness (t) on the (a) area-averaged HTC at $G = 400$ kg/m^{2}s and $Re_{in} = 3950.7$, and (b) pressure drop (Δp) for the FM-3P orientation; Here $\dot{q}'' = 40$ kW/m^2, $p = 8$ MPa and $T_{in} = 305$ K

The thickness of the individual obstructions determines the effective length of the constricted passages and can consequently modulate the area of the heated wall in contact with the highest-velocity fluid. FM-3P orientation with a obstruction height of 0.35 mm has been selected to explore the role of thickness and the observations are illustrated in Fig. 4.13. Substantial rise in HTC can be observed by widening the obstructions from $t = 0.1$ mm to $t = 0.2$ mm. It must be noted that an increase in the thickness of the obstruction, without any change in the pitch, reduces the width of the flow passage between two adjacent plates as well. While that increases the velocity of the fluid interior to the smaller cells, it also induces a reduction in the average velocity level over the entire channel. For example, the average velocity reduces from 0.981 m/s to 0.954 m/s, as the thickness is increased from 0.1 mm to 0.2 mm. It can properly be comprehended following the crosswise velocity profiles presented in Fig. 4.14 at the immediate downstream of the first and third baffles. While the increase in baffle thickness induces substantial rise in the velocity level of sCO_2, there is also noticeably lesser variation across the channel, with the velocity profile becoming more uniform at the downstream position. This advocates toward strong advection current for channels with thicker obstructions, engendering improved HTC. A notable increase in the turbulent kinetic energy can be observed from Fig. 4.15, particularly in the obstruction

segment. That is manifested in the rise in HTC with t, while also being accompanied by greater frictional losses.

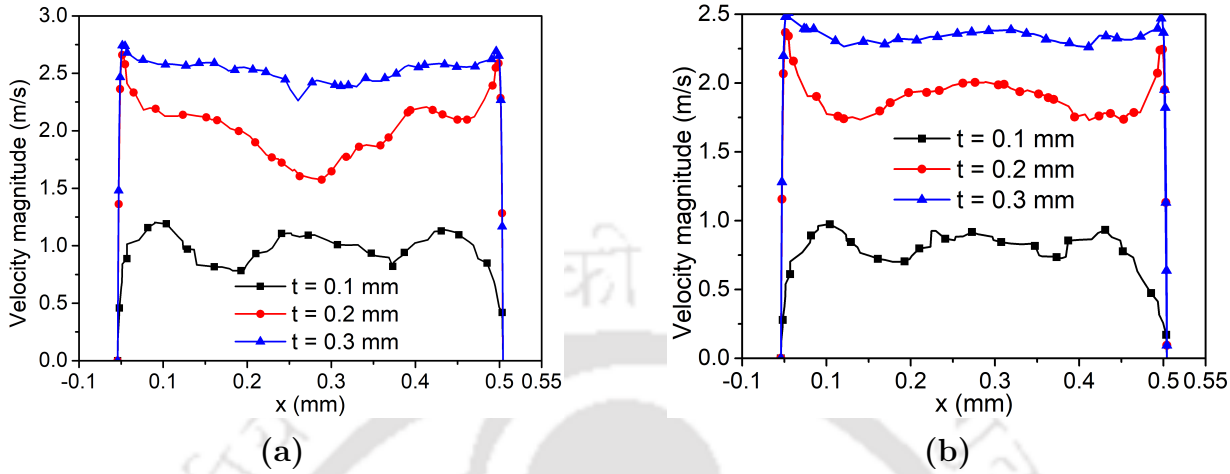

Fig. 4.14: Effect of baffle thickness (t) on the local fluid velocity along the x-direction for $y = 250$ μm at the immediate downstream of (a) the first baffle and (b) the third baffle for the FM-3P orientation; Here $\dot{q}'' = 40$ kW/m^2, $G = 400$ kg/m^{2}s, $p = 8$ MPa and $T_{in} = 305$ K

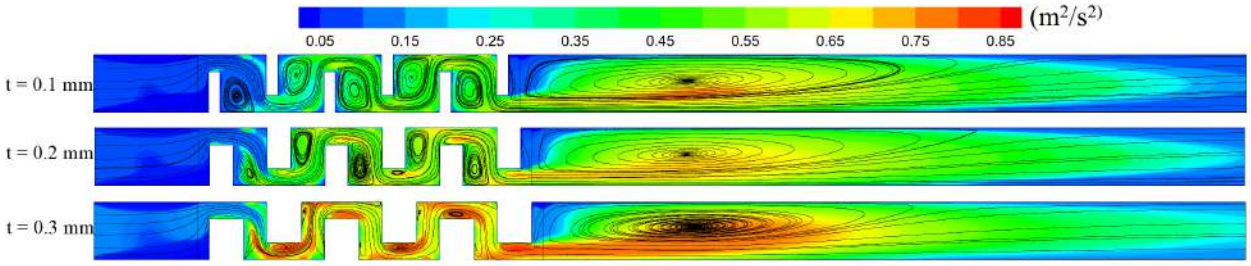

Fig. 4.15: Effect of obstruction thickness (t) on the contours of the turbulent kinetic energy and streamlines along the mid-vertical ($y - z$, $x = 250$ μm) plane for the FM-3P orientation at $\dot{q}'' = 40$ kW/m^2, $G = 400$ kg/m^{2}s, $p = 8$ MPa and $T_{in} = 305$ K

Further thickening of the obstruction to $t = 0.3$ mm, however, hardly creates any impact. Here the variation in the width of the flow passage is rather small, virtually eliminating the expansion-and-contraction effect experienced by the fluid while flowing over any obstruction. The impact is demonstrated by the smooth streamlines within the obstruction section, where hardly any vortices can be seen. The magnitudes of absolute velocity presented in Fig. 4.14 are also much closer for $t = 0.2$ mm and 0.3 mm, particularly after the third baffle, with the difference continually reducing further downstream. That possibly offsets

the favorable influence of enhanced turbulence on mixing across layers, as manifested by the inconsequential changes in the axial profile of HTC and $\Delta p - Re$ curve, as well as on the overall thermalhydraulic assessment. While the change in t from 0.1 mm to 0.2 mm administers about 16% gain in PEC, hardly any change of significance can be found with further change to 0.3 mm, endorsing $t = 0.2$ mm as the optimum choice for the subsequent discussion. The exact magnitudes can be identified from table 4.4.

Table 4.4: Summary of effect of parameters on PEC and pressure drop (Δp) for the FM-3P orientation

Height **b** (mm)	**Thickness** **t** (mm)	**Inclination** θ	**PEC**	$\mathbf{\Delta p_1}$ (Pa)	$\mathbf{\Delta p_2}$ (Pa)
0.30	0.10	90^o	1.39	14704.42	653.37
0.35			1.67	24876.11	1107.10
0.40			1.19	46145.74	1336.36
0.35	0.1	90^o	1.67	24876.11	1107.10
	0.2		1.93	24197.66	1069.30
	0.3		1.91	19924.85	672.37
0.35	0.2	30^o	1.14	5603.90	508.37
		45^o	1.39	11488.09	869.68
		60^o	1.96	17647.43	993.21
		90^o	1.93	24197.66	1069.30

4.4.5 Inclination of individual obstructions (θ)

The inclination of the obstruction to the base surface controls the extent of obstruction and hence is expected to be a key design parameter. All the simulations reported till now have been performed for vertical plates, corresponding to $\theta = 90°$, measured at the rear face. In order to envisage the role of this parameter, simulations have been performed using the FM-3P channel, having $b = 0.35$ mm and $t = 0.2$ mm. As illustrated in Fig. 4.16(a), a change in inclination from 90° to 60° does not induce any significant alteration in the axial profile of area-averaged HTC. While a small dip in the peak magnitude can be noted for $\theta = 60°$, the level of HTC after the first peak consistently remains higher, subsequently offering a marginally greater value averaged over the entire channel. The pressure drop with 60°

tilting of obstructions is also considerably lower, particularly at higher flow rates, offering a lucrative proposition.

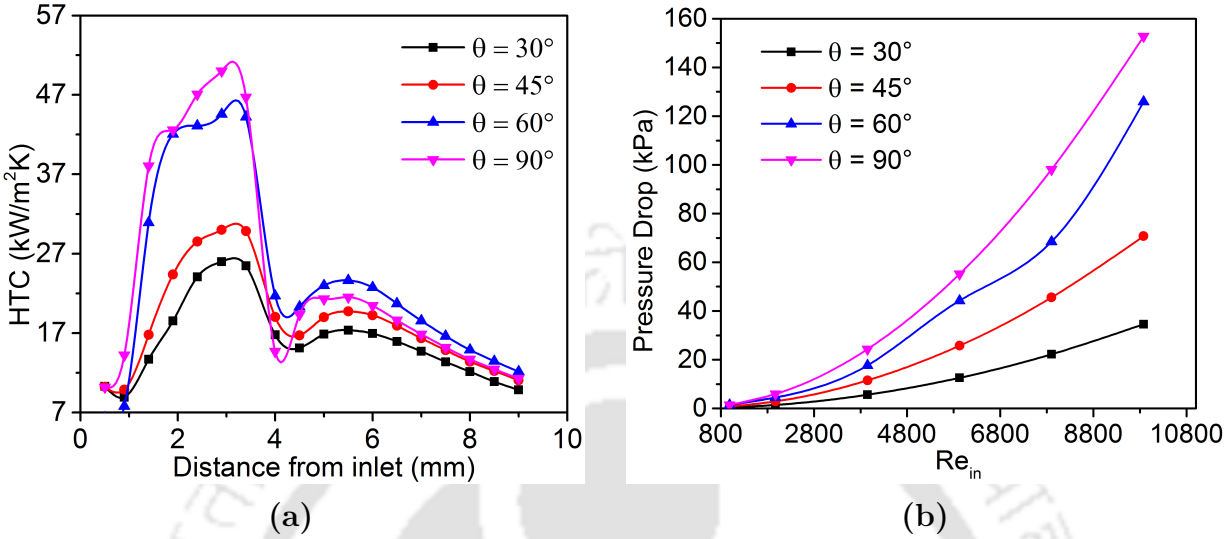

Fig. 4.16: Effect of inclination angle (θ) on the (a) area-averaged HTC at G = 400 kg/m^{2}s and Re_{in} = 3950.7, and (b) pressure drop (Δp) for the FM-3P orientation; Here $\dot{q}''$ = 40 kW/m^2, p = 8 MPa and T_{in} = 305 K

Any reduction in the tilt angle, however, leads to a large decline in the heat transfer behavior in terms of both local and averaged quantities, albeit at a reduced penalty in pressure losses. It can be explained following the velocity contours presented in Fig. 4.17. Plates inclined at 60° yield high velocity levels adjacent to each of the obstructions by allowing smooth expansion of the fluid over them, in contrast to the sudden expansion experienced with vertical plates. Changes in fluid velocity are much lesser with smaller tilt angles, characterized by smooth streamlines through wider openings, affecting the thermal communication between the supercritical fluid and heated surface. A larger value of θ enhances turbulent mixing and imposes greater diversion to the primary direction of motion, simultaneously affecting both HTC and Δp. It needs to be remembered that the energy addition is facilitated through the side walls ($x-y$ planes) and the axial profiles, therefore, may not always suffice in explaining the nature of wall-to-fluid energy interaction. To aid better conception, temperature contours at four different axial planes are presented in Fig. 4.18 corresponding to each of the inclination angles explored here. No discernible change in the profiles can be noted by altering the angle from 90^o to 60^o, especially adjacent to the walls. The rate of heat transfer, and accordingly HTC, is determined by the thermal conductivity of the fluid layer in the neighborhood of the heated surface, and that remains quite similar here.

However, further change in angle to 45^o inflicts a noticeable change, with the temperature of the concerned fluid layer increasing nearly by 15 K. Effect of local buoyancy forces are also vividly apparent, with higher-temperature being present in the upper part of any cross-section. Such a rise in temperature enforces substantial decline in thermal conductivity of the fluid adjoining the heated surface, and same is externalized through the deterioration in HTC (Fig. 4.16(a)). The high-temperature fluid is also characterized by low viscosity, effecting a reduction in wall shear stress and subsequently in overall pressure drop. An increase in θ from 45° to 60° facilitates about 41% gain in PEC, which, however, remains virtually unchanged with further change to 90°, while costing augmented pressure loss. Therefore, an inclination angle of 60° can be viewed to be the optimum one among the considered cases, which confers the complete description of the optimum orientation of the obstruction MCHS under appraisal. A summary of the same is presented in table 4.5.

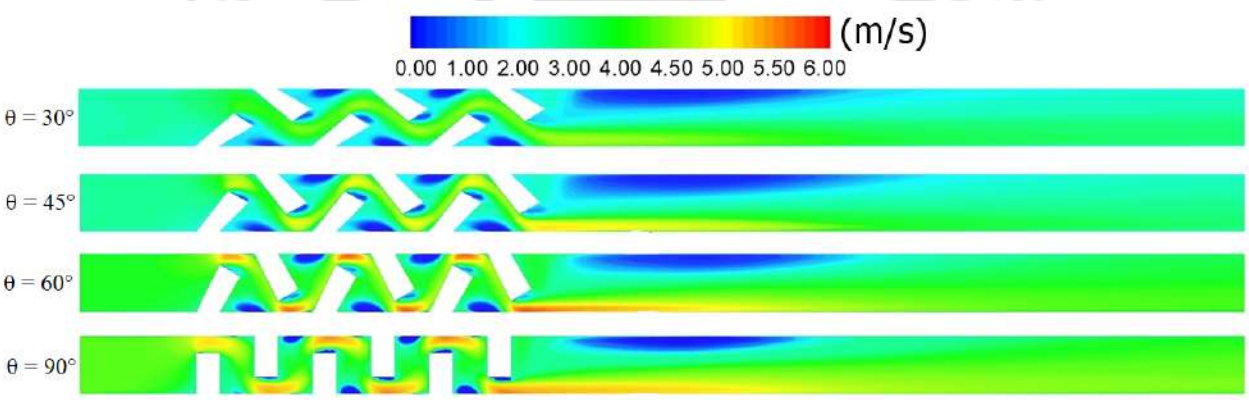

Fig. 4.17: Effect of inclination angle (θ) on the velocity contours along the mid-vertical ($y-z$, $x = 250$ μm) plane for the FM-3P orientation at $\dot{q}'' = 40$ kW/m^2, $G = 400$ kg/m^{2}s, $p = 8$ MPa and $T_{in} = 305$ K

Table 4.5: Details of the optimum orientation

Configuration	FM-3P
Number of pairs of obstructions	3
obstruction height (b)	0.35 mm
obstruction thickness (t)	0.20 mm
Center-to-center distance (d)	0.50 mm
Inclination angle (θ)	60°

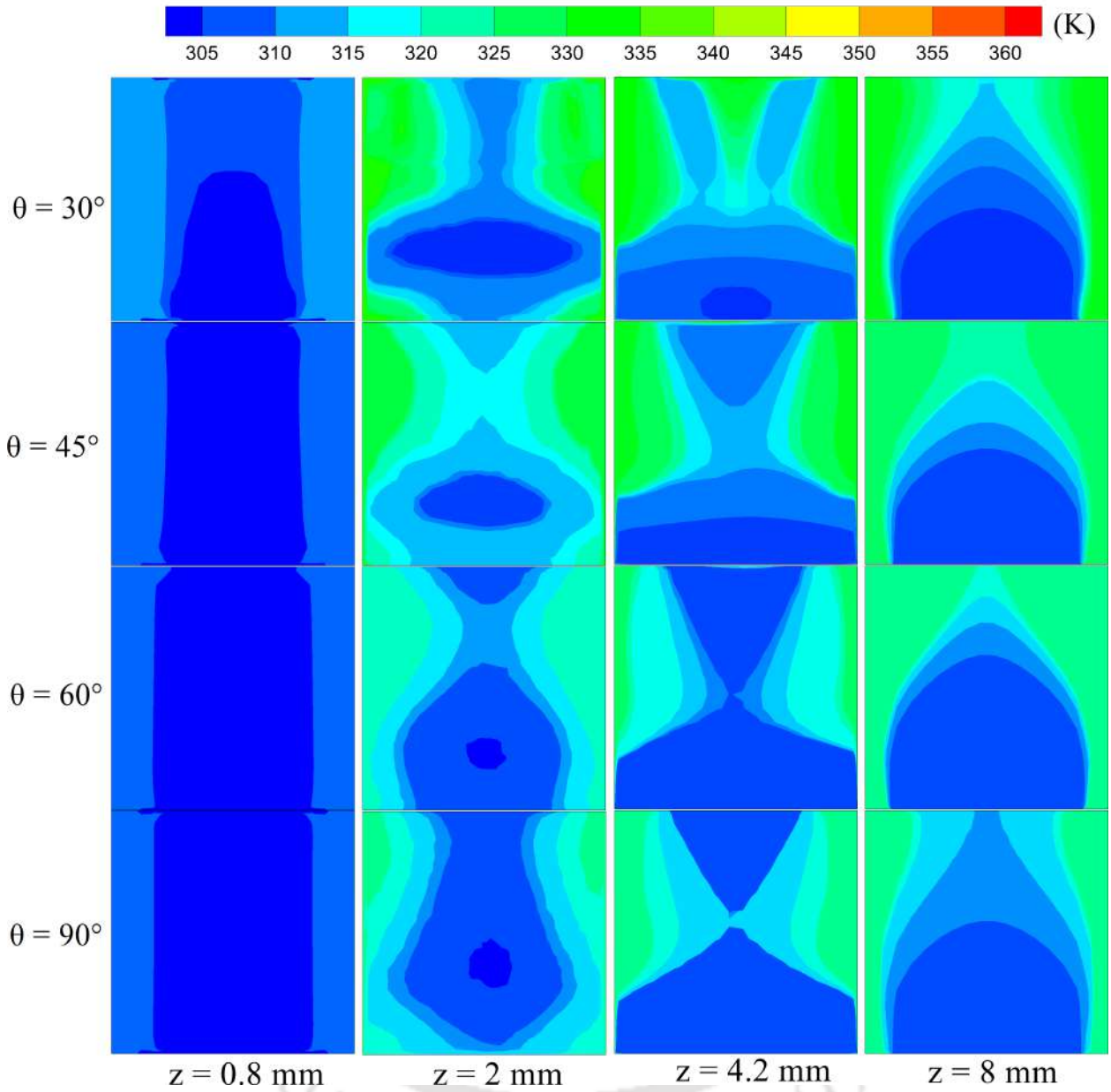

Fig. 4.18: Effect of inclination angle (θ) on the temperature contours at four different z-positions ($x-y$ planes) for the FM-3P orientation at $\dot{q}'' = 40$ kW/m^2, $G = 400$ kg/m^{2}s, $p = 8$ MPa and $T_{in} = 305$ K

4.5 Thermalhydraulic Assessment of the Optimum Configuration

Once the optimum orientation has been earmarked, it has been subjected to systematic parametric analyses in order to envision the respective influence of different operating parameters, such as heat flux ($\dot{q}''$), mass flux (G), operating pressure (p) and inlet temperature

(T_{in}). Corresponding observations are discussed in the subsequent sections.

4.5.1 Effect of heat flux ($\dot{q}''$)

The nature of the effect of heat flux on the heat transfer performance of the system can vary depending on the level of the supplied mass flux. For higher supply rates, area-averaged HTC monotonically increases with $\dot{q}''$ at every $z-$locations, as is demonstrated in Fig. 4.19. The deviations between the axial profiles, however, are increasingly indistinguishable, which is quite logical, as the axial gradient of bulk enthalpy of sCO_2 for any specified power level linearly falls with the rise in G. Intensification in turbulent mixing at such high Re also minimizes the variations in the transverse direction. Accordingly, the temperature contours over the entire flow passage are quite similar for all high-G cases, and the thermal conductivity in the near-wall zones also varies, adhering to a similar pattern, offering comparable HTC profiles. A different trend can be observed at lower flow rates ($G \leq 200$ kg/m^{2}s). While a higher heat flux produces an improved HTC till the appearance of the first peak, the trend is reversed downstream of that. The flow is essentially laminar at such levels of G ($Re_{in} < 1000$), minimizing the role of the turbulent mixing across the fluid layers and allowing the development of a significant thermal gradient normal to the heated surface. Accordingly, the fluid adjacent to the wall attains T_{pc} a bit earlier at higher power levels and also suffers a steeper drop in thermal conductivity, establishing a bigger difference between the HTCs corresponding to the first peak and following minima. The deterioration is always more drastic at higher power levels, owing to the early-initiation of HTD. While the enriched mixing at higher Re is able to counter that to some extent, thereby producing a consistent pattern, it is not possible with weakened flow rates, which is vividly illustrated in Fig. 4.19(a) and also for any G values lower than 200 kg/m^{2}s. Heat flux, however, has no notable impact on the pressure drop at any level of mass flux explored here.

4.5.2 Effect of mass flux (G)

The distinct nature of system responses against the variations in heat flux at low and high levels of mass flux has already been discussed above. The sole impact of mass flux, for any specific power levels, is to introduce greater turbulence in the system, which is characterized by velocity fluctuations and more randomized cross-motion, and also to enhance the velocity levels, both of which contribute favorably in raising the level of energy interaction between the solid and fluid. The predictions are presented in Fig. 4.20 for two different levels of heat fluxes ($\dot{q}''$). Clearly, a higher G leads to elevated HTC, with both the peaks appearing

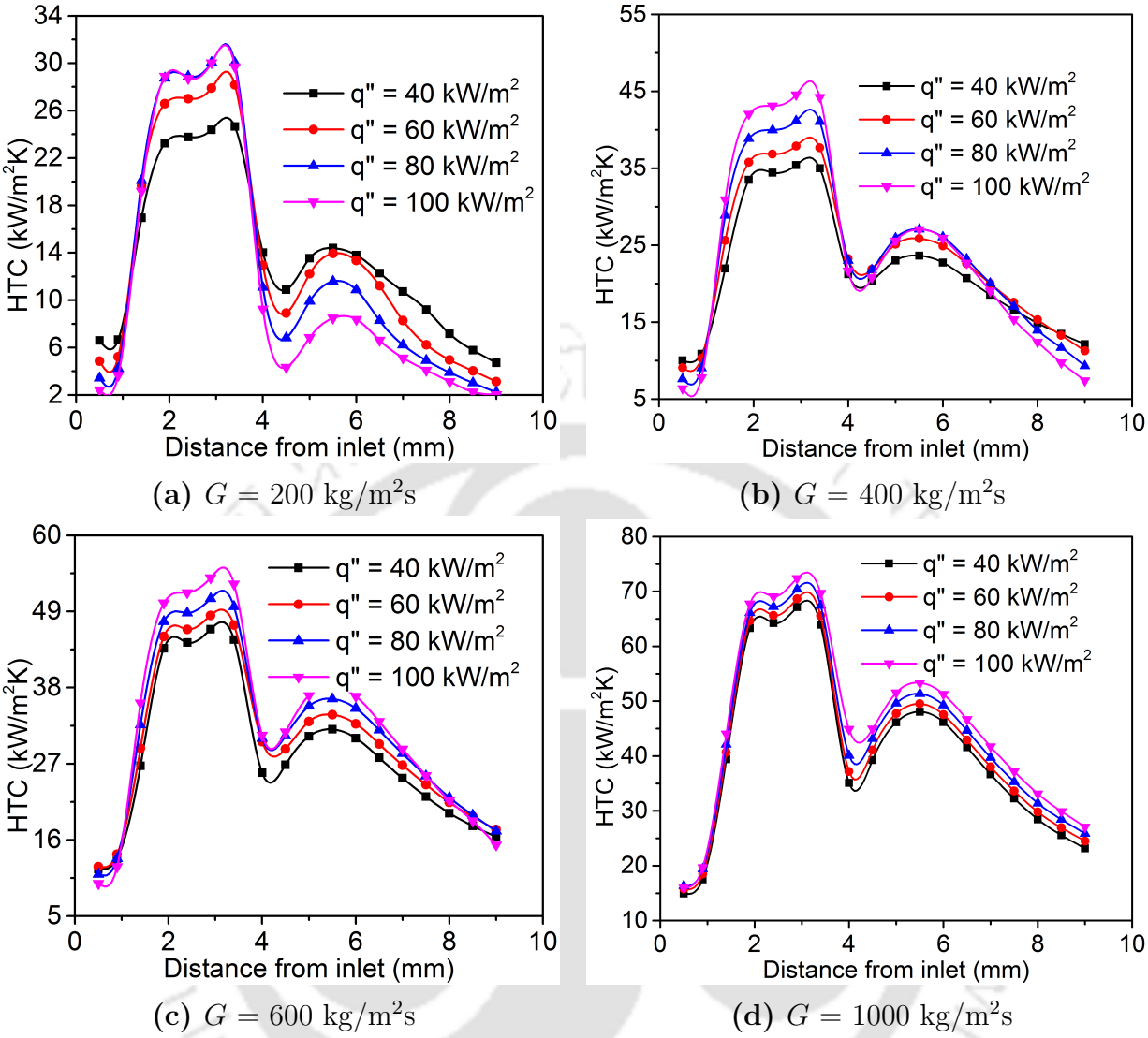

(a) $G = 200$ kg/m^{2}s **(b)** $G = 400$ kg/m^{2}s

(c) $G = 600$ kg/m^{2}s **(d)** $G = 1000$ kg/m^{2}s

Fig. 4.19: Effect of heat flux ($\dot{q}''$) on the area-averaged HTC at different four different levels of mass fluxes for the optimum orientation; Here $p = 8$ MPa and $T_{in} = 305$ K

virtually at identical axial locations, albeit with substantial differences in their respective magnitudes. It is, therefore, always preferable to operate with greater mass flux, as that will facilitate persistently-higher HTC for any heat flux, but at the obvious cost of increased pumping power (observed earlier in Fig. 4.5(b)) and also need to be in consensus with the connected appliances.

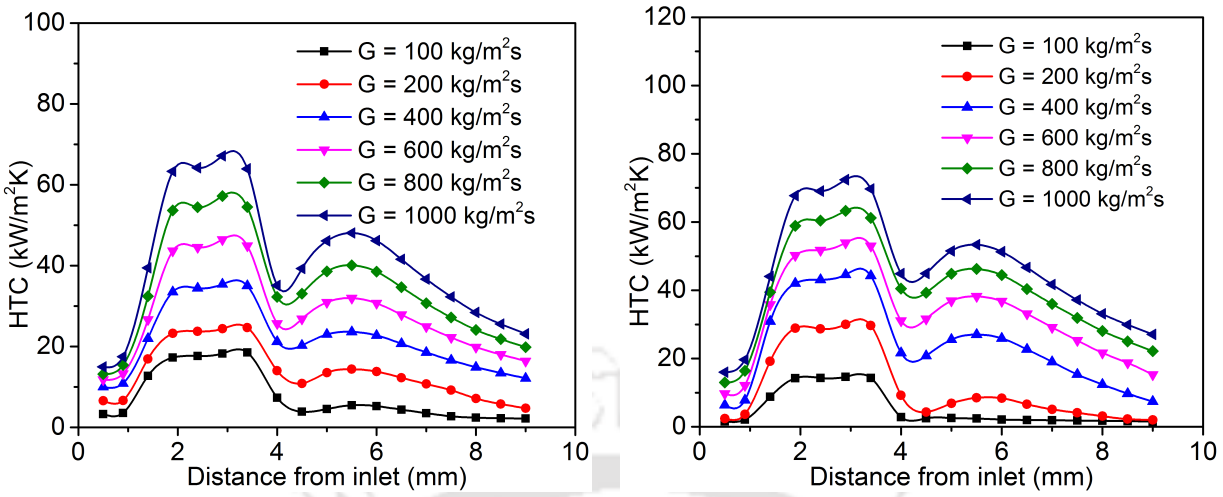

(a) $\dot{q}'' = 40$ kW/m^2 **(b)** $\dot{q}'' = 80$ kW/m^2

Fig. 4.20: Effect of mass flux (G) on the area-averaged HTC at two different levels of heat fluxes for the optimum orientation; Here $p = 8$ MPa and $T_{in} = 305$ K

4.5.3 Effect of operating pressure (p)

The most intriguing feature of any supercritical fluid is the dramatic variation in thermo-physical properties around T_{pc}, and the transition is most severe along isobars defined by pressures immediately above the critical value. Consequently, the sharpest variation in parameters of interest is expected at such pressures. Figure 4.21 presents the axial profiles of area-averaged HTC at five different pressures. It is evident that higher operating pressure leads to a reduction in HTC regardless of the imposed power, and the greatest level, as expected, corresponds to $p = 8$ MPa, which is the one closest to p_c among the considered cases. Increasing the operating pressure from 8 to 8.5 MPa results in a reduction in peak HTC from 35.40 kW/m^{2}K to 27.95 kW/m^{2}K, which is consistent with the drop in k_{max} from 88.99 mW/mK to 77.55 mW/mK. Changes are rather minimal for even higher pressures because of the not-so-significant variation in properties around T_{pc}. It can, therefore, be suggested to operate at pressure levels close to p_c. The pressure drop, however, reduces a bit with a rise in pressure, owing to the diminishing difference in the level of viscosity on either side of T_{pc} at higher pressures.

4.5.4 Effect of inlet temperature (T_{in})

When the inlet temperature of sCO_2 is well above T_{pc}, the thermal conductivity is poor owing to the gas-like behavior and hence is expected to yield inferior heat transfer performance. The

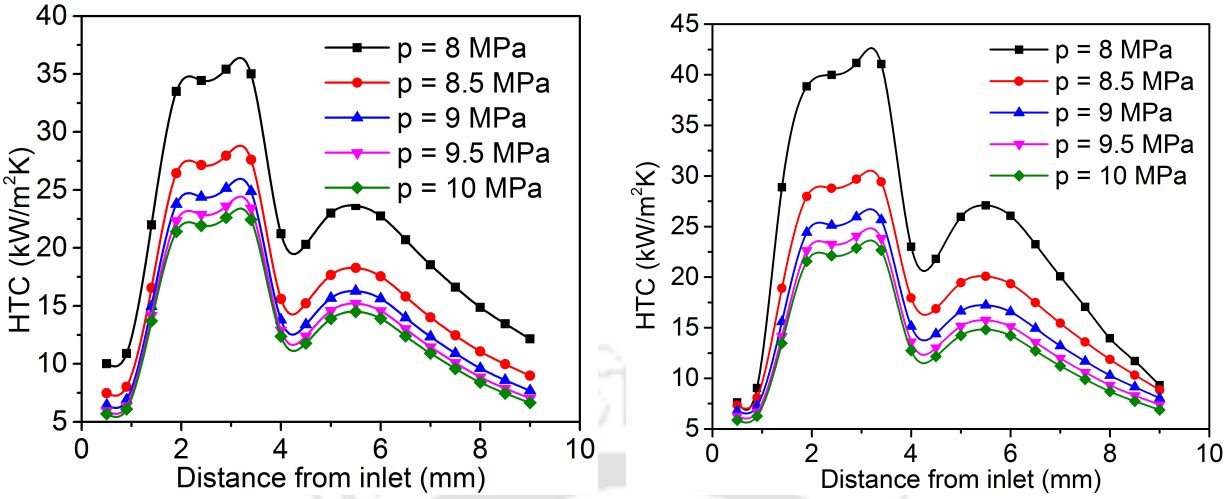

(a) $\dot{q}'' = 40$ kW/m^2 **(b)** $\dot{q}'' = 80$ kW/m^2

Fig. 4.21: Effect of operating pressure (p) on the area-averaged HTC at two different levels of heat fluxes for the optimum orientation; Here $G = 400$ kg/m^{2}s and $T_{in} = 305$ K

same can be substantiated following the profiles presented in Fig. 4.22. An inlet temperature of 305 K is lesser than T_{pc} at $p = 8$ MPa, while the others are higher. Accordingly, it furnishes the highest level of thermal conductivity (k) = 76.57 mW/mK at the inlet plane compared to the others. However, $T_{in} = 310$ K is not very far away from T_{pc}, offering a reasonably high $k = 56.98$ mW/mK. Hence, favorable heat transfer characteristics can be obtained for both the cases with $T_{in} = 305$ K and 310 K, which is authenticated by the considerably large magnitude of HTC within the obstruction section for both these cases compared to the other ones. Thermal conductivity for $T_{in} = 315$ K is merely 38.99 mW/mK, resulting in a drastic reduction in maximum HTC by 47% with respect to $T_{in} = 305$ K. Of course, the best thermal performance is achieved with $T_{in} = 305$ K, advocating toward maintaining the inlet temperature below the pseudocritical value. Any further reduction in the inlet temperature has the potential of enhancing HTC even more, owing to the rise in k. But that is expected to incur greater pressure losses because of the simultaneous rise in dynamic viscosity (Fig. 1.2), necessitating a trade-off.

4.6 Thermodynamic Assessment

A brief thermodynamic appraisal is performed following the second-law perspective to investigate the role of the orientation of obstructions on the rate of entropy generation. In order to be consistent with earlier analyses, the dimensions introduced in section **??** are followed

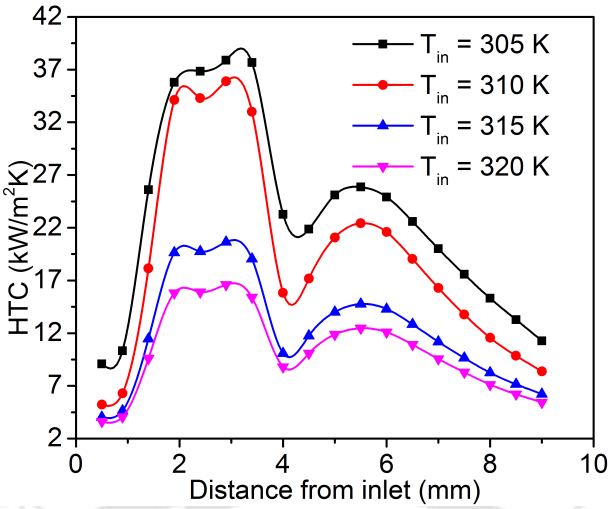

Fig. 4.22: Effect of inlet temperature (T_{in}) on the area-averaged HTC for the optimum orientation; Here $\dot{q}^{''} = 40$ kW/m^2, $G = 400$ kg/m^{2}s and $p = 8$ MPa

here as well and not any optimized configuration. Entropy generation in an open system can have contributions from both the pressure drop across the channel and heat transfer with finite temperature differences. Following [177], the former can be defined as,

$$\delta\dot{S}_{gen,\Delta p} = \frac{\mu}{T_b}\left[2\left(\frac{\partial u_j}{\partial x_j}\right)^2\right] + 2\left[\left(\frac{\partial u_j}{\partial x_k} + \frac{\partial u_k}{\partial x_j}\right)^2\right] \tag{4.5}$$

Integrating the above equation over the MCHS under consideration, the rate of entropy generation associated with the pressure drop can be estimated as,

$$\dot{S}_{gen,\Delta p} = \frac{\dot{m}}{\rho T_f}\Delta p \tag{4.6}$$

Similarly, the component owing to the heat transfer can be expressed as[177],

$$\delta\dot{S}_{gen,Q} = \frac{k_b}{T_b^2}\left(\frac{\partial T}{\partial x_j}\overrightarrow{e}_j\right)^2 \tag{4.7}$$

with $\overrightarrow{e}_j$ being the basis vector in the j^{th}-direction. Accordingly, the integration yields the total magnitudes as,

$$\dot{S}_{gen,Q} = \frac{\dot{q}^{''} A_w}{T_b T_w}\left(T_w - T_b\right) \tag{4.8}$$

The variations in both the components with Re for all the five configurations are presented in Fig. 4.23. Entropy generation rate owing to the pressure drop is quite negligible in the

plane channel (PM) and increases substantially with the installation of the obstructions, as it is a direct function of the incurred pressure drop and hence meticulously follows Fig. 4.5(b). As expected, it is the highest for FM-4P configuration because of the largest flow resistance offered in this channel. There is, however, a noticeable decline in the entropy generation rates associated with heat transfer for the channels with obstructions (Fig. 4.23(b). Such a trend can be attributed to the enhanced level of mixing in the ducts, which disrupts the formation of the thermal boundary layer and minimizes the difference between the wall and bulk temperatures. The role of turbulent mixing in enhancing the HTC has already been elaborated before, and the same helps in lowering $\dot{S}_{gen,Q}$. Any increase in Re further augments the mixing, consequently decreasing $\dot{S}_{gen,Q}$ even more. A higher flow rate, however, strengthens the frictional forces, which is being reflected in the increase in $\dot{S}_{gen,\Delta p}$. The magnitude of the contribution from pressure drop, though, is substantially greater than the other one, apart from very low Re-flows. Therefore, it can be concluded that the supercritical MCHS with obstructions will experience higher irreversibility in pursuit of enhanced heat transfer performance.

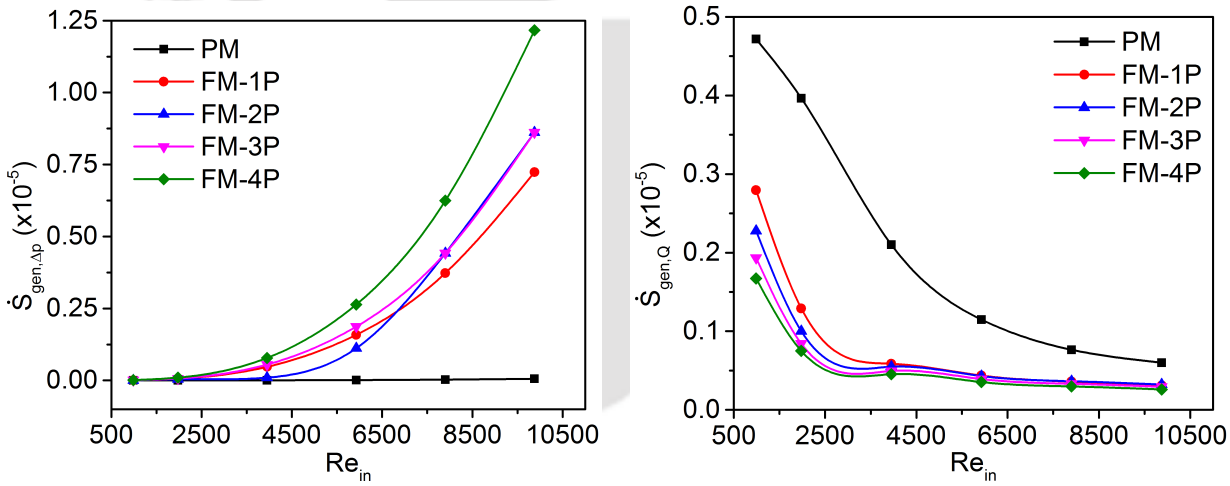

(a) $\dot{S}_{gen,\Delta p}$ at $\dot{q}'' = 40$ kW/m^2 **(b)** $\dot{S}_{gen,Q}$ at $\dot{q}'' = 80$ kW/m^2

Fig. 4.23: Effect of inlet Reynolds number (Re_{in}) on both the components of the rate of entropy generation ($\dot{S}_{gen}$); Here $G = 400$ kg/m^{2}s, $p = 8$ MPa and $T_{in} = 305$ K

4.7 Summary

The present study computationally explores the option of employing flow obstructions in MCHS with sCO$_2$ as the working medium for overall enhancement in the thermalhydraulic

performance. Pairs of rectangular plates have been installed in an alternate orientation on the inner walls of a square minichannel, and systematic effort is made to identify the optimum dimensions for the same. The primary variable under consideration is PEC, which provides a combined perspective of the alteration in both the average HTC and pressure drop across the channel over the basic configuration without any obstruction. Major observations from the thermalhydraulic assessment are summarized below.

- The prime influence of the obstructions can be viewed to be the enhancement in turbulent mixing among the fluid layers, hampering the formation of thermal boundary layers on the heated surface and maintaining a low wall-to-bulk temperature differential. That is manifested by the augmentation in average HTC with the incorporation of every additional pair of obstructions.

- Two distinct peaks of area-averaged HTC can be earmarked, with both being located downstream of the last obstruction and separated by a span of deteriorated heat transfer. Flow separation, demonstrated by the appearance of vortices inside the smaller cells and large recirculation bubble beyond the obstruction segment, is another important factor in maintaining a comparatively lower level of fluid temperature.

- While the use of a single or two pairs can provide favorable PEC only over a limited range of Re_{in}, a consistently high level can be achieved with more pairs, albeit at the cost of rapidly escalating pressure drop, where the major contributor is the increased viscosity level of the fluid around the obstructions. Overall, the FM-3P configuration, housing three pairs of obstructions has been recognized as the optimum one.

- The most preferable dimensions associated with this specific orientation (height, thickness, and inclination angle) have also been identified, with the emphasis being on maximizing PEC. Detailed thermalhydraulic assessment of the optimum design has also been reported over a wide range of operating parameters, such as heat flux, mass flux, pressure, and inlet temperature.

A substantial rise in the driving power requirement and irreversibility, both being directly proportional to the imposed pressure drop, is the major issue to be contemplated with the MCHS with obstruction. The present study considers the obstructions solely to have the shape of rectangular plates. Shape optimization may provide possible improvement in this particular front and hence can be viewed as a possible next step of research. Experimental verification of the reported conclusions is also desirable. The present research effort still

makes a significant contribution in the performance appraisal of MCHS involving sCO_2 and is expected to encourage more innovative designs in the near future.

Chapter 5

Thermalhydraulic comparison and performance prediction of supercritical MCHS with obstructions

5.1 Preamble

Development and appraisal of efficient cooling techniques, in conjunction with both conventional and alternate working fluids, are active domains of scientific research in the recent years. Logical option for thermal management is critical for the working of several engineering systems involving high heat fluxes, such as, MEMS, data centers, avionics, electric vehicles and thin-film-based solar cells. The favorable heat transport characteristics, as well as the feasible temperature and pressure ranges of operation, of certain supercritical fluids make them potentially appealing alternative in devices experiencing very high heat fluxes ($\geq$ 100 kW/m^2), especially in mini-/microchannel geometries [141, 219]. Consequently, a miniaturized or mini-channel heat sink (MCHS), operating on supercritical fluid (SCF), has been earmarked as an enticing choice for near future, owing to the amalgamation of high heat transfer coefficient of SCF and large area-to-volume ratio of MCHS.

Geometric optimization of MCHSs, distribution of wall heat flux and modifying the thermophysical properties of working fluids are parameters to consider while enhancing the heat transfer performance of MCHS. However, while several researchers have explored different heat transfer enhancement technique as discussed in Section 4.1. It is evident from the discussion that the presence of flow obstruction inside the MCHS a Heat performance and fluid flow are often a trade-off between heat transfer maximization and pressure drop minimization. In

most cases, enhancing heat transfer means enhancing pressure drop too, thereby providing conflicting objective functions. Minimizing the pressure drop is an important requirement in the thermal management of high-heat-flux electronic systems. Increasing pressure drop is undesirable in electronic systems because an appreciable pressure drop significantly increases the required pumping power, and the corresponding increase in power consumption compromises the energy efficiency of the entire system. Moreover, drastic pressure changes can severely degrade the reliability of electronic devices. Thus, except for applications in which pressure drop and pumping power are not an issue, a tradeoff between these two performance indicators needs to be achieved.

Drastic pressure change on the coolant-side can severely degrade the reliability of minuscule devices, while lowering the overall energy efficiency of the concerned appliance. Any trial to delay HTD in MCHS results in longer flow-path for the higher-viscosity fluid ($T < T_{pc}$), thereby enhancing the shear stress, along with the direct losses incurred around the obstacles. That necessitates a trade-off between the gain in the heat transfer characteristics and loss in terms of Δp, introducing an ideal topic for multi-objective optimization, with the aim being simultaneous maximization of HTC and minimization of Δp. A few efforts can be found in recent literature to optimize the cooling fluid, and the geometric shape and arrangements of micro-fins, targeting augmentation in the overall thermal performance. Lee *et al.* [220] used artificial neural network (ANN) to optimize the heights of micro-fin in a subcritical heat sink, employing both conventional regression method and multilayer perceptron neural network, and obtained about 37% reduction in pressure drop, without sacrificing the thermal performance. Performance of response surface methodology (RSM) and ANN was compared by Jha *et al.* [221] for extraction of supercritical fluid, with them highlighting the prediction accuracy to depend on the particular process, as well as the independent and dependent parameters. ANN was also employed by Son *et al.* [222] for predicting the inner pitch of a sCO_2-driven heat exchanger with creditable success. No similar work can, however, be identified for SCF-filled MCHS, preparing the backdrop for the present study.

A square minichannel with sCO_2 as the working medium is considered as a part of the present numerical study. The channel accommodates tiny flow obstructions or obstructions, in the shape of airfoils, more details on which are available in section 5.2.1. Firstly, the thermalhydraulic performance of rectangular obstructions, discussed in Chapter 4, is compared with the airfoil shaped obstructions. Each of the geometric parameters, primarily associated with the design of individual obstructions and the entire arrangement of obstructions, can simultaneously affect the overall thermalhydraulic response of such a channel. Therefore,

their individual impacts have methodically been ascertained through 3D computational simulations. Subsequently, an ANN-based multi-objective optimization tool has been developed and trained to envision the overall response of the MCHS with any designated architecture of the array of obstructions, with the primary focus being on the maximization of HTC and minimization of Δp simultaneously. The major variables under consideration here are the number of pairs of obstructions, their center-to-center distance and several dimensions of the individual ones, more on which can be found in section 5.5. Successful attainment of the entrenched objectives can definitely help with the future designs of supercritical minichannels, especially in avoiding or delaying the appearance of HTD and accordingly ensure superior energy transport characteristics.

5.2 Development of Computational Model

5.2.1 Physical geometry

As mentioned earlier, a square minichannel is considered here, the schematic representation of which is shown in Fig. 5.1 and all the dimensional information are summarized in table 5.1. NACA-6412 airfoil-shaped obstructions are installed in pairs on the top and bottom walls ($x - z$ plane) of the channel in alternate orientation. Each obstruction is characterized by a fixed height ($c = 350$ μm), while the width (W) and inclination angle with the horizontal wall (θ) for individual obstructions, as well as the center-to-center distance between the neighboring obstructions, referred as the pitch (d), are varied as a part of the optimization procedure. Zoomed view of a single isolated obstruction is also available in Fig. 5.1(a), while the side-view of the concerned channel with two pairs of vertical ($\theta = 90°$) obstructions can be found in Fig. 5.1(b). The surfaces of the obstructions, as well as the top and bottom walls of the channels, are considered to be perfectly adiabatic, whereas the side walls ($y - z$ planes) are subjected to uniform heat flux. Supercritical CO_2 with regulated mass flow rate is supplied through the inlet plane, and the pressure outlet boundary condition is imposed at the exit to facilitate the numerical replication of the facility.

Steady-state versions of the mass, momentum, and energy conservation equations are solved as a part of the present work in three-dimensional Cartesian coordinate, which has been discussed in Chapter 2.

The conservation equations have been solved following the finite-volume approach of ANSYS-Fluent and has been discussed in Chapter 2.

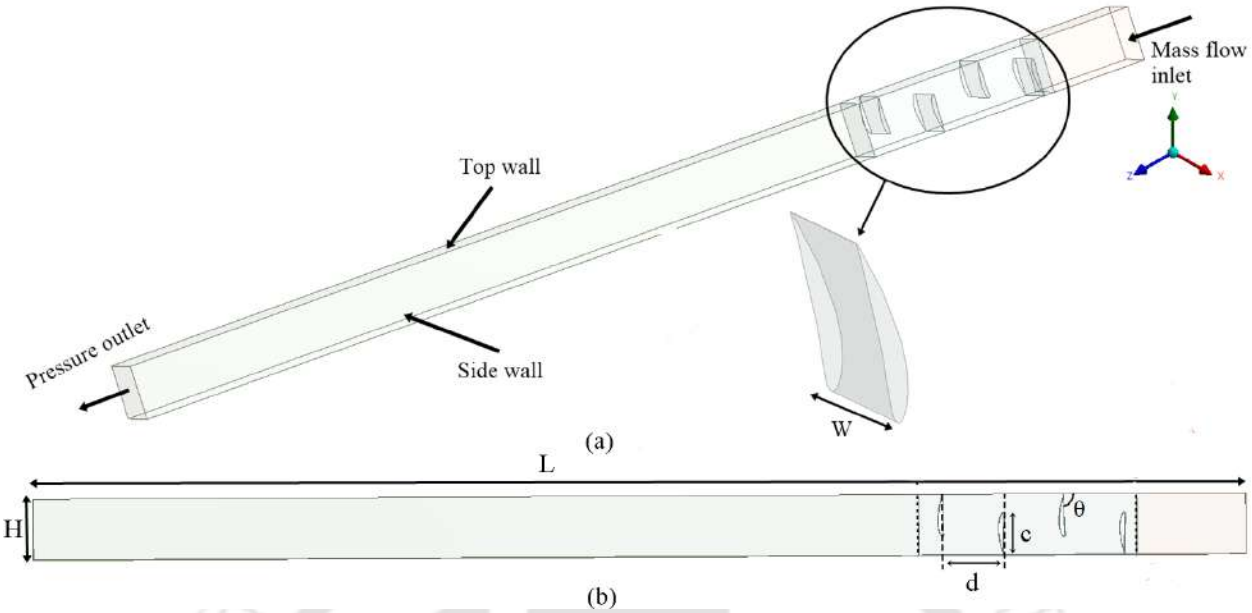

Fig. 5.1: Schematic representation of the computational domain: (a) Three-dimensional view, with the zoomed section showing two pairs of airfoil-shaped obstructions; (b) Two-dimensional side view ($y - z$ plane), marking important dimensions of the considered minichannel

Table 5.1: Geometric details of the adopted minichannel

Parameter	Values
Channel height (H)	500 μm
Channel width (W)	500 μm
Channel length (L)	10 mm
obstruction height (c)	350 μm
obstruction width (W)	200 – 500 μm
Pitch (d)	0.5 – 1.5 mm
Inclination angle (θ)	30° – 90°

5.2.2 Grid-independence study

Large variation in the thermophysical properties of sCO_2, initiated by small changes in temperature or pressure, can result in the appearance of steep gradients within the flow domain, thereby compelling high mesh resolution even in a regular geometry. Instillation of curved surfaces in the present configuration in form of airfoils adds further complexity

to the same, making the generation of an appropriate mesh structure an arduous task. To have a better control on the smallest acceptable grid size, while maintaining a respectable mesh quality, the grid generation is accomplished by segregating the complete domain into two components, namely, the region with obstructions and the one without any. Hybrid mesh with hexahedron is found to be pertinent for the latter region, whereas tetrahedral mesh suffices around the obstructions. Mesh is refined within the boundary layers and also adjacent to the obstructions, with 11 layers in the boundary region and a first layer thickness of 0.2 μm. Magnitude of maximum fluid velocity and pressure drop (Δp) across the channel, as well as the average HTC, are selected as the parameters to compare the impact of grid refinement. Corresponding observations are summarized in table 5.2 for the channel with three pairs of vertical obstructions (referred as FM-3P in section 4.3) at $G = 400$ kg/m^{2}s, $\dot{q}'' = 40$ kW/m^2, $p = 8$ MPa and $T_{in} = 305$ K. It is clearly evident that a change from mesh 3 to mesh 4 augments the number of elements by more than 36%, with consequent rise in the computational resource requirement. That, however, inflicts about 1% change in both maximum velocity and pressure drop, and a mere 1.4% change in the average HTC (defined in section 2.3.1). Therefore, mesh 3 is persisted with for all the subsequent discussions involving this particular orientation and a pictorial view of the same is available in Fig. 5.2. Of course, any modulation in the mesh structure requires re-adjustment and re-examination, which has been methodically performed complying to the same procedure. An overall survey of each of the adopted grid structures suggests a variation in the selected number of elements from 457 371 to 749 726, with the highest aspect ratio of 81 neighboring to the obstructions.

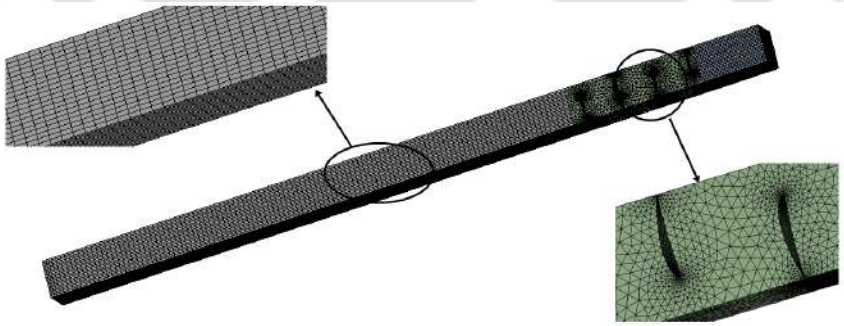

Fig. 5.2: View of the adopted mesh structure: a zoomed view of the region housing the airfoils at the top and an expanded view of the other segment below

Table 5.2: Details of various mesh systems employed

Mesh structure	**Number of elements**	**Maximum velocity** (m/s)	Δp (kPa)	**HTC** (kW/m^{2}K)
Mesh 1	312328	4.68	10.883	17.09
Mesh 2	457371	4.85	10.541	16.68
Mesh 3	623614	4.96	10.153	16.44
Mesh 4	849726	5.01	10.012	16.21

5.3 Discussion on the Thermalhydraulic Characteristics

It is imperative to comprehend the impact of incorporating the flow obstructions, in the form of airfoil-shaped obstructions in the present work, within the MCHS on both the local and gross energy transport characteristics, as well as the shearing losses. Therefore, a systematic approach has been followed to diagnose the thermalhydraulics of each of the conceived sets, to gain a proper understanding on the underlying physics and also to develop the dataset required for optimization, more details on which are available in section 5.5.

5.3.1 Impact of introduction of airfoils

The first question necessary to be addressed is regarding the overall impact of incorporating flow obstructions in a supercritical minichannel. Therefore, first set of simulations have been performed with each of the five configurations, while maintaining identical geometric parameters as $c = 0.35$ mm, $W = 0.5$ mm, and $\theta = 90°$, and a center-to-center distance $d = 0.5$ mm. Associated operating conditions are detailed in the figure caption. Corresponding variations in the area-averaged HTC (α_z) in the axial direction for a specific site of boundary conditions, and the variations in Δp with Re_{in} are presented in Fig. 5.3. Here the inlet Reynolds number (Re_{in}) has been estimated using the supply flow rate and the fluid properties at the inlet plane. HTC remains virtually unchanged after a small span of initial development for the plain minichannel (PM). The trend is quite similar for FM-1P configuration, albeit with a noticeably higher magnitude of HTC throughout the flow passage, suggesting favorable heat transport characteristics for the channel with obstructions. Substantially greater magnitude, as well as axial variations, of HTC can be observed for the other channels, with the level remaining quite similar over the segment with obstructions, and suffering a drastic drop at the immediate downstream of the last obstruction, as a possible consequence of the lowering in fluid velocity owing to the sudden expansion in the flow

path. The supercritical fluid, however, is able to recover, as is indicated by the appearance of a weaker second peak in HTC. While there is considerable rise in HTC_{max} from FM-2P to FM-3P configuration, further gain is not significant on installation of a fourth pair of obstructions. Of course, sCO_2 is able to sustain operation with the highest level of HTC for the FM-4P channel over a longer stretch, allowing a greater length-averaged HTC or $\overline{Nu}$. The average HTC with the concerned set of boundary conditions for the FM-1P, FM-2P, FM-3P and FM-4P configurations are 5.402 kW/m^{2}K, 9.451 kW/m^{2}K, 16.443 kW/m^{2}K and 22.084 kW/m^{2}K respectively, authenticating the sustained improvement in the overall thermal communication with the incorporation of airfoil-shaped obstructions.

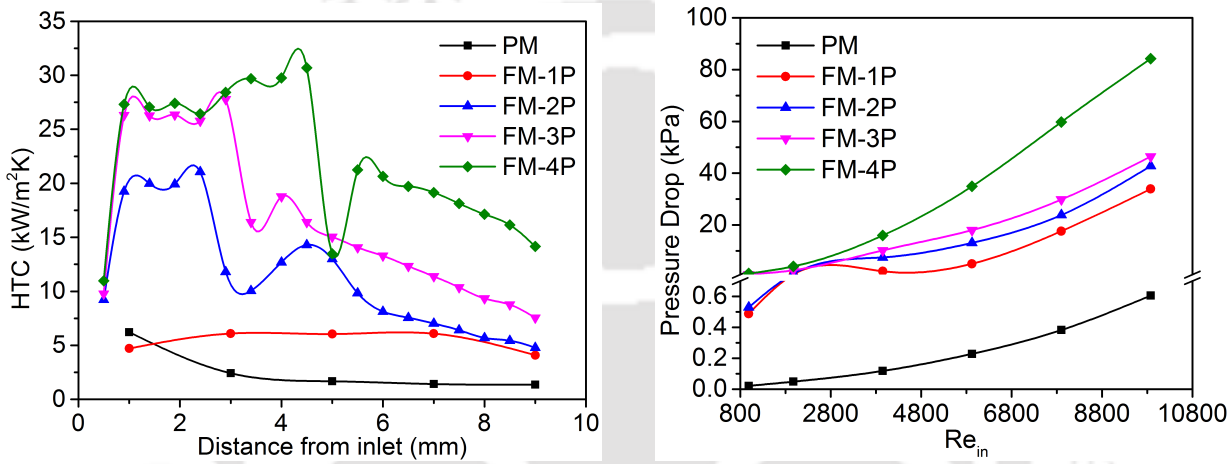

(a) Axial variation in area-averaged HTC at $G = 400$ kg/m^{2}s and $Re_{in} = 3950.8$

(b) Variation in pressure drop (Δp) with the inlet Reynolds number (Re_{in})

Fig. 5.3: Performance comparison of all the five configurations at $\dot{q}'' = 40$ kW/m^2, $p = 8$ MPa and $T_{in} = 305$ K

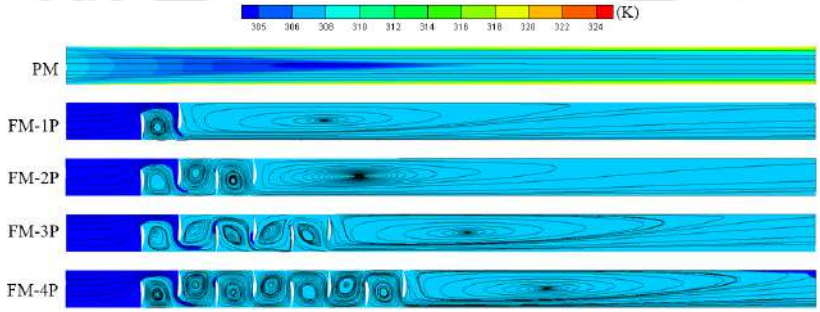

Fig. 5.4: Streamlines and contours of absolute temperature along the mid-vertical plane ($y - z$ plane, $x = 250$ μm) for all the five configurations at $G = 400$ kg/m^{2}s, $\dot{q}'' = 40$ kW/m^2, $p = 8$ MPa and $T_{in} = 305$ K

The rationale behind such gain can be explained following the associated velocity and temperature profiles, as is shown in Fig. 5.4. The streamlines along the mid-vertical planes are quite regular for PM, with consistent development in the thermal boundary layer on the heated surfaces. Accordingly, the temperature of the fluid layer in contact with the hot wall crosses T_{pc} (307.8 K at 8 MPa) quite early in the channel, forcing a sharp reduction in thermal conductivity of the concerned fluid, and consequent deterioration in the local heat transfer coefficient. That explains the steady reduction in α_z till about $z = 3$ mm for PM and a flatter profile afterwards, as thermal conductivity of sCO_2 with $T > T_{pc}$ declines only very slowly with further increase in temperature. The presence of obstructions obliges the flow to deviate from its original contour, with flow separation and development of local recirculation zone at the rear face of the first airfoil itself. Vortices are clearly visible in the space between each pairs of neighboring obstructions, as sCO_2 is forced to change the primary flow direction owing to the alternate arrangements of the obstructions. The streamlines are sufficiently compressed near the obstructions and very much dilated after passing through the segment with airfoils, resulting in the larger recirculation bubble at the downstream of that segment.

The most notable impact of the presence of the airfoils is the disruption in the development of the thermal boundary layer and also degradation in the momentum of the fluid around them, with sCO_2 being repeatedly forced to change the primary flow direction. That allows greater mixing across the fluid layers and enhanced convection, and also the presence of fluid with comparatively lower temperature in the vicinity of the heated surface. It needs to be noted that energy addition takes place through the side walls ($y - z$ planes) and hence, Fig. 5.4, which corresponds to the mid-vertical plane, may not be adequate for visualizing wall-to-fluid energy interaction. To facilitate better comprehension, temperature contours at a few selected $x - y$ planes, allied to different z-locations, are presented in Fig. 5.5 for each of the configurations contemplated here. The first plane picked here is located in immediate upstream to the first obstruction for all the baffled channels. Following the first column of Fig. 5.5, it is quite clear that the temperature variation in PM is restricted only in the neighborhood of the heated walls, as the thermal boundary layer can develop without any hindrance and also reasonably uniformly over the entire of the vertical surface. The temperature of sCO_2 adjoining the side walls is already above T_{pc}, which is consistent with the smooth development of the thermal boundary layer observed for PM in Fig. 5.4, and also justifies poor HTC observed for such a channel. Highest temperature level at this z-location for all the baffled channels, however, is noticeably lower. As the fluid is coerced to move

upward owing to the first airfoil being installed on the bottom surface, crosswise advective transport of thermal energy results in deeper encroachment of relatively high-temperature fluid into the bulk, especially in the upper part of the concerned cross-section. Accordingly, while the bulk temperature/enthalpy is expected to be the same for all the configurations to satisfy the conservation of energy, there is definite reduction in temperature of sCO_2 in contact with the wall. That has a decisive influence in maintaining the concerned temperature below T_{pc}, thereby promoting enhanced heat transfer.

The same deliberation can be extended to the second column of Fig. 5.5, which conforms to the cross-sectional plane adjacent to the rear face of the first pair of baffles. Development in thick thermal boundary layer for PM is very much evident, inducing large wall-to-bulk temperature differential, resulting in further worsening of HTC, as was also observed earlier in Fig. 5.3(a). The profiles are quite similar in the two subsequent downstream locations, with distinguishable change in the thickness of the high-temperature layers. That sufficiently explains the flattened axial profile of HTC. For the FM-1P configuration, development of any stable boundary layer is only initiated from this position, as the fluid is not enforced to any further change in principal flow direction. That allows the growth of boundary layer in the downstream locations. As can be seen for $z = 3.7$ mm, the wall temperature has crossed T_{pc} over majority of the surfaces, suspending any further improvement in heat transfer, whereas the wall temperature on the entire of both the side walls is greater than the pseudocritical for z-locations beyond 7 mm. The gradual decline in HTC observed around such location for FM-1P from Fig. 5.3(a) endorses the same assertion. That, however, is not applicable for the other configurations, with the fluid being required to periodically change the direction of motion over a much longer path. It is very much apparent from Fig. 5.5 that wall temperature for the channels housing more than one pair of baffles crosses T_{pc} further downstream, with majority of the surface still continuing to be in contact with fluid having $T < T_{pc}$. Here the third selected location of $z = 3.7$ mm is in the immediate rear of the forth pair of airfoils. As a direct implication, no boundary layer can be seen here for the FM-4P channel and only limited growth at $z = 8$ mm. That substantiates the considerable increase in the corresponding HTC level. All the observations can be integrated to infer that sCO_2 is able to maintain $T < T_{pc}$ over the entire segment housing the obstructions, yielding significant enhancement in the overall thermal communication between the walls and fluid, and hence improved heat transfer characteristics. Deterioration in HTC is observed only after sCO_2 navigates past the baffled segment and high-temperature, and hence with inferior thermal conductivity, fluid layer starts to evolve on the heated surface. That emanates in

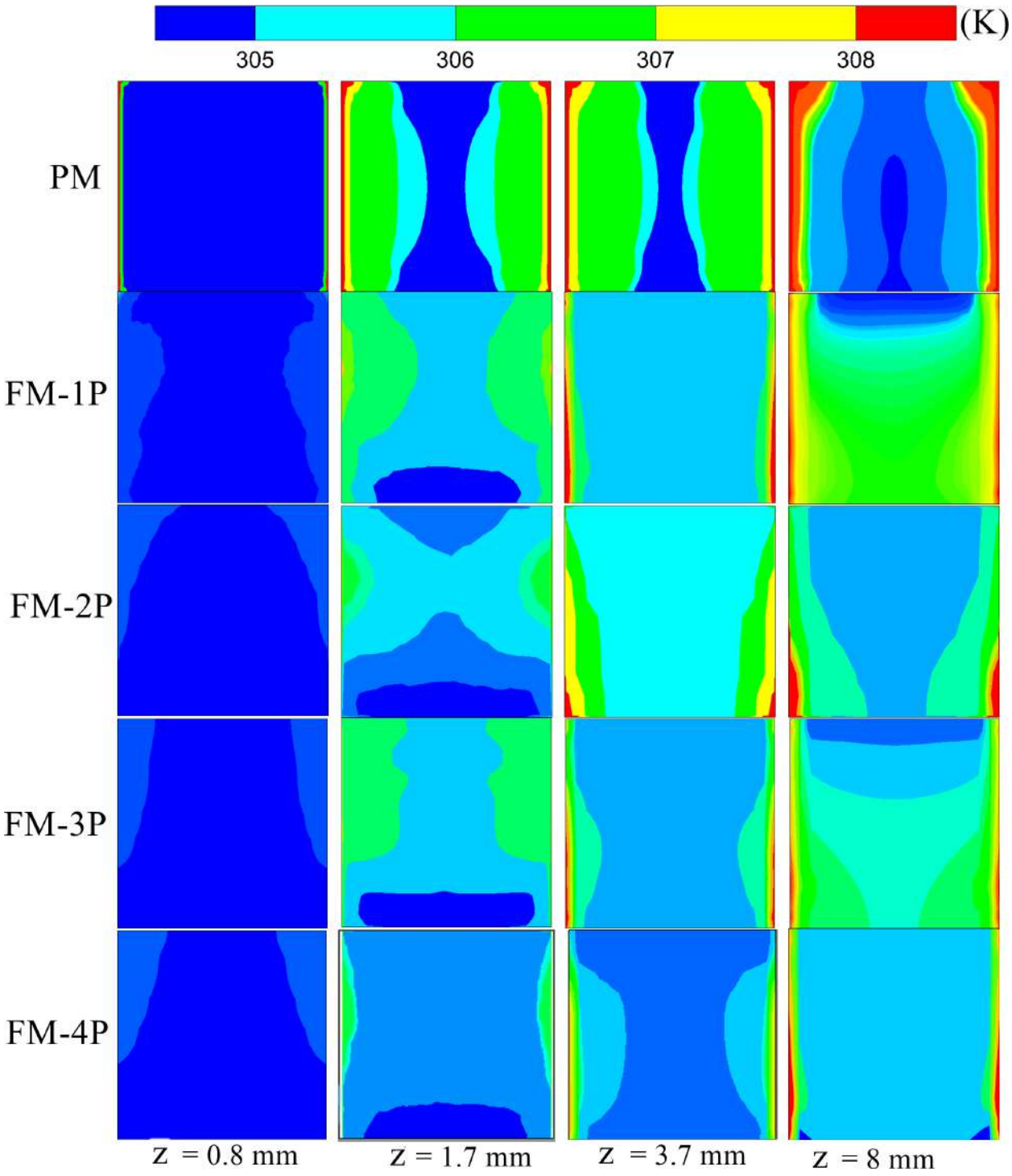

Fig. 5.5: Temperature contours at a few selected $x-y$ planes for all the five configurations at $G = 400$ kg/m^{2}s, $\dot{q}^{''} = 40$ kW/m^2, $p = 8$ MPa and $T_{in} = 305$ K

substantial increase in average HTC with rise in the number of airfoils, as noted earlier.

It needs to be noted here that amount of energy received by the fluid is same for all the considered cases, while maintaining identical values for inlet temperature and exit pressure, as the system must be energy-conserving. Accordingly, sCO_2 in each of the systems experiences identical rise in bulk enthalpy, which is 4 kJ/kg for the case explored in this section. That, however, is not guaranteed to yield identical change in T_b, because of the simultaneous dependence of fluid enthalpy on both pressure and temperature. Narrowing of the flow passage around the airfoils results in substantial augmentation in the fluid velocity, with maximum value of 0.6 m/s for PM escalating to 1.13 m/s, 1.69 m/s and 2.01 m/s for FM-2P, FM-3P and FM-4P respectively, which also induces accretion of similar order in turbulence intensity. The appearance of higher velocity levels and enhanced turbulent mixing, however, augments the total pressure loss with increase in the number of airfoils, as can be seen from Fig. 5.3(b). With $G = 400$ kg/m^{2}s, Δp for the FM-1P, FM-2P, FM-3P and FM-4P configurations are 9.998 kPa, 14.801 kPa, 17.968 kPa and 33.339 kPa respectively, which is in stark contrast to the negligible loss of around 0.2 kPa for the plain minichannel. That demands a consequent rise in the pressure at the inlet plane with installation of more obstructions, where a constant temperature condition has been imposed. Enthalpy of sCO_2 gradually reduces with increase in pressure under isothermal condition, and for present T_{in} = 305 K, inlet enthalpy for FM-4P is lowered by about 0.639 kJ/kg from the original magnitude of 295.302 kJ/kg pertinent of PM. This obligates a reduction in T_b at exit plane by a mere 0.16 K for FM-4P, in comparison with 305.589 K for PM. While this may seem a negligible number, it can be more significant at larger levels of $\dot{q}''/G$. Besides, as discussed above, the heat transport characteristics are dominated by the local fluid temperature adjacent to the heated surface, instead of the area-averaged one. It can, therefore, be concluded that the incorporation of airfoil-shaped obstructions enhances the thermal performance quite substantially, albeit with rapid upsurge in cost to overcome pressure losses, necessitating a more judicial approach for identification of the preferred geometry.

5.3.2 Impact of number of pairs of obstructions

It is, therefore, evident that the introduction of airfoil-shaped obstructions enhances the averaged level of heat transfer coefficient in MCHS and reduces the temperature level, thereby delaying the appearance of HTD, albeit at the expense of greater pressure losses. Both of the above factors can be combined in terms of PEC, and hence, consequent variations in PEC with Re_{in} for each of the four channels under consideration are presented in Fig. 5.6

at $\dot{q}'' = 40$ kW/m^2, while continuing with the values of other parameters maintained in the previous section. Steep enhancement in PEC can be noted with the rise in supply flow rate for the lower range of Re_{in}, till it attains a maxima, and gradually descends afterward. This is a clear indication about the large amplification in the heat transfer rate at lesser Re_{in} and considerably higher pressure losses incurred at greater flow rates, which is able to subside the gain in HTC, resulting in the decline in PEC. It is consistently greater than 1.4 for FM-3P channel over the entire range of flow rate explored here, with a peak level of about 1.85, illustrating significant performance acquisition compared to the plain minichannel, and thereby advocating about the use of airfoil obstructions. The highest attainable PEC for FM-1P and FM-2P configurations, however, are just about 1.2 and 1.4 respectively, and PEC can even be less than one on either ends of the flow rate spectrum, suggesting toward exercising caution about the choice of obstruction orientation. FM-2P performs favourably only for $1900 \lessapprox Re_{in} \lessapprox 8500$. Installation of more than 3 pairs of obstructions has been observed to result in inconsequential benefit in terms of PEC over the entire range of Re_{in} explored here, as a direct consequence of larger pressure losses with the presence of more obstructions within the flow path, which subsides the gain in terms of $\overline{Nu}$. For example, PEC_{max} with FM-4P is only about 2.6% greater than the same for FM-3P, despite offering greater fabrication challenges. It also needs to be noted here that the FM-4P configuration may suffer from probable backflow from the exit plane under certain sets of operating conditions, as the length available for the fluid beyond the last airfoil may not always be sufficient. It is not conclusive from Fig. 5.4 whether the fluid has attained reattachment in this channel and a longer MCHS may become necessary. Therefore, the subsequent discussion focuses solely on FM-2P and FM-3P configurations, to explore the impact of other geometric parameters and also to look for the optimized designs for both.

5.3.3 Impact of center-to-center distance between obstructions

The effect of change in pitch (d) can be ascertained from Fig. 5.7 for both FM-2P and FM-3P configurations. Substantial enhancement in the average HTC can be observed with the widening of the gap between the obstructions for both of these configurations. The larger space available between the obstructions results in bigger vortices, allowing for early detachment of the thermal boundary layer, ensuing intensified mixing across the fluid layers and strong advection effect. Accordingly, change in d from 0.5 mm to 1 mm ensures about 26% rise in average HTC, whereas a further 23% gain can be conceived by increasing d from 1 mm to 1.5 mm for the FM-2P channel. There is, however, notable oscillations in

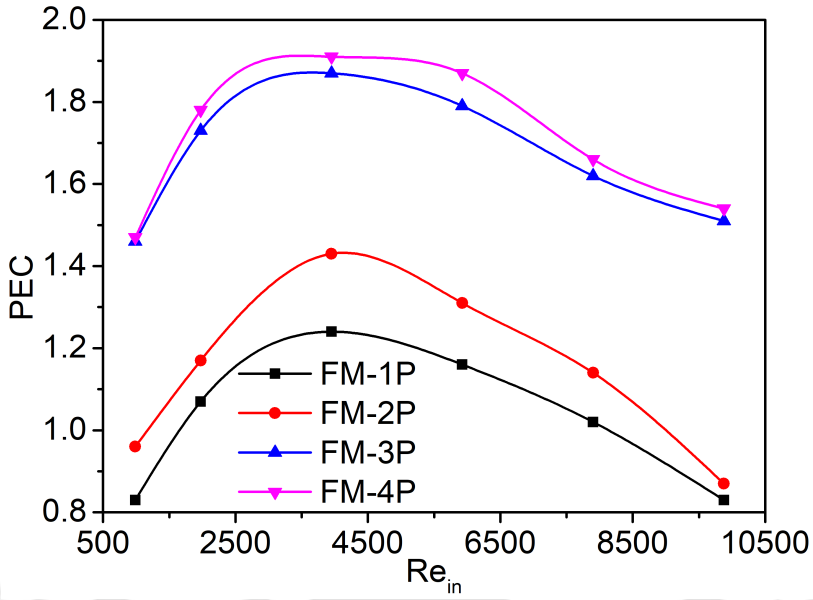

Fig. 5.6: Variation in PEC with the inlet Reynolds number (Re_{in}) for all the four channels with obstructions considered here at $\dot{q}'' = 40$ kW/m^2, $p = 8$ MPa and $T_{in} = 305$ K

α_z in the space between the adjacent airfoils, which gets amplified with the increase in d and can be explained following Fig. 5.8. As the fluid has sufficient space to expand at the rear of each airfoil, local velocity level can reduce quite noticeably around the center of the vortices, lowering the associate intensity of turbulence. A change in d from 0.5 mm to 1.5 mm for FM-3P channel decrements the overall level of turbulence intensity by about 38.5%, while the radical diminution in local values are evident from Fig. 5.8. That weakens the area-averaged HTC interior to the gap and raises the local temperature. Supercritical CO_2, however, accelerates again as it approaches the next obstruction, improving both the local velocity and level of turbulence because of consequent compression, emanating into another peak in α_z. The general reduction in turbulence, of course, helps in pressure recovery interior to the channel. Increase in d from 0.5 mm to 1 mm and 1.5 mm for FM-2P configuration reduces Δp by 14.2% and 24.4% respectively from the initial value of 7.47 kPa, while the corresponding numbers are 20.0% and 27.3% for the FM-3P channel. Increase in pitch, therefore, is a very favorable proposition, as it simultaneously offers augmentation in $\overline{Nu}$ and lowering in Δp, with both contributing toward the gain in PEC. Change in pitch from 0.5 mm to 1.5 mm allows an enhancement in PEC from 1.430 to 1.906 for FM-2P channel, and 1.870 to 2.261 for the FM-3P configuration. There is, however, practical constraint in changing d in terms of the total length of the channel. For example, it is not possible to

employ $d = 1.5$ mm for FM-4P configuration, whereas the last obstruction is quite close to the exit plane in FM-3P channel, thereby imposing an upper limit.

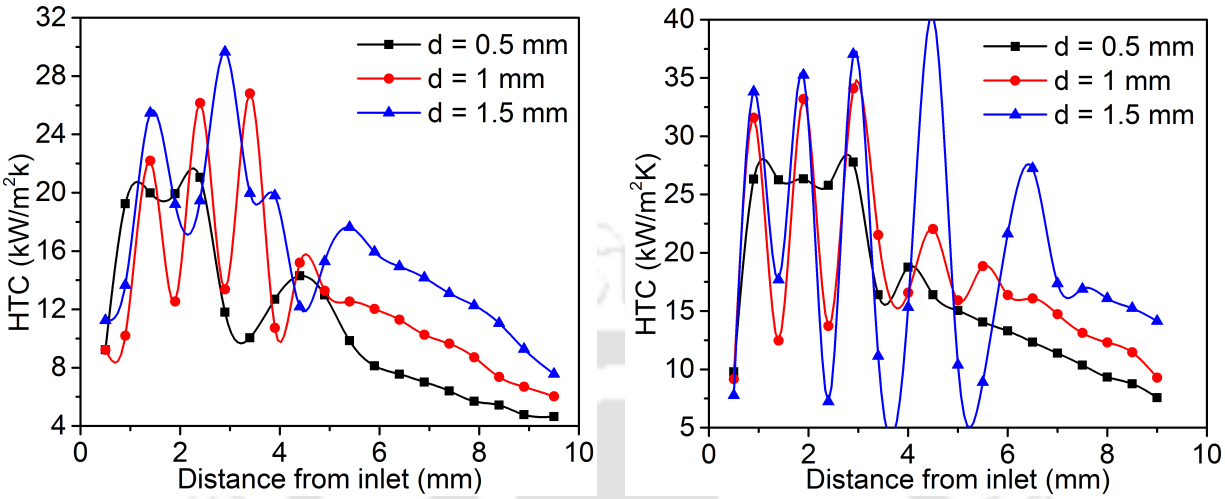

(a) FM-2P configuration **(b)** FM-3P configuration

Fig. 5.7: Effect of center-to-center distance (d) on the axial variation in area-averaged HTC at $G = 400$ kg/m^{2}s, $\dot{q}'' = 40$ kW/m^2, $p = 8$ MPa and $T_{in} = 305$ K

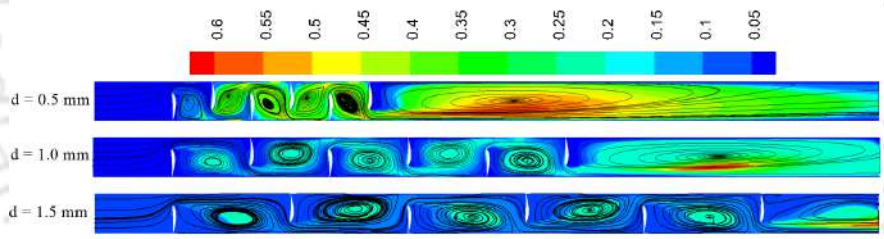

Fig. 5.8: Streamlines and contours of turbulence intensity along the mid-vertical plane ($y - z$ plane, $x = 250$ μm) for FM-3P configuration and three different pitch (d) at $G = 400$ kg/m^{2}s, $\dot{q}'' = 40$ kW/m^2, $p = 8$ MPa and $T_{in} = 305$ K

5.3.4 Impact of width of obstructions

Simulations have now been performed with FM-2P and FM-3P configurations and with three different widths (W) of the individual obstructions for both, to apprehend the role of W. Corresponding axial variations in area-averaged HTCs (α_z) are presented in Fig. 5.9. Considerable rise in both local and average HTC can be noted with the widening of the obstructions, which is particularly prominent for a change in W from 0.35 mm to 0.5

mm. A wider obstruction instills greater obstruction to the movement of sCO_2, thereby raising the level of local velocity and turbulence intensity. That enriches the mixing within the fluid layers, disrupting the development of the thermal boundary layer, and creating a favorable temperature gradient on the heated surface. The vortices originating within the space between the neighboring obstructions also have greater volume available for their respective growth, which draws more fluid particles to participate in the thermal transport. The combined effect of the narrated dynamics is the improvement in the level of HTC for a channel with wider obstructions, but at the expense of greater frictional losses. Reduction in obstruction width for FM-2P from 0.5 mm to 0.35 mm causes about 17% deterioration in averaged-HTC, while the drop is about 34% for FM-3P. That, however, is accompanied by about 81.4% and 83.1% reduction in Δp respectively, as the fluid experiences lesser resistance to flow in the channel with narrower obstructions, causing a much lesser impact on PEC. For FM-2P, PEC marginally reduces from 1.51 with $W = 0.5$ mm to 1.43 for $W = 0.35$ mm, whereas the consequent degradation is from 1.95 to 1.87 for the FM-3P configuration, clearly emphasizing the weaker significance of W on PEC.

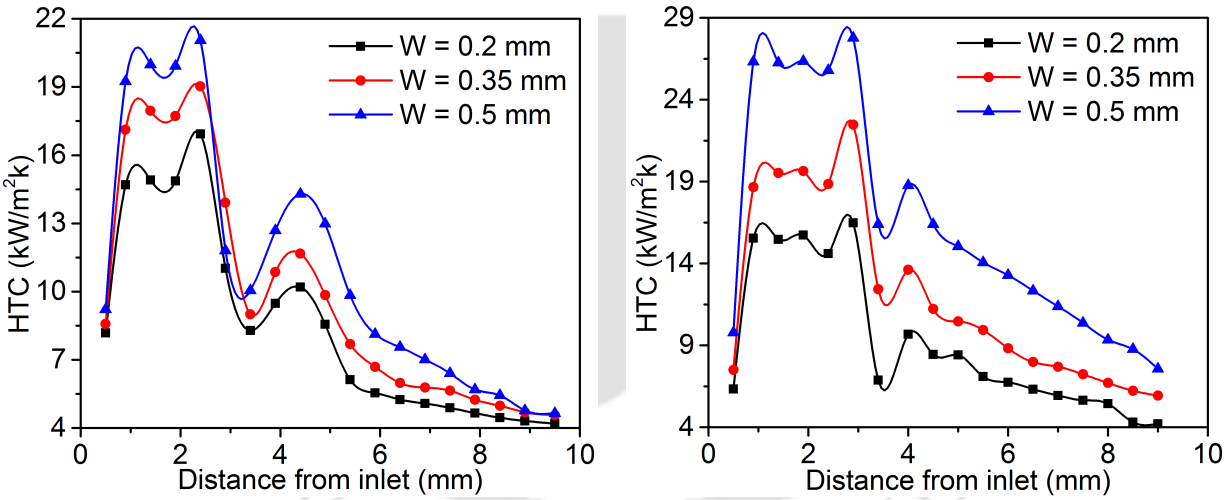

(a) FM-2P configuration **(b)** FM-3P configuration

Fig. 5.9: Effect of width of obstructions (W) on the axial variation in area-averaged HTC at $G = 400$ kg/m^{2}s, $\dot{q}'' = 40$ kW/m^2, $p = 8$ MPa and $T_{in} = 305$ K

5.3.5 Impact of inclination angle of obstructions

The space available for sCO_2 to flow around the obstructions can further be modulated by changing the angle of inclination to the base surface. Entire of the above discussion

corresponds to the vertical obstructions ($\theta = 90°$). Simulations have now been performed by varying the angle over the range of 90°–30° with both FM-2P and FM-3P configurations, and the consequences are reported in Fig. 5.10. Considerable reduction in HTC can be observed with any change in inclination, in terms of both the peak magnitude and the local level at any axial position, subsequently presenting a noticeably lower value averaged over the entire channel. For FM-2P, change in θ from 90° to 60° results in about 20% deterioration in average HTC, and a further 23% for a modification to $\theta = 30°$. An inclined obstruction allows lesser velocity gradient in the vicinity of obstructions and also a smoother expansion toward the downstream, reducing the corresponding pressure loss. Moreover, changes in fluid velocity throughout the channel are less for obstructions with smaller inclination angles, characterized by smooth streamlines through the wider openings, affecting the thermal communication between sCO_2 and the heated surface. On the contrary, higher θ enhances turbulent mixing and imposes greater diversion to the primary direction of motion. Therefore, reduction in θ from vertical is associated with the opposing impact of decline in both HTC and Δp, which culminates to a decrement in PEC. While the number drops from 1.43 to 0.977 on changing the angle from 90° to 30° for the FM-2P channel, corresponding reduction is from 1.87 to 1.02 with FM-3P, advocating in favour of the vertical airfoils.

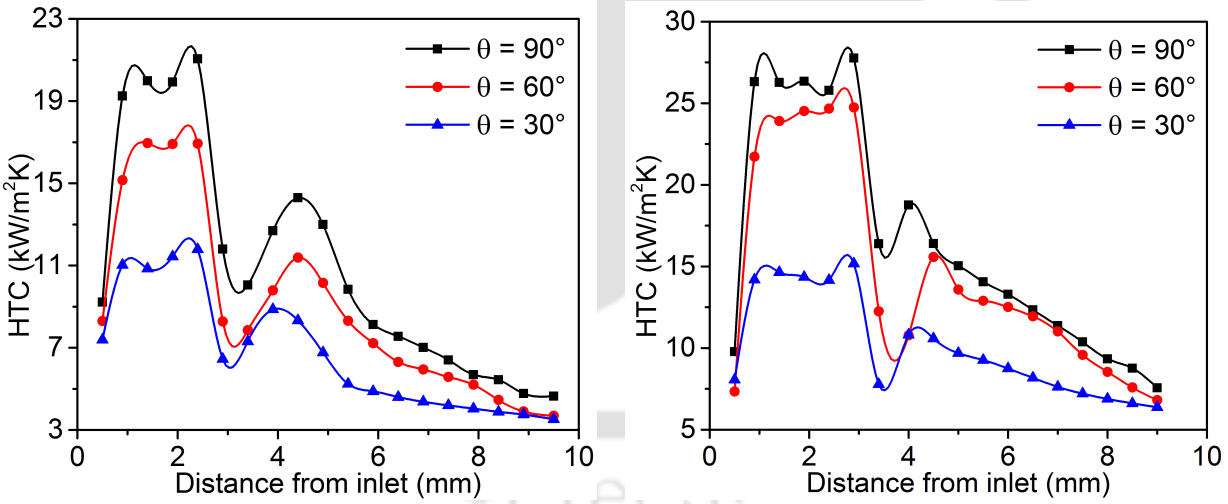

(a) FM-2P configuration **(b)** FM-3P configuration

Fig. 5.10: Effect of inclination angle (θ) on the axial variation in area-averaged HTC at G = 400 kg/m^{2}s, $\dot{q}''$ = 40 kW/m^2, p = 8 MPa and T_{in} = 305 K

It can, therefore, be concluded that each of the geometric parameters characterizing the individual obstructions, as well the number of pairs of obstructions, installed within

MCHS affect the overall thermalhydraulic performance by altering the localized, peak and average level HTC within the channel, and also the total pressure drop. So, each of them directly affect the PEC, necessitating the identification of an optimized configuration to ensure the most desirable performance. The details of the adopted optimization technique are elucidated below, with subsequent identification of the best possible combination of parameters separately for the FM-2P and FM-3P configurations.

5.4 Thermalhydraulic Comparison of MCHS with Rectangular and Airfoil Obstructions

5.4.1 Comparison of effect of number of obstructions in MCHS

The effect of micro obstructions on heat transfer performance of minichannel heat sinks is quantified in terms of relative Nusselt number and is depicted in Fig. 5.11a. Nu_o stands for the average Nusselt number for plane microchannel heat sink selected as the base case to compare improvement in heat transfer performance. For both RBHS and ABHS, the relative average Nusselt number is greater than one implying that providing flow obstruction improved heat transfer due to interruption of flow field. For all channel configurations, relative Nusselt number increases with Re_{in} because of enhanced flow mixing and disruption of thermal boundary layer with increasing flow velocity. For same boundary and geometric configurations, ABHS-3P showed 28% higher relative Nusselt number compared to RBHS-3P configuration and ABHS-2P yields about 16% higher Nusselt number compared to RBHS-2P configuration. The effect of fin configurations on relative pressure drop is presented in Fig. 5.11b. In the present figure PD_{RB} and PD_{AB} represents pressure drop in RBHS and ABHS, respectively. As it can be seen from the figure that pressure drop increases with Re for both MCHS configuration. Rectangular-shaped obstructions demonstrated highest pressure drop relative to airfoil-shaped obstruction. At $Re_{in} = 3950.8$, the relative pressure drop for rectangular-shaped obstruction was larger by 100% for 3 pair configuration and by 60% for 2 pair configurations.

Consequent variations in PEC with Re_{in}, which is defined in terms of the parameters specified at the inlet plane, for all the four channels with obstructions is depicted in Fig. 5.12a. PEC increases quite steeply with an increase in the supplied mass flux for all the configurations at lower levels of Re_{in}, before attaining a respective maxima and falls thereafter with a lesser gradient. That indicates toward the dominance of enhancement in Nu at smaller Re_{in}, which is suppressed by the magnified pressure drop at larger flow rates. For

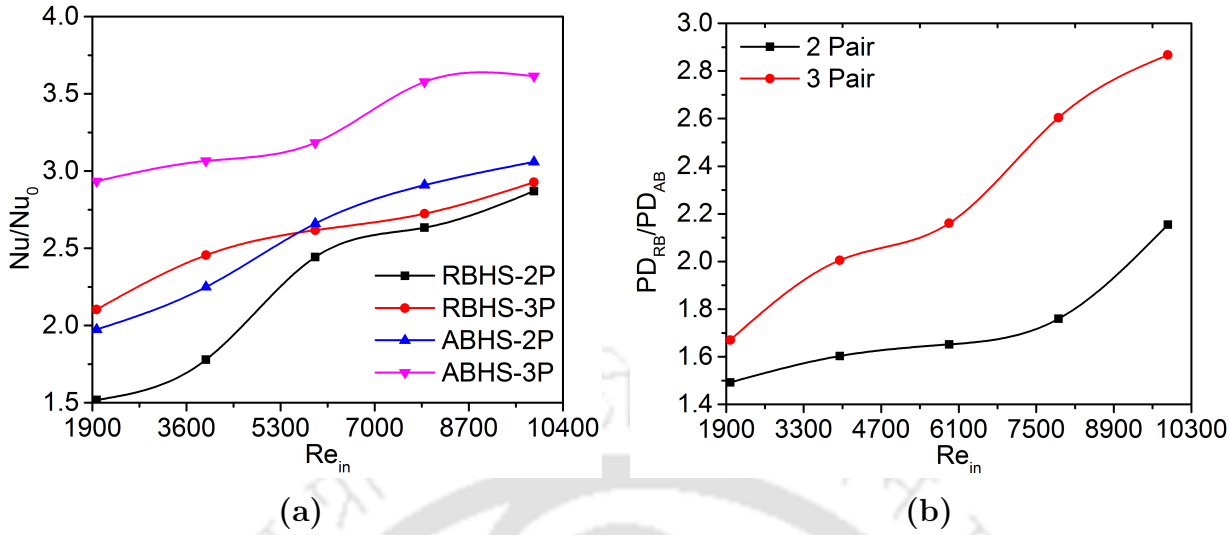

Fig. 5.11: Variation in (a) relative Nusselt number and (b) relative pressure drop for different configuration of MCHS

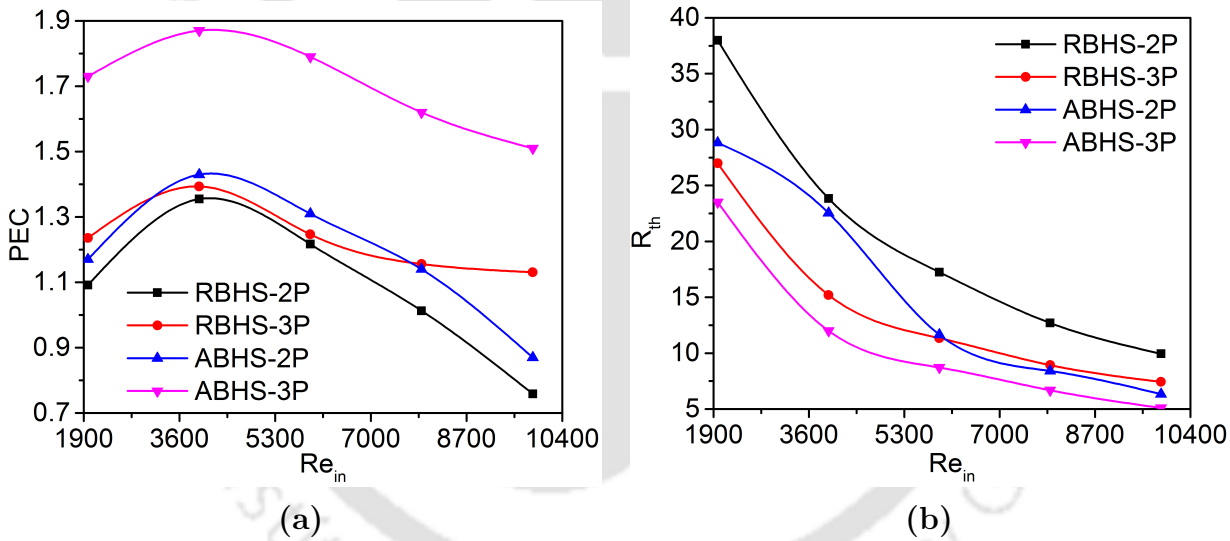

Fig. 5.12: Variation in (a) *PEC* with inlet Reynolds number and (b) thermal resistance

both RBHS-2P and ABHS-2P channels, *PEC* is greater than one only for a limited range of Re_{in} with favourable value lies between 1900 $\lessapprox$ Re_{in} $\lessapprox$ 6000, advocating caution about their use. For both RBHS-2P and ABHS-2P channels, a favorable value is possible for 1900 $\lessapprox$ Re_{in} $\lessapprox$ 6000, with a peak of mere 1.15, which may not be a significant gain considering the practical intricacies involved in fabricating such a channel.

The variation of thermal resistance with Reynolds number is depicted in Fig. 5.12b.

In general, thermal resistance decreases with the increase in Reynolds number because of enhancement in heat transfer coefficient. The presence of obstruction causes greater constriction for the fluid to pass through, thereby simultaneously enhancing the local velocity and intensity of turbulence, both of which contribute to the augmentation in the mixing of fluid layers and help to maintain favourable temperature near the heated walls, which in turn reduces the thermal resistance. For the same value of Reynolds number, both rectangular and airfoil based MCHS showed lower thermal resistance compared to plane MCHS. However, for the simulated range of Reynolds number airfoil based MCHS demonstrated lower thermal resistance in comparison to rectangular shaped MCHS. For $Re_{in} = 3600$, the thermal resistance of the airfoil based MCHS is 45% lower than that of the MCHS with rectangular shaped MCHS.

5.4.2 Comparison of effect of inclination angle of obstructions in MCHS

As we have seen in earlier section that thermalhydraulic characteristics if MCHS with obstructions is also affected by inclination angle of obstruction. In this regard, the variation of relative Nusselt number for both ABHS and RBHS is depicted in Fig. 5.13a. For all the inclination angle considered in the present simulation, ABHS showed higher Nusselt number with increasing magnitude with Re_{in}. At $Re_{in} = 3950.8$, for $\theta = 30°$, $60°$ and $90°$ the relative Nu for airfoil-shaped obstruction was larger by 42%, 28% and 33%, respectively. The effect of fin configurations on relative pressure drop is presented in Fig. 5.13b. For each MCHS configuration, it can be seen from the figure that pressure drop increases with Re_{in}. Rectangular-shaped obstructions demonstrated highest pressure drop relative to airfoil-shaped obstruction with increasing pressure drop with Re. At $Re_{in} = 3950.8$, for $\theta = 30°$, $60°$ and $90°$ the relative pressure drop for rectangular-shaped obstruction was larger by 250%, 125% and 90%, respectively.

The variation of relative Nu and pressure drop can be quantified in terms of PEC which is shown in Fig. 5.14. For both channel configuration, PEC increases initially with Re_{in} attains a maxima at $Re_{in} = 3950.8$ and then it decreases gradually. For $\theta = 30°$, the peak value of PEC for RBHS-3P is 23% smaller compared to ABHS-3P. For $\theta = 60°$, the peak value of PEC for RBHS-3P is 24% smaller compared to ABHS-3P. Similarly, For $\theta = 90°$, the peak value of PEC for RBHS-3P is 25% smaller compared to ABHS-3P. The above statistics clearly advocates the advantages of airfoil-shaped obstructions over rectangular-shaped obstruction. Further, the variation of thermal resistance with Reynolds number is depicted in Fig. 5.15. For all MCHS configuration, thermal resistance decreases with

increasing inclination angle. The average thermal resistance for RBHS-2P configuration is higher by 6% from ABHS-2P configuration and the average thermal resistance for RBHS-3P configuration is higher by 16% from ABHS-3P configuration.

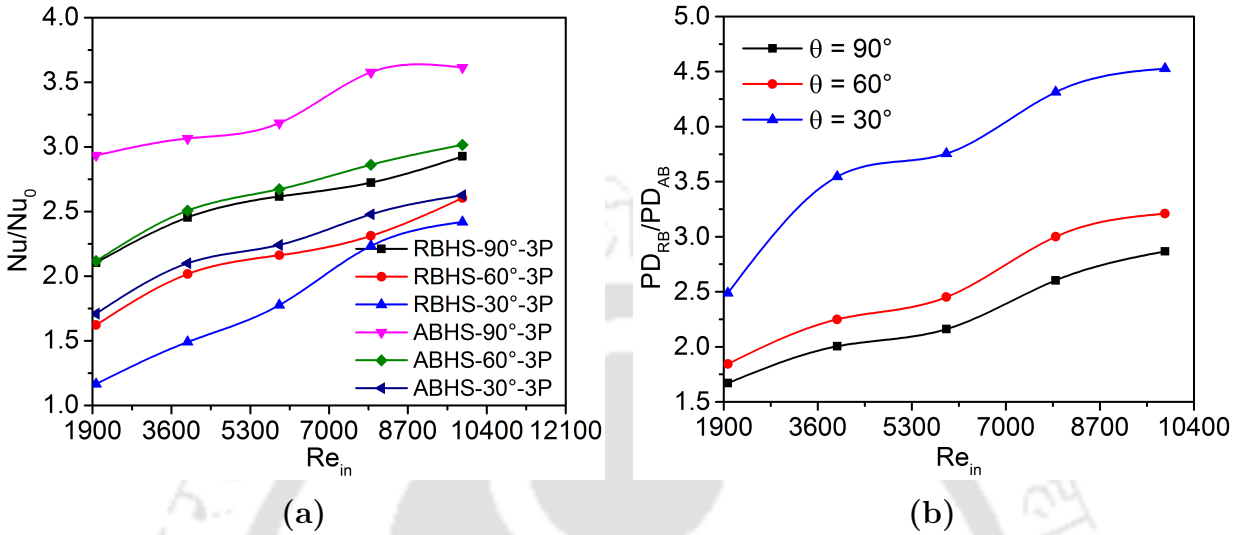

Fig. 5.13: Effects of inclination angle on (a) relative Nusselt number and (b) relative pressure drop

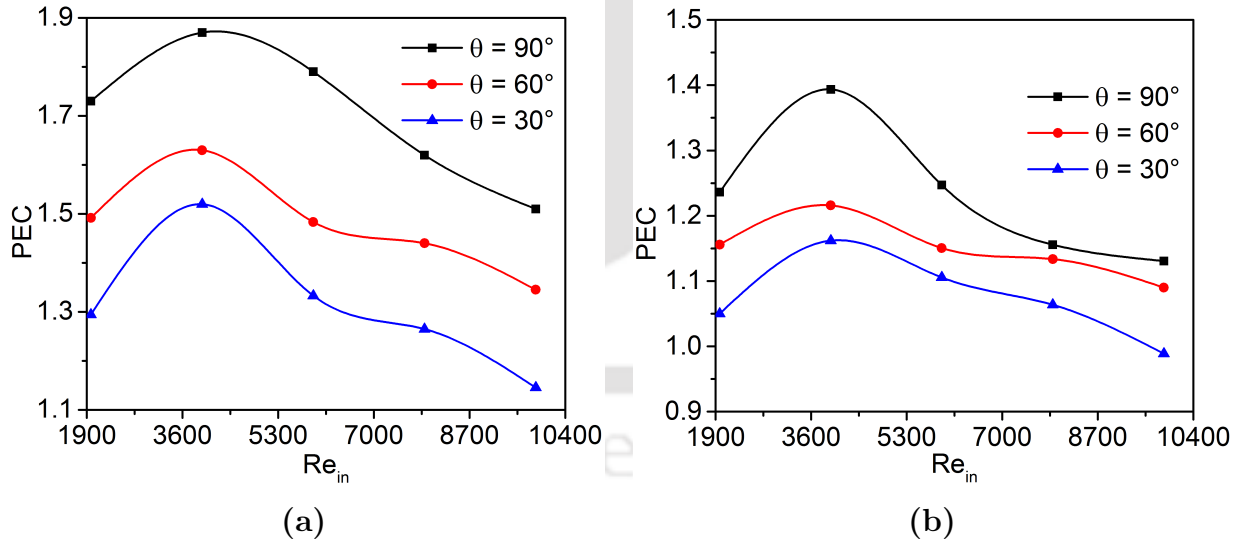

Fig. 5.14: Variation in *PEC* with Reynolds number at different inclination angle for (a)RBHS-3P and (b) ABHS-3P

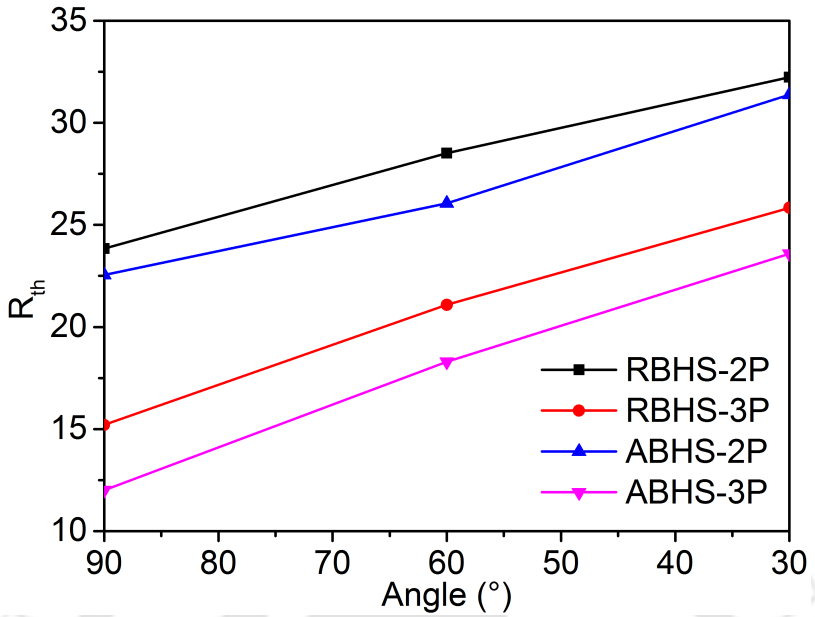

Fig. 5.15: Variation in thermal resistance with inclination angle for RBHS and ABHS

5.4.3 Comparison of effect of center-to-center distance between obstructions in MCHS

The effect of change in pitch (d) on relative Nusselt number can be ascertained from Fig. 5.16a for both FM-2P and FM-3P configurations. The relative Nusselt number increases gradually for all the channel configuration with ABHS showing superior heat transport for all inlet Reynolds number. Accordingly, at Re_{in} = 3950.8, for d = 0.5 mm, 1 mm and 1.5 mm the relative Nu for airfoil-shaped obstruction was larger by 29%, 38% and 25%, respectively. Similar to relative Nusselt number, relative pressure drop also showed similar characteristics with ABHS ascertaining lower pressure drop compared to RBHS. The relative pressure drop at smallest center-to-center distance is also small and with increase in d it increases significantly with highest relative pressure drop up to 4.4 times for d = 1.5 mm. Pressure drop in both the channel configuration decreases at larger center-to-center distance, however the increasing relative pressure drop at larger center-to-center distance shows that reduction in pressure drop in ABHS channel is higher compared to RBHS channel.

MCHS that possess lower thermal resistance are associated with lower average temperature and are considered to exhibit better heat transfer than those with higher thermal resistance. The variation of thermal resistance for different center-to-center distance of obstructions is depicted in Fig. 5.17, from which the decrease in thermal resistance with Re_{in}

is evident. At the same Re_{in}, thermal resistance in ABHS-3P is lower than that in RBHS-3P, due to higher heat transfer coefficient obtained with the former. For instance, at Re_{in} = 3950.8, for d = 0.5 mm, 1 mm and 1.5 mm the thermal resistance for airfoil-shaped obstruction was larger by 22%, 16% and 13%, respectively.

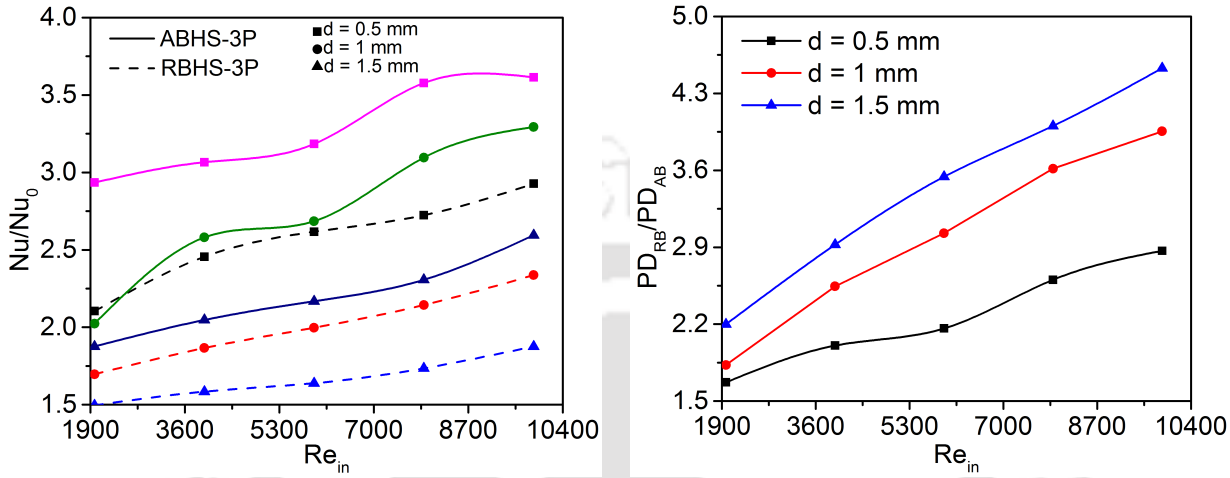

Fig. 5.16: Variation in (a) relative Nusselt number and (b) relative pressure for different configuration of MCHS showing effects of center-to-center distance

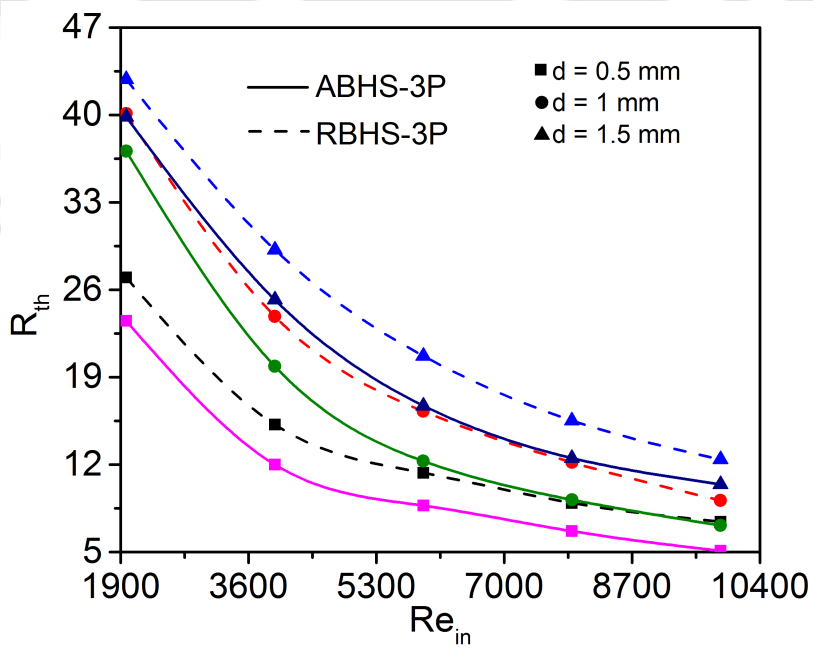

Fig. 5.17: Variation in thermal resistance with center-to-center for RBHS and ABHS

5.5 Forecasting Methodology: Computational Intelligence-based Neural Network

5.5.1 ANN structure

Computational intelligence-based neuro-biological models are mathematical frameworks inspired by the robust learning ability, structure, processing speed, and decision-making capability of biological neurons and the laws of nature. Neural networks (NN) are neural computational modelling approaches. The mathematical framework of NN emulates the biological neuronal system and consists of a large cluster of neural units (nodes). In the present investigation, the robust self-learning capability of NN is utilized to model the complex nonlinear correlation between the performance of a supercritical mini channel heat sink and the input parameters of the heat sink in terms of the number of used baffles, baffle inclination angle (θ), the pitch of the baffle placement in the channel (d), and baffle width (W).

A computational intelligence (CI)-based neural network (NN) is identified as a complex network structure consisting of several neurons' interconnections, which simulate the activities of neurons using a mathematical framework. The important parts of the NN model which control the performance of the NN are an input layer, hidden layers, an output layer, network structure, transfer function of the neurons, and the coefficient of the transfer function for each neuron in each layer. Here, the problem is formulated as to forecast the performance of the supercritical mini channel heat sink (PEC as defined in Eq. 4.3) by knowing the parameters like the number of used baffles, baffle inclination angle, the pitch of the baffle placement in the channel, and the baffle width.

For the successful prediction of the supercritical mini channel heat sink (MCHS) performance corresponding to different geometric constructions of the heat sink, a multi layer feed forward NN (MLFF-NN) is trained by the back propagation (BP) algorithm. The problem is defined to predict the performance of the supercritical mini channel heat sink (PEC as defined in Eq. 4.3) by knowing the geometric construction of the heat sink in terms of the used baffle number, baffle mount inclination in the channel, pitch at which the baffles are installed in the channel, and the width of the baffles. Thus, the baffle number, baffle inclination, baffle pitch, and baffle width are set as the input parameters of the NN, and the corresponding performance of the heat sink is considered as the NN output. A single hidden layer is considered in the present NN modelling. The structural framework of the proposed MLFF-NN is shown in Fig. 5.18. The MLFF-NN computation is done using 'C' programming language in a Linux operating system. A linear transfer function is used for

the neurons in the input layer. The tan-sigmoid transfer function is used for the neurons in hidden and output layers. The input layer consists of three neurons corresponding to baffle inclination, the pitch of the baffle placement, and baffle width. The output layer contains only one neuron corresponding to the heat sink performance. The performance of the network is studied by varying the number of neurons in the hidden layer. The three inputs of the three neurons in the input layer are denoted by A_{1i}, A_{2i}, and A_{3i}, respectively, as shown in Fig. 5.18. The outputs of these three neurons in the input layer are represented by A_{1o}, A_{2o}, and A_{3o}, respectively. Similarly, the input and output of the j^{th} neuron in the hidden layer are represented by B_{ji} and B_{jo}, respectively. C_{1i} and C_{1o} represent the input and output of the neuron in the output layer. The connecting weight between the first neuron in the input layer and the j^{th} neuron in the hidden layer is denoted by IH_{1j}. In the same way, HO_{j1} denote the connecting weights between the j^{th} neuron of the hidden layer and the neuron of the output layer. HB_j denotes the hidden layer bias for the j^{th} neuron, and OB_1 is the bias for the output layer neuron. The transfer function for the hidden layer is represented by F_h, and F_o denotes the same for the output layer. The below-mentioned relations have been used for the chosen network.

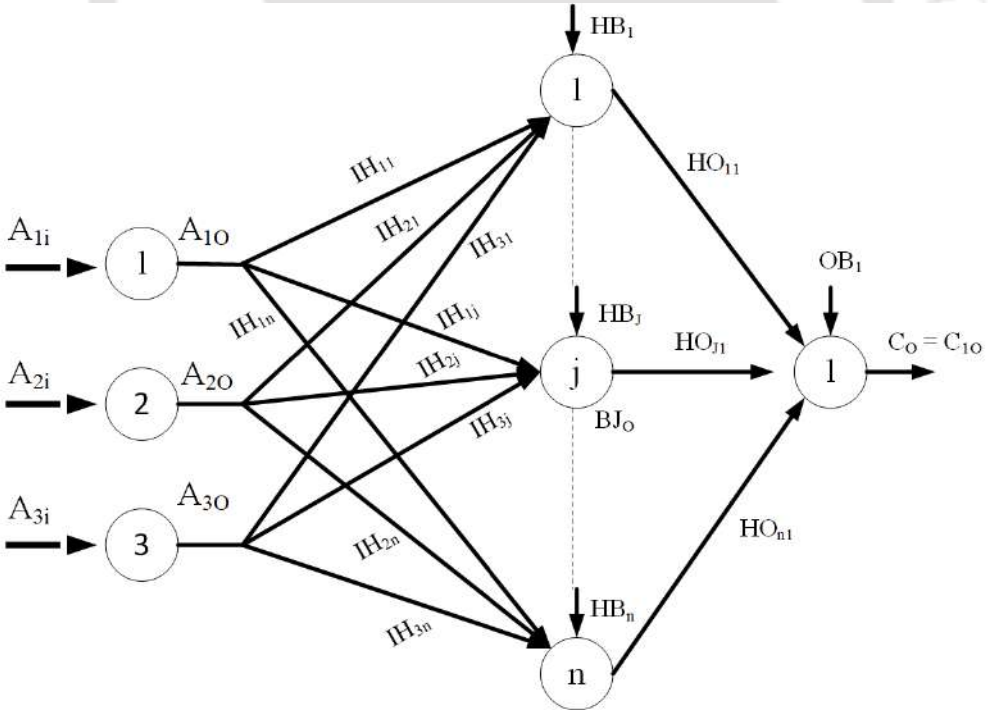

Fig. 5.18: Proposed fully-connected ANN architecture with hidden layers

$$B_{ji} = \sum_{k=1}^{3} IH_{kj} A_{ko} \tag{5.1a}$$

$$B_{jo} = F_h \left(B_{ji} + HB_j \right) \tag{5.1b}$$

$$C_{1i} = \sum_{k=1}^{n} HO_{k1} B_{ko} \tag{5.1c}$$

$$C_o = C_{1o} = F_o \left(C_{1i} + OB_1 \right) \tag{5.1d}$$

To extract the training and test data set, numerical simulations of fluid flow and heat interaction in the supercritical mini channel heat sink considering different combinations of the baffle number, baffle inclination, baffle pitch, and baffle width are rigorously conducted. During these simulations, the channel width, height, inlet velocity, inlet temperature, and operating condition are kept fixed.

5.5.2 Training of the MLFF-NN

Three input parameters (baffle inclination, baffle pitch, and baffle width) have been varied for both FM-2P and FM-3P configurations, in order to establish sufficiently large datasets for each of them. The height of the individual baffles and the operating conditions have been maintained identical over this entire set of simulations (G = 200 kg/m^{2}s, $\dot{q}''$ = 40 kW/m^2, p = 8 MPa and T_{in} = 305 K). Back-propagation (BP) algorithm is employed to train the network. Both incremental and batch modes of training are utilized for training. In the batch training mode, changes in the weights are gathered together for all the data in the training set and then each weight is updated only once for the complete training set. In the incremental (one-line) mode of training, weights are updated for each of the data in the training set. Two different cases are considered during the development of the prediction model; Case 1: baffle pair number = 2, Case 2: baffle pair number = 3. Accordingly, two different training data sets are utilized to train the network for the two cases, with each comprising of 27 training data. The two training sets prepared through numerical simulation are shown below in tables 5.3 and 5.4 respectively.

5.5.3 Testing of the MLFF-NN

It is imperative to test the performance of the trained model to assess the reliability of its prediction, and that can be realized by comparing the PEC values predicted by the MLFF-NN with the ones obtained through the computational model. Two different data

Table 5.3: Training data for Case I (Two pairs of baffles)

	θ (°)	d (mm)	W (mm)	PEC
Case I: Two pairs of baffles	90	0.5	0.20	0.81
	90	0.5	0.35	0.90
	90	0.5	0.50	1.17
	90	1.0	0.20	0.79
	90	1.0	0.35	0.83
	90	1.0	0.50	0.91
	90	1.5	0.20	0.57
	90	1.5	0.35	0.69
	90	1.5	0.50	0.69
	60	0.5	0.20	0.63
	60	0.5	0.35	0.81
	60	0.5	0.50	0.93
	60	1.0	0.20	0.62
	60	1.0	0.35	0.74
	60	1.0	0.50	0.80
	60	1.5	0.20	0.53
	60	1.5	0.35	0.63
	60	1.5	0.50	0.67
	30	0.5	0.20	0.67
	30	0.5	0.35	0.73
	30	0.5	0.50	0.82
	30	1.0	0.20	0.58
	30	1.0	0.35	0.60
	30	1.0	0.50	0.69
	30	1.5	0.20	0.50
	30	1.5	0.35	0.56
	30	1.5	0.50	0.56

sets are used to test the optimized network (to assess the prediction results generated from the developed MLFF-NN model) for the two cases (Case 1: baffle number = 2, Case 2: baffle number = 3). The configurations of the supercritical mini channel heat sink (combinations of the baffle number, baffle inclination, baffle pitch, and baffle width) considered for the test sets are completely different from those used for training sets. The performance of the supercritical mini channel heat sink (PEC as defined in Eq. 4.3) predicted by the developed CI-based MLFF-NN model against a combination of the baffle inclination, baffle pitch, and baffle width for a given baffle number, is compared with that obtained through corresponding

Table 5.4: Training data for Case II (Three pairs of baffles)

	θ (°)	d (mm)	W (mm)	PEC
Case II: Three pairs of baffles	90	0.5	0.20	1.51
	90	0.5	0.35	1.68
	90	0.5	0.50	1.73
	90	1.0	0.20	1.38
	90	1.0	0.35	1.58
	90	1.0	0.50	1.65
	90	1.5	0.20	1.10
	90	1.5	0.35	1.18
	90	1.5	0.50	1.34
	60	0.5	0.20	1.43
	60	0.5	0.35	1.56
	60	0.5	0.50	1.63
	60	1.0	0.20	1.27
	60	1.0	0.35	1.37
	60	1.0	0.50	1.46
	60	1.5	0.20	1.07
	60	1.5	0.35	1.11
	60	1.5	0.50	1.27
	30	0.5	0.20	1.35
	30	0.5	0.35	1.41
	30	0.5	0.50	1.52
	30	1.0	0.20	1.17
	30	1.0	0.35	1.26
	30	1.0	0.50	1.31
	30	1.5	0.20	1.01
	30	1.5	0.35	1.07
	30	1.5	0.50	1.15

numerical simulation. It is repeated for each test data. The two test sets prepared through numerical simulations are shown below in table 5.5.

5.5.4 Genetic algorithm (GA) tuned MLFF-NN

The connecting weights in the network are optimized through the BP algorithm. The optimal values of those connecting weights decide the proposed MLFF-NN's performance. Apart from the connecting weights, the MLFF-NN's performance also depends on the 'learning rate (L)' and 'momentum factor (M)' in the BP algorithm, hidden layer's neuron numbers (n),

Table 5.5: Test data for Cases I and II.

Configuration	θ (°)	d (mm)	W (mm)	PEC
Case I: Two pairs of baffles	85°	0.50	0.20	0.79
	65°	1.00	0.35	0.77
	55°	1.50	0.50	0.65
	35°	0.45	0.25	0.70
Case II: Three pairs of baffles	85°	0.50	0.20	1.49
	65°	1.00	0.35	1.38
	55°	1.50	0.50	1.25
	35°	0.45	0.25	1.37

the transfer function coefficient of the neurons in input (T_i), hidden (T_h), and output layers (T_o). Thus, optimization of these parameters (learning rate, momentum factor, input layer's transfer function coefficient, hidden layer's transfer function coefficient, output layer's transfer function coefficient, and hidden layer's neuron numbers) is also essentially required to optimize the prediction capability of the proposed MLFF-NN. A global optimizer inspired by the evolutionary algorithm (namely GA) is employed here to find the optimal set of the values of those parameters (learning rate, momentum factor, input layer's transfer function coefficient, hidden layer's transfer function coefficient, output layer's transfer function coefficient, and hidden layer's neuron numbers). A binary coded GA is adopted to optimize the above-mentioned six parameters. Here the optimum set of those six parameters means the combination of the values of those parameters that provides the least percentage error in prediction. The error in prediction is calculated as the difference between the results obtained through numerical simulations and that predicted by MLFF NN. The average percentage error in prediction can be calculated as given below in Eq. 5.2.

$$\text{Average percentage error in prediction} = \frac{1}{Z}\sum_{z=1}^{Z}\frac{|\,(T_o)^z - (C_o)^z\,|}{(T_o)^z} \times 100 \tag{5.2}$$

Here, Z represents the number of training or test scenarios, $(T_o)^z$ denotes the target output (numerically calculated) corresponding to the z^{th} scenario, and $(C_o)^z$ indicates the network predicted value for the same. The average percentage error in prediction of the performance of the said supercritical mini channel heat sink (PEC as defined in Eq. 4.3) is considered as the fitness value for the individual GA strings. The GA is also coded using 'C' programming language in a Linux operating system. The flow chart of the proposed hybrid modelling scheme (the GA tuned MLFF-NN with BP optimized connecting weights and GA optimized performance parameters) is shown in Fig. 5.19.

5.6 Performance Estimation of MCHS using Artificial Neural Network

A global optimizer, namely GA has been used to optimize the NN parameters (L, M, n, T_i, T_h, T_o), whereas a local optimizer (BP algorithm) has been used to optimize the connecting weights of the MLFF-NN. For each case (FM-2P and FM-3P configurations), a GA-parametric study has been conducted to fix the GA parameters (population size, generation number, tournament size, and mutation probability) values. For both configurations (FM-2P and FM-3P), the optimum values of the GA parameters obtained through the GA parametric study are 120, 130, 2, and 0.05 for the population size, generation number, tournament size, and mutation probability, respectively. A uniform crossover operator with a constant probability of 0.99 is employed for the crossover operation, and thus, it is not included in the GA parametric study. GA with the optimum set of GA parameters generates the optimum sets of NN parameters. The optimum sets of NN parameters obtained from the GA for the two different configurations of the supercritical MCHS are shown in Table 5.6. The performances of the proposed GA-tuned MLFF-NN with the BP algorithm using various configurations of the MCHS are shown in Tables 7 and 8. The predicted performances and percentage error in prediction against the test cases using the optimized MLFF-NN (using GA and BP algorithm) for the MCHS with FM-2P and FM-3P configurations are shown in Tables 5.7 and 5.8, respectively. It is also pertinent to mention here that the average percentage errors in prediction on the training datasets have been estimated to be 4.2% and 3.5% for the FM-2P and FM-3P configurations, respectively.

Tables 5.7 and 5.8 show that the MLFF-NN (optimized using GA and BP algorithm) almost accurately estimates the performances of the MCHS using different configurations. Thus, the developed GA tuned MLFF-NN with BP algorithm is able to predict the MCHS

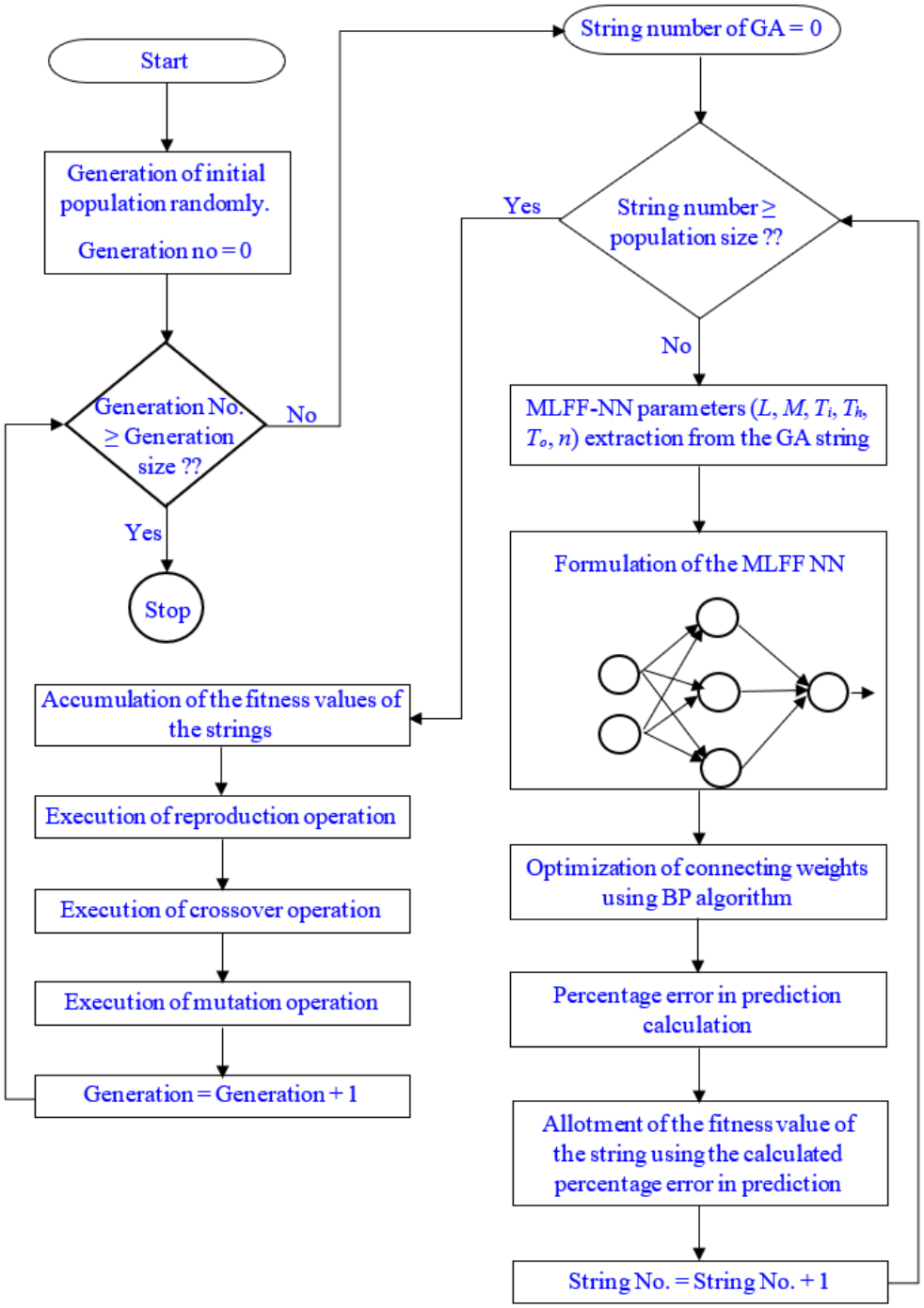

Fig. 5.19: GA tuned MLFF-NN with BP optimized connecting weights and GA optimized performance parameters

performance under different working conditions perfectly.

Table 5.6: Optimized NN parameters

NN Parameter	Values	
	FM-2P	FM-3P
L	0.1904	0.0922
M	0.4662	0.0851
T_i	1.5081	1.4205
T_h	5.4582	3.1455
T_o	3.2695	7.5055
n	17	14

5.7 Summary

Present study computationally explores the option of installing airfoil-shaped flow obstructions in a sCO_2-driven MCHS, with the simultaneous focus on enhancement in heat transfer performance and reduction in pressure drop. Four different designs have been conceived, along with the plain minichannel without any obstruction, and each of the design parameters has been varied over a wide range for all the configurations, with the aim of comprehending their individual impacts on the thermalhydraulic performance of the channel. Local and axial variations in crucial flow variables have been systematically explored, and PEC is recognized as a primary parameter for drawing conclusions. Major observations from the thermalhydraulic assessment are summarized below.

- Installation of obstructions delays the appearance of HTD by maintaining a high level of area-averaged HTC over the segment with airfoils, consequently raising the average HTC of the channel. Acceleration of sCO_2 around the obstructions owing to the compression of the streamlines, and consequent intensification in the level of turbulence can be earmarked as the key factors in enhancing HTC.

- Introduction of any obstruction inflicts upsurge in pressure losses. Accordingly, favorable PEC is feasible only for a limited range of Re_{in} for FM-1P and FM-2P channels, whereas incorporation of more than two pairs of obstructions consistently yields encouraging levels of PEC. The gain, however, is not significant for more than three pairs.

- Increase in the distance between the adjacent obstructions offers the promising situation of improvement in average HTC and reduction in pressure losses, accordingly

Table 5.7: Performance of the developed prediction model (GA tuned MLFF-NN) to forecast the performance (PEC) of the supercritical MCHS with FM-2P configuration (Case 1).

Case 1	Input			Targeted output	Forcasted output	Prediction (%) error
MCHS with FM-3P configuration	θ (°)	d (mm)	W (mm)	Targeted PEC	Forcasted PEC	
	85	0.50	0.20	0.79	0.763	3.412
	65	1.00	0.35	0.77	0.768	0.263
	55	1.50	0.50	0.65	0.348	0.384
	35	0.45	0.25	0.70	0.763	3.412
The average error in prediction (%) 1.033						

Table 5.8: Performance of the developed prediction model (GA tuned MLFF-NN) to forecast the performance (PEC) of the supercritical MCHS with FM-3P configuration (Case II).

Case 1	Input			Targeted output	Forcasted output	Prediction (%) error
MCHS with FM-3P configuration	θ (°)	d (mm)	W (mm)	Targeted PEC	Forcasted PEC	
	85	0.5	0.2	1.490	1.488	0.163
	65	1.00	0.35	1.380	1.390	0.706
	55	1.50	0.50	1.250	1.255	0.371
	35	0.45	0.25	1.370	1.389	1.419
The average error in prediction (%)						0.665

enhancing PEC. Weakening of turbulence intensity interior to the vortices generated in the gap between the neighboring airfoils, though, results in considerable oscillation in α_z.

- Enhancement in PEC has been observed with widening of the individual airfoils and orientation close to vertical.

The above conclusions provide quite comprehensive design guidelines about MCHS with airfoil-shaped obstructions, and it can definitely be contemplated as an expedient option to ensure improved thermalhydraulic characteristics. Corresponding dataset has also been employed to train a GA-tuned MLFF-NN algorithm, capable of forecasting the performance of MCHS based on PEC. Separate training datasets, comprising of 27 individual cases, have been prepared for FM-2P and FM-3P channels, while also identifying several test cases to gauge the capability of the tool. Satisfactory level of performance has been obtained for all the considered cases, highlighting the utility of such an algorithm in presaging the most desirable design of sCO_2-coupled MCHS. Present work can now be extended to include other supercritical fluids and also other possible designs of the obstructions, to expand the knowledge base on supercritical heat sinks and promote industrial applications in near future.

Chapter 6

Experimental investigation of MCHS with supercritical carbon dioxide using Infrared thermography

6.1 Preamble

Over the last decades, numerous experimental and theoretical studies on supercritical fluids have been conducted in response to design requirements for industrial systems such as heat pumps, cryogenic engines, nuclear power plants, or extraction processes. The ongoing and expanding interest derives from the fundamental issues that need to be resolved for the numerous practical systems that use supercritical fluids. Due to their relatively small size and great efficiency, power systems based on the supercritical CO_2 cycle have gained attention as a result of technological advancements.

Recently researchers have been interested in exploring thermalhydraulic characteristics of supercritical carbon dioxide in minichannel owning to high surface area-to-volume ratio, which leads to higher heat transfer performance. For the design and optimization of a gas cooler and internal heat exchanger, the supercritical CO_2 cooling in tubes' heat transfer and pressure drop properties are crucial. In recent decades, a number of experiments have been carried out to study the heat transfer of sCO_2 under various conditions. Duffy and Pioro [223] conducted a review on experimental heat transfer of sCO_2, and summarized the heat transfer into three modes, i.e., normal, deteriorated and improved heat transfer. Rao *et al.* [224] discussed the flow behaviour and heat transfer of sCO_2 in various channels. The effects of tube diameter, heat flux, mass flux, pressure and inlet temperature on convection

heat transfer characteristics of sCO_2 were focused. Cabeza *et al.* [225] summarized the heat transfer characteristics of sCO_2 in heat exchangers for different applications. Ehsan *et al.* [226] discussed the heat transfer characteristics of sCO_2 under both heating and cooling conditions, and presented possible reasons for heat transfer deterioration.

An extensive literature review suggested that the existing correlations for convective heat transfer did not exhibit sufficient agreement with experiments, except under extremely specific circumstances, to warrant their use. Therefore, before being used in a real engineering application, every suggested correlation should be thoroughly examined for the particular flow state. To accurately comprehend the thermal and hydraulic characteristics of the supercritical fluids under various situations, more experimental research is necessary. The understanding of fundamental events in mass and energy transport in supercritical fluids is still quite incomplete in spite of this considerable research. Most of the available literature investigated minichannel in vertical flow conditions subjected to cooling. Therefore, the present work focuses on foreshortening this specific gap and extending the available understanding to minichannel under heating conditions. The present study experimentally investigates the heat transfer behaviour of supercritical carbon dioxide (sCO_2) in horizontal minichannel with an outer diameter 3.175 mm and inner diameter 1.575 mm for various heat fluxes, mass fluxes, operating pressure, and inlet temperature.

6.2 Materials and methods

6.2.1 Experimental setup

To study the thermalhydraulics of sCO_2 under the influence of a constant wall heat flux, an experimental set up is fabricated, schematic of which is depicted in Fig. 6.1. The experimental test-loop was initially made vacuum to remove air which was present in the experimental loop. After that, the loop was charged directly with CO_2 from the CO_2 cylinder tank available at a pressure of 6.5 MPa. Liquid CO_2 was accumulated in a accumulator, and a constant-flow pump was used to drive the fluid into the test loop. The system operating pressure above the critical pressure was achieved by using the high-pressure N_2 cylinder tank (12 MPa), which pressurized the experimental loop above the critical point. To avoid entering of the N_2 gas in the experimental loop, the N_2 cylinder was not directly connected to the experimental loop and it was connected through an accumulator that was directly connected to the experimental loop and contained CO_2.

Fig. 6.1b demonstrates the detailed arrangement of the test section. The test section

was a horizontal mini circular tube. The test section is a horizontal 500 mm long, stainless steel tube with heating length of 300 mm and two 100 mm long adiabatic sections before and after the heating section so that thermally developed flow can be established in some parts of the heated domain of the tube. The material of the tube was 316 L stainless steel with the inner diameter of the channel is 1.175 mm and outer diameter 3.175 mm. The test section was directly heated by DC power source, and the effective heated length was 300 mm.

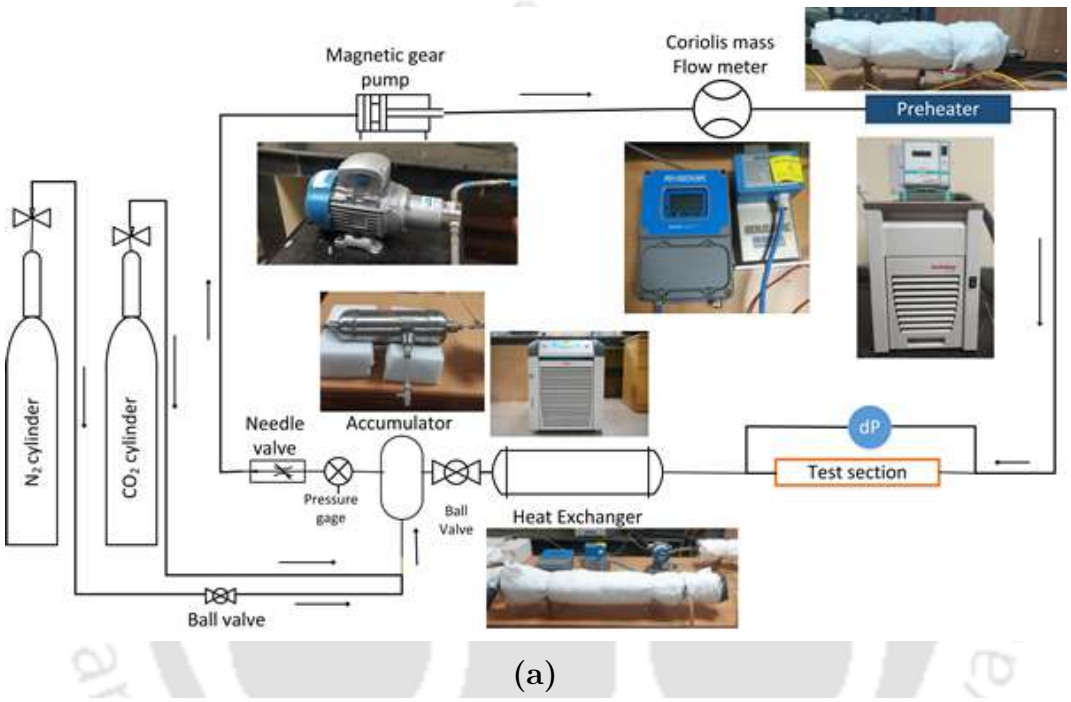

(a)

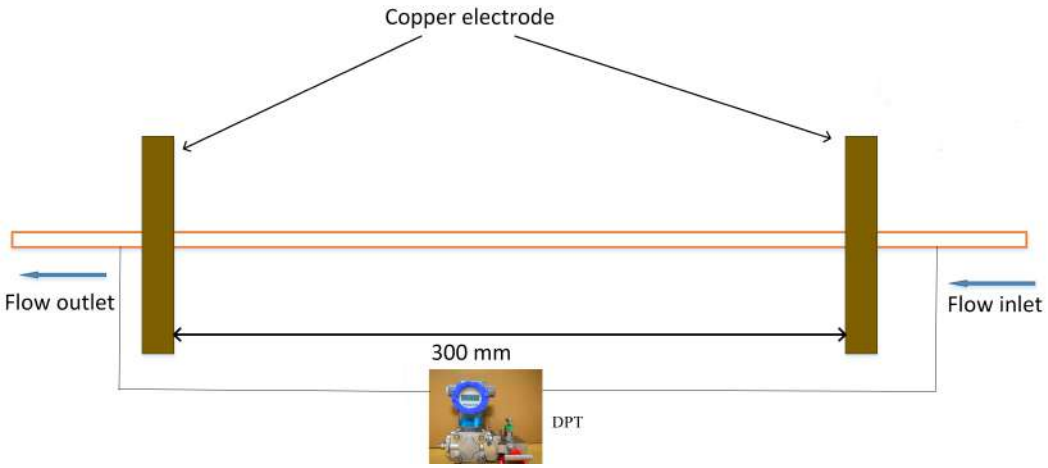

(b)

Fig. 6.1: Schematic of (a) experimental loop and (b) test section

6.2.2 Parameter measurement

The present experiments were carried out in the range of pressure p = 7.5–9 MPa, heat flux $\dot{q}'' = 10$–30 kW/m^2, mass flux G = 300–500 kg/m^{2}s, inlet temperature T_{in} = 28-35 $°C$. The wall temperature measurement of the test section was performed using an infrared thermal imaging camera (FLIR A655sc) to capture continuous wall temperature variation in the axial direction. In addition, the test section's outside wall was painted black (thermal conductivity, $k = 0.15$ W/mk and emissivity, $\epsilon = 0.98$), which was done to get the values as close to unity as possible so that the IR camera could measure the wall temperature with accuracy. Prior to detecting the actual wall temperature, the outer coated surface's emissivity was corrected by measuring the coated surface's temperature separately. To reduce the interference from nearby radiation, all experiments were carried out in a dark room. The heated length of 500 mm was the focal point of the infrared camera (640 pixels per 500 mm). 0.015 mm per pixel in the axial direction and 0.2 mm per pixel in the transverse direction were found to be the spatial resolution. When there was a consistent wall heat flux, wall temperatures were measured once they had stabilised. The input and outlet temperatures are measured using two K-type thermocouples with 0.1 mm beads. The output temperature is recorded in an insulated chamber. The thermocouple bead is put into the chamber at the outflow such that it stays submerged in the flow. Data acquisition cards (Temperature module NI 9212) and the software suite NI LabView 2017 are used to record temperature values. The sheathed thermocouple had an accuracy of ±0.5% and a response time of less than 0.4 s.

A magnetic drive gear pump (M-25 series) which is installed in this loop, precisely controlled the mass flow rate. The flow rate of working fluid was controlled by VFD (variable frequency drive), which controlled the rotational speed (rpm) of the magnetic gear pump that causes the mass flow rate to vary. The mass flow rate was measured using a Coriolis mass flow meter (Rheonik RHM05 model), which has a measurement range from 0.00125 to 0.003 kg/s with an accuracy of 0.01%. Uniform wall heat flux condition is maintained by using Joule heating with a DC power supply of power rating of 0-32 V and 0-30 A (Make: Aplab). Digital Multimeter (accuracy ± 0.1 V and ± 0.01 A) has been incorporated with the DC source to measure the electrical power input to the SS tube.

The uncertainty of experimental parameters were analysed using the approach in Moffat [227] and has been discussed in Appendix A.

6.2.3 Data reduction

The temporal and spatial data obtained with the help of IR camera is used to calculate the averaged Nusselt number. The local Nusselt number along the flow direction is calculated as:

$$Q_{in} = V.I - Q_l \tag{6.1}$$

$$\overline{h} = \frac{\dot{q}''}{T_w - T_b} \tag{6.2}$$

$$\overline{Nu} = \frac{\overline{h}d}{k_b} \tag{6.3}$$

where $\dot{q}'' = Q_{in}/(\pi dl)$, is the wall heat flux along the flow direction, V is the potential drop across the heated length and I is the current supplied, and l is the length of the heated zone. The heat that the heated SS tube dissipates into the surrounding air is called Ql. This is independently calculated by running dry tube heat transfer experiments. When heat is applied to an SS tube in dry condition, that is, when no fluid is flowing inside the tube, at steady state, the applied heat will be equal to the heat lost to the environment. By repeating these experiments for different heat input, a calibration curve for heat lost and surface temperature has been obtained. This calibration allowed for the identification of the heat input in the actual experiments.

The mass flux G is calculated as:

$$G = \frac{\dot{m}}{A} = \frac{4\dot{m}}{\pi d_i^2} \tag{6.4}$$

According to heat balance, the local fluid enthalpy H_b at certain section can be obtained:

$$H_b = H_{b,in} + \frac{z(H_{b,out} - H_{b,in})}{L} \tag{6.5}$$

where z is the axial distance from the inlet section, and $H_{b,in}$ is the fluid enthalpy at inlet section. Then, the local fluid temperature T_b at axial position z is acquired from the REFPROP program by inputting the parameters of enthalpy and pressure.

The heat transfer coefficient observed in the current experiment are compared with data measured in Dittus-Boelter correlation to validate our experimental apparatus. The comparison of experimental results with the predictions from the Dittus-Boelter correlation as

shown in Fig. 6.2 for $\dot{q}'' = 19$ kW/m^2, $G = 450$ kg/m^{2}s, $T_{in} = 30$ °C, and $p = 9$ MPa. While the qualitative trend is reasonably similar, the values are noticeably over-predicted near the pseudocritical region, with the largest difference of 12.24%. The predictions are much closer for in the downstream locations.

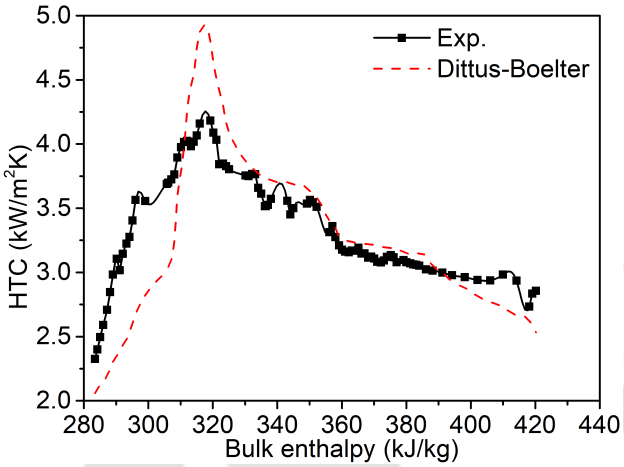

Fig. 6.2: Validation of experimental data with Dittus-Boelter correlation for $\dot{q}'' = 19$ kW/m^2, $G = 450$ kg/m^{2}s, $T_{in} = 30$ si°C, and $p = 9$ MPa.

6.3 Result and Discussion

In order to investigate the parametric effect on the heat transfer of sCO$_2$ under different working conditions, the experiments were performed at different levels of heat fluxes (15, 19, 25 and 29 kW/m^2), mass fluxes (300, 400 and 500 kg/m^{2}s), pressures (7.5, 8, 8.5 and 9 MPa) and inlet temperatures (28, 30 snd 32 °C).

6.3.1 Effect of wall heat flux

The fluctuations in heat transfer coefficient with the bulk fluid enthalpy under various heat fluxes under pressure of 7.5 MPa and mass flow of 400 kg/m^{2}s are shown in Fig. 6.3. It is abundantly obvious that when heat flux increases, heat transfer weakens. According to the simulation results, which are shown in Fig. 3.9, HTC decreases at increased heat flux, which is consistent with the present experimental findings. Increased wall heat flux results in a steeper axial temperature gradient and an earlier arrival at the pseudocritical point, which mitigates the effects of increased c_p around that point. As a result, the flow is divided into a liquid-like regime in the core and a gas-like regime close to the channel wall.

However, the low-density layer's thickness varies significantly at each axial site, leading to a significant divergence in the temperature profiles under consideration. These inversions become more noticeable at increasing heat fluxes, highlighting the importance of the axial temperature gradient, which has a significant impact on the type of thermal asymmetry. As heat flow increases, more vapor-like fluid is applied to the hot wall surface, raising heat transfer resistance and decreasing heat transfer coefficient.

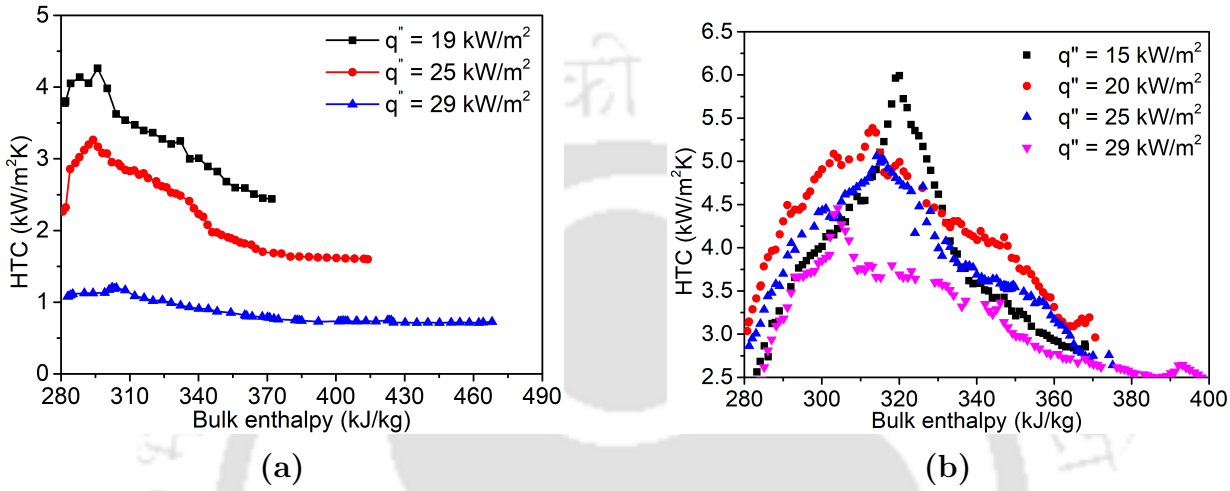

Fig. 6.3: Axial variation in area-averaged heat transfer coefficient with heat flux at $p = 8$ MPa, $T_{in} = 30°$C (a) $G = 300$ kg/m^{2}s (b) $G = 450$ kg/m^{2}s

6.3.2 Effect of mass flux

Fig. 6.4 for two different operating pressures illustrates how mass flux affects heat transport characteristics. No matter the power level, higher mass flux results in higher HTC. Greater Reynolds number is produced by higher flow rates, and as a result, the intensity of the turbulent flow increases. As a result, there is an increase in cross-motion randomness and augmented turbulent mixing, which eventually results in more interaction and magnified HTC. The peak of HTC shifts downstream for increasing mass fluxes, which is an interesting observation. As discussed in the Fig. 3.14 , the simulation results reveal that augmentation of HTC occurs at higher mass flux, which is consistent with the present experimental findings. With T_{in} remaining constant, the system needs more heating time to reach pseudocritical point, delaying peak HTC, albeit by a sizeably larger amount. In damaged regions, HTC can be enhanced by increasing mass flux, as the difference between near-wall and bulk fluids decreases with greater mass fluxes. Increased mass flux causes the carbon dioxide fluid's

boundary layer to become thinner and the thickness of the low-conductivity fluid near the hot wall to decrease, both of which are advantageous for the convection of sCO_2.

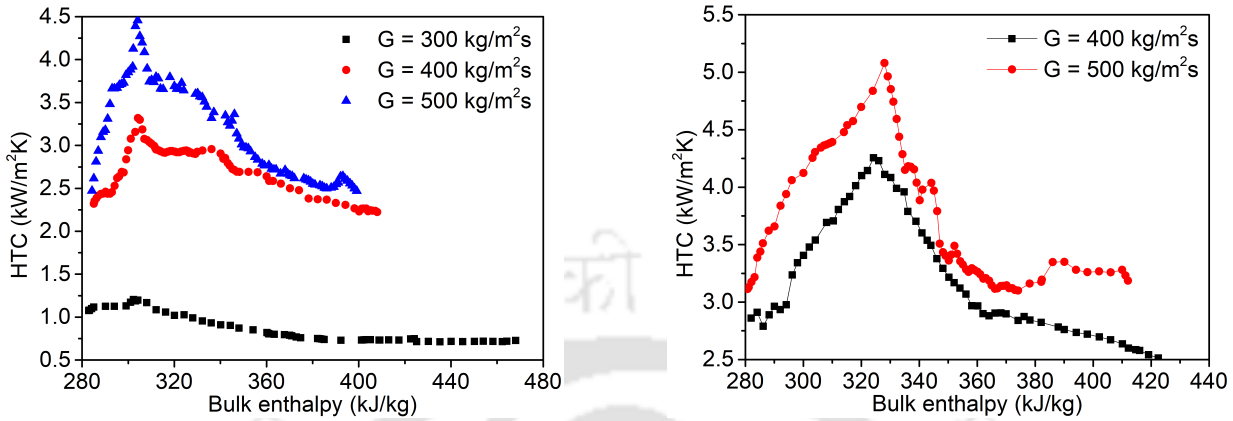

Fig. 6.4: Axial variation in average heat transfer coefficient for different mass fluxes: $\dot{q}'' = 29$ kW/m^2, $T_{in} = 30$ °C (a) $p = 8$ MPa (b) $p = 8.5$ MPa

Table 6.1: Variation in pressure drop with mass flux of sCO_2

Mass flux (kg/m^{2}s)	**Pressure drop** (kPa)
300	0.868
400	1.451
500	1.980

6.3.3 Effect of operating pressure

The role of operating pressure can be apprised at this precise context by following Fig. 6.5. Because the heat capacity of a fluid is significantly dependent on pressure, prior studies have shown that the pressure influence on heat transfer of sCO2 is considerable at low heat flux conditions. As a result, the current experimental findings are consistent with the earlier findings. When illustrated in 1.2, the dramatic nature of property fluctuation also significantly lessens as the pressure of supercritical fluid diverges away from the critical point. That is seen by the significant decline in HTC with an increase in system pressure while the trend is constant. As discussed in the Fig. 3.13 , the simulation results shows that HTC reduces at higher operating pressure, which is coherent with the present experimental results.

A similar observation was also made by Liao and Zhao [9] under the operating conditions shown in Fig. 6.5, where heat transfer degradation occurs under all pressures due to the substantial heating effect and wall temperatures are much higher than the pseudo critical values. At larger heat fluxes, the impact of a change in system pressure is significantly less noticeable because pseudocritical point is reached earlier and there is less asymmetry in the flow domain as a result. Because the temperature of the wall is much higher than the pseudocritical point, the thermophysical characteristics of near-wall fluids are relatively similar at various pressures. The difference between the hot wall and bulk fluids is therefore minimal. It is also reasonable to infer that pressure has less of an effect on HTC than does heat flux.

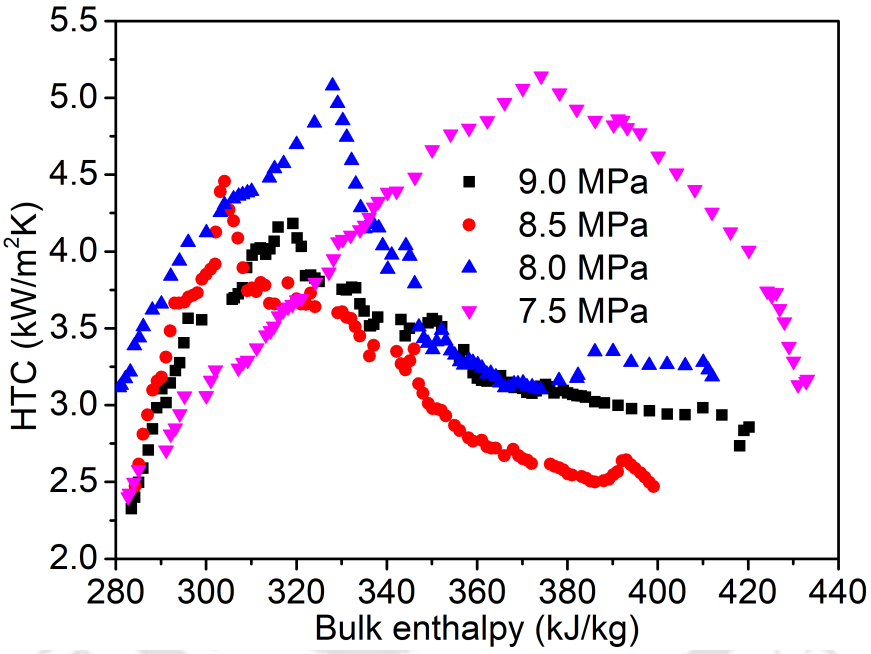

Fig. 6.5: Variation in average heat transfer coefficient with bulk enthalpy for different combinations of pressure and heat flux at $G = 450$ kg/m^{2}s

6.3.4 Effect of inlet temperature

Heat transfer variation due to different fluid inlet temperature is depicted in Fig. 6.6. As inlet temperature increases, heat transfer coefficient magnitude decreases because isobaric specific heat and thermal conductivity decreases with inlet temperature. With increase in inlet peak value of heat transfer shifted towards upstream direction. The simulation results shows that HTC reduces at higher operating pressure, which is coherent with the present

experimental results. Also, as inlet temperature becomes much higher than pseudocritical temperature, peak in heat transfer coefficient vanishes because thermophysical properties variation far away from pseudocritical point becomes less significant and value of specific heat decreases.

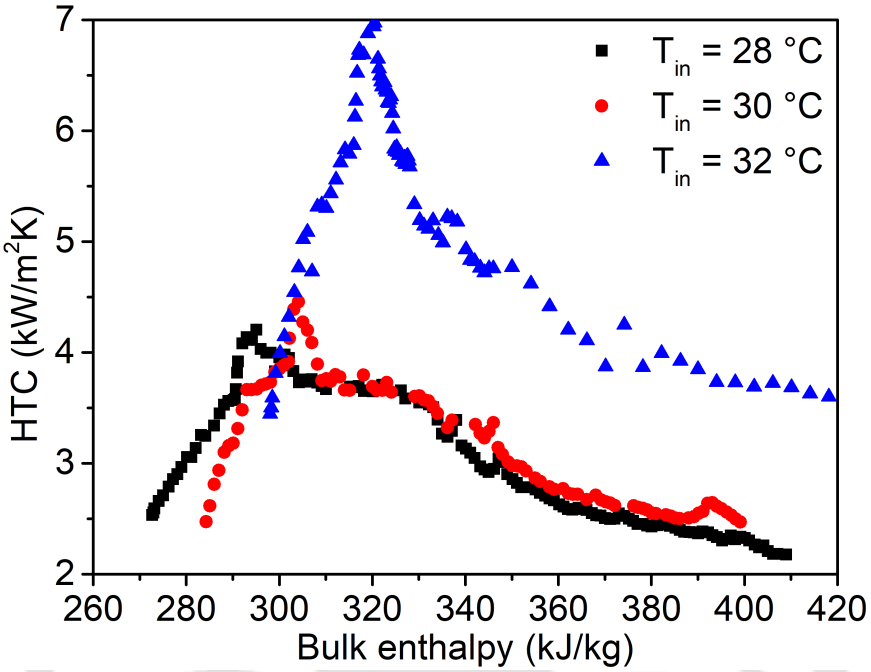

Fig. 6.6: Variation in average heat transfer coefficient with bulk enthalpy for different inlet temperature at $\dot{q}'' = 29$ kW/m^2, $G = 450$ kg/m^{2}s and $p = 8$ MPa

6.4 Numerical Methods

6.4.1 Physical geometry

As mentioned above, present study explores the thermalhydraulic of sCO_2 flow through a heated horizontal minichannel. Corresponding schematic representation is shown in Fig. 6.7. A computational domain of 500 mm length with inner and outer diameter as 1.175 mm and 3.175 mm, respectively is selected, where an adiabatic section of length 100 mm is provided for flow to be fully developed before entering the heated section. No-slip walls and uniform wall heat flux in the heated area have also been imposed, coupled with specified mass flux input and constant outlet pressure boundary conditions.

Steady-state versions of the mass, momentum and energy conservation equations in

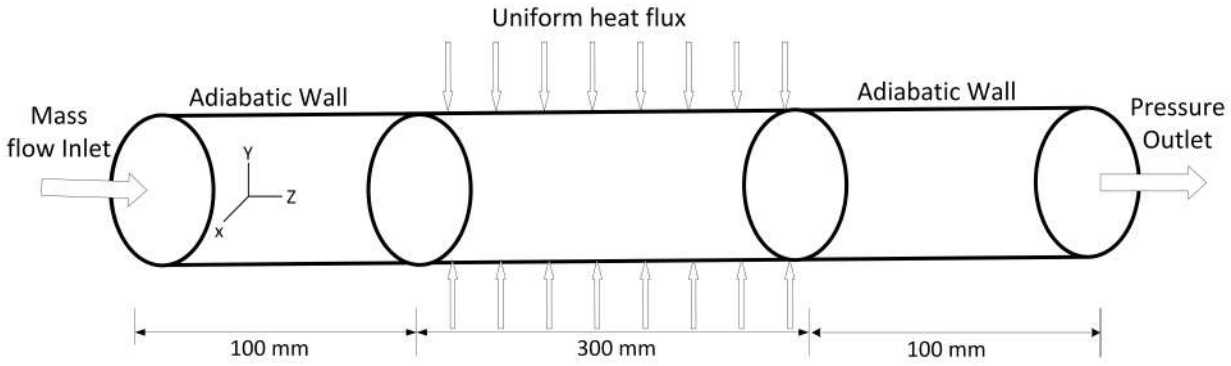

Fig. 6.7: Schematic of the computational domain under consideration

Cartesian coordinate are adopted in the present study, which has been discussed in Chapter 2.

The conservation equations have been solved following the finite-volume approach of ANSYS-Fluent and has been discussed in Chapter 2.

6.4.2 Mesh-independency study and validation

The meshing methodology is discussed in details in Chapter 2. Four different structures are tested in order to remove the mesh dependence of the solution, and the corresponding values of bulk temperature near the outlet, rise in bulk temperature of the fluid during its passage through the heated section, and pressure drop across the channel are presented in Table 6.2. It is evident that increasing the number of elements from mesh 3 to mesh 4 yields about 1.19% change in the temperature differential and 2.61% difference in pressure drop, both of which can be considered to be negligible. The mesh system must be reliable enough to effectively simulate the steep temperature and velocity gradients that are anticipated close to the wall. Therefore, mesh 3 is continued with for all the simulations reported below.

Table 6.2: Details of various mesh systems employed

Mesh structure	**Number of elements**	**Bulk temperature near outlet** (K)	**Rise in bulk temperature** (K)	**Pressure drop** (kPa)
Mesh 1	236538	311.13	8.13	1.605
Mesh 2	482364	310.84	7.84	1.501
Mesh 3	751835	310.52	7.52	1.451
Mesh 4	842356	310.61	7.61	1.413

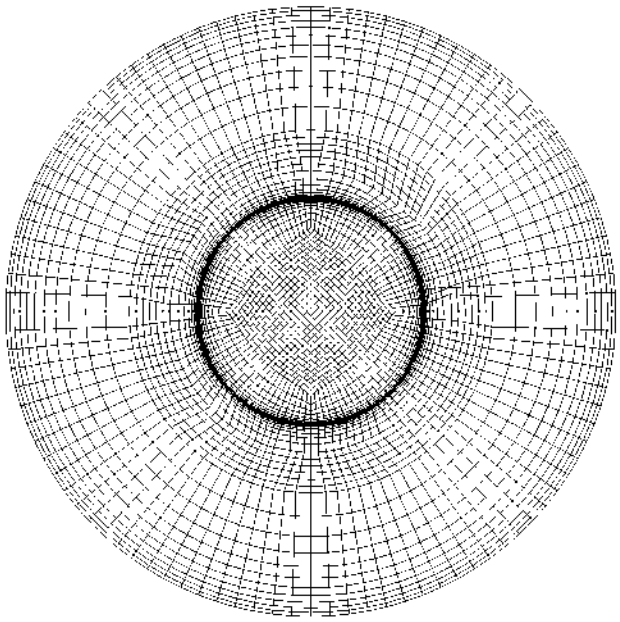

Fig. 6.8: Cross sectional view of the adopted mesh structure

6.4.3 Comparison of of experimental result with Numerical data

The present experimental results are further compared with the numerical results as shown in Fig. 6.9 for the heat transfer of sCO_2. These experimental results demonstrate the effectiveness of the measurement and data processing methods used in the current investigation, particularly the IR Thermography (IRT). The simplified method used to get the experimental results, where the bulk enthalpy was determined using just energy balance and calculated values for the outer wall temperature, can be blamed for the difference around the peak in heat transfer coefficient (HTC). A good agreement of the experimental results with the uncertainty $\pm 7\%$ has been found with the correlation, whereas the largest difference between experimental observation and numerical observation is about 7.69%.

6.5 Summary

In this study, the heat transfer of sCO_2 is experimentally investigated in a horizontal circular mini tube for sCO_2 heat exchanger applications. The heat transfer characteristics of sCO_2 under the conditions of low q/G are obtained. The major conclusions of this study are summarized as follows:

- The comparison of experimental data with simulated results showed similar qualitative

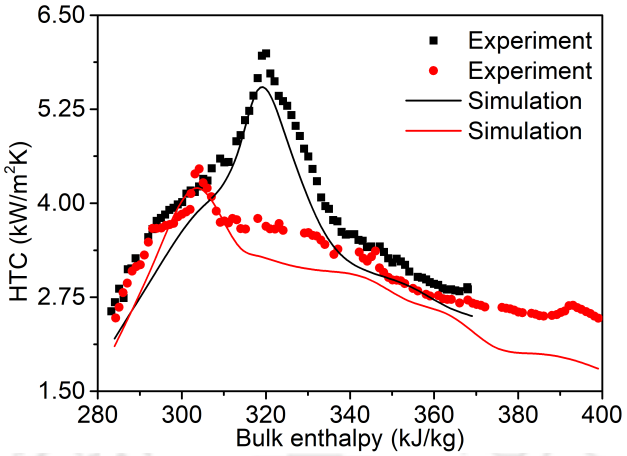

Fig. 6.9: Comparison of experimental data (hollow curve) with simulation results(solid curve) at (a) black curve $\dot{q}^{''} = 15$ kW/m^2, $G = 450$ kg/m^{2}s and $p = 8$ MPa and $T_{in} = 30$ °C (b) red curve $\dot{q}^{''} = 29$ kW/m^2, $G = 450$ kg/m^{2}s and $p = 8$ MPa and $T_{in} = 30$ °C.

trend with largest deviation of 7.69% which is very near the uncertainty value of ± 7%.

- Increasing mass flux resulted in elevated HTC for all heat flux and the peak of the HTC shifts downstream for high mass fluxes. With inlet temperature remaining the same, system requires longer heating length to attain pseudocritical point, resulting in the delay in peak HTC, albeit with substantially increased magnitude.

- As the inlet temperature increases much higher than pseudocritical temperature at a fixed pressure, peak in heat transfer coefficient vanishes because thermophysical properties variation far away from pseudocritical point becomes less significant and value of specific heat decreases.

- Impact of change in system pressure is much less apparent at higher heat fluxes, owing to the early attainment of pseudocritical temperature and consequent lesser degree of asymmetry within the flow domain. It is also safe to conclude that the heat flux has a more assertive impact on HTC compared to pressure.

Chapter 7

Transient analysis of supercritical MCHS

7.1 Preamble

High heat flux thermal management techniques are crucial components of various engineering systems such as micro-electrical engineering and solar thermal power production. In recent years, supercritical carbon dioxide has been explored as a working fluid in power cycles and heat pump systems. The thermophysical properties variation of sCO_2 near the pseudocritical point make it a potentially appealing fluid for the thermal management of high heat fluxes ($\geq$ 100 kW/m^2) in microchannel geometries [141, 219]. The non-linear properties variation of supercritical fluids causes coupling process of thermal relaxation and mechanical disturbance/instability. However, the above mentioned literature focused on the steady state aspect of the supercritical CO_2 heat transfer process. A few of the experimental study have shown that thermal fluctuations is possible in convective heat transfer of supercritical fluids. Different oscillations modes, such as thermoacoustic and thermal-induced flow oscillations, have been clearly induced.

Owning to the incomprehensive investigation of supercritical heat transfer in a microchannel under transient flow conditions, the present study is an attempt to abridge this specific gap by quantifying the thermalhydraulic characteristics of sCO_2 in a horizontal microchannel under transient heat flux boundary condition. This study numerically investigates the transient response of sCO_2. The 2D minichannel having width 300 μm and length 10 mm is considered in the current study. The influence of time period, heat flux amplitude, mass flux, and operating pressure on thermalhydraulics of sCO_2 have been comprehensively in-

vestigated.

7.2 Computational Model Development

7.2.1 Physical geometry and Boundary conditions

The transient heat transfer of sCO_2 in a 2D channel, as shown in Fig. 7.1, is numerically investigated at supercritical pressures. The total length of the cooling tube is 10 mm, and its diameter is 0.3 mm. To ensure a fully developed flow before heat transfer begins and to prevent the impact of flow oscillations on inlet boundary conditions, a 3 mm entrance section is thermally insulated. An end section of 7 mm in length is heated with a non-uniform wall heat flux. In the current fundamental investigations, standard boundary conditions are applied; constant fluid temperature and mass flow rate are defined at the tube inlet, and constant pressure is defined at the tube outlet. The fluid flow of sCO_2 is initially permitted to stabilise in the current experiments with a uniform wall heat flux at the heated portion. The heated area is then immediately subjected to an unstable wall heat flux, which initiates a momentary fluid flow and heat transfer process. The user-defined function that implements the unsteady heat flux is given as follows:

$$q_w^{"} = q^{"} + Asin\left(\frac{2\pi t}{T_d}\right) \tag{7.1}$$

where, A is the amplitude , t is flow time, T_d is time period of oscillation.

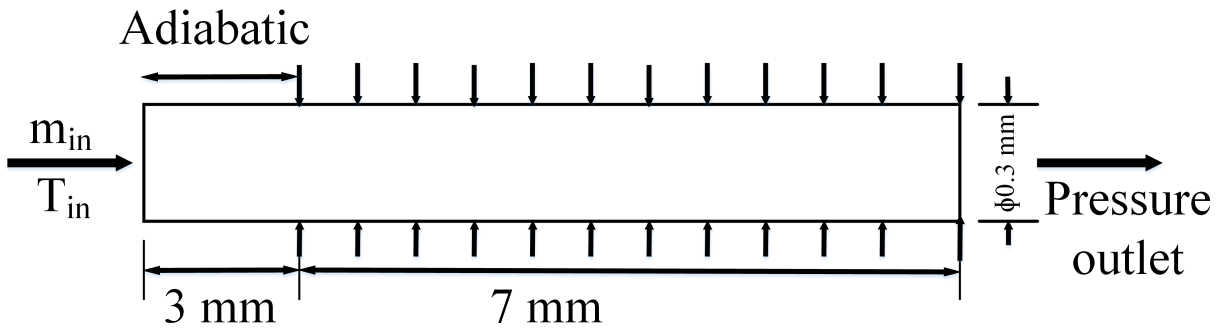

Fig. 7.1: Schematic of 2D minichannel with imposed boundary condition

Table 7.1: Details of boundary condition parameters in the present study

Parameter	Values
Heat flux (q")	100 - 300 kW/m^2
Mass flux (G)	300 - 450 kg/m^{2}s
Pressure (p)	8 - 8.5 MPa
Inlet temperature (T$_{in}$)	305 K
Time period (T$_d$)	1 - 3 ms

7.2.2 Governing equations

Steady-state versions of the mass, momentum and energy conservation equations in Cartesian coordinate are adopted in the present study, which are summarized below.

$$\frac{\partial \rho}{\partial t} + \nabla \cdot (\rho \mathbf{w}) = 0 \tag{7.2}$$

$$\frac{\partial (\rho \mathbf{w})}{\partial t} + \nabla \cdot (\rho \mathbf{w}\mathbf{w}) = -\nabla p + \nabla \cdot \bar{\bar{\tau}} + \rho \mathbf{g} \tag{7.3}$$

$$\frac{\partial}{\partial t}(\rho h) + \nabla \cdot (\rho \mathbf{w} h) = \nabla \cdot (k \nabla T) \tag{7.4}$$

where, $\mu_{eff} = \mu + \mu_t$ is the effective viscosity, with μ as the dynamic viscosity and μ_t as the turbulent viscosity, and $\Psi = \sigma_{ij}\left(\frac{\partial u_i}{\partial x_j}\right)$ is the dissipation function, with σ_{ij} being the stress tensor.

The Shear Stress Transport $\kappa - \omega$ (SST $\kappa - \omega$) turbulent model is used to study the turbulent behavior. The reason behind using SST $\kappa - \omega$ lies in its dual advantage of employing $\kappa - \epsilon$ in the near-wall region and precise calculation of $\kappa - \omega$ in the bulk flow domain.

7.2.3 Numerical scheme

In the present study, the governing equations (Eq. 7.2 - 7.4) subjected to the boundary conditions are solved using finite volume approach. The pressure and velocity terms are coupled using the pressure-implicit with splitting of operators (PISO) technique. The PISO technique has already been proven to be effective for the study of both normal and acoustic time scales [228–230]. The second order upwind method discretizes the momentum and energy terms in the transport equation and uses upstream values and gradients to determine the control volume face values. To encounter the nonlinear temperature and pressure dependence

of the relevant transport properties, NIST Standard Reference Database 23 (REFPROP) version 9 [176] is used, thus rendering relatively precise qualitative predictions [231, 232]. The solutions are assumed to be converged when following criteria are satisfied for the flow variables:

$$|\frac{\phi^{n+1}-\phi^n}{\phi^n}| \leq 10^{-3} \text{ where } \phi \equiv u,\ v,\ w,\ \kappa \text{ and } \omega$$

$$|\frac{\phi^{n+1}-\phi^n}{\phi^n}| \leq 10^{-6} \text{ where } \phi \equiv T$$

7.2.4 Mesh-independency study

For mesh-independent results and accurate resolution of the flow behaviour in the steep gradient sections, non-uniform mesh is utilised in the simulation at hand, with finer meshes used near the wall and in some internal locations. The $y+$ value for the SST $\kappa-\omega$ turbulent model should fall within one [186]. With a total of 11 layers, each with a thickness of 0.0002 mm, the inflation method is utilised to assure that. Four different structures are evaluated in order to remove the mesh dependence of the solution, and the related changes in heat transfer coefficient and wall shear stress are shown in Fig. 7.3. It is clear that going from mesh 3 to mesh 4 results in a decrease of the heat transfer coefficient of less than 2% and a decrease of the wall shear stress of less than 6.5%. Thus, mesh 3 is continued for the entirety of the simulations detailed below.

The fixed time step is appropriately evaluated as the initial setting for the current simulation, which uses a transient computation method. The specific time step size Δt is determined using the generic Courant-Friedrich-Levy (CFL) criterion in order to accurately represent the transient oscillations in the entire field which is expressed as

$$\frac{u\Delta t}{\Delta x} < 1 \tag{7.5}$$

where u and Δx are the velocity scale and mesh element length scale, respectively. The u is determined by the inlet axial velocity. Further, time independent study is study is conducted for three different time step size as shown in Fig. 7.4. Thus, the calculated time step size is $3.5 \times 10^{-}5$ s.

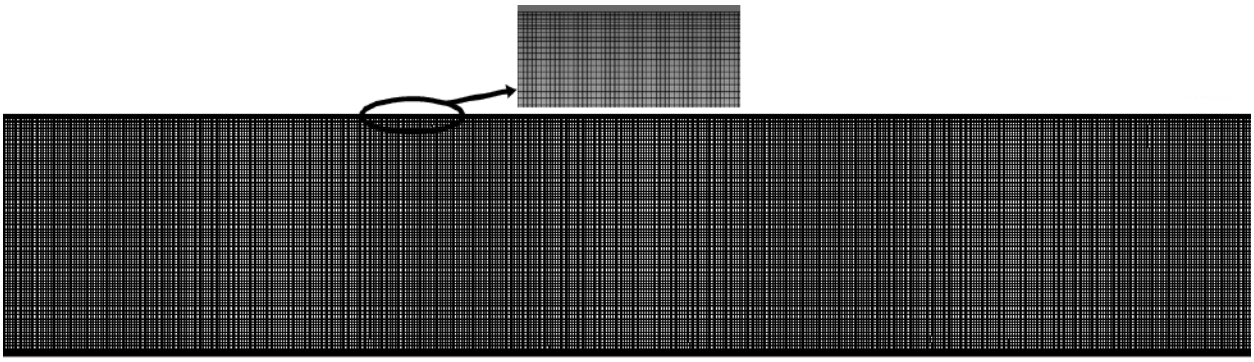

Fig. 7.2: Cross-sectional view of the adopted mesh structure

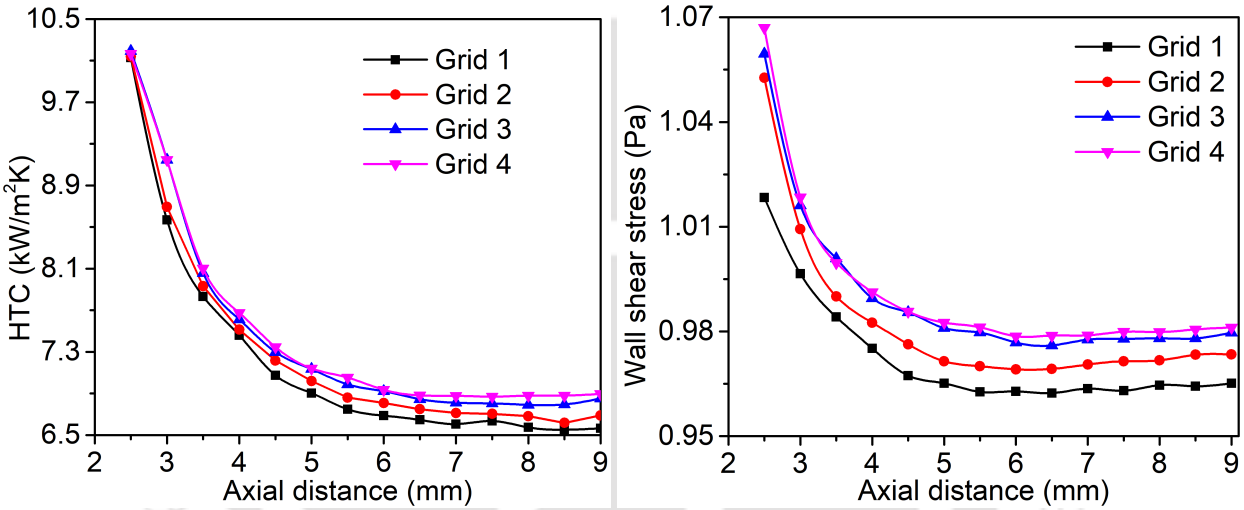

Fig. 7.3: Grid independent study for the chosen grid size

7.3 Results and Discussion

7.3.1 Local behaviors of parameter

Fig. 7.5 shows the transient variation of mass flow rate for different time period of oscillation. It is interesting to note that the mass flow rate variation does not depend on the time period and it reaches to the dynamic steady state at around 10 ms. The evolution of velocity perpendicular to the flow direction at x/L = 0.5 is shown in Fig. 7.6. Although the velocity fluctuation is not periodic it fluctuates with time and distortion in velocity profile can be clearly seen. The figure also depicts symmetric bilateral expansion process with extreme perturbation near the wall region. Similar observation was also reported in the study by

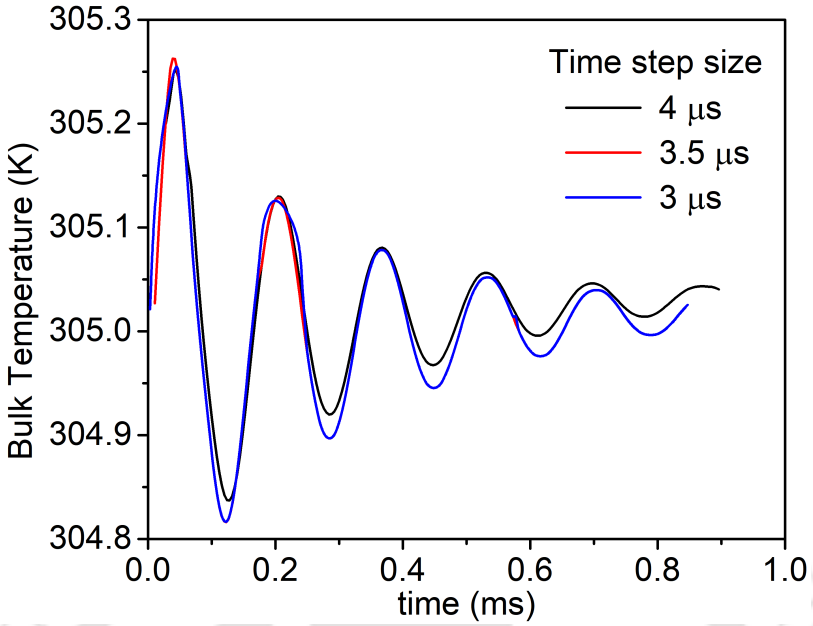

Fig. 7.4: Time independent study for the chosen grid size

[233, 234].

The transient variation of wall shear stress at two different axial location is shown in Fig.7.7. Again, wall shear stress variation remains unchanged for different time period. At a given time period and in the initial transient, the fluctuation and average wall shear stress is larger at section downstream (at x = 5 mm) of the flow due to the fluid expansion in the downstream region which causes sudden reduction in density and large velocity fluctuations. But as the time progresses at dynamic steady-state condition is reached, though the fluctuations are still larger at x = 5 mm, but average value of wall shear stress becomes more or less the same. Although the amplitude of wall shear stress is different, time period of oscillation is same which signifies that fluctuation is closely related to the heat flux oscillation. As the time period of heat flux changes, wall shear stress fluctuation changes which consolidates the response of wall shear stress variation with heat flux.

Figure 7.8 depicts transient variation of wall temperature at two different points. The wall temperature increases gradually with time and then reaches to the dynamic steady state. At the same location, the response time for both time periods are same. For same time period, response time at different location is different. Similarly, transient variation of bulk temperature is shown in Fig. 7.9. Since bulk temperature depends on velocity profile and specific heat at constant pressure fluctuation, it is clear that bulk temperature variation is significantly different from wall temperature change. The response time is the same for

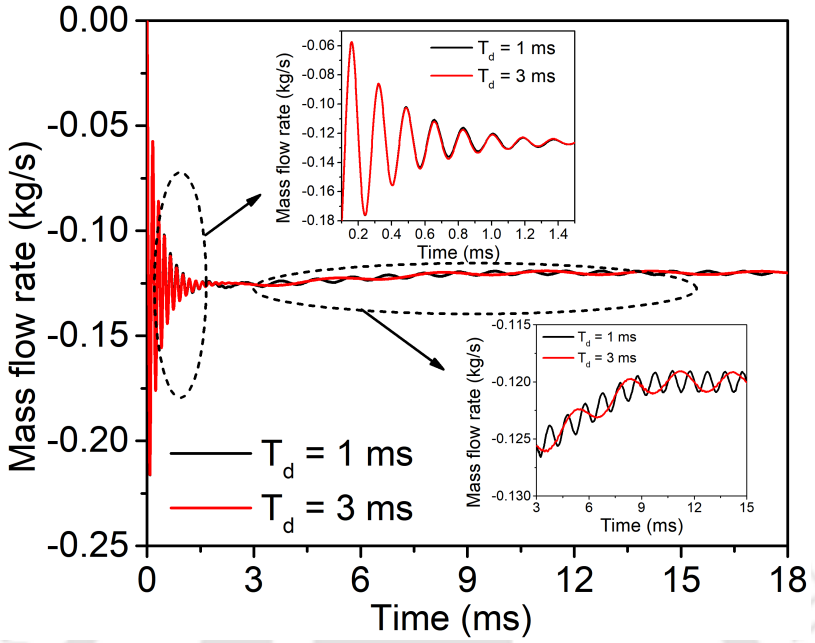

(a)

Fig. 7.5: Transient variations in mass flow rate under different time period.

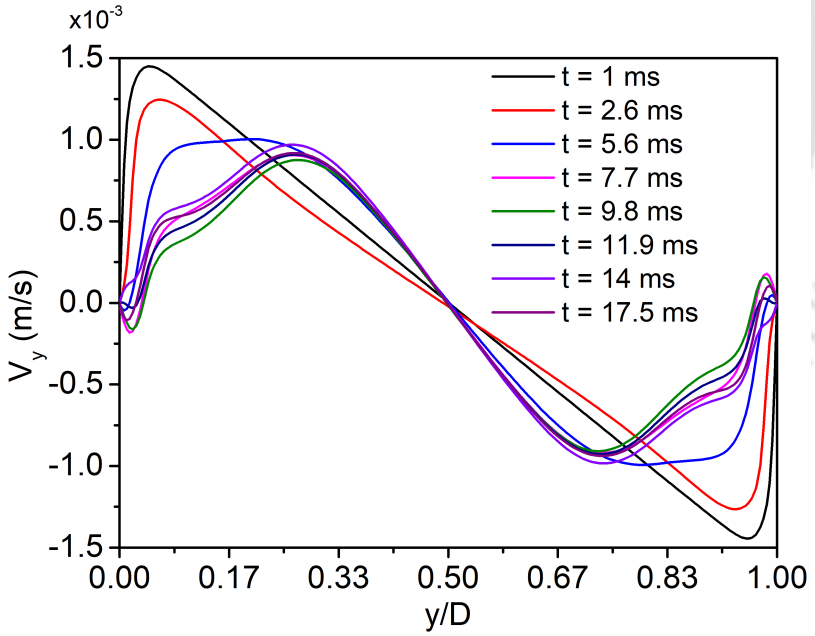

(a)

Fig. 7.6: y-velocity propagation with time.

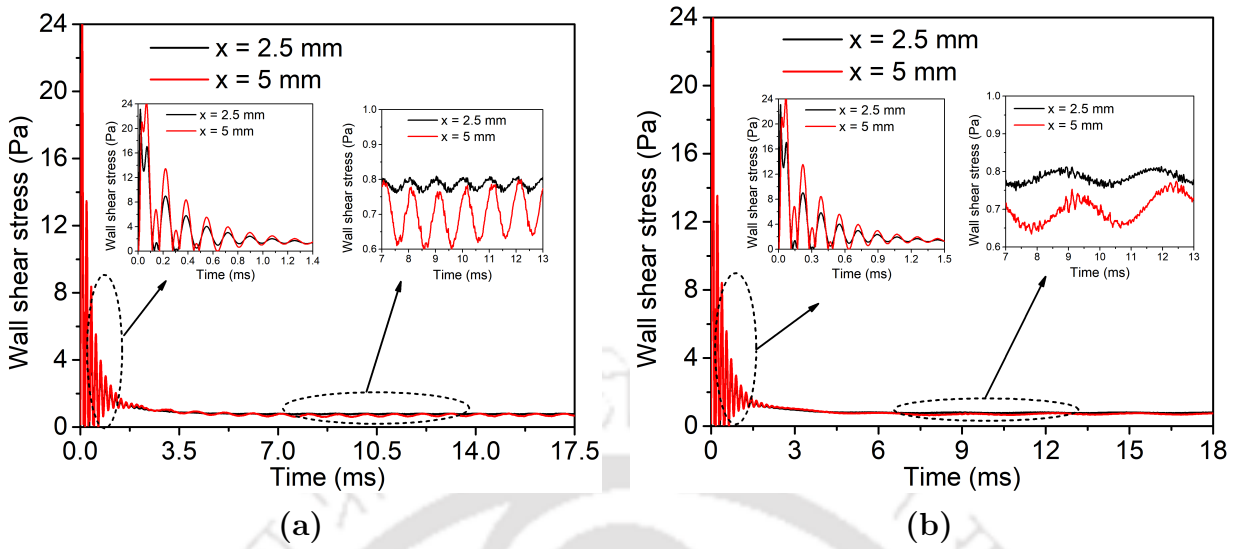

Fig. 7.7: Transient variations in wall shear stress at different point for (a) $T_d = 1ms$ (b) $T_d = 3ms$

both time periods at the same location, much like the wall temperature. The time period of the forced oscillation, similar to the previous case, closely matches the time period of the oscillations of both the wall and bulk temperatures. Since the temperature at downstream section reaches near to the T_{pc}, which consequently leads to more fluctuations in the bulk temperature at x = 5 mm compared to flat T_b at x = 2.5 mm. That is why there is a time lag between the emergence of dynamic steady-state. It is interesting to see that time period of heat flux does not affect the appearance of T_{pc} at any section. While the wall temperature did not experience these changes in the beginning, the bulk temperature did. This demonstrates how the imposed disturbance quickly diffuses from the fluid close to the wall to the bulk fluid.

Figure 7.10 presents pressure and velocity oscillations at three different locations and a fundamental difference in oscillation can be seen at different locations. Largest pressure changes are visible at the location closest to the inlet. On the other hand, due to the constant pressure outlet boundary condition imposed at the outlet, the fluctuations at the location closest to the outlet have the smallest fluctuations in pressure magnitude. Ruan *et al.* [235] explored the transitory behaviour of supercritical n-decane and found a finding that was similar to theirs. The local velocity variation is depicted in Fig. 7.10b. The magnitude and variation of the velocity are greatest towards the outlet and lowest close to the entrance. Additionally, it can be seen that velocity changes grow more pronounced near the outlet, supporting the idea that supercritical fluid expands significantly in a downstream direction.

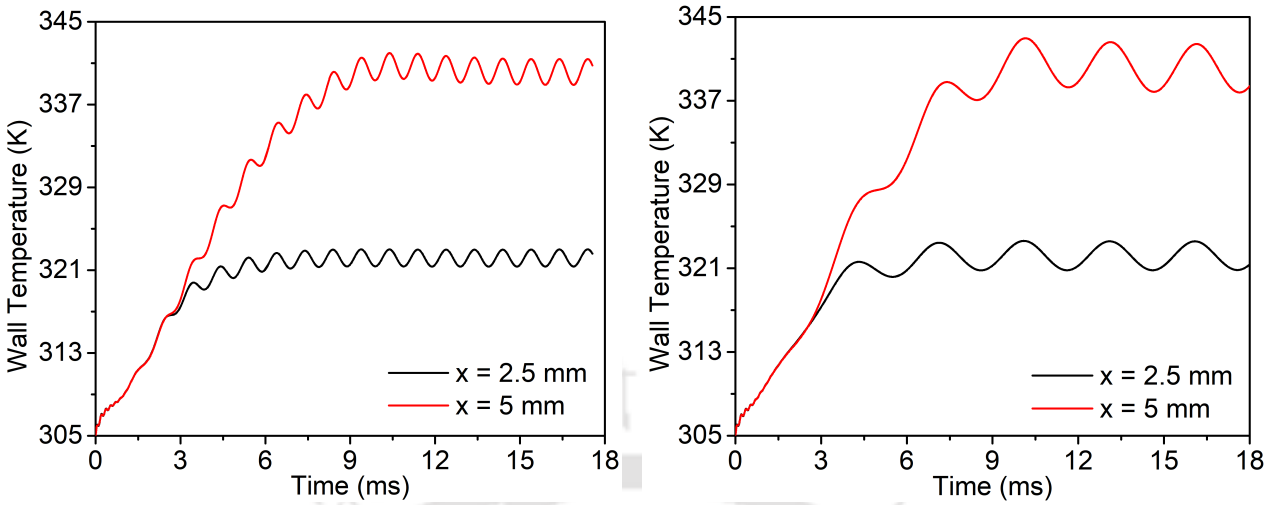

Fig. 7.8: Transient variations in wall temperature at different point for (a) $T_d = 1ms$ (b) $T_d = 3ms$

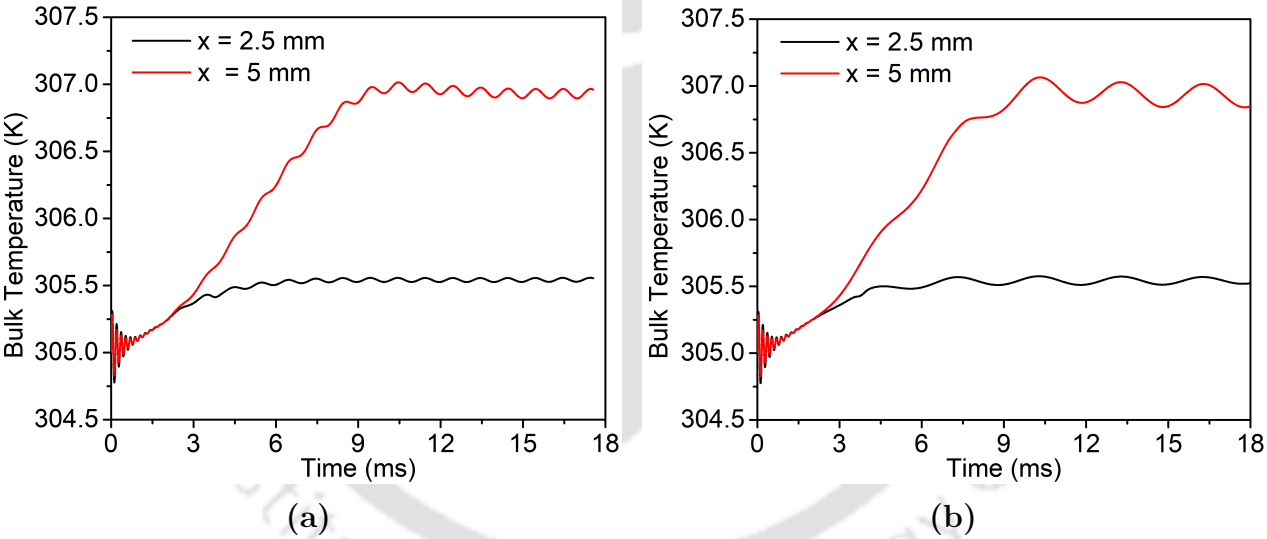

Fig. 7.9: Transient variations in bulk temperature at different point for (a) $T_d = 1ms$ (b) $T_d = 3ms$

7.3.2 Heat flux effect

The fluctuations of mass flow rate, wall shear stress, and wall temperature in the channel at various heat fluxes are shown in Fig. 7.11. Mass flow rate is higher at lower heat flux. The fluid expands during the heat transfer process, forcing some of the mass that was kept in the channel to flow out. Additionally, the fluid mass in a finite volume falls as density declines.

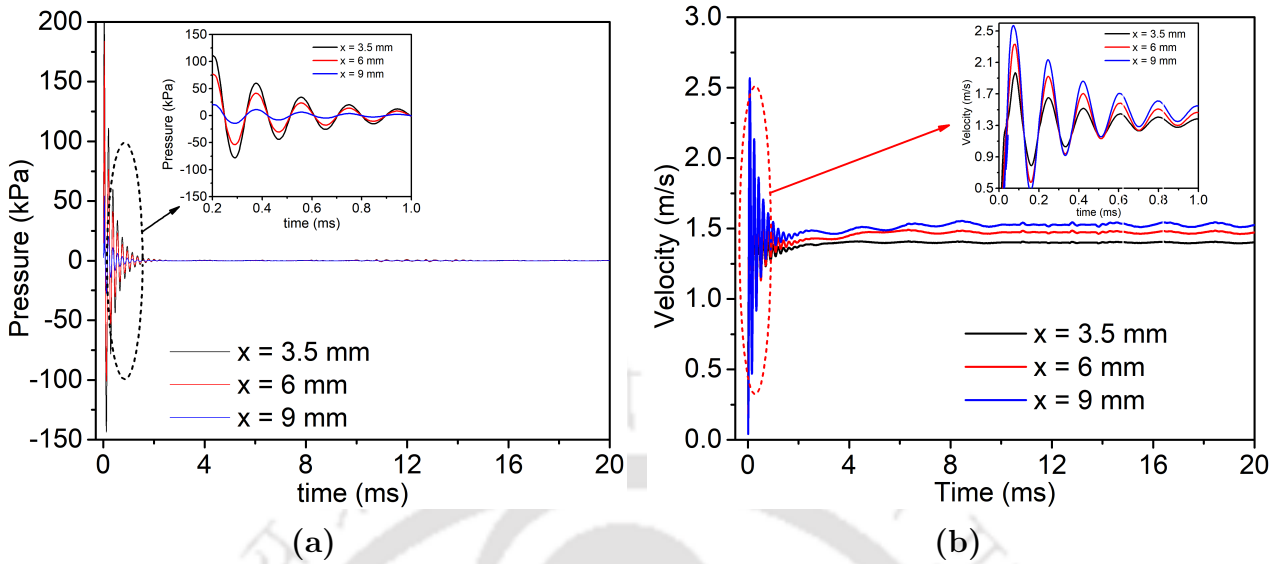

Fig. 7.10: Thermally induced (a) pressure oscillation (b) velocity oscillation at three different locations

This explains why the early stages of the transient process in Fig. 7.11a showed an increased mass flow rate. With the application of heat flux, the fluid layer's density variation is not uniform and leads to significant stratification of the fluid's density and other thermophysical parameters. This ultimately causes the development of a heated boundary layer (HBL). The density fluctuations across the microchannel for supercritical flows can reach several hundred kg/m^3, which was more than 500 kg/m^3 in the current work and agrees with the findings of [236, 231, 228].

The effect of heat flux on wall shear stress is shown in Fig. 7.11b. Similar to mass flow rate, wall shear stress is also higher at lower heat flux. Furthermore, due to fluctuations in flow velocity, the wall shear stress oscillates. As the heat flux is applied to the microchannel walls and strong stratification takes place, thin boundary layers begin to develop, eventually leading to steep velocity gradients. The variation of sCO_2 viscosity plays a crucial role in the hot boundary layer together with the stratification of density and velocity. The fluid in the core region has a relatively high viscosity and Reynolds number, while the viscosity of the sCO_2 gets comparably reduced in the heated boundary layer.

Fig. 7.11c shows transient variations of the temperature of sCO_2 under different surface heat fluxes at point $x = 5$ mm. The temperature of sCO_2 rises continuously as it is heated until it eventually approaches a dynamic steady-state value. The density of sCO_2 dramatically drops as temperature rises. In the initial phase of the transient process, the increased

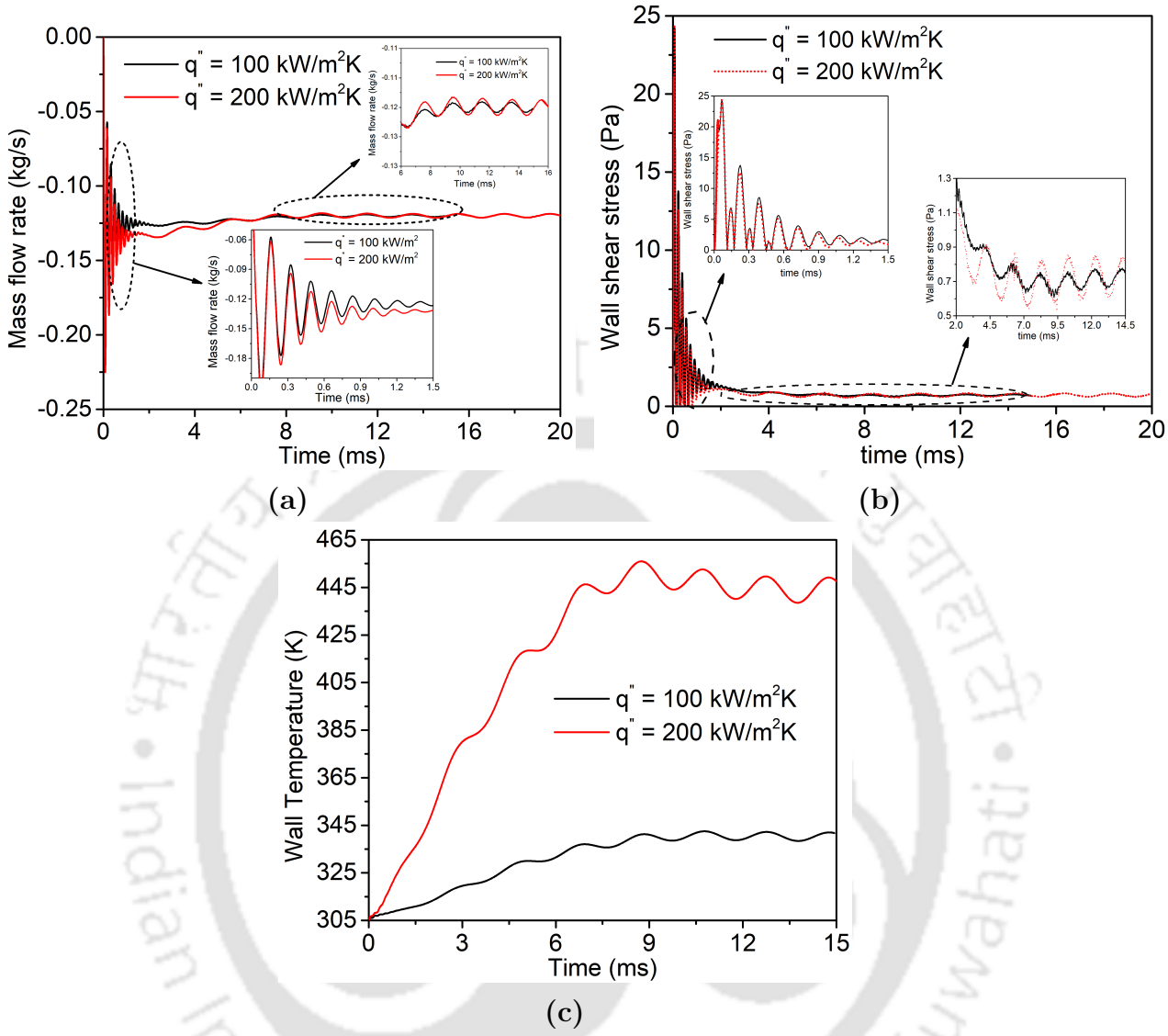

Fig. 7.11: Transient variations in (a) mass flow rate (b) wall shear stress and (c) wall temperature at different heat flux

velocity and pressure are a direct result of the decreasing fluid density. This powerful fluid thermal expansion phenomena causes the velocity and pressure to initially exceed their final steady-state values. On the other hand, the subsequent correction results in an undershoot. The heat transfer process consequently results in temperature-dependent flow oscillations.

7.3.3 Effect of operating pressure

The most fascinating characteristic of any supercritical fluid is the significant change in thermophysical properties near T_{pc}, and the transition is most severe along isobars defined by pressures immediately above the critical value. Therefore, at such pressures, the most abrupt variation in the parameters of interest is anticipated. By following Fig. 7.12, it is possible to understand the operating pressure's significance in this specific situation. The findings demonstrate that operating pressure has an impact on transient heat transfer as well. The transient fluctuation in mass flow rate at various pressures is likewise varied, with the peak occurring at 8 MPa and the trough occurring at 8.5 MPa. Additionally, the oscillation's amplitude is greater at 8 MPa than it is at 8.5 MPa. The inlet mass flow rate displays a decreasing trend to adapt the overall pressure drop throughout the channel as the heating power increases. At greater operating pressures, both the variations in the mass flow rate and the wall shear stress decreased. It demonstrates how a rise in operating pressure can improve system stability. This is due to the milder density change of supercritical fluid at higher pressures. So the inducement for flow instability is weaken, which reinforces the flow instability.

Wall shear stress exhibits comparable transient phenomena, as depicted in Fig. 7.12b. At greater pressures, the combined effects of reduced viscosity and velocity fluctuation result in a reduction in oscillation amplitude. Although the wall shear stress oscillation's amplitude varies depending on the pressure, the response time is constant. With the introduction of heat flux, the fluid layer's viscosity varies unevenly close to the wall, leading to large oscillations in wall shear stress.

7.3.4 Effect of mass flux

The rapid fluctuations in wall temperature and wall shear stress at a point in the heated portion of the microchannel are shown in Fig. 7.13 for different inlet mass flux. Wall temperature and response time both decrease with increasing mass flux. Because of this, the wall temperature rises with lower Reynolds numbers, which is consistent with human intelligence. Fluid and thermal expansion as well as flow variations are eventually brought on by the decreased fluid density brought on by the elevated bulk mean temperature. It is evident that at larger intake mass flux, supercritical carbon dioxide's unsteady flow behaviour and thermal phenomena intensify and last longer. In this instance, the unsteady response period is approximately 8.5 ms.

Fig. 7.13 depicts the transient variations of wall temperature and wall shear stress at

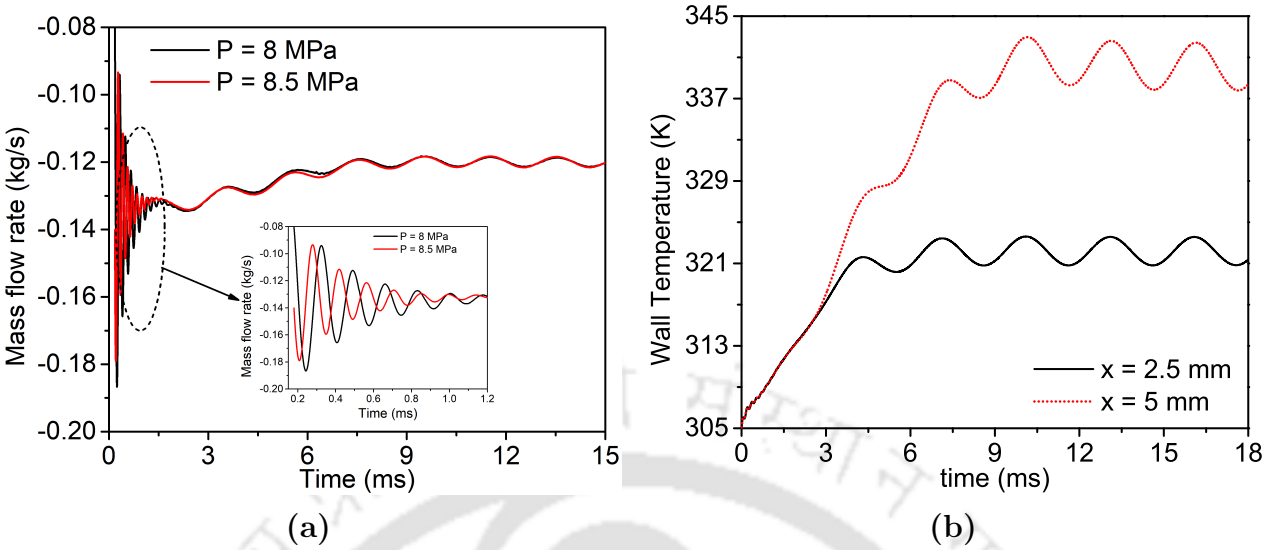

Fig. 7.12: Transient variations in (a) mass flow rate (b) wall shear stress at different operating pressure

a point in the mid-plane of the heated region of the microchannel, for various inlet mass flux. At higher mass flux, wall temperature along with response time are also reduced. As a consequence, the wall temperature becomes higher at lower Reynolds number, which is coherent with universal cognition. The increased bulk mean temperature causes reduction in fluid density, eventually leading to fluid and thermal expansion and flow fluctuations. It can be clearly concluded that the unsteady flow behavior and thermal phenomena of supercritical carbon dioxide becomes intense and occurs for longer duration at higher inlet mass flux, and the unsteady response period in this case, is around 8.5 ms. The wall heat flow is oscillatory in character, however the wall temperature rises relatively steadily before entering a dynamic steady state, demonstrating that the oscillation of the wall temperature is not strongly related to the oscillation of the heat flux. A comparable observation of a greater oscillation amplitude at higher mass flow is seen in Fig. 7.13b, which illustrates the impact of mass flux on wall shear stress. Additionally, the transient fluid flow process takes longer at higher mass fluxes, increasing response time.

7.4 Summary

simulation of heat transfer to supercritical CO_2 under heating condition is performed in the present study. The effect of time period, heat flux ,mass flux, and operating pressure on transient heat transfer process has been investigated. The main findings of the present

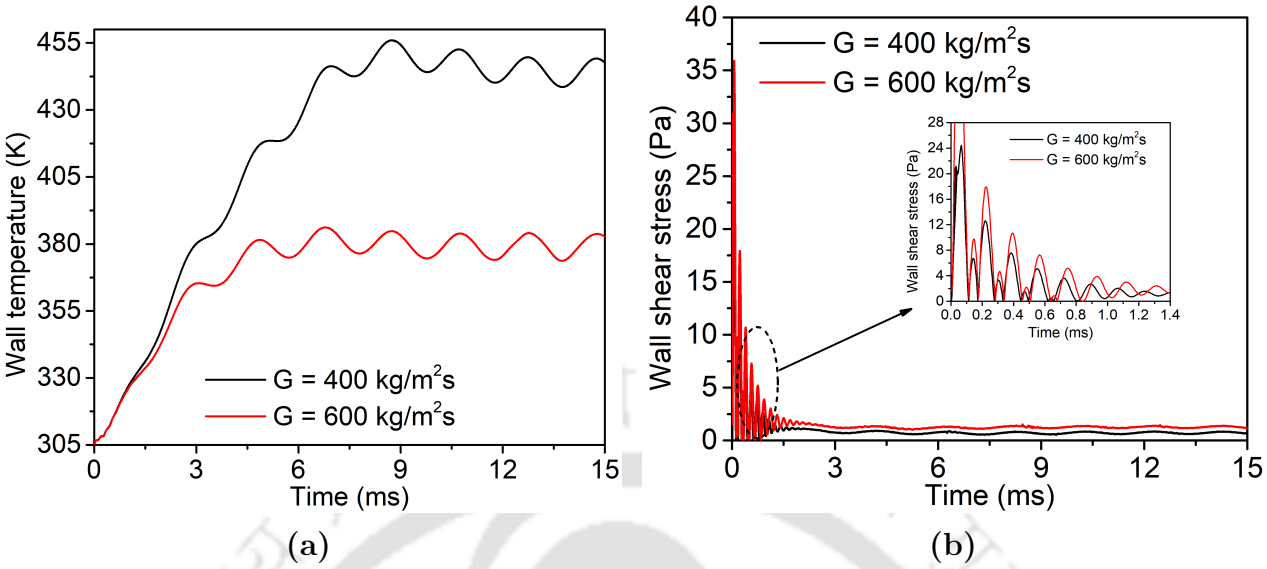

Fig. 7.13: Transient variations in (a) wall temperature(b) wall shear stress at different mass flux

study are as follows:

- It is interesting to note that transient variation of mass flux, wall shear stress and temperature does not depend upon time period of heat flux. The average wall shear stress magnitude and the transient fluctuation increases in the downstream location.
- At lower heat flux, mass flow rate as well as wall shear stress is higher As the CO_2 is heated, the bulk temperature increases and attains dynamic steady-state. Higher magnitude of T_b leads to significantly lesser density, leading to higher fluctuation in velocity and pressure in the early stage of the flow transient.
- The fluctuations in mass flow rate and wall shear stress both subsided at higher operating process. At higher operating pressure, the fluctuation in the mass flow rate as well as wall shear stress abates, hence inducing stability in the system. Though the effect of pressure is not significantly pronounced when the system attains dynamics steady-state.
- At higher mass flux wall temperature as well as response time also reduced. Results clearly reveal that the transient fluid flow and heat transfer process at a supercritical pressure becomes stronger and lasts longer at higher inlet mass flux.

Chapter 8

Conclusion and Scope for Further Work

8.1 Summary

The present work reports a numerical investigation of thermalhydraulics of sCO_2 flow in minichannels. The objective of the first study was the thermalhydraulic assessment of five different SCFs(R134a, CO_2, NH_3, N_2O, C_2H_6) using macroscopic scaling principles and the validity of such laws for its application in minichannel heat sinks. Of all the considered fluids R134a displayed better heat transfer behavior. However, the use of R134a is being phased out due to it's being a potent greenhouse gas having very high global warming potential. The present analysis can also be extended to design of nuclear reactors using newer SCFs, characterized by easily-achievable critical point properties. That makes sCO_2 a better option as a working fluid. The next study explored the effect of buoyancy on heat transport of sCO_2 in a minichannel under heating conditions. The influence of associated control parameters, such as heat flux, mass flux, inlet temperature and system pressure, on the heat transport is also explored. The substantial property gradient in the vicinity of pseudocritical point induces thermal asymmetry and large azimuthal variation, which can lead to consequent heat transfer deterioration. One of the major concerns with the application of SCF in forced convective channels is the premonition of heat transfer deterioration (HTD). Heat transfer deterioration is signified by thickening of viscous sub-layer and lessening in Prandtl number at higher mass flow rates, whereas flattening of the velocity profile owing to the buoyancy-induced acceleration at lower mass flow rates. The next study explores the option of employing flow obstructions in MCHS with sCO_2 as the working medium for

overall enhancement in the thermalhydraulic performance in the form of rectangular baffles. The most preferable dimensions associated with this specific orientation (height, thickness, and inclination angle) have also been identified, with the emphasis being on maximizing PEC. Detailed thermalhydraulic assessment of the optimum design has also been reported over a wide range of operating parameters, such as heat flux, mass flux, pressure, and inlet temperature. A substantial rise in the driving power requirement and irreversibility, both being directly proportional to the imposed pressure drop, is the major issue to be contemplated with the baffled MCHS. Shape optimization may provide possible improvement in this particular front and hence can be viewed as a possible next step of research. The next work compares the thermalhydraulics performance of sCO_2-driven MCHS with rectangular-shaped and airfoil-shaped flow obstructions. Corresponding dataset has also been employed to train a GA-tuned MLFF-NN algorithm, capable of forecasting the performance of MCHS based on PEC. Separate training datasets, comprising of 27 individual cases, have been prepared for FM-2P and FM-3P channels, while also identifying several test cases to gauge the capability of the tool. The experimental investigation of heat transfer behaviour of supercritical carbon dioxide in horizontal minichannel under heating conditions. The effect of various control parameters such as heat fluxes, mass fluxes, operating pressure, and inlet temperature is investigated under low $\dot{q}^{"}/G$ conditions. The non-linear properties variation of supercritical fluids causes coupling process of thermal relaxation and mechanical disturbance/instability. The next study is an attempt to explore different oscillations modes, such as thermoacoustic and thermal-induced flow oscillations. The influence of time period, heat flux amplitude, mass flux, and operating pressure on thermalhydraulics of sCO_2 have been comprehensively investigated. The highlights that can be drawn from the present study is summarized below:

- HTC-level with a SCF-filled MCHS is substantially greater than conventional single-phase fluids and comparable with boiling channels, without any constraint of critical heat flux.

- The difference in pressure drop characteristics can be attributed to the Pr, thermal profile of which has not been considered during scaling. Similarly, the variation in the dimensionless thermal conductivity can be identified as the primary contributor toward the deviation in thermal profiles.

- HTC at the bottom half surface is consistently higher than the same at the top half surface, which, in turn, is characterized by slightly higher wall temperature and greater

wall-to-bulk temperature differential. The disparity is more apparent at higher heat fluxes, but subside with rise in pressure.

- Large azimuthal variation can yield more than 400% change in HTC and about 6 K variation in wall temperature in a single cross-section, with peak HTC appearing on the horizontal plane. Lower fluid temperature in contact with the bottom half surface provided enhanced local shear stress, allowing to fluid slid slower along the same.

- The prime influence of the baffles can be viewed to be the enhancement in turbulent mixing among the fluid layers, hampering the formation of thermal boundary layers on the heated surface and maintaining a low wall-to-bulk temperature differential. That is manifested by the augmentation in average HTC with the incorporation of every additional pair of baffles.

8.2 Future Scopes

Bases on the present simulation, following are the recommendation for future investigations:

- In the present dissertation, the macroscopic scaling laws has been adopted to study the thermalhydraulic behavior of different supercritical fluids. However, the adopted scaling laws needs to be modified. In future, the profiles of Pr and k^* needs to be taken into consideration, which can possibly lead to more appropriate scaling methodology for thermalhydraulic comparison of supercritical fluids at miniscale.

- The present study considers flow obstruction in the shape of rectangular and airfoils. More shapes can be considered in the future and further optimization of shapes may provide possible improvement in their performance. Present simulation only considered single channel case for study. Parallel channels is used in numerous investigations therefore simulation needed to be conducted for those cases.

- In the present numerical study, 2D model is used for transient analysis of thermalhydraulic of sCO_2 in minichannel. In extension of the present work a extensive transient analysis can be carried out by using 3D model with different working fluids. The present work can also be extended to study the transient behavior in microchannel.

- The experimental analysis has been carried out with considering sCO_2 as working fluids flowing through minichannel. The present experimental work can be extended

for different fluids and thermalhydraulic of supercritical fluids in microchannel also needs to be studied.

References

[1] R. R. Schmidt, E. E. Cruz, M. Iyengar, Challenges of data center thermal management, IBM Journal of Research and Development 49 (4.5) (2005) 709–723.

[2] A. Onuki, H. Hao, R. A. Ferrell, Fast adiabatic equilibration in a single-component fluid near the liquid-vapor critical point, Physical Review A 41 (4) (1990) 2256.

[3] B. Zappoli, D. Bailly, Y. Garrabos, B. Le Neindre, P. Guenoun, D. Beysens, Anomalous heat transport by the piston effect in supercritical fluids under zero gravity, Physical Review A 41 (4) (1990) 2264.

[4] P. Carlès, A brief review of the thermophysical properties of supercritical fluids, The Journal of Supercritical Fluids 53 (1-3) (2010) 2–11.

[5] Y. Kato, Advanced high temperature gas-cooled reactor systems, Journal of Engineering for Gas Turbines and Power 132 (1) (2010) 012902.

[6] H. Pham, N. Alpy, J. Ferrasse, O. Boutin, J. Quenaut, M. Tothill, D. Haubensack, M. Saez, Mapping of the thermodynamic performance of the supercritical CO_2 cycle and optimisation for a small modular reactor and a sodium-cooled fast reactor, Energy 87 (2015) 412–424.

[7] B. Halimi, K. Y. Suh, Computational analysis of supercritical CO_2 Brayton cycle power conversion system for fusion reactor, Energy Conversion and Management 63 (2012) 38–43.

[8] P. Kumar, K. Srinivasan, Carbon dioxide based power generation in renewable energy systems, Applied Thermal Engineering 109 (2016) 831–840.

[9] S. Liao, T. Zhao, An experimental investigation of convection heat transfer to supercritical carbon dioxide in miniature tubes, International Journal of Heat and Mass Transfer 45 (25) (2002) 5025–5034.

[10] P.-X. Jiang, R.-F. Shi, Y.-J. Xu, S. He, J. Jackson, Experimental investigation of flow resistance and convection heat transfer of CO_2 at supercritical pressures in a vertical porous tube, The Journal of Supercritical Fluids 38 (3) (2006) 339–346.

[11] G. Lorentzen, J. Pettersen, A new, efficient and environmentally benign system for car air-conditioning, International Journal of Refrigeration 16 (1) (1993) 4–12.

[12] G. Sulzer, Verfahren zur erzeugung von arbeit aus warme, Swiss Patent 269599 (1950) 15.

[13] E. G. Feher, The supercritical thermodynamic power cycle, Energy conversion 8 (2) (1968) 85–90.

[14] H. J. Yoon, Y. Ahn, J. I. Lee, Y. Addad, Potential advantages of coupling supercritical CO_2 brayton cycle to water cooled small and medium size reactor, Nuclear Engineering and Design 245 (2012) 223–232.

[15] J. Lee, J. I. Lee, H. J. Yoon, J. E. Cha, Supercritical carbon dioxide turbomachinery design for water-cooled small modular reactor application, Nuclear Engineering and Design 270 (2014) 76–89.

[16] W. S. Jeong, J. I. Lee, Y. H. Jeong, Potential improvements of supercritical recompression CO_2 brayton cycle by mixing other gases for power conversion system of a sfr, Nuclear Engineering and Design 241 (6) (2011) 2128–2137.

[17] J. I. Linares, L. E. Herranz, I. Fernández, A. Cantizano, B. Y. Moratilla, Supercritical CO_2 brayton power cycles for demo fusion reactor based on helium cooled lithium lead blanket, Applied Thermal Engineering 76 (2015) 123–133.

[18] J. I. Linares, A. Cantizano, B. Y. Moratilla, V. Martín-Palacios, L. Batet, Supercritical CO_2 brayton power cycles for demo (demonstration power plant) fusion reactor based on dual coolant lithium lead blanket, Energy 98 (2016) 271–283.

[19] J. Sarkar, Second law analysis of supercritical CO_2 recompression brayton cycle, Energy 34 (9) (2009) 1172–1178.

[20] J. M. Cardemil, A. K. da Silva, Parametrized overview of CO_2 power cycles for different operation conditions and configurations–an absolute and relative performance analysis, Applied Thermal Engineering 100 (2016) 146–154.

[21] B. Middleton, J. J. Pasch, A. M. Kruizenga, M. Walker, Coupling a supercritical carbon dioxide brayton cycle to a helium-cooled reactor., Tech. rep., Sandia National Lab.(SNL-NM), Albuquerque, NM (United States); Sandia ... (2016).

[22] L. Santini, C. Accornero, A. Cioncolini, On the adoption of carbon dioxide thermodynamic cycles for nuclear power conversion: A case study applied to mochovce 3 nuclear power plant, Applied Energy 181 (2016) 446–463.

[23] H. Yu, D. Hartanto, J. Moon, Y. Kim, A conceptual study of a supercritical CO_2-cooled micro modular reactor, Energies 8 (12) (2015) 13938–13952.

[24] J. Stepanek, S. Entler, J. Syblik, L. Vesely, V. Dostal, P. Zacha, Parametric study of s-CO_2 cycles for the demo fusion reactor, Fusion Engineering and Design 160 (2020) 111992.

[25] L. Hu, D. Chen, S. Gao, Y. Cao, Thermodynamic and heat transfer analyses of the s-CO_2 brayton cycle as the heat transport system of a nuclear reactor, Heat Transfer Research 47 (10) (2016).

[26] M.-J. Li, H.-H. Zhu, J.-Q. Guo, K. Wang, W.-Q. Tao, The development technology and applications of supercritical CO_2 power cycle in nuclear energy, solar energy and other energy industries, Applied Thermal Engineering 126 (2017) 255–275.

[27] M. T. White, G. Bianchi, L. Chai, S. A. Tassou, A. I. Sayma, Review of supercritical CO_2 technologies and systems for power generation, Applied Thermal Engineering 185 (2021) 116447.

[28] F. Crespi, G. Gavagnin, D. Sánchez, G. S. Martínez, Supercritical carbon dioxide cycles for power generation: A review, Applied energy 195 (2017) 152–183.

[29] Z. Roy, G. Halder, Replacement of halogenated refrigerants towards sustainable cooling system: A review, Chemical Engineering Journal Advances 3 (2020) 100027.

[30] K. Thu, K. Takezato, N. Takata, T. Miyazaki, Y. Higashi, Drop-in experiments and exergy assessment of hfc-32/hfo-1234yf/r744 mixture with gwp below 150 for domestic heat pumps, International Journal of Refrigeration 121 (2021) 289–301.

[31] V. Oruç, A. G. Devecioğlu, Experimental investigation on the low-gwp hfc/hfo blends r454a and r454c in a r404a refrigeration system, International Journal of Refrigeration 128 (2021) 242–251.

[32] Y. He, J. Deng, Y. Li, X. Zhang, Synergistic effect of geometric parameters on CO_2 ejector based on local exergy destruction analysis, Applied Thermal Engineering 184 (2021) 116256.

[33] K. Tsamos, Y. Ge, I. Santosa, S. Tassou, G. Bianchi, Z. Mylona, Energy analysis of alternativeCO_2 refrigeration system configurations for retail food applications in moderate and warm climates, Energy Conversion and Management 150 (2017) 822–829.

[34] S. White, M. Yarrall, D. Cleland, R. Hedley, Modelling the performance of a transcritical CO_2 heat pump for high temperature heating, International Journal of Refrigeration 25 (4) (2002) 479–486.

[35] G. Lorentzen, J. Pettersen, A new, efficient and environmentally benign system for car air-conditioning, International journal of refrigeration 16 (1) (1993) 4–12.

[36] D. Wang, B. Yu, J. Hu, L. Chen, J. Shi, J. Chen, Heating performance characteristics of CO_2 heat pump system for electrical vehicle in a cold climate, International Journal of Refrigeration 85 (2018) 27–41.

[37] Y. Chen, H. Zou, J. Dong, H. Xu, C. Tian, D. Butrymowicz, Experimental investigation on refrigeration performance of a CO_2 system with intermediate cooling for automobiles, Applied Thermal Engineering 174 (2020) 115267.

[38] D. Jefferies, T. Ly, A. Kunith, D. Göhlich, Energiebedarf verschiedener klimatisierungssysteme für elektro-linienbusse, Deutsche Kälte-und Klimatagung: Dresden, Germany (2015).

[39] X. Song, D. Lu, Q. Lei, D. Wang, B. Yu, J. Shi, J. Chen, Energy and exergy analyses of a transcriticalCO_2 air conditioning system for an electric bus, Applied Thermal Engineering 190 (2021) 116819.

[40] H. Wang, S. Li, Y. Song, X. Yin, F. Cao, P. Gullo, Experimental thermodynamic investigation on the refrigerant charge in a transcritical CO_2 electric bus air conditioning system, Applied Sciences 11 (12) (2021) 5614.

[41] Ø. Christensen, Reversible r744 CO_2heat pumps applied in public trains in norway, Master's thesis, Institutt for energi-og prosessteknikk (2009).

[42] S. Wang, H. Tuo, F. Cao, Z. Xing, Experimental investigation on air-source transcritical CO_2 heat pump water heater system at a fixed water inlet temperature, International Journal of Refrigeration 36 (3) (2013) 701–716.

[43] G. Lorentzen, The use of natural refrigerants: a complete solution to the cfc/hcfc predicament, International journal of refrigeration 18 (3) (1995) 190–197.

[44] S. Riffat, C. Afonso, A. Oliveira, D. Reay, Natural refrigerants for refrigeration and air-conditioning systems, Applied Thermal Engineering 17 (1) (1997) 33–42.

[45] M. Khanam, T. U. Daim, A regional technology roadmap to enable the adoption of CO_2 heat pump water heater: A case from the pacific northwest, usa, Energy strategy reviews 18 (2017) 157–174.

[46] F. Cao, Z. Ye, Y. Wang, Experimental investigation on the influence of internal heat exchanger in a transcritical CO_2 heat pump water heater, Applied Thermal Engineering 168 (2020) 114855.

[47] J. Sarkar, Performance optimization of transcritical CO_2 refrigeration cycle with thermoelectric subcooler, International journal of energy research 37 (2) (2013) 121–128.

[48] R. Llopis, R. Cabello, D. Sánchez, E. Torrella, Energy improvements of CO_2 transcritical refrigeration cycles using dedicated mechanical subcooling, International Journal of Refrigeration 55 (2015) 129–141.

[49] D. Astrain, A. Merino, L. Catalán, P. Aranguren, M. Araiz, D. Sánchez, R. Cabello, R. Llopis, Improvements in the cooling capacity and the cop of a transcritical CO_2 refrigeration plant operating with a thermoelectric subcooling system, Applied Thermal Engineering 155 (2019) 110–122.

[50] D. Sánchez, P. Aranguren, A. Casi, R. Llopis, R. Cabello, D. Astrain, Experimental enhancement of a CO_2 transcritical refrigerating plant including thermoelectric subcooling, International Journal of Refrigeration 120 (2020) 178–187.

[51] V. Chatoorgoon, Stability of supercritical fluid flow in a single-channel natural-convection loop, International Journal of Heat and Mass Transfer 44 (10) (2001) 1963–1972.

[52] V. Chatoorgoon, A. Voodi, D. Fraser, The stability boundary for supercritical flow in natural convection loops: Part i: H_2O studies, Nuclear Engineering and Design 235 (24) (2005) 2570–2580.

[53] A. K. Yadav, M. R. Gopal, S. Bhattacharyya, Cfd analysis of a CO_2 based natural circulation loop with end heat exchangers, Applied Thermal Engineering 36 (2012) 288–295.

[54] A. K. Yadav, M. Ram Gopal, S. Bhattacharyya, Computational fluid dynamic analysis of a supercritical CO_2 based natural circulation loop with end heat exchangers, International Journal of Advances in Engineering Sciences and Applied Mathematics 4 (3) (2012) 119–126.

[55] L. Chen, B.-L. Deng, X.-R. Zhang, Experimental study of trans-critical and supercritical CO_2 natural circulation flow in a closed loop, Applied thermal engineering 59 (1-2) (2013) 1–13.

[56] L. Chen, B.-L. Deng, X.-R. Zhang, Experimental investigation of CO_2 thermosyphon flow and heat transfer in the supercritical region, International Journal of Heat and Mass Transfer 64 (2013) 202–211.

[57] H. Tokanai, Y. Ohtomo, H. Horiguchi, E. Harada, M. Kuriyama, Heat transfer of supercritical CO_2 flow in natural convection circulation system, Heat transfer engineering 31 (9) (2010) 750–756.

[58] L. Chen, X.-R. Zhang, H. Yamaguchi, Z.-S. S. Liu, Effect of heat transfer on the instabilities and transitions of supercritical CO_2 flow in a natural circulation loop, International journal of heat and mass transfer 53 (19-20) (2010) 4101–4111.

[59] L. Chen, X.-R. Zhang, B. Jiang, Effects of heater orientations on the natural circulation and heat transfer in a supercritical CO_2 rectangular loop, Journal of heat transfer 136 (5) (2014).

[60] B. Swapnalee, P. Vijayan, M. Sharma, D. Pilkhwal, Steady state flow and static instability of supercritical natural circulation loops, Nuclear Engineering and Design 245 (2012) 99–112.

[61] Sports - a simple non-linear thermalhydraulic stability code, Nuclear Engineering and Design 93 (1) (1986) 51–67.

[62] V. Chatoorgoon, A. Voodi, P. Upadhye, The stability boundary for supercritical flow in natural-convection loops: Part ii: CO_2 and H_2, Nuclear engineering and design 235 (24) (2005) 2581–2593.

[63] P. K. Jain, et al., Numerical analysis of supercritical flow instabilities in a natural circulation loop, Nuclear Engineering and Design 238 (8) (2008) 1947–1957.

[64] M. Sharma, D. S. Pilkhwal, P. K. Vijayan, D. Saha, R. K. Sinha, Steady-state behavior of natural circulation loops operating with supercritical fluids for open and closed loop boundary conditions, Heat transfer engineering 33 (9) (2012) 809–820.

[65] M. Sharma, P. Vijayan, D. Pilkhwal, Y. Asako, Steady state and stability characteristics of natural circulation loops operating with carbon dioxide at supercritical pressures for open and closed loop boundary conditions, Nuclear Engineering and Design 265 (2013) 737–754.

[66] J. Yu, S. Che, R. Li, B. Qi, Analysis of ledinegg flow instability in natural circulation at supercritical pressure, Progress in Nuclear Energy 53 (6) (2011) 775–779.

[67] B. Petukhov, Heat transfer and friction in turbulent pipe flow with variable physical properties, in: Advances in Heat Transfer, Vol. 6, Elsevier, 1970, pp. 503–564.

[68] W. Hall, Heat transfer near the critical point, in: Advances in Heat Transfer, Vol. 7, Elsevier, 1971, pp. 1–86.

[69] J. Jackson, W. Hall, J. Fewster, A. Watson, M. Watts, Heat transfer to supercritical pressure fluids, UKAEA, AERER 8158 (1975).

[70] E. Krasnoshchekov, Experimental study of heat exchagne in carbon dioxide in the supercritical range at high temperature drops, High Temperature 4 (1966) 375–382.

[71] K. Yamagata, K. Nishikawa, S. Hasegawa, T. Fujii, S. Yoshida, Forced convective heat transfer to supercritical water flowing in tubes, International Journal of Heat and Mass Transfer 15 (12) (1972) 2575–2593.

[72] V. Protopopov, Generalizing relations for the local heat-transfer coefficients in turbulent flows of water and carbon dioxide at supercritical pressure in a uniformly heated circular tube, Teplofizika Vysokikh Temperatur 15 (1977) 815–821.

[73] V. Popov, Y. P. Valueva, Mixed turbulent fluid convection in vertical tubes, Teploenergetika 2 (1988) 17–22.

[74] V. Kurganov, A. Kaptilnyi, Flow structure and turbulent transport of a supercritical pressure fluid in a vertical heated tube under the conditions of mixed convection. Experimental data, International Journal of Heat and Mass Transfer 36 (13) (1993) 3383–3392.

[75] S. He, W. Kim, P. Jiang, J. Jackson, Simulation of mixed convection heat transfer to carbon dioxide at supercritical pressure, Proceedings of the Institution of Mechanical Engineers, Part C: Journal of Mechanical Engineering Science 218 (11) (2004) 1281–1296.

[76] J. Song, H. Kim, H. Kim, Y. Bae, Heat transfer characteristics of a supercritical fluid flow in a vertical pipe, The Journal of Supercritical Fluids 44 (2) (2008) 164–171.

[77] D. E. Kim, M.-H. Kim, Experimental investigation of heat transfer in vertical upward and downward supercritical CO_2 flow in a circular tube, International Journal of Heat and Fluid Flow 32 (1) (2011) 176–191.

[78] P.-X. Jiang, Y. Zhang, Y.-J. Xu, R.-F. Shi, Experimental and numerical investigation of convection heat transfer of CO_2 at supercritical pressures in a vertical tube at low Reynolds numbers, International Journal of Thermal Sciences 47 (8) (2008) 998–1011.

[79] P.-X. Jiang, R.-F. Shi, Y.-J. Xu, S. He, J. Jackson, Experimental investigation of flow resistance and convection heat transfer of CO_2 at supercritical pressures in a vertical porous tube, The Journal of supercritical fluids 38 (3) (2006) 339–346.

[80] Z.-B. Liu, Y.-L. He, Y.-F. Yang, J.-Y. Fei, Experimental study on heat transfer and pressure drop of supercritical CO_2 cooled in a large tube, Applied Thermal Engineering 70 (1) (2014) 307–315.

[81] S. S. Pitla, E. A. Groll, S. Ramadhyani, New correlation to predict the heat transfer coefficient during in-tube cooling of turbulent supercritical CO_2, International journal of refrigeration 25 (7) (2002) 887–895.

[82] H.-K. Oh, C.-H. Son, New correlation to predict the heat transfer coefficient in-tube cooling of supercritical CO_2 in horizontal macro-tubes, Experimental Thermal and Fluid Science 34 (8) (2010) 1230–1241.

[83] C.-H. Son, S.-J. Park, An experimental study on heat transfer and pressure drop characteristics of carbon dioxide during gas cooling process in a horizontal tube, International Journal of Refrigeration 29 (4) (2006) 539–546.

[84] S. H. Yoon, J. H. Kim, Y. W. Hwang, M. S. Kim, K. Min, Y. Kim, Heat transfer and pressure drop characteristics during the in-tube cooling process of carbon dioxide in the supercritical region, International journal of refrigeration 26 (8) (2003) 857–864.

[85] Y.-Y. Bae, H.-Y. Kim, Convective heat transfer to CO_2 at a supercritical pressure flowing vertically upward in tubes and an annular channel, Experimental Thermal and Fluid Science 33 (2) (2009) 329–339.

[86] S. Gupta, D. McGillivray, P. Surendran, L. Trevani, I. Pioro, Developing heat-transfer correlations for supercritical CO_2 flowing in vertical bare tubes, in: International Conference on Nuclear Engineering, Vol. 44991, American Society of Mechanical Engineers, 2012, pp. 321–333.

[87] Y.-Y. Bae, H.-Y. Kim, D.-J. Kang, Forced and mixed convection heat transfer to supercritical CO_2vertically flowing in a uniformly-heated circular tube, Experimental Thermal and Fluid Science 34 (8) (2010) 1295–1308.

[88] H. Kim, H. Y. Kim, J. H. Song, Y. Y. Bae, Heat transfer to supercritical pressure carbon dioxide flowing upward through tubes and a narrow annulus passage, Progress in Nuclear Energy 50 (2-6) (2008) 518–525.

[89] J. K. Kim, H. K. Jeon, J. S. Lee, Wall temperature measurements with turbulent flow in heated vertical circular/non-circular channels of supercritical pressure carbon-dioxide, International journal of heat and mass transfer 50 (23-24) (2007) 4908–4911.

[90] B. S. Shiralkar, P. Griffith, Deterioration in heat transfer to fluids at supercritical pressure and high heat fluxes (1969).

[91] B. Shiralkar, P. Griffith, The effect of swirl, inlet conditions, flow direction, and tube diameter on the heat transfer to fluids at supercritical pressure (1970).

[92] V. B. Ankudinov, V. A. Kurganov, Intensification of deteriorated heat transfer in heated tubes at supercritical pressures, Teplofizika vysokikh temperatur 19 (6) (1981) 1208–1212.

[93] P. Bourke, D. Pulling, An experimental explanation of deterioration in heat transfer to supercritical carbon dioxide, Atomic Energy Research Establishment, 1971.

[94] V. Kurganov, A. Kaptilnyi, Flow structure and turbulent transport of a supercritical pressure fluid in a vertical heated tube under the conditions of mixed convection. experimental data, International journal of heat and mass transfer 36 (13) (1993) 3383–3392.

[95] X. Du, X. Zhu, X. Yu, F. Wu, Q. Qiu, Heat transfer deterioration and visualized flow state of supercritical CO_2 in a vertical non-circular channel, Nuclear Engineering and Design 386 (2022) 111574.

[96] S. S. Pitla, E. A. Groll, S. Ramadhyani, Convective heat transfer from in-tube cooling of turbulent supercritical carbon dioxide: part 2—experimental data and numerical predictions, HVAC&R Research 7 (4) (2001) 367–382.

[97] N. Petrov, V. Popov, Heat-transfer and resistance of carbon-dioxide being cooled in the supercritical region, Thermal Engineering 32 (3) (1985) 131–134.

[98] N. Petrov, V. Popov, Heat transfer and hydraulic resistance with turbulent flow in a tube of water at supercritical parameters of state, Thermal Engineering 35 (10) (1988) 577–580.

[99] S. H. Lee, J. R. Howell, Turbulent developing convective heat transfer in a tube for fluids near the critical point, International journal of heat and mass transfer 41 (10) (1998) 1205–1218.

[100] X. R. Zhang, H. Yamaguchi, Forced convection heat transfer of supercritical CO_2 in a horizontal circular tube, The Journal of supercritical fluids 41 (3) (2007) 412–420.

[101] S.-h. Liu, Y.-p. Huang, J.-f. Wang, L. K. Leung, Numerical investigation of buoyancy effect on heat transfer to carbon dioxide flow in a tube at supercritical pressures, International Journal of Heat and Mass Transfer 117 (2018) 595–606.

[102] J. Guo, J. Song, Z. Han, K. S. Pervunin, C. N. Markides, Investigation of the thermohydraulic characteristics of vertical supercritical CO_2 flows at cooling conditions, Energy 256 (2022) 124628.

[103] S. G. Kandlikar, W. J. Grande, Evolution of microchannel flow passages – thermohydraulic performance and fabrication technology, Heat Transfer Engineering 24 (1) (2003) 3–17.

[104] J. Pfahler, J. Harley, H. Bau, J. Zemel, Liquid transport in micron and submicron channels, Sensors and Actuators A: Physical 22 (1-3) (1990) 431–434.

[105] D. Yu, An experimental and theoretical investigation of fluid flow and heat transfer in microtubes, in: ASME/JSME Thermal Engineering Conference, Vol. 1, 1995, pp. 523–530.

[106] Y. W. Hwang, M. S. Kim, The pressure drop in microtubes and the correlation development, International journal of heat and mass transfer 49 (11-12) (2006) 1804–1812.

[107] T.-H. Yen, N. Kasagi, Y. Suzuki, Forced convective boiling heat transfer in microtubes at low mass and heat fluxes, International Journal of Multiphase Flow 29 (12) (2003) 1771–1792.

[108] G. Celata, M. Cumo, A. Mariani, H. Nariai, F. Inasaka, Influence of channel diameter on subcooled flow boiling burnout at high heat fluxes, International journal of heat and mass transfer 36 (13) (1993) 3407–3410.

[109] B. Schilder, S. Y. C. Man, N. Kasagi, S. Hardt, P. Stephan, Flow visualization and local measurement of forced convection heat transfer in a microtube, Journal of heat transfer 132 (3) (2010).

[110] T. Adams, S. Abdel-Khalik, S. Jeter, Z. Qureshi, An experimental investigation of single-phase forced convection in microchannels, International Journal of Heat and Mass Transfer 41 (6-7) (1998) 851–857.

[111] C. Y. Park, P. Hrnjak, Flow boiling heat transfer, pressure drop, and flow pattern for CO_2 in a 3.5 mm horizontal smooth tube (2009).

[112] C. Dang, N. Haraguchi, E. Hihara, Flow boiling heat transfer of carbon dioxide inside a small-sized microfin tube, International Journal of Refrigeration 33 (4) (2010) 655–663.

[113] M. Ducoulombier, S. Colasson, J. Bonjour, P. Haberschill, Carbon dioxide flow boiling in a single microchannel–part ii: Heat transfer, Experimental Thermal and Fluid Science 35 (4) (2011) 597–611.

[114] L. Gao, T. Honda, S. Koyama, Experiments on flow boiling heat transfer of almost pure CO_2 and CO_2-oil mixtures in horizontal smooth and microfin tubes, Hvac&R Research 13 (3) (2007) 415–425.

[115] K. Miyata, H. Mori, Y. Hamamoto, Correlation for the flow boiling heat transfer in small diameter tubes, in: Proceedings of the 23rd IIR International Congress of Refrigeration, 2011.

[116] M. H. Maqbool, B. Palm, R. Khodabandeh, Experimental investigation of dryout of propane in uniformly heated single vertical mini-channels, Experimental thermal and fluid science 37 (2012) 121–129.

[117] M. H. Maqbool, B. Palm, R. Khodabandeh, Boiling heat transfer of ammonia in vertical smooth mini channels: Experimental results and predictions, International Journal of thermal sciences 54 (2012) 13–21.

[118] J. Jovanović, W. Zhou, E. V. Rebrov, T. Nijhuis, V. Hessel, J. C. Schouten, Liquid–liquid slug flow: hydrodynamics and pressure drop, Chemical Engineering Science 66 (1) (2011) 42–54.

[119] P. Urbant, A. Leshansky, Y. Halupovich, On the forced convective heat transport in a droplet-laden flow in microchannels, Microfluidics and Nanofluidics 4 (6) (2008) 533–542.

[120] Z. Che, T. N. Wong, N.-T. Nguyen, Heat transfer enhancement by recirculating flow within liquid plugs in microchannels, International Journal of Heat and Mass Transfer 55 (7-8) (2012) 1947–1956.

[121] Z. Che, T. N. Wong, N.-T. Nguyen, Heat transfer in plug flow in cylindrical microcapillaries with constant surface heat flux, International journal of thermal sciences 64 (2013) 204–212.

[122] T. Bandara, S. C. Cheung, G. Rosengarten, Slug flow heat transfer in microchannels: A numerical study, Computational Thermal Sciences: An International Journal 7 (1) (2015).

[123] A. Asthana, I. Zinovik, C. Weinmueller, D. Poulikakos, Significant nusselt number increase in microchannels with a segmented flow of two immiscible liquids: An experimental study, International Journal of Heat and Mass Transfer 54 (7-8) (2011) 1456–1464.

[124] M. M. G. Eain, V. Egan, J. Punch, Local nusselt number enhancements in liquid–liquid taylor flows, International Journal of Heat and Mass Transfer 80 (2015) 85–97.

[125] Z. Dai, Z. Guo, D. F. Fletcher, B. S. Haynes, Taylor flow heat transfer in microchannels—unification of liquid–liquid and gas–liquid results, Chemical Engineering Science 138 (2015) 140–152.

[126] X. Huai, S. Koyama, T. Zhao, An experimental study of flow and heat transfer of supercritical carbon dioxide in multi-port mini channels under cooling conditions, Chemical engineering science 60 (12) (2005) 3337–3345.

[127] S. Liao, T. Zhao, An experimental investigation of convection heat transfer to supercritical carbon dioxide in miniature tubes, International journal of heat and mass transfer 45 (25) (2002) 5025–5034.

[128] C. Dang, K. Iino, K. Fukuoka, E. Hihara, Effect of lubricating oil on cooling heat transfer of supercritical carbon dioxide, International Journal of Refrigeration 30 (4) (2007) 724–731.

[129] R.-N. Xu, F. Luo, P.-X. Jiang, Buoyancy effects on turbulent heat transfer of supercritical CO_2 in a vertical mini-tube based on continuous wall temperature measurements, International journal of heat and mass transfer 110 (2017) 576–586.

[130] P. Guo, S. Liu, J. Yan, J. Wang, Q. Zhang, Experimental study on heat transfer of supercritical CO_2 flowing in a mini tube under heating conditions, International Journal of Heat and Mass Transfer 153 (2020) 119623.

[131] S. Bovard, M. Abdi, M. R. K. Nikou, A. Daryasafar, Numerical investigation of heat transfer in supercritical CO_2 and water turbulent flow in circular tubes, The Journal of Supercritical Fluids 119 (2017) 88–103.

[132] X. Cao, Z. Rao, S. Liao, Laminar convective heat transfer of supercritical CO_2 in horizontal miniature circular and triangular tubes, Applied Thermal Engineering 31 (14-15) (2011) 2374–2384.

[133] S. Pandey, E. Laurien, X. Chu, A modified convective heat transfer model for heated pipe flow of supercritical carbon dioxide, International Journal of Thermal Sciences 117 (2017) 227–238.

[134] X. Chu, E. Laurien, Flow stratification of supercritical CO_2 in a heated horizontal pipe, The Journal of Supercritical Fluids 116 (2016) 172–189.

[135] X. Chu, E. Laurien, Direct numerical simulation of heated turbulent pipe flow at supercritical pressure, Journal of Nuclear Engineering and Radiation Science 2 (3) (2016).

[136] M. Xiang, J. Guo, X. Huai, X. Cui, Thermal analysis of supercritical pressure CO_2 in horizontal tubes under cooling condition, The Journal of Supercritical Fluids 130 (2017) 389–398.

[137] Y. Cao, R. Xu, J. Yan, S. He, P. Jiang, Direct numerical simulation of convective heat transfer of supercritical pressure in a vertical tube with buoyancy and thermal acceleration effects, Journal of Fluid Mechanics 927 (2021).

[138] A. Kruizenga, H. Li, M. Anderson, M. Corradini, Supercritical carbon dioxide heat transfer in horizontal semicircular channels, Journal of Heat transfer 134 (8) (2012) 081802.

[139] S. Liao, T. Zhao, Measurements of heat transfer coefficients from supercritical carbon dioxide flowing in horizontal mini/micro channels, Journal of Heat Transfer 124 (3) (2002) 413–420.

[140] P.-X. Jiang, R.-N. Xu, Z.-H. Li, C.-R. Zhao, Influence of flow acceleration on convection heat transfer of CO_2 at supercritical pressures and air in a vertical micro tube, in: International Heat Transfer Conference, Vol. 49415, 2010, pp. 1–13.

[141] B. M. Fronk, A. S. Rattner, High-flux thermal management with supercritical fluids, Journal of Heat Transfer 138 (12) (2016).

[142] M. Nabil, A. S. Rattner, Les simulation of turbulent supercritical CO_2 heat transfer in microchannels, in: 6th International Supercritical CO_2 Power Cycles Symposium, 2018.

[143] S. A. Jajja, K. R. Zada, B. M. Fronk, Experimental investigation of supercritical carbon dioxide in horizontal microchannels with non-uniform heat flux boundary conditions, International Journal of Heat and Mass Transfer 130 (2019) 304–319.

[144] S. A. Jajja, J. M. Sequeira, B. M. Fronk, Geometry and orientation effects in non-uniformly heated microchannel heat exchangers using supercritical carbon dioxide, Experimental Thermal and Fluid Science 112 (2020) 109979.

[145] M. M. Ehsan, Z. Guan, A. Klimenko, A comprehensive review on heat transfer and pressure drop characteristics and correlations with supercritical CO_2 under heating and cooling applications, Renewable and Sustainable Energy Reviews 92 (2018) 658–675.

[146] S. G. Kandlikar, W. J. Grande, Evolution of microchannel flow passages–thermohydraulic performance and fabrication technology, Heat transfer engineering 24 (1) (2003) 3–17.

[147] J. Zhao, P. Saha, M. S. Kazimi, Stability of supercritical water-cooled reactor during steady-state and sliding pressure startup conditions, in: International topical meeting on nuclear reactor thermal hydraulics (NURETH 11); Avignon (France), 2005, pp. 2–6.

[148] W. Ambrosini, M. Sharabi, Dimensionless parameters in stability analysis of heated channels with fluids at supercritical pressures, Nuclear Engineering and Design 238 (8) (2008) 1917–1929.

[149] T. O. Gómez, A. Class, R. Lahey Jr, T. Schulenberg, Stability analysis of a uniformly heated channel with supercritical water, Nuclear Engineering and Design 238 (8) (2008) 1930–1939.

[150] I. L. Pioro, R. B. Duffey, Heat transfer and hydraulic resistance at supercritical pressures in power engineering applications, American Society of Mechanical Engineers, New York, USA, 2007.

[151] F. D'Auria, G. Galassi, Scaling in nuclear reactor system thermal-hydraulics, Nuclear Engineering and Design 240 (10) (2010) 3267–3293.

[152] N. Aksan, F. D'auria, H. Glaeser, Thermal-hydraulic phenomena for water cooled nuclear reactors, Nuclear Engineering and Design 330 (2018) 166–186.

[153] T. D. Roberto, M. A. da Silva, C. M. Lapa, Development of a test facility for analyzing transients in supercritical water-cooled reactors by fractional scaling analysis, Nuclear Engineering and Design 296 (2016) 9–18.

[154] J. Jackson, W. Hall, Influences of buoyancy on heat transfer to fluids flowing in vertical tubes under turbulent conditions, in: S. Kakac, D. Spalding (Eds.), Turbulent Forced Convection in Channels and Bundles, Hemisphere, 1979, pp. 613–640.

[155] W. Ambrosini, M. Sharabi, Dimensionless parameters in stability analysis of heated channels with fluids at supercritical pressures, Nuclear Engineering and Design 238 (8) (2008) 1917–1929.

[156] W. Ambrosini, Discussion of similarity principles for fluid-to-fluid scaling of heat transfer behaviour at supercritical pressures, Nuclear engineering and design 241 (12) (2011) 5149–5173.

[157] X. Cheng, X. Liu, H. Gu, Fluid-to-fluid scaling of heat transfer in circular tubes cooled with supercritical fluids, Nuclear Engineering and Design 241 (2) (2011) 498–508.

[158] A. Pucciarelli, W. Ambrosini, Fluid-to-fluid scaling of heat transfer phenomena with supercritical pressure fluids: Results from RANS analyses, Annals of Nuclear Energy 92 (2016) 21–35.

[159] A. Pucciarelli, W. Ambrosini, A successful general fluid-to-fluid similarity theory for heat transfer at supercritical pressure, International journal of heat and mass transfer 159 (2020) 120152.

[160] H. Zahlan, D. Groeneveld, S. Tavoularis, Fluid-to-fluid scaling for convective heat transfer in tubes at supercritical and high subcritical pressures, International Journal of heat and mass transfer 73 (2014) 274–283.

[161] A. Mouslim, S. Tavoularis, Direct tests of fluid-to-fluid scaling expressions for supercritical heat transfer in tubes, International Journal of Heat and Mass Transfer 147 (2020) 118862.

[162] S. Kassem, A. Pucciarelli, W. Ambrosini, Insight into a fluid-to-fluid similarity theory for heat transfer at supercritical pressure: Results and perspectives, International Journal of Heat and Mass Transfer 168 (2021) 120813.

[163] G. Yu, C. Jiang, L. Wang, G. Su, S. Qiu, A new method on fluid-to-fluid scaling for heat transfer in tubes at supercritical pressures, International Journal of Heat and Mass Transfer 126 (2018) 809–822.

[164] M. H. Fard, CFD modeling of heat transfer of CO_2 at supercritical pressures flowing vertically in porous tubes, International Communications in Heat and Mass Transfer 37 (1) (2010) 98–102.

[165] M. Xiang, J. Guo, X. Huai, X. Cui, Thermal analysis of supercritical pressure CO_2 in horizontal tubes under cooling condition, The Journal of Supercritical Fluids 130 (2017) 389–398.

[166] S. Pandey, E. Laurien, X. Chu, A modified convective heat transfer model for heated pipe flow of supercritical carbon dioxide, International Journal of Thermal Sciences 117 (2017) 227–238.

[167] X. Cao, Z. Rao, S. Liao, Laminar convective heat transfer of supercritical CO_2 in horizontal miniature circular and triangular tubes, Applied Thermal Engineering 31 (14-15) (2011) 2374–2384.

[168] M. M. Ehsan, Z. Guan, A. Klimenko, A comprehensive review on heat transfer and pressure drop characteristics and correlations with supercritical CO_2 under heating and cooling applications, Renewable and Sustainable Energy Reviews 92 (2018) 658–675.

[169] Z.-x. Hu, D. Liu, H.-y. Gu, Study on spacer-induced heat transfer deterioration of supercritical water in annular channel, International Journal of Heat and Mass Transfer 125 (2018) 552–558.

[170] K. Podila, Y. Rao, CFD modelling of supercritical water flow and heat transfer in a 2 × 2 fuel rod bundle, Nuclear Engineering and Design 301 (2016) 279–289.

[171] Y. Xiao, J. Pan, H. Gu, Numerical investigation of spacer effects on heat transfer of supercritical fluid flow in an annular channel, International Journal of Heat and Mass Transfer 121 (2018) 343–353.

[172] N. Agrawal, S. Bhattacharyya, J. Sarkar, Optimization of two-stage transcritical carbon dioxide heat pump cycles, International Journal of Thermal Sciences 46 (2) (2007) 180–187.

[173] P. F. Lisboa, J. Fernandes, P. C. Simões, J. P. Mota, E. Saatdjian, Computational-fluid-dynamics study of a Kenics static mixer as a heat exchanger for supercritical carbon dioxide, The Journal of Supercritical Fluids 55 (1) (2010) 107–115.

[174] Y.-Y. Bae, H.-Y. Kim, T. H. Yoo, Effect of a helical wire on mixed convection heat transfer to carbon dioxide in a vertical circular tube at supercritical pressures, International journal of heat and fluid flow 32 (1) (2011) 340–351.

[175] E. W. Lemmon, M. Huber, M. McLinden, NIST standard reference database 23: Refprop version 9.0, Reference Fluid Thermodynamic and Transport Properties, Standard Reference Data Program, National Institute of Standards and Technology, Gaithersburg, MD (2010).

[176] E. W. Lemmon, M. Huber, M. McLinden, NIST standard reference database 23: Refprop version 9.0,“, Reference Fluid Thermodynamic and Transport Properties,” Standard Reference Data Program, National Institute of Standards and Technology, Gaithersburg, MD (2010).

[177] A. Bejan, Advanced engineering thermodynamics, John Wiley & Sons, 2016.

[178] A. Jounet, B. Zappoli, A. Mojtabi, Rapid thermal relaxation in near-critical fluids and critical speeding up: discrepancies caused by boundary effects, Physical Review Letters 84 (15) (2000) 3224.

[179] C. Dang, E. Hihara, In-tube cooling heat transfer of supercritical carbon dioxide. Part 1. Experimental measurement, International Journal of Refrigeration 27 (7) (2004) 736–747.

[180] F. R. Menter, Two-equation eddy-viscosity turbulence models for engineering applications, AIAA journal 32 (8) (1994) 1598–1605.

[181] Y. Zhang, J. Wang, W. Liu, Z. Liu, Heat transfer and pressure drop characteristics of r134a flow boiling in the parallel/tandem microchannel heat sinks, Energy Conversion and Management 148 (2017) 1082–1095.

[182] J. R. Thome, Wolverine engineering databook III, Wolverine Tube, Inc, 2006, Ch. 20.

[183] N. Kumar, D. N. Basu, Role of buoyancy on the thermalhydraulic behavior of supercritical carbon dioxide flow through horizontal heated minichannel, International Journal of Thermal Sciences 168 (2021) 107051.

[184] A. Bejan, A study of entropy generation in fundamental convective heat transfer, Journal of Heat Transfer 101 (4) (1979) 718–725.

[185] J. Sarkar, Improving thermal performance of micro-channel electronic heat sink using supercritical CO_2 as coolant, Thermal Science 23 (1) (2019) 243–253.

[186] F. R. Menter, Two-equation eddy-viscosity turbulence models for engineering applications, AIAA journal 32 (8) (1994) 1598–1605.

[187] P. Guo, S. Liu, J. Yan, J. Wang, Q. Zhang, Experimental study on heat transfer of supercritical CO_2 flowing in a mini tube under heating conditions, International Journal of Heat and Mass Transfer 153 (2020) 119623.

[188] B. Zhu, J. Xu, X. Wu, J. Xie, M. Li, Supercritical "boiling" number, a new parameter to distinguish two regimes of carbon dioxide heat transfer in tubes, International Journal of Thermal Sciences 136 (2019) 254–266.

[189] M. Shitsman, Impairment of the heat transmission at supercritical pressures, Teplofizika Vysokikh Temperatur 1 (2) (1963) 267–275.

[190] T. Hiroaki, N. Niichi, H. Masaru, T. Ayao, Forced convection heat transfer to fluid near critical point flowing in circular tube, International Journal of Heat and Mass Transfer 14 (6) (1971) 739–750.

[191] K. Yamagata, K. Nishikawa, S. Hasegawa, T. Fujii, S. Yoshida, Forced convective heat transfer to supercritical water flowing in tubes, International Journal of Heat and Mass Transfer 15 (12) (1972) 2575–2593.

[192] R. Bellinghausen, U. Renz, Pseudocritical heat transfer inside vertical tubes, Chemical Engineering and Processing: Process Intensification 28 (3) (1990) 183–186.

[193] G. A. Adebiyi, W. Hall, Experimental investigation of heat transfer to supercritical pressure carbon dioxide in a horizontal pipe, International journal of heat and mass transfer 19 (7) (1976) 715–720.

[194] S. Koshizuka, N. Takano, Y. Oka, Numerical analysis of deterioration phenomena in heat transfer to supercritical water, International Journal of Heat and Mass Transfer 38 (16) (1995) 3077–3084.

[195] S. E.-D. El-Morshedy, S. M. Ibrahim, A. Alyan, A. Abdelmaksoud, Heat transfer deterioration mechanism for water at supercritical pressure, International Journal of Thermofluids 7 (2020) 100020.

[196] Q. Wen, H. Gu, Numerical simulation of heat transfer deterioration phenomenon in supercritical water through vertical tube, Annals of Nuclear Energy 37 (10) (2010) 1272–1280.

[197] H. Cheng, J. Zhao, M. K. Rowinski, Study on two wall temperature peaks of supercritical fluid mixed convective heat transfer in circular tubes, International Journal of Heat and Mass Transfer 113 (2017) 257–267.

[198] S. Zhang, X. Xu, C. Liu, C. Dang, A review on application and heat transfer enhancement of supercritical CO_2 in low-grade heat conversion, Applied Energy 269 (2020) 114962.

[199] M. Pizzarelli, The status of the research on the heat transfer deterioration in supercritical fluids: A review, International Communications in Heat and Mass Transfer 95 (2018) 132–138.

[200] Y. Alihosseini, M. Z. Targhi, M. M. Heyhat, N. Ghorbani, Effect of a micro heat sink geometric design on thermo-hydraulic performance: A review, Applied Thermal Engineering 170 (2020) 114974.

[201] J. Ackerman, Pseudoboiling heat transfer to supercritical pressure water in smooth and ribbed tubes, Journal of Heat Transfer 92 (3) (1970).

[202] B. Y. Kamenetskii, The effectiveness of turbulence promoters in tubes with nonuniformly heated perimeters under conditions of impaired heat transfer, Therm. Eng. (Engl. Transl.); (United Kingdom) 27 (4) (1980).

[203] W. Kohler, W. Kastner, Heat transfer and pressure loss in rifled tubes, in: International Heat Transfer Conference Digital Library, Begel House Inc., 1986.

[204] Z. Zhao, X. Wang, D. Che, Numerical study on heat transfer and resistance characteristics of supercritical water inside internally-ribbed tube, Heat and mass transfer 50 (4) (2014) 559–572.

[205] Z. Li, Y. Wu, G. Tang, J. Lu, H. Wang, Numerical analysis of buoyancy effect and heat transfer enhancement in flow of supercritical water through internally ribbed tubes, Applied Thermal Engineering 98 (2016) 1080–1090.

[206] Z. Li, J. Lu, G. Tang, Q. Liu, Y. Wu, Effects of rib geometries and property variations on heat transfer to supercritical water in internally ribbed tubes, Applied Thermal Engineering 78 (2015) 303–314.

[207] N. Yuan, D. Bi, Y. Zhai, Y. Jin, Z. Li, H. Wang, Flow and heat transfer performance of supercritical pressure carbon dioxide in pipes with discrete double inclined ribs, International Journal of Heat and Mass Transfer 149 (2020) 119175.

[208] J. Gu, Z. Li, Q. Wang, J. Lyu, Y. Wu, Geometry optimization for supercritical water heat transfer enhancement in non-uniformly heated rifled tubes, Applied Thermal Engineering 187 (2021) 116566.

[209] X. Xu, C. Liu, C. Dang, Y. Wu, X. Liu, Experimental investigation on heat transfer characteristics of supercritical CO_2 cooled in horizontal helically coiled tube, International journal of refrigeration 67 (2016) 190–201.

[210] Z. Li, Y. Zhai, D. Bi, K. Li, H. Wang, J. Lu, Orientation effect in helical coils with smooth and rib-roughened wall: Toward improved gas heaters for supercritical carbon dioxide rankine cycles, Energy 140 (2017) 530–545.

[211] Y. Li, F. Sun, G. Xie, B. Sunden, J. Qin, Numerical investigation on flow and thermal performance of supercritical CO_2 in horizontal cylindrically concaved tubes, Applied Thermal Engineering 153 (2019) 655–668.

[212] Z. Yu, L. Tao, L. Huang, D. Wang, S. Zhang, Q. Yu, M. Li, Numerical investigation on cooling heat transfer and flow characteristics of supercritical CO_2 in spirally fluted tube at various inclination angles, International Journal of Thermal Sciences 166 (2021) 106916.

[213] A. Eter, D. Groeneveld, S. Tavoularis, Convective heat transfer in supercritical flows of CO_2 in tubes with and without flow obstacles, Nuclear Engineering and Design 313 (2017) 162–176.

[214] H. Zhang, J. Guo, X. Huai, K. Cheng, X. Cui, Studies on the thermal-hydraulic performance of zigzag channel with supercritical pressure CO_2, The Journal of Supercritical Fluids 148 (2019) 104–115.

[215] G. Kuang, M. Ohadi, S. Dessiatoun, Semi-empirical correlation of gas cooling heat transfer of supercritical carbon dioxide in microchannels, HVAC&R Research 14 (6) (2008) 861–870.

[216] S. Mokry, P. Kirillov, I. Pioro, Y. Gospodinov, Supercritical water heat transfer in a vertical bare tube: Normal, improved, and deteriorated regimes, Nuclear technology 172 (1) (2010) 60–70.

[217] M. E. Steinke, S. G. Kandlikar, Single-phase liquid friction factors in microchannels, International journal of thermal sciences 45 (11) (2006) 1073–1083.

[218] L. Chai, G. D. Xia, H. S. Wang, Parametric study on thermal and hydraulic characteristics of laminar flow in microchannel heat sink with fan-shaped ribs on sidewalls–part 3: Performance evaluation, International Journal of Heat and Mass Transfer 97 (2016) 1091–1101.

[219] O. C. da Rosa, F. G. Battisti, G. M. Hobold, A. K. da Silva, Enhancing heat rejection from electronic devices with a supercritical carbon dioxide minichannel heat exchanger, International Journal of Refrigeration 106 (2019) 463–473.

[220] H. Lee, M. Kang, K. W. Jung, C. R. Kharangate, S. Lee, M. Iyengar, C. Malone, M. Asheghi, K. E. Goodson, H. Lee, An artificial neural network model for predicting frictional pressure drop in micro-pin fin heat sink, Applied Thermal Engineering 194 (2021) 117012.

[221] A. K. Jha, N. Sit, Comparison of response surface methodology (RSM) and artificial neural network (ANN) modelling for supercritical fluid extraction of phytochemicals from Terminalia chebula pulp and optimization using RSM coupled with desirability function (DF) and genetic algorithm (GA) and ANN with GA, Industrial Crops and Products 170 (2021) 113769.

[222] S. Son, J. Y. Heo, J. I. Lee, Prediction of inner pinch for supercritical CO_2 heat exchanger using Artificial Neural Network and evaluation of its impact on cycle design, Energy Conversion and Management 163 (2018) 66–73.

[223] R. B. Duffey, I. L. Pioro, Experimental heat transfer of supercritical carbon dioxide flowing inside channels (survey), Nuclear Engineering and Design 235 (8) (2005) 913–924.

[224] N. T. Rao, A. Oumer, U. Jamaludin, State-of-the-art on flow and heat transfer characteristics of supercritical CO_2 in various channels, The Journal of supercritical fluids 116 (2016) 132–147.

[225] L. F. Cabeza, A. de Gracia, A. I. Fernández, M. M. Farid, Supercritical CO_2 as heat transfer fluid: A review, Applied thermal engineering 125 (2017) 799–810.

[226] M. M. Ehsan, Z. Guan, A. Klimenko, A comprehensive review on heat transfer and pressure drop characteristics and correlations with supercritical CO_2 under heating and cooling applications, Renewable and Sustainable Energy Reviews 92 (2018) 658–675.

[227] R. J. Moffat, Describing the uncertainties in experimental results, Experimental thermal and fluid science 1 (1) (1988) 3–17.

[228] S. Amiroudine, B. Zappoli, Piston-effect-induced thermal oscillations at the rayleigh-bénard threshold in supercritical h e 3, Physical review letters 90 (10) (2003) 105303.

[229] L. Chen, X.-R. Zhang, J. Okajima, S. Maruyama, Numerical investigation of near-critical fluid convective flow mixing in microchannels, Chemical Engineering Science 97 (2013) 67–80.

[230] L. Chen, X.-R. Zhang, J. Okajima, S. Maruyama, Thermal relaxation and critical instability of near-critical fluid microchannel flow, Physical Review E 87 (4) (2013) 043016.

[231] A. Jounet, B. Zappoli, A. Mojtabi, Rapid thermal relaxation in near-critical fluids and critical speeding up: discrepancies caused by boundary effects, Physical Review Letters 84 (15) (2000) 3224.

[232] C. Dang, E. Hihara, In-tube cooling heat transfer of supercritical carbon dioxide. Part 1. Experimental measurement, International Journal of Refrigeration 27 (7) (2004) 736–747.

[233] P. Carlès, Thermoacoustic waves near the liquid-vapor critical point, Physics of Fluids 18 (12) (2006) 126102.

[234] A. Jounet, A. Mojtabi, J. Ouazzani, B. Zappoli, Low-frequency vibrations in a near-critical fluid, Physics of Fluids 12 (1) (2000) 197–204.

[235] B. Ruan, S. Huang, H. Meng, X. Gao, Flow dynamics in transient heat transfer of n-decane at supercritical pressure, International Journal of Heat and Mass Transfer 115 (2017) 206–215.

[236] B. Zappoli, Near-critical fluid hydrodynamics, Comptes Rendus Mecanique 331 (10) (2003) 713–726.

Publications

Journals

1. **N. Kumar**, and D. N. Basu, Role of buoyancy on the thermalhydraulic behavior of supercritical carbon dioxide flow through horizontal heated minichannel, *International Journal of Thermal Sciences*, 168 (2021), 107051.
2. **N. Kumar**, and D. N. Basu, Thermalhydraulic comparison of supercritical fluids in minichannel heat sink to assess the suitability of macroscopic scaling rules, *Nuclear Engineering and Design*, 392 (2022), 111750.
3. **N. Kumar**, and D. N. Basu, Thermalhydraulic Assessment and Design Optimization of Incorporating Flow Obstructors in a Supercritical Minichannel Heat Sink, *Applied Energy*, (under review).
4. **N. Kumar**, Tanuj Srivastava, and D. N. Basu, Flow dynamics in transient heat transfer of carbon dioxide at supercritical pressure in microchannel, *Heat Transfer Engineering*, (under review).
5. **N. Kumar**, S. Ghosh and D. N. Basu, Thermalhydraulic Assessment and Performance Prediction of Supercritical Minichannel Heat Sink with Airfoil-shaped Obstructions using GA-tuned Neural Network, (Submitted).
6. **N. Kumar**, and D. N. Basu, Thermalhydraulic comparison of overall performance of microchannel heat sinks utilizing a variety of baffles, (under preparation).
7. **N. Kumar**, Tanuj Srivastava and D. N. Basu, Investigation into the thermalhydraulic of supercritical carbon dioxide flowing through miniature channel by Infrared Thermography, (under preparation).

Conference proceedings

1. **N. Kumar**, and D. N. Basu, Computational appraisal of the thermalhydraulic characteristics of supercritical carbon dioxide in heated mini-channel for HVAC applications, *IOP Conference Series: Earth and Environmental Science*, Thailand, (2019).
2. **N. Kumar**, and D. N. Basu, Computational Analysis of Thermalhydraulics of Supercritical sCO_2 in Horizontal Finned Square Microchannel Heat-sink, *The* 8^{th} *International and* 47^{th} *National Conference on Fluid Mechanics and Fluid Power*, IIT Guwahati, (2020)
3. **N. Kumar**, and D. N. Basu, Numerical Investigation on Heat Transfer Coefficient of Supercritical sCO_2 in a extended surface Micro Heat-sink, *Proceedings of the* 26^{th} *National and* 4^{th} *International ISHMT-ASTFE Heat and Mass Transfer Conference*, IIT Madras, (2021).
4. **N. Kumar**, and D. N. Basu, Analysis of Thermal Performance for Supercritical Fluid Flowing in a Microchannel Heat Sink Utilizing Internal Fins, 7^{th} *Thermal and Fluids Engineering Conference (TFEC)*, University of Nevada, Las Vegas, (2022).
5. **N. Kumar**, and D. N. Basu, Flow dynamics in transient heat transfer of carbon dioxide at supercritical pressure in microchannel, *1st International Conference in Fluid Thermal and Energy Systems (ICFTES'22)*, NIT Calicut, (2022).
6. **N. Kumar**, and D. N. Basu, Thermalhydraulic optimization of microchannel heat-sink with carbon-dioxide at supercritical pressure, *The* 1^{st} *World Conference on Multiphase Transportation, Conversion and Utilization of Energy MTCUE 2022*, Xi'an, China (2022).

Book chapter

1. **N. Kumar**, D. N. Basu and L. Chen , Effect of Flow Acceleration and Buoyancy on Thermalhydraulics of sCO_2 in Mini/Micro-Channel, *Handbook of Research on Advancements in Supercritical Fluids Applications for Sustainable Energy Systems*, *IIGI Global*, 161-182 (2021).

Uncertainty analysis

In the present investigation the single sample analysis as proposed by Moffat (1988) are applied to the experimental data's. The principle of estimation of uncertainty is as follows: Consider a variable N dependent on various independent measured variables such as $u_1, u_2, \ldots u_n$, then,

$$N = f(u_1, u_2, u_3, u_4, ...u_n) \tag{1}$$

If the uncertainty in measured quantity N be ΔN and that for independent variables be $\Delta u_1, \Delta u_2, \Delta u_3, \Delta u_4, \ldots \Delta u_n$, then the uncertainty ΔN is given by,

$$\Delta N = \frac{\Delta N}{N} = \sqrt{[(\frac{\partial f}{\partial u_1})\Delta u_1]^2 + [(\frac{\partial f}{\partial u_2})\Delta u_2]^2 + ... + [(\frac{\partial f}{\partial u_n})\Delta u_n]^2} \tag{2}$$

where, $\pm\ \partial N$ is the error in N. The primary measured parameters in the experimental investigations are temperature, the flow rate of sCO_2, heat transfer coefficient, and operating pressure. Hence, the error in their individual measurements are estimated.

Uncertainty in temperature measurements

The temperature at different locations is measured using calibrated infrared camera. The maximum possible uncertainty in the case of temperature measurement is estimated from the minimum value of the measured quantity and its accuracy. The accuracy of infrared camera is $\pm$ 2 $^{\circ}C$. The minimum temperature measured during the experiment is 28 $^{\circ}C$, therefore the maximum uncertainty in temperature measurement is:

$$\frac{\partial T}{T} = \pm\frac{2}{28} = \pm 7.14\% \tag{3}$$

Uncertainty in heat transfer measurements

The heat power supplied to the system is calculated by measuring the electrical power delivered to the system as given by

$$\dot{Q} = V.I \tag{4}$$

$$\frac{\delta \dot{Q}}{\dot{Q}} = \sqrt{(\frac{\delta V}{V})^2 + (\frac{\delta I}{I})^2} \tag{5}$$

The heat transfer coefficient is calculated as

$$h = \dot{q}^{''}/(T_w - T_f) \tag{6}$$

Therefore, the uncertainty in the heat transfer coefficient is given by

$$\frac{\delta h}{h} = \sqrt{(\frac{\delta \Delta T}{\Delta T})^2 + (\frac{\delta \dot{q}^{''}}{\dot{q}^{''}})^2} \tag{7}$$

where $\Delta T = T_w - T_f$ and $\delta(\Delta T) = \sqrt{(\delta T_w)^2 + (\delta T_f)^2}$.

Uncertainty in mass flow rate measurements

The amount of sCO_2 transferred is obtained from Coriolis mass flow meter. The minimum value of hydrogen transferred was 2.57 g in 60 s. Hence, the maximum uncertainty in measurement of sCO_2 flow is:

$$\frac{\delta \dot{m}_{CO_2}}{m_{CO_2}} = \pm\sqrt{(\frac{0.001}{2.57})^2 + (\frac{0.1}{60})^2} \tag{8}$$

Uncertainty in pressure measurements

The supply pressure is set through pressure regulator by monitoring pressure transmitter. The minimum set pressure was 10 bar and the accuracy of pressure transmitter is ± 0.5 bar. Hence, the maximum uncertainty in supply pressure measurement is:

$$\frac{\delta p}{p} = \pm\frac{0.5}{10} = \pm 0.05 = \pm 5\% \tag{9}$$